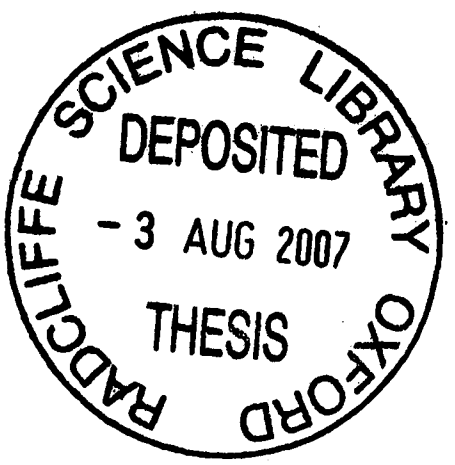
Diode Laser Absorption Studies of Gas Phase Species

A thesis submitted for the degree of
Doctor of Philosophy
at the University of Oxford

Lee James Thornton
Christ Church
Trinity Term, 2006



Abstract

Diode Laser Absorption Studies of Gas Phase Species

A Thesis submitted for the Degree of Doctor of Philosophy
Lee James Thornton, Christ Church, Oxford University
Trinity Term 2006

Sensitive and selective absorption spectroscopy techniques are applied to the detection of the excited species present in a range of low pressure inductively coupled plasmas (ICPs). The state densities and temperatures of various species are investigated across the parameter space accessible (plasma power and pressure) to aid in the understanding of the kinetic processes occurring. The experimental methods are based upon various forms of absorption spectroscopy, incorporating wavelength modulation and/or an optical enhancement cavity. The probing radiation is generated either directly using a CW diode laser or indirectly through the use of frequency conversion techniques.

The absolute number densities of all four levels ($1s_2$, $1s_3$, $1s_4$ & $1s_5$) present in the first excited manifold of atomic argon and neon are determined as a function of plasma operating conditions. A kinetic model is constructed to simulate these populations using cross-sections taken from the literature together with further measurements on the electron density and temperature obtained with a Langmuir probe. The model elucidates the importance of populational redistribution within the 1s manifold *via* excitation to the $2p_n$ levels, and highlights the mechanism of radiative decay (with radiative trapping taken into account) as the ultimate loss route for the 1s manifold. Measurements are made using cavity enhanced absorption spectroscopy (CEAS) on the $2p_5$ and $2p_6$ state densities in argon in order to draw additional conclusions about the nature of the discharge and to verify the kinetic model. The populations of the $1s_3$ and $1s_4$ states are probed in a neon plasma with helium, argon and nitrogen as a dopant gas, with the aim of manipulating the EEDFs. The addition of N_2 and Ar to the neon discharge resulted in a reduction in the $1s_3$ and $1s_4$ populations, while the addition of He resulted in an increase. These observations are consistent with a decrease and an increase, respectively, in the electron temperatures.

The populations of the vibrational levels $v = 0$, 1, 3, and 6 of the $A(^3\Sigma_u^+)$ state of molecular nitrogen are determined as a function of plasma operating conditions in a N_2 discharge using CEAS. A selection of vibrational bands within the $B(^3\Pi_g)\leftarrow A(^3\Sigma_u^+)$ system are probed, with calibration achieved using cavity ring-down spectroscopy. At 25 mTorr and 200 W power the populations of the $v = 0$, 1, 3, and 6 levels are $(1.31 \pm 0.16) \times 10^{11}$ cm^{-3}, $(8.44 \pm 1.01) \times 10^{10}$ cm^{-3}, $(2.83 \pm 0.34) \times 10^{10}$ cm^{-3} and $(5.27 \pm 0.63) \times 10^{9}$ cm^{-3}, respectively, corresponding to a vibrational temperature of 3600 ± 150 K. In addition, the observation of the $N_2^+(X^2\Sigma_g^+)$ molecular ion in $v = 0$ using both CEAS and CEAS in combination with wavelength modulation spectroscopy is presented (which is found to improve the sensitivity for this measurement by approximately an order of magnitude). At 10 mTorr and 400 W the total population in $N_2^+(X^2\Sigma g^+, v = 0)$ is $(1.26 \pm 0.15) \times 10^9$ molecules cm^{-3}, consistent with data obtained using a Langmuir probe.

The density of oxygen atoms present in their ground state ($^3P_2$) is investigated using the technique of CEAS, and at 500 W and 100 mTorr the concentration is estimated to be $(2.2 \pm 0.3) \times 10^{14}$ cm^{-3}. This corresponds to a dissociation efficiency, δ, of O_2 of 0.06. Furthermore, a difference frequency generation (DFG) system is constructed to generate radiation at 1.9 μm in order to probe the (0,0) band of the $O_2(b^1\Sigma_g^+\leftarrow a^1\Delta_g)$ quadrupolar system. A minimum detectable absorbance of 1.3×10^{-5} over a 10 cm cell is determined by calibrating the system on an ammonia absorption, placing a limit of 1.8×10^{16} cm^{-3} on the total $v = 0$ population of $O_2(a^1\Delta_g)$ in a microwave discharge operating with 5 Torr pure O_2.

Acknowledgments

Many thanks must firstly go to Prof. Gus Hancock for granting me a position in his research group and providing the funding, equipment and ideas necessary for the completion of this thesis. I am also immensely grateful to him for affording many opportunities to attend conferences; I will never forget what I can remember about my times in Toronto, Brindisi, Les Houches, Bad Honef, Norwich, Bristol and Edinburgh.

The invaluable input and guidance I have received over the course of the last five years from Rob Peverall and Grant Ritchie must also be mentioned. Their intelligent suggestions, continued patience and experimental know-how are much appreciated, and by keeping a constant eye on the pace of my research they have enabled the production of a thesis to the best of my ability. Without their assistance, I would not be where I am today.

To the fellow plasma lab researchers over the years I am also indebted. One cannot easily forget the wit, charm and intelligence of Ben Bakowski, who provided inspiration for my decision to continue studying within the Hancock group. Thanks also to the various part II's and summer students I have worked with, especially Stuart Lumsden, Sarah Prince and Martin Bell, for their assistance in the construction of several of the experiments described within this thesis.

The research group as a whole has provided an entertaining backdrop (to say the least) to my graduate years in Oxford. I have greatly enjoyed the various banter and company on our many, many social occasions.

Finally, thanks to my parents for their continued and unwavering love and support throughout my university education.

Contents

1. Introduction 1

1.1 Defining a Plasma 2

1.2 Creation of Plasmas 3

1.2.1 Capacitively Coupled Plasmas (CCPs) 4

1.2.2 Inductively Coupled Plasmas (ICPs) 5

1.2.3 Other Plasma Sources 6

1.2.4 The ICP Chamber 7

1.3 Discharge Structure 9

1.3.1 Debye Length 9

1.3.2 Sheath Formation 11

1.4 Plasma Kinetics 13

1.4.1 Plasma Density 13

1.4.2 Temperatures and Energy Distribution Functions (EDFs) 13

1.5 Experimental Methods 16

1.5.1 Electrical Probes 17

1.5.2 Optical Techniques 19

1.5.2.1 Optical Emission Spectroscopy (OES) 19

1.5.2.2 Laser Induced Fluorescence (LIF) 20

1.5.2.3 Laser Optogalvanic Spectroscopy (LOGS) 21

1.5.2.4 Thomson Scattering 21

1.5.3 Absorption Spectroscopy 22

1.5.3.1 Homodyne Absorption Spectroscopy 24

1.5.3.2 Line Broadening 25

1.5.3.3 Cross-sections 27

1.5.3.4 Sensitivity and Noise 28

1.5.3.5 Polarization Spectroscopy 29

1.6 Aims 31

References 33

2. The techniques of sensitive and selective absorption spectroscopy 35

2.1 Generation of Radiation 36

2.1.1 Diode Lasers 36

2.1.2 Background to Non-Linear Optical Techniques 38
2.1.3 Phase Matching Criterion 39
2.1.4 Quasi Phase Matching 42
2.1.5 Second Harmonic Generation (SHG) 43
2.1.6 Demonstration of SHG using Quasi Phase Matching 44
2.1.7 Sum and Difference Frequency Generation (SFG & DFG) 46
2.2 Modulation Techniques 47
2.2.1 General Theory 47
2.2.2 Frequency Modulation Spectroscopy (FMS) 49
2.2.3 Wavelength Modulation Spectroscopy (WMS) 50
2.3 Cavity Methods 53
2.3.1 Optical Cavities 54
2.3.2 Fabry-Perot Cavity 56
2.3.3 Optical Modes 58
2.3.4 Techniques 1: Cavity Ring-down Spectroscopy (CRDS) 58
2.3.5 Techniques 2: Cavity Enhanced Absorption Spectroscopy (CEAS) 61
2.3.6 Intracavity Laser Absorption Spectroscopy (ICLAS) 63
References 65

3. Noble gas discharges: Key elements of the chemistry of Ne and Ar plasmas 68
3.1 Introduction 69
3.2 Experimental 72
3.3 Results 74
3.3.1 Power Variation 76
3.3.2 Pressure Variation 77
3.3.3 Electrical Measurements 78
3.4 Discussion 79
3.4.1 Argon Modelling 80
3.4.2 Comparison to Neon 87
3.5 Further Study 91
3.5.1 Argon $2p_5$ and $2p_6$ Concentrations 92
3.5.2 Manipulating EEDFs in a Neon Plasma 95

3.6 Summary 102
References 104

4. Molecular discharges I: The vibrational distribution of $N_2(A^3\Sigma_u^+)$ and detection of the $N_2^+(X^2\Sigma_g^+)$ ion in a nitrogen plasma 106
4.1 Introduction 107
4.2 Nitrogen Spectroscopy 110
4.2.1 Spectroscopy of N_2 111
4.2.2 Spectroscopy of N_2^+ 113
4.3 Experimental 115
4.4 Results 116
4.4.1 $N_2(A)$ Detection 116
4.4.2 $N_2^+(X)$ Detection 122
4.5 Discussion 125
4.6 Summary 131
References 133

5. Molecular discharges II: Detection of $O(^3P_2)$ and $O_2(^1\Delta_g)$ in an oxygen plasma 135
5.1 Introduction 136
5.2 Experimental 142
5.2.1 $O(^3P_2)$ Atom Detection 142
5.2.2 $O_2(a^1\Delta_g)$ Detection 143
5.3 Results 146
5.3.1 $O(^3P_2)$ Atom Detection 146
5.3.2 Measurements of $O_2(a^1\Delta_g)$ 147
5.4 Discussion 152
5.5 Summary 158
References 160

Glossary

AOM	Acousto Optic Modulator
ASE	Amplified Spontaneous Emission
DFB	Distributed Feedback
CCP	Capacitively Coupled Plasma
CEAS	Cavity Enhanced Absorption Spectroscopy
COIL	Chemical Oxygen Iodine Laser
CRDS	Cavity Ring-down Spectroscopy
CW	Continuous Wave
DC	Direct Current
DFG	Difference Frequency Generation
EEDF	Electron Energy Distribution Function
EEPF	Electron Energy Probability Function
FMS	Frequency Modulation Spectroscopy
FWHM	Full Width Half Maximum
HR	High Reflectivity
ICOS	Integrated Cavity Output Spectroscopy
ICLAS	Intra-Cavity Laser Absorption Spectroscopy
ICP	Inductively Coupled Plasma
LIF	Laser Induced Fluorescence
LOGS	Laser Optogalvanic Spectroscopy
OES	Optical Emission Spectroscopy
PMT	Photon Multiplier Tube
RF	Radio Frequency
SFG	Sum Frequency Generation
SHG	Second Harmonic Generation
S/N	Signal-to-Noise ratio
TALIF	Two Photon Laser Induced Fluorescence
TEM	Transverse Electromagnetic
VUVAS	Vacuum Ultraviolet Absorption Spectroscopy
WMS	Wavelength Modulation Spectroscopy

All wavelengths given in this thesis are quoted for a vacuum (unless otherwise stated)

Chapter 1

Introduction

For many years, low temperature plasmas have been a constant focus of research interest which has highlighted their unique chemical kinetics and spatial structure. However, despite this intense scrutiny the operation of such systems is far from understood and they are often treated pragmatically. The utility they have found in manufacturing and industrial processes includes such diverse applications as diamond deposition, surface hardening and enhancement, etching and the treatment of harmful waste. At the high end of the energy and particle density spectrum, fusion plasma research is of recent renewed interest due to its potential as an energy source. Nature provides us with plasmas of her own; examples include aurorae, planetary ionospheres, flames, stars and the interstellar medium.

The various excited states created in plasma discharges, and their behaviour under changing plasma conditions, is the focus of the research presented in this thesis. A wide range of spectroscopic techniques are applied to different plasmas (both of atomic and molecular origin) to yield information on the concentrations and temperatures of the various species present. Where appropriate, these data are used in the construction of kinetic models (in combination with cross-sections taken from the literature) in order to identify and understand the various processes occurring and their relative importance within the discharge.

1.1 Defining a Plasma

A plasma is a system of interacting ions, electrons and neutral species that exhibits collective behaviour and is, as a whole, electrically neutral. This latter point can be expressed using the principle of quasineutrality, which states that within the total volume of the plasma there is an equal number of positively and negatively charged species. However, this allows for local variations in the charge balance which gives rise to some interesting facets to the plasma structure. The two most important plasma parameters are the heavy particle density and electron temperature, which can be used to categorise the entire array of plasma types that have either been created in the laboratory or observed in nature, a selection of which are shown in figure 1.1[1].

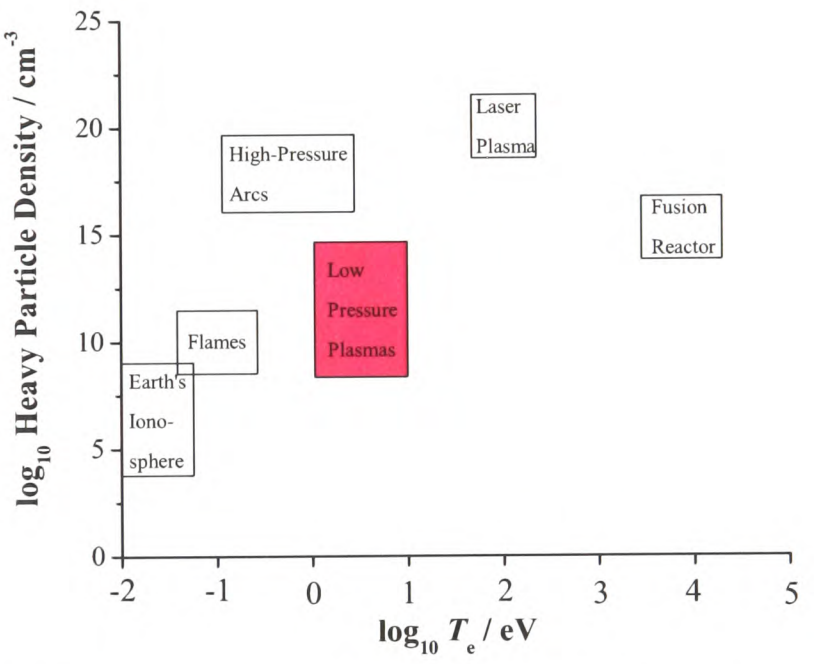


Figure 1.1: Various types of plasma observed in nature and in the laboratory, parameterized by heavy particle density and electron temperature, T_e.

In low pressure plasmas, the neutral species are composed of atoms and molecules in a variety of electronically excited states; in the case of molecules, rotational and vibrational excitation can also occur. The ions are generally singly charged and can be either negative or positive, although the latter is a far more common occurrence. Energy is transferred in a plasma *via* non-radiative as well as radiative processes. Metastable energy levels can be quenched or excited to higher energy states through collisions with other excited states or electrons, while radiative states emit radiation which can subsequently be reabsorbed before being lost to the chamber walls.

A discharge in its simplest form consists of a voltage source that drives a current through a low pressure gas present between two parallel conducting plates (electrodes). The gas in essence 'breaks down' to form a plasma which is weakly ionised (the charged species density comprises only a small fraction of the neutral gas density). Such plasmas are termed steady state in that they are continually driven through the coupling of energy from a constant power source. Note the use of the term 'discharge' in this context, describing the formation of a plasma through the input of energy; often the word 'discharge' is used interchangeably in place of 'plasma'.

This thesis deals with weakly ionised plasmas which have the following features[2]:

1) They are electrically driven (*via* a radio frequency (RF) in the case here)
2) Charged particle collisions with neutral gas molecules are important
3) There are boundaries at which surface losses are important
4) Ionisation of neutrals sustains the plasma in the steady state
5) The electrons are not in thermal equilibrium with the ions or neutrals

These types of discharge have found utility in the materials processing industry, where they are used to enhance the surface properties of materials (such as hardening[3] or thin film deposition[4,5]), and in the manufacture of integrated circuits by providing a method for anisotropic etching[6]. Uses also extend to the biomedical industry in the creation of new materials, and in toxic waste management for the destruction of harmful chemicals. Fusion plasmas, which consist solely of electrons and ions, are in true thermal equilibrium and are currently a source of major research interest. As can been seen from figure 1.1, the parameters of fusion plasmas in terms of particle density and electron temperature are many orders of magnitude greater than those studied here.

1.2 Creation of Plasmas

Radio frequency (RF) discharges are the most commonly used type in industry; the name derives from the fact that such discharges use MHz RF power sources to sustain them. The energy from the source is deposited almost exclusively into the electrons due to their fast response to the applied EM field (a consequence of their low mass), resulting in a non-equilibrium discharge with $T_e >> T_i, T_g$. The two main approaches of coupling power

into RF discharges are through either capacitive or inductive means. These are outlined below, together with a brief overview of other discharge setups and a technical description of the chamber used for the experiments detailed in this thesis.

1.2.1 Capacitively Coupled Plasmas (CCPs)

Figure 1.2 shows an idealised CCP chamber in plane-parallel geometry, however other coaxial geometries such as the 'hexode' are in common use. In this system, two electrodes are separated by a fixed distance inside an evacuated chamber. Gas is flowed into the chamber and the application of RF power creates a discharge; effluent gasses are removed by the vacuum pump. A matching network consisting of two capacitors (one in series and one in parallel) connects the plasma chamber to the power source and permits more efficient power coupling by impedance matching. Power is generally provided at a frequency of 13.56 MHz (although other frequencies are used) up to 2 kW, and water cooling of the chamber is needed to remove the excess heat.

A capacitive discharge is initially struck by the application of the RF potential across the two electrodes, creating an electric field which ionises the species present with the lowest ionisation energy (commonly spurious contaminants such as water). The resultant ion/electron pair undergo acceleration, and their ionising collisions and the consequent acceleration of the new ion/electron pair (and so on) sustain the discharge in an avalanche process. The use of EM frequencies lower than ~ 1 MHz is not possible as in such a regime the accelerating ions and electrons neutralise the potential difference between the two electrodes[7]. The loss of energy within the discharge through the various chemical processes, together with the emission of radiation and collisions with the walls, necessitates the continual input of power.

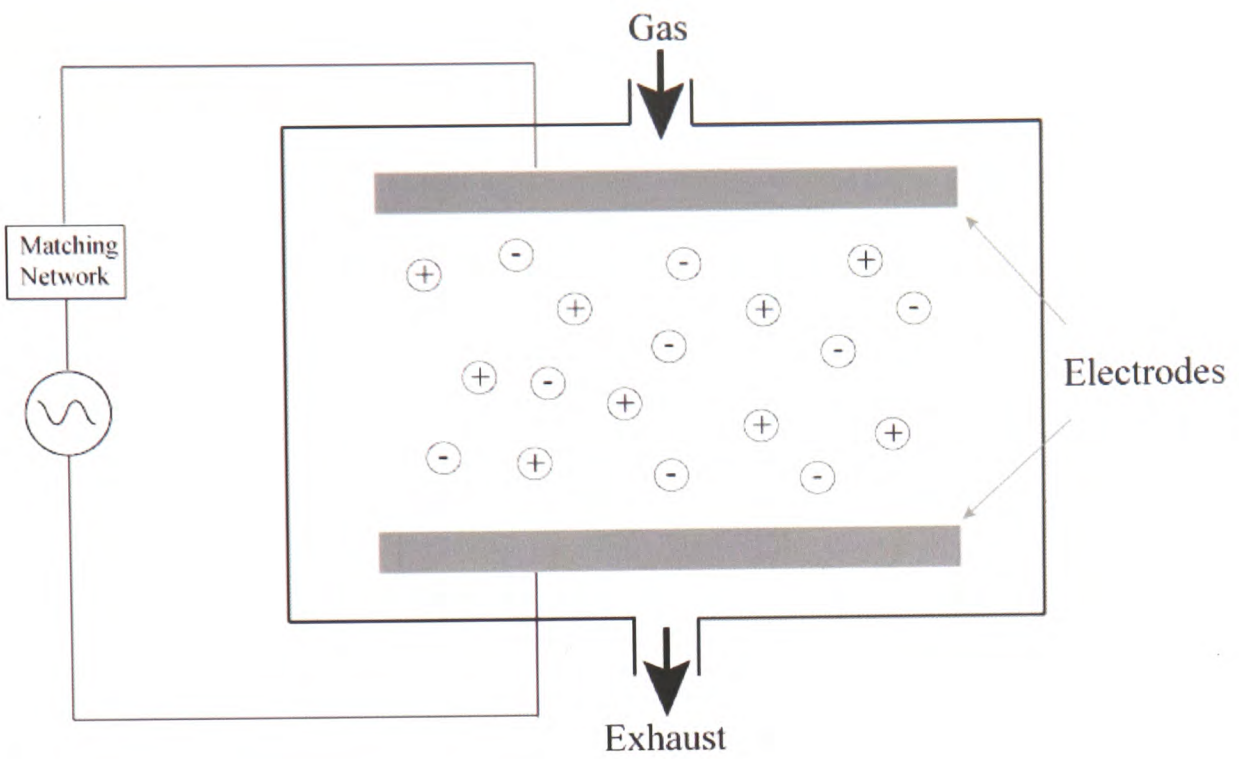


Figure 1.2: Schematic of a CCP discharge.

1.2.2 Inductively Coupled Plasmas (ICPs)

One of the major disadvantages of CCP chambers arises from the large electric fields that necessarily exist between the different surfaces, causing the formation of large sheath regions (see section 1.3). This can be reduced by coupling power into the discharge through a dielectric window resulting in much lower surface potentials and hence smaller sheaths[8]. Such systems are termed inductively coupled plasma chambers, and while operating in the same pressure regime as CCP discharges, generally have higher plasma densities (i.e. a higher electron/neutral gas density ratio)[9,10]. It is also possible to control the ion energy in an ICP through independent biasing of the lower (unpowered) electrode, allowing control of the plasma chemistry in this region[11].

Figure 1.3 shows a schematic of an ICP chamber with power coupling through the dielectric window using a 'stovetop' coil for the RF antenna[12]. ICPs are often more spatially uniform in terms of plasma density[13,14,15], and the absence of metal electrodes inside the plasma chamber reduces contamination (of particular importance in plasma processing). Magnetic confinement of ICPs (where permanent magnets are placed inside the chamber walls) enables an even greater plasma density to be achieved, and has been shown in a RF argon discharge to increase the ion density by a factor of 2 [16].

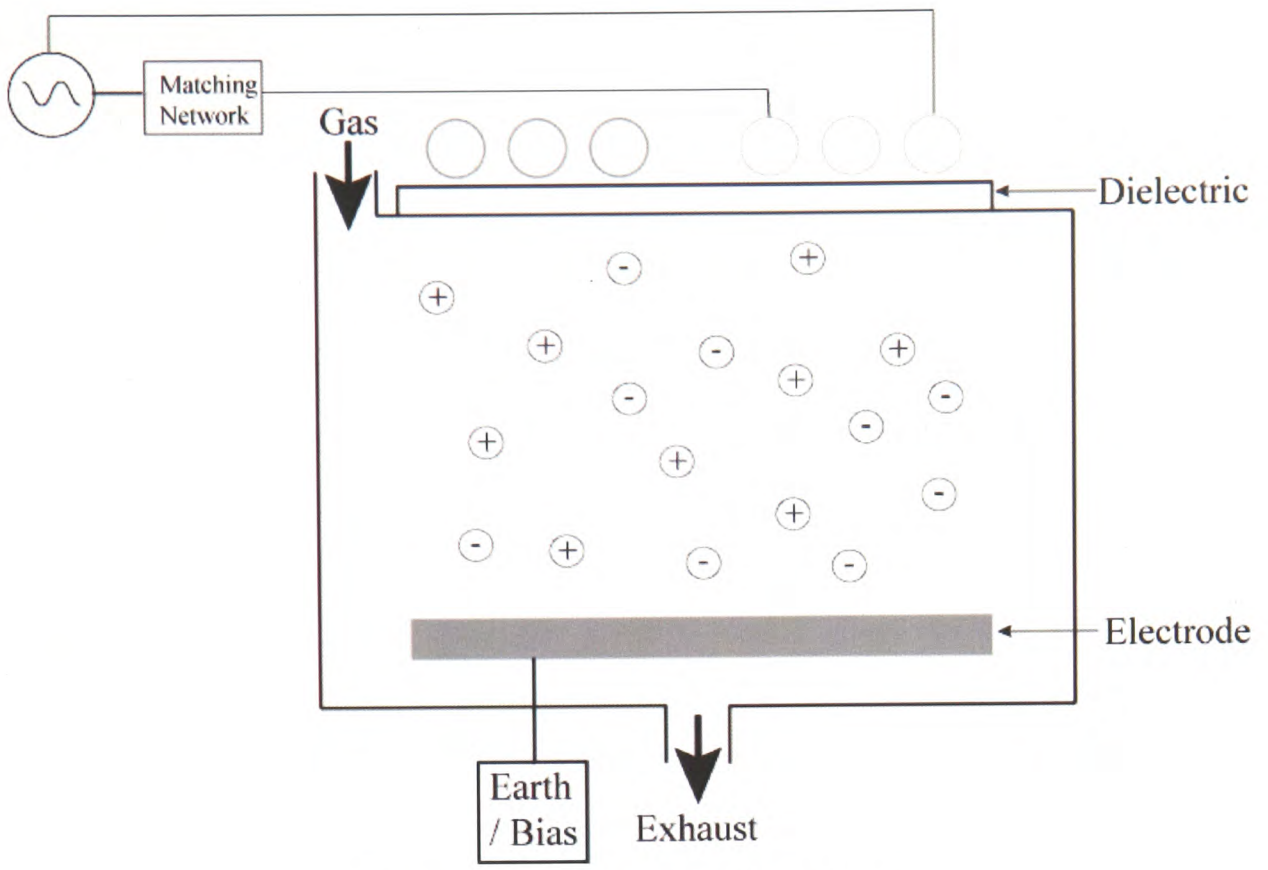


Figure 1.3: Schematic of an ICP discharge.

1.2.3 Other Plasma Sources

Several varieties based around the inductively coupled discharge exist which differ by the means in which power is coupled into the plasma. The planar discharge, where the antenna possesses a "stovetop" configuration, is the simplest form of an ICP (shown in figure 1.3), and is the type used in the experiments presented in this thesis. A more complicated setup is the electron cyclotron resonance (ECR) source, in which microwave power (~ 2450 MHz) is injected axially into a cylindrical source chamber surrounded by one or more electromagnetic coils which provide a varying DC magnetic field. This generates a circularly polarised wave that propagates into a resonance zone where the wave is absorbed and the resultant plasma generated flows into a process chamber.

A dielectric cylinder surrounded by a weak DC magnetic field and a RF driven antenna forms the initiation chamber in a helicon source (another commonly used discharge system), in which the helicon wave created undergoes a resonant wave-particle interaction leading to a transfer of energy to the plasma. An external helix and conducting chamber surround the dielectric source chamber in a helical resonator allowing support of an EM wave with a low phase velocity, and efficient power coupling is achieved by excitation of a resonant axial mode. These varieties of inductive discharge differ primarily

from the one shown in figure 1.3 in that they require a DC magnetic field to operate, complicating the experimental setup.

1.2.4 The ICP Chamber

The studies presented within this thesis were all conducted using an ICP chamber designed and constructed in the Physical and Theoretical Chemistry Laboratory, Oxford University. The chamber, shown schematically in figure 1.4[17], is comprised of a) a power coupling system, b) an aluminium main reactor chamber and c) gas handling networks. The internal dimensions of the chamber are 350 mm in diameter and 275 mm in height, with optical or electrical access allowed through twelve windows of 15 mm by 65 mm located in two perpendicular pairs at three different heights. A further window is located at the top of the chamber. Magnetic confinement is achieved by 128 high flux magnets contained within the chamber walls, which, together with chamber lid, are cooled by refrigerated water. The lower electrode can be driven, earthed or left floating; for the experiments described within this thesis it was earthed.

The desired gas mixture is fed into the chamber by equally spaced inlets around the outer diameter of the lid, with the flow rate controlled by a mass flow device (Tylan R023). Upon activation, the chamber is rough pumped to around 1 Torr using a rotary pump (Edwards E2M2), with the pressure measured using a Pirani gauge. A bypass value is subsequently closed allowing the rotary pump to back a turbo molecular fan pump (Varian V70D) which lowers the pressure to the operating region of 5 mTorr – 100 mTorr. The pressure inside the chamber is monitored (using a capacitance manometer – Millipore CMH4) and kept constant using active control of a butterfly value.

An analogue RF power supply at 13.56 MHz (ENI HF-300) provides power (up to 500 W) to the chamber by means of a 1½ turn copper coil (6 mm in diameter and water cooled) with a stovetop configuration and an internal diameter of 120 mm and an external diameter of 180 mm. A pyrex disc of 12 mm thickness and 240 mm diameter acts as the dielectric by separating the inductor coil from the plasma. The matching network allows maximisation of power transfer by matching the impedance of the plasma system with that of the RF power source. This consists of two variable capacitors (one in series and one in parallel with the inductor coil) contained inside an aluminium can (acting as a Faraday cage) to minimise interference from the plasma itself. The gas handling system, water

cooling system and RF power supply are interlocked and supervised by a home built programmable controller[18].

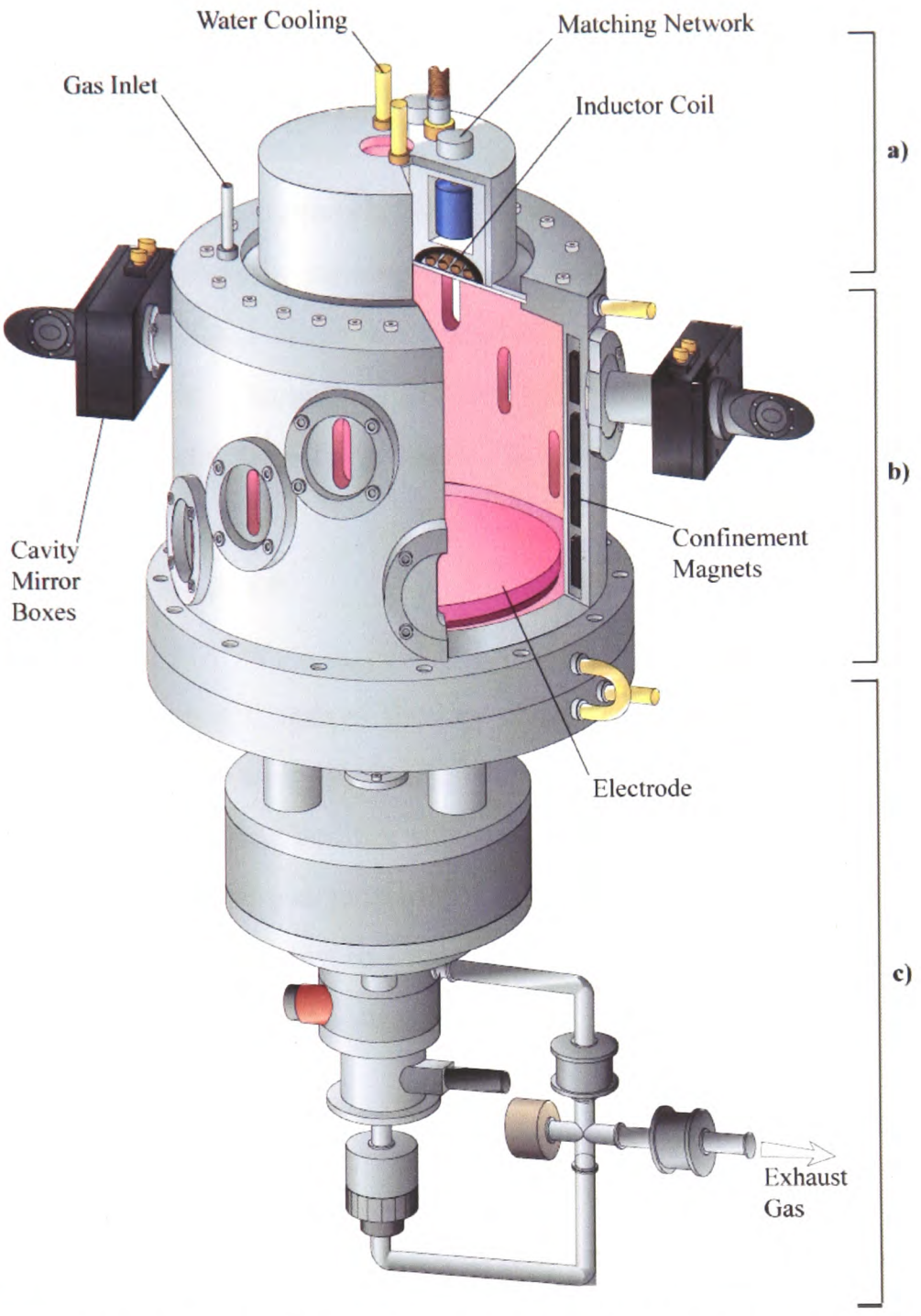


Figure 1.4: Schematic of the ICP chamber used for the experiments described within this thesis; the mirror boxes contain the cavity mirrors utilized in CRDS and CEAS experiments (see section 2.3).

Despite the fact that this is nominally an ICP chamber, such systems usually operate bimodally, with a low density capacitive (E) mode and a high density inductive (H) mode[19]. Initially, the discharge is struck in the E-mode with the large electric fields required provided by the potential difference between the loops of the inductor coil. As the power is increased, a critical point (dependent on the feedstock gas and its pressure) is reached at which the electron density is sufficiently high to support the H-mode. This is

observed as a change in the plasma behaviour, and has been studied using optical emission[20], Langmuir probes[21] and a combination of the two methods[22]. The nature of the H-mode is electromagnetic in which the plasma is sustained by its response to the induced azimuthal electric field produced by the oscillating magnetic field in the inductor coil. The changeover conditions between the E- and H- modes, together with their hysteresis, has been studied in this chamber previously by monitoring the optical emission and reflected power through the matching network, thus allowing a characterisation of the ICP chamber's characteristics whilst sustaining a N_2 discharge[17,23]. Unless otherwise stated, the measurements described in this thesis were carried out with plasma conditions consistent with the inductive H-mode. Changeover regions have been noted in chapter 3 for argon and neon plasmas, and in chapter 4 for nitrogen discharges.

1.3 Discharge Structure

As stated in section 1.1, one of the key characteristics of low pressure plasmas is the importance of surface losses by the various species. This, combined with the presence of potentials between the plasma and the surfaces, leads to a non-uniform structure inside the discharge. However, before a discussion of this can take place, a return must be made to the assumption of quasineutrality in order to outline some of the important properties and parameters that can describe a plasma.

1.3.1 Debye Length

The Debye length, λ_D, is the characteristic length scale in a plasma and is the distance over which significant changes in charge densities can exist. To determine this parameter, consider the insertion of a conducting probe into an infinitely extending plasma of density $n_e = n_i = n_0$ (where n_e, n_i and n_0 are the electron, ion and neutral gas densities, respectively). If this probe is biased to a negative potential, positively charged ions will surround it (with electrons repelled) in an envelope in order to shield the potential from the rest of the plasma in a process known as Debye shielding. The electron density in the region immediately adjacent to the probe will be reduced and will tend towards the bulk electron density at greater distances, tracking the change in the potential $\Phi(x)$ (see figure

1.5). To determine this potential and electron density, Poisson's equation is invoked, which in one dimension can be written as

$$\frac{\mathrm{d}^2\Phi}{\mathrm{d}x^2} = -\frac{e}{\epsilon_0}\left(n_i(x) - n_e(x)\right). \tag{1.1}$$

Combining this with the Boltzmann relation

$$n_e = n_e^0 e^{-\Phi(x)/T_e}, \tag{1.2}$$

where n_e^0 is the electron density at $\Phi(x) = 0$ and T_e is the electron temperature in eV, and taking $n_i = n_e^0$ (and assuming immobile ions), Poisson's equation can now be expressed as

$$\frac{\mathrm{d}^2\Phi}{\mathrm{d}x^2} = \frac{en_e^0}{\epsilon_0}\left(e^{\Phi(x)/T_e} - 1\right). \tag{1.3}$$

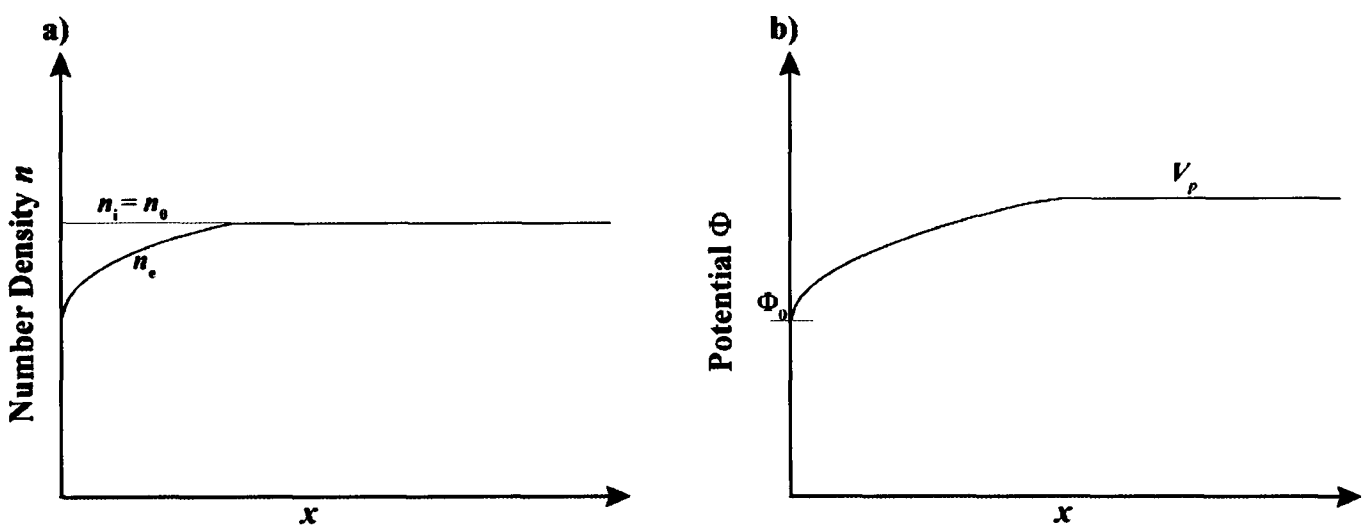


Figure 1.5: The change in a) number density and b) potential with distance from a probe biased to a potential Φ_0.

Expanding the exponential in equation (1.3) in a Taylor series for $\Phi(x) << T_e$, and applying the boundary condition $\Phi(\pm\infty) = 0$, yields the solution

$$\Phi(x) = \Phi_0 e^{-|x|/\lambda_D}. \tag{1.4}$$

The Debye length is thus given by equation (1.5), and characterizes the dimensions over which quasineutrality will be maintained. This parameter can also be applied to help define the term plasma, in that the Debye length of a collection of charges must be small compared to the geometry of the discharge. For typical plasma parameters of $T_e = 2$ eV and $n_e^0 = 10^{10}$ cm^{-3}, $\lambda_D = 0.11$ mm.

$$\lambda_D = \left(\frac{\epsilon_0 T_e}{e n_e^0} \right)^{1/2} \tag{1.5}$$

1.3.2 Sheath Formation

The bulk region of a plasma is joined to the chamber walls (and indeed any other surface) by regions known as sheaths, characterised by their absence of optical emission (hence they are also referred to as dark space). To understand their formation, consider a plasma with $n_e = n_i$ confined between two grounded walls; as the net charge density is zero, the electric potential and electric field are zero everywhere. The electrons have a thermal velocity at least 100 times that of the ions, and hence are lost rapidly in the regions near the walls. On a short timescale, only some electrons are lost and the potential decreases towards the walls in a manner shown by figure 1.5. This leads to the formation of thin positive sheath regions in which $n_i >> n_e$, with the resultant electric fields pointing from the plasma to the wall. Thus, the force acting on the electrons repels them back into the plasma, and any positive ions that enter the sheath are accelerated towards the walls. If the walls were not grounded, they would reach some floating potential, V_f, and by taking the plasma potential as V_p, $(V_p - V_f)$ would only need to be a few T_e to confine the majority of the electrons.

A more mathematical understanding of the sheath region can be constructed on the assumptions that the electrons are Maxwellian at a temperature T_e, the ions are cold ($T_i = 0$) and $n_e(0) = n_i(0)$ at the plasma-sheath interface. If the ions have a velocity u_s at $\Phi(0) = 0$, ion energy conservation across the sheath (on the assumption there are no collisions) yields

$$\frac{1}{2} M u^2(x) = \frac{1}{2} M u_s^2 - e\Phi(x), \tag{1.6}$$

where M is the mass of the ions. Provided there is no ionization in the sheath, the continuity of ion flux is given by equation (1.7), where n_{is} is the ion density at the sheath edge.

$$n_i(x)u(x) = n_{is}u_s \tag{1.7}$$

Combining equations (1.6) and (1.7) with Poisson's equation, and using an electron density given by the Boltzmann relation (equation (1.2)) yields equation (1.8) (on setting $n_{es} = n_{is} = n_i$ at the sheath edge).

$$\frac{d^2\Phi}{dx^2} = \frac{en_s}{\epsilon_0}\left[e^{\Phi/T_e} - \left(1 - \frac{2e\Phi}{Mu_s^2}\right)^{-1/2}\right] \tag{1.8}$$

Stable solutions to equation (1.8) only exist for sufficiently large u_s, defined by a fulfillment of the Bohm sheath criterion given in equation (1.9). This necessitates the creation of a pre-sheath region in which the ions are accelerated by an additional, albeit small, electric field. The resultant potentials and densities this creates are shown in figure 1.6.

$$u_s \geq u_B = \left(\frac{eT_e}{M}\right)^{1/2} \tag{1.9}$$

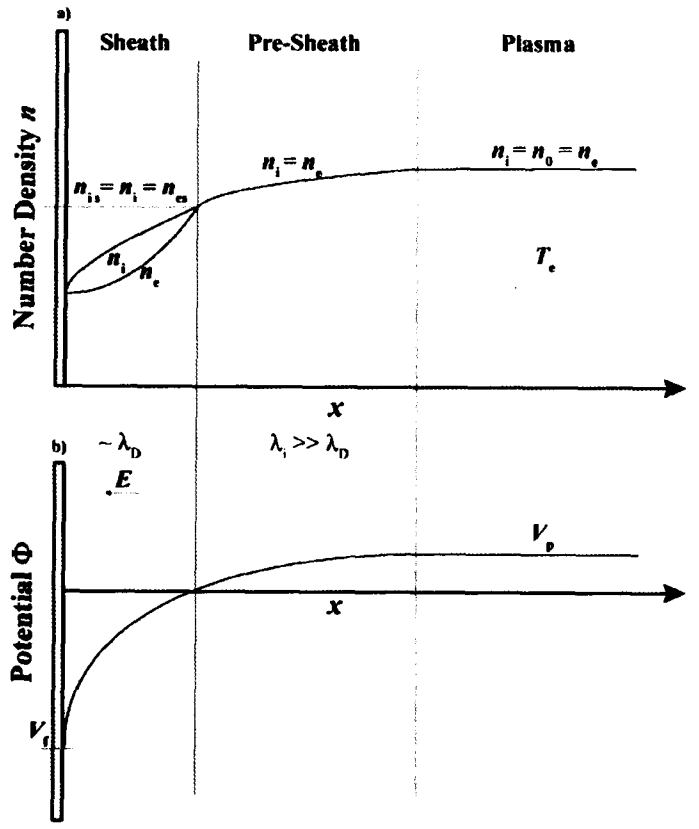


Figure 1.6: The variation near a wall of a) number density and b) potential, leading to the formation of the sheath and pre-sheath regions.

1.4 Plasma Kinetics

The two most important parameters that characterise the plasma kinetics are the electron density and electron temperature. Whilst the concentrations of the various other excited states, including ions and metastables, play key roles in the discharge chemistry, ultimately the electron density and temperature determine the rate of formation and loss of these states and thus drive the kinetics of the discharge.

1.4.1 Plasma Density

This thesis is concerned with low pressure, non-equilibrium plasmas which are characterised by a pressure in the 1 mTorr – 1 Torr region with electron temperatures, T_e, < 10 eV and with $T_e >> T_g$, T_i. The plasma density (number of charged species per unit volume) can be used to define this type of plasma on the assumption that electrons make up the vast majority of the negatively charged species (such discharges are referred to as electropositive). On the assumption of quasineutrality equation (1.10) is valid, where V is the plasma volume and n_i and n_e are the ion and electron densities, respectively, and the sum j is over the multiple types of positively charged (z_j) species.

$$\int n_e . dV = \int \sum_j z_j n_{i,j} . dV \qquad (1.10)$$

If one considers that under the discharge regimes studied in this thesis the plasmas are composed of singly charged species, $n_i = n_e$ can be adopted as the condition for quasineutrality. This allows for the use of an alternative description of a plasma in terms of the degree of ionization, $\delta_i = n_i/n_g$, where n_g is the plasma gas density. The value of δ_i is typically $10^{-4} – 10^{-6}$ in a low pressure, non equilibrium plasma[2].

1.4.2 Temperatures and Energy Distribution Functions (EDFs)

The temperature of each species in the plasma will influence the various kinetic processes in which they are involved (denoted as T_e, T_i and T_g for the electrons, ions and neutral gas species, respectively). The ions and neutrals are in thermal equilibrium and

merely exchange energy by collisions, and hence can truly be described by a temperature (i.e. they possess a Boltzmann distribution of velocities). The electrons have a much higher energy as their mobility allows them to respond efficiently to the applied RF radiation and hence absorb the vast majority of the applied power. In order to possess a thermal distribution, the electron-electron collisions would need to occur on a timescale faster than the heating provided by the RF field; in low pressure discharges this will clearly not be the case. Typical values in a low pressure plasma of T_i and T_g are of the order of 300 – 1000 K, while T_e lies in the region of 20000 K. However, assigning the electrons a temperature is an oversimplification as many processes exist in a plasma environment that can significantly alter the electron energy distribution functions (EEDFs) from that of a Maxwellian distribution, consequences of which can be seen throughout the experimental results presented in this thesis.

A general form of the EEDF in isotropic velocity space is given by Gudmundson[24], shown by equation (1.11), where E is the electron energy and c_1 and c_2 are obtained from the boundary condition of $\langle E \rangle = 3/2 T_e$ (which also allows the electron 'temperature' to be reported in terms of its average energy) and through normalizing the distribution (shown by equations (1.12) and (1.13)). The parameter x characterizes the shape of the distribution.

$$f(E)\mathrm{d}E = c_1 \sqrt{E} e^{-c_2 E^2 / \langle E \rangle^x} \tag{1.11}$$

$$c_1 \int_0^\infty \sqrt{E} e^{-c_2 E^2 / \langle E \rangle^x} \mathrm{d}E = 1 \tag{1.12}$$

$$c_1 = \frac{x}{\langle E \rangle^{3/2}} \frac{\Gamma(\varsigma_2)^{3/2}}{\Gamma(\varsigma_1)^{5/2}} \quad \text{and} \quad c_2 = \frac{1}{\langle E \rangle^x} \left(\frac{\Gamma(\varsigma_2)}{\Gamma(\varsigma_1)} \right)^x \tag{1.13}$$

The symbol Γ represents a gamma function given by equation (1.14), where $\zeta_1 = 3/(2x)$ and $\zeta_2 = 5/(2x)$.

$$\Gamma(\varsigma) = \int_0^\infty t^{\varsigma - 1} e^{-t} \mathrm{d}t \tag{1.14}$$

The resulting distributions for x = 1, 2, 3 and 4 are shown in figure 1.7a with $\langle E \rangle = 5$ eV . It should be noted that x = 1 corresponds to a Maxwellian distribution, x = 2 to a Druyvesteyn[25] and $x = 4$ to the $F4$ distribution[26].

The actual value of $\langle E \rangle$ depends to varying degrees on the plasma parameters (as does the value of x, although generally less dramatically). An increase in T_e is generally seen with plasma power, a decrease with plasma pressure, and the addition of a dopant gas often alters the EEDF in a complicated manner (see sections 3.4 and 3.5). The ability to control the EEDF is desirable due to its influence on the rate constant for electron impact excitation or ionization reactions (k^{EI}), shown in equation (1.15), where $\sigma(E)$ is the (energy dependent) electron impact cross-section and $f(E)$ the EEDF.

$$k^{EI} = \sqrt{\frac{2}{m_e}} \int_0^\infty E^{1/2} \sigma(E) f(E) \mathrm{d}E \qquad (1.15)$$

Whilst electron impact excitation and ionisation are two important processes that occur in the plasma kinetics, many other reactions exist in which electron impact plays a role. These include electron impact dissociation, electron-ion recombination and more indirectly Penning ionisation (ionisation from an electronically excited state).

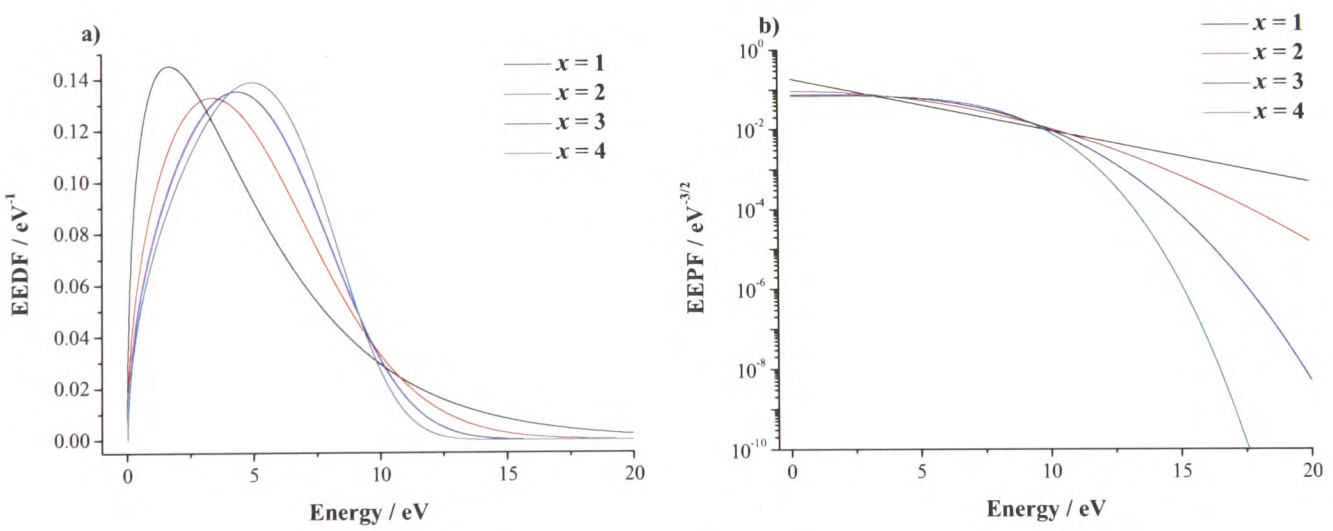


Figure 1.7: Simulated a) EEDFs and b) EEPFs using equation (1.11) with <E> = 5 eV and x = 1, 2, 3 & 4.

At low electron temperatures of $T_e \sim 2$ eV, a significant fraction of the electrons will still possess enough energy to be involved in electron impact reactions (which often have barriers over 10 eV). This is particularly relevant to noble gas discharges, where

typically the lowest lying electronically excited state lies at energies over 10 eV (with ionisation occurring several eVs higher). In these instances, a depletion of the electrons in the high energy tail of the EEDF occurs resulting in complex EEDFs which can not always be expressed using equation (1.11) and a changing value of x. High energy electrons can also be lost to the walls *via* diffusion, although this can typically be reduced by magnetic confinement. In molecular discharges, the EEDF is often much more complicated as the existence of a vast array of electronic and vibrational levels cause a depletion of the electrons at different energy regions within the EEDF.

Numerous other EEDFs have been proposed, most notably two and three temperature distributions which can formally be described using two or more groups of electrons each with their own temperature and density. In the specific case of a two temperature bi-Maxwellian distribution, the EEDF can be described by equation (1.16), where $f(E, T_e)$ and $f(E, T_e')$ are the two Maxwellian distributions and α is the fractional component of the latter.

$$f(E)\mathrm{d}E = (1-\alpha) f(E,T_e) + \alpha f(E,T_e') \qquad (1.16)$$

An alternative way to express the EEDF is using the electron energy probability function (EEPF) defined by $p(E) = \sqrt{E} f(E)$. Figure 1.7b shows the EEPF for the distribution given by equation (1.11) with $\langle E \rangle = 5\,\mathrm{eV}$ and x = 1, 2, 3 and 4. Deviations from Maxwellian behaviour appear as deviations from linearity in the EEPF. Kiehlbauch & Graves[9] demonstrate the utility of EEPFs in their simulations which parameterize inductively coupled argon plasmas. Gudmundsson[8] demonstrates a similar approach in fitting an EEPF to Langmuir probe data measured in a H_2/Ar planar inductive discharge.

1.5 Experimental Methods

A wide variety of diagnostic tools exist for probing the various parameters that can be used to define a gas phase plasma. In a broad sense, these can be divided into invasive and non-invasive methods. The former consists of such experimental techniques as chemical titration and mass spectrometry, where a sample of the plasma gas is tested for the presence of a certain species. Such techniques are often not practical for use in the in-

situ examination of stationary discharges (the type studied in this thesis), where electrical probes are more commonplace. These are placed inside a plasma environment where the response to an applied electric field (created by a voltage bias on the probe) is used to gather information on the electrical characteristics of the discharge (electron and ion densities and energy distribution functions). While such methods are indeed intrusive as they alter the dynamics of the discharge, recent improvements have allowed this disturbance to be minimised both experimentally[33] and through enhanced analysis of the resultant data[27]. However, such probes are useless in gathering information on neutral species which are also of importance in the discharge kinetics.

The optical probing of electronic states (both atomic and molecular) is the most commonly used non-invasive means to explore the kinetics of a plasma, and a review of its applications has been given by Kroesen and de Hoog[28]. The simplest form of such a method is optical emission spectroscopy (OES), where the intensity and wavelength of the emitted radiation can be monitored to infer the identity and concentration of the various species present. However, such a method is not universal as the state must spontaneously emit radiation, a requirement which naturally precludes ground and metastable electronic levels.

Absorption spectroscopy, or more specifically tunable diode laser absorption spectroscopy (TDLAS), is in its many variations the focus of this thesis as the primary experimental tool. It can provide absolute, quantitative, instantaneous and spectrally resolved information on any state that can absorb radiation. The utility of TDLAS has been realised from the invention of the diode laser in the 1960's, and the field has subsequently grown by encompassing the development of devices to access new wavelength regions (and new non-linear techniques to reach others). The ability to probe ever weaker transitions has also increased due to the invention of methods to either shift the detection to regions where the background noise is lower (modulation spectroscopy), or by increasing the absorbance *via* multi-passing through a sample (cavity techniques).

1.5.1 Electrical Probes

Probe methods are one of the most commonly used in the investigation of plasmas, and can provide spatially resolved information on the electron density, ion density and EEDFs. In this thesis, Langmuir probe[29] measurements were utilised to provide information on the electrical characteristics of the various plasmas investigated. Probes

effectively measure the flux of charged species to a biased conductor to gather information, but are not without their drawbacks.

A Langmuir probe is composed of a fine metal tip (typically tungsten) that is mounted inside the plasma chamber. The construction of our chamber allows access to all spatial dimensions within the plasma, but for the experiments described in this thesis, measurements were recorded in the centre of the chamber within the bulk region of the plasma (characterised by V_p). The probe potential V gradually reaches the floating potential V_f due to the incidence of the various charged species (ions and electrons), and thus no net current is drawn by the probe. However, the application of a voltage allows the retardation of either positively or negatively charged species and thus a current is drawn. In using a Langmuir probe, the voltage is swept from negative to positive allowing measurements of both the cation and electron fluxes, producing an I/V characteristic.

In reality, Langmuir measurements are complicated by other factors. The formation of a sheath around the biased tip occurs and hence the true collection area of the charged species is difficult to determine. This effect is partially mitigated by the use of a guard ring of greater area which is biased to the same potential, and allows for a more precise calculation of the collection area. However, this is limited to use with $V < V_p$, as at higher potentials the electron drain from the plasma is too great and causes a significant perturbation to the plasma. An example of an I/V characteristic obtained at 10 mTorr, 100 W in an argon plasma is shown in figure 1.8a. The resulting EEDF, extracted using the Hiden software suite (see section 3.2), is shown in figure 1.8b. The EEDFs are typically fitted to the expressions of Gudmundsson[24] (equation (1.11)) to obtain the x and $\langle E \rangle$ values. The electron densities extracted using this probe are utilised in chapter 3 of this thesis in the modelling of Ar and Ne plasmas.

There have been countless studies of plasmas using Langmuir probes. Some interesting examples include the probing of electronegative plasmas by Maundrill *et al.*[30], where investigations into the electron and ion densities indicated the presence of negative ions. A RF compensated Langmuir probe has been used by Seo *et al.*[31] to observe a bi-Maxwellian two temperature EEDF in an inductively coupled argon discharge. A comparison of electrical probe techniques with Thomson scattering is provided by Bowden *et al.*[32]; they find that the results for the electron temperature and pressure are in agreement over the pressure range investigated. However, significant deviations occurred between the EEDFs found from the two methods, and clear evidence of the invasive nature of the probe was observed. The spatially resolved electrical characteristics of a CF_4/Ar RF plasma have

been investigated and the electron and ion densities, together with the plasma potential, have been found to decrease towards the wall, but with the electron temperature remaining fairly constant[11]. An alternative electrical probe, the planar probe, has been used by Braithwaite *et al.*[33] to measure the EEDF in argon and CF_4 RF plasmas and they report two and three temperature distributions.

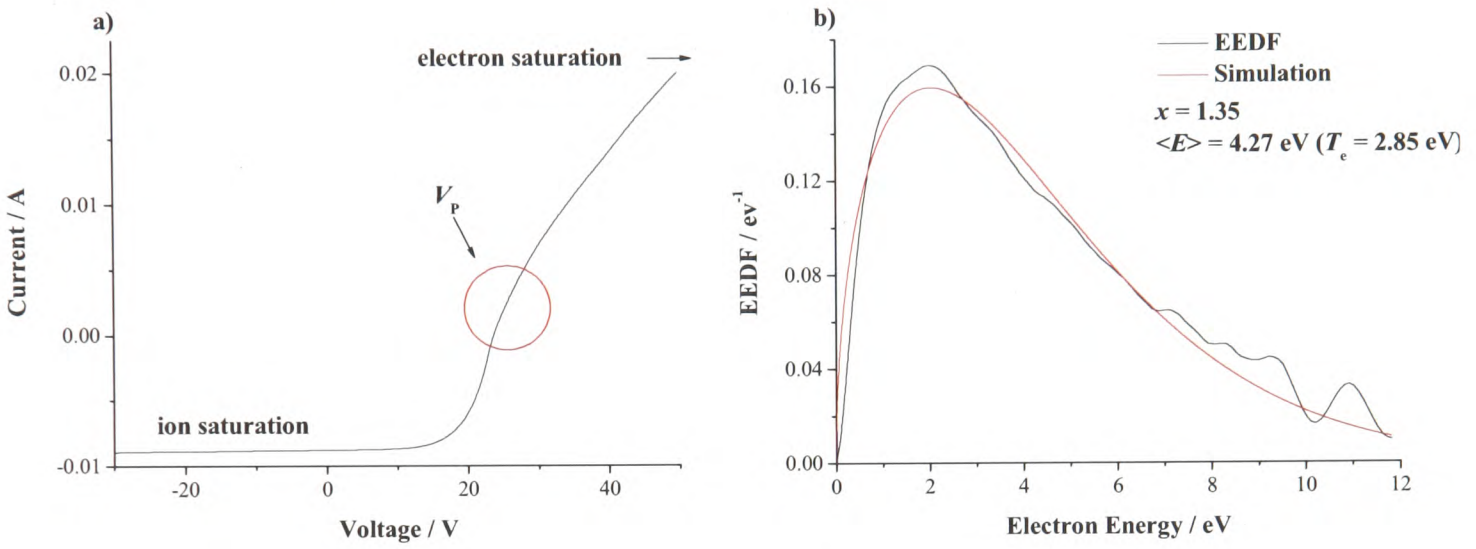


Figure 1.8: The a) *I/V* characteristic and b) EEDF, measured using a Langmuir probe, in an argon plasma at 10 mTorr and 100 W plasma pressure and power.

1.5.2 Optical Techniques

A wide variety of absorption and emission techniques exist for the probing of excited states in a plasma. The basics of the former are discussed in section 1.5.3, with the specific details of these methods presented in chapter 2. In this section, an outline of the various emission techniques is presented.

1.5.2.1 Optical Emission Spectroscopy (OES)

Optical emission spectroscopy is perhaps the most basic investigative tool used in the study of plasmas. The radiation emitted from a discharge is analysed in wavelength and intensity in order to identify the species present and to deduce their relative concentrations. The most obvious approach in analysing such data is in assuming a steady state has been reached between the excitation of a species and its radiative decay. In this way, information is obtained on both the concentration of the upper emitting state and on the excitation efficiency of production from the ground state. However, in order to achieve a

quantitative analysis, all the other competing factors must be taken into account (such as collisional decay and initial excitation from other energy states), requiring a detailed knowledge of the chemistry of the plasma. Despite its experimental simplicity, OES is limited by its low sensitivity (determined by the upper state concentrations and the Einstein A-factors) and the need for a good calibration method in order to obtain quantitative information. The added complexity of molecular discharges (in terms of the large number of emission lines observed) effectively limits quantitative OES to atomic plasmas.

This technique has been used across the spectral region, from the infrared to probe the vibrational and rotational temperatures in silane[34], to the visible and VUV to investigate the structure of a xenon barrier discharge[35]. Information on the EEDF of the discharge can be obtained through a knowledge of the excitation efficiency which depends on both the lower ground state concentration and on the rate constant for excitation (provided all other discharge kinetics are known or can be neglected). Crolly & Oechsner[36] have measured the electron temperature in both an argon and a nitrogen plasma by comparing the emission intensities of two lines; their results compare well with those obtained from further electrical measurements. The excitation efficiency can also be determined using the emission from an inert "actinometer" gas added to a discharge, but again the chemistry must be properly understood[37]. Furthermore, it has been suggested that the addition of even a small amount of dopant gas to a plasma can significantly change the chemistry, and that only information on the high energy electrons (> 12 eV) is obtained as the electron impact excitation cross-sections for the dopant gasses are generally insignificant below this value[38].

1.5.2.2 Laser Induced Fluorescence (LIF)

In LIF, a laser is tuned into a one or two photon resonance with an absorption feature and the resultant fluorescence from the upper level is detected. The narrow bandwidth and high power of the lasers used allows for the detection of fluorescence from very weak transitions. As a result, even the populations of individual ro-vibrational levels with high quantum numbers can be detected, and the populations of the levels in the lower state can thus be inferred. However, in order to obtain quantitative information using LIF factors, such as saturation effects, the excitation volume and the decay kinetics need to be considered. A review of the wide ranging utility of LIF in the detection of a variety of different species is provided by Hancock[39] and Dobele *et al.*[40] Measurements conducted

using LIF include the detection of the CH radical in an electron cyclotron resonance methane plasma, where the experimental uncertainty in the concentration is estimated at 30 %[41].

1.5.2.3 Laser Optogalvanic Spectroscopy (LOGS)

In this conceptually simple technique, a laser is tuned into resonance with a transition, resulting in optical pumping which increases the concentration of the upper level relative to the lower. As the ionization probability from the two levels differs, the discharge current will change slightly, and this can be detected as a voltage change across a resistor with a constant supply voltage. By definition, this technique is limited to gas *discharges*, but is very sensitive as even with moderate laser powers (a few milliwatts) large signals (μV to mV) can be achieved in gas discharges of several milliamperes[42]. However, as the signal is proportional to the ratio of the excitation volume compared to that of the discharge volume, it is limited to smaller discharges. This technique has been demonstrated on the detection of argon excimers in a DC discharge with supersonic expansion[43], and for the measurement of nitrogen metastables[44].

1.5.2.4 Thomson Scattering

The electrons present in a gas discharge respond in an oscillatory manner to the E-field of laser radiation, the scattering of which on passing through the plasma can be measured to yield an electron density after suitable calibration[45]. The Doppler shift of the resultant radiation gives information on the EEDFs, although analysis to determine its exact character can be difficult[46]. Comparison of the measured electron parameters to those derived from a Langmuir probe has been provided by Bowden *et al.*[32]. However, this technique is limited by the small scattering cross-sections which restrict its use to plasmas with high electron densities ($> 10^{11}$ cm^{-3}). Stray light, Rayleigh scattering from atoms and molecules and Raman scattering all act to mask the resultant signal, further reducing this technique's sensitivity.

1.5.3 Absorption Spectroscopy

Absorption spectroscopy is based on the fact that the electric field from a radiation source is attenuated and dispersed by interaction with a medium. The general expression of an electromagnetic (EM) wave travelling in the z-direction with a time-dependent amplitude $E(t)$ is given in equation (1.17), where E_0 is the maximum field amplitude, k the wave vector and ω the angular frequency (related to the linear frequency by $\omega = 2\pi\nu$).

$$E(t) = E_0 e^{i(\omega t - kz)} \tag{1.17}$$

After interaction with a medium (represented by a complex refractive index $n = n' - i\kappa$), the electromagnetic wave, while maintaining the same frequency as in a vacuum ($\omega_n = \omega_0$), is altered in wavevector to $k_n = k_0 n$. By recognising that $k_0 = 2\pi/\lambda_0$, and assuming the interaction between the EM wave and medium is in the weak limit (and therefore linear), equation (1.17) can be written as

$$E(t) = E_0 e^{-2\pi\kappa z/\lambda_0} e^{ik_0(ct - n'z)}. \tag{1.18}$$

This interaction can be characterized by two different processes. The resultant attenuation of the EM wave is described by *absorption* and depends on the imaginary part κ of the refractive index n. *Dispersion* depends on the real part of the refractive index n' and describes the dependence of the phase velocity $v(\omega) = c/n'(\omega)$ on the frequency. The absorption and dispersion terms are thus related through the complex refractive index, with the exact nature of this given by the Kramers-Kronig relations[47,48]. The absorption $\delta(\omega)$ and dispersion $\phi(\omega)$ components can be included together in the *transmission function* $T(\omega)$,

$$T(\omega) = e^{[-\delta(\omega) - i\phi(\omega)]}. \tag{1.19}$$

This allows the resultant interaction of the EM radiation with matter ($E_T(t)$) to be written

$$E_T(t) = E(t) \cdot T(\omega). \tag{1.20}$$

In spectroscopy, common expressions for $\delta(\omega)$ and $\phi(\omega)$ lineshapes (see section 1.5.3.2) are Lorentzian and Gaussian functions, shown in equations (1.21)-(1.24), where, δ_c is the amplitude attenuation at line centre, ω_c, and χ is the frequency detuning parameter.

Lorentzian:

$$\delta(\omega) = \delta_c \left(\frac{1}{\chi^2 + 1} \right) \tag{1.21}$$

$$\phi(\omega) = \delta_c \left(\frac{\chi}{\chi^2 + 1} \right) \tag{1.22}$$

Gaussian:

$$\delta(\omega) = \delta_c e^{-\chi^2} \tag{1.23}$$

$$\phi(\omega) = -\frac{2\delta_c}{\sqrt{\pi}} e^{-\chi^2} \int_0^{\chi} e^{u^2} du \tag{1.24}$$

While the Lorentzian case does have an analytical solution, the Gaussian profile must be computed numerically. The absorption line profiles are shown schematically in figure 1.9.

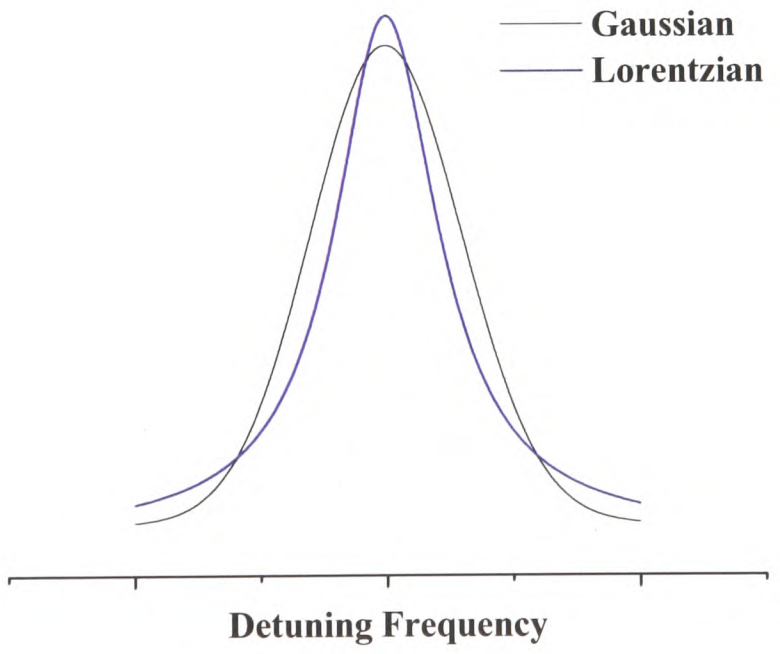


Figure 1.9: Simulations of the Gaussian and Lorentzian absorption profiles for the same peak area.

1.5.3.1 Homodyne Absorption Spectroscopy

In a simple experimental setup, absorption spectroscopy can be performed by passing laser radiation through an absorbing sample, with the attenuated beam incident upon a detector. The intensity of the wave, I, passing in a given direction (z) decreases through the absorbing sample along the distance dz in a manner given by equation (1.25), where the absorption coefficient α_{ik} (in cm^{-1}), shown in equation (1.26), depends on the population densities of the upper (N_k) and lower (N_i) levels, and on the optical cross-section σ_{ik} (in cm^2) of each absorbing species.

$$dI = -\alpha_{ik} I dz \tag{1.25}$$

$$\alpha_{ik}(\omega) = \sigma_{ik}(\omega)\left[N_i - (g_i/g_k)N_k\right] \tag{1.26}$$

Provided the incident radiation intensity I is low, the induced absorption rate is small compared to the refilling rate of the lower level I, and thus the population density N_i does not depend on the intensity I (the absorption is linear). Integration of equation (1.25) yields the Beer-Lambert law

$$I = I_0 e^{-\alpha(\omega)z}. \tag{1.27}$$

In a physical sense, the transition dipole moment in the absorption medium is driven at the same frequency as the incident radiation (hence the term *homodyne*). The oscillating dipole interferes destructively with this radiation, resulting in an exponential decay $f(z)$ in the intensity. Armed with a knowledge of the cross-section and the path length, one can readily determine the concentration of the absorbing species from the attenuation of the laser radiation. It should be noted that as this type of experiment is conducted with a photodiode (or a device akin to one), only the intensity of the radiation incident upon its surface is measured, and all information on the dispersive part of the interaction is lost.

1.5.3.2 Line Broadening

Spectral lines observed in discrete absorption (or emission) spectra are never truly monochromatic, with one observing a spectral distribution $I(\omega)$ of the absorbed (or emitted) intensity around the transition feature's centre, ω_c. This distribution is referred to as the line profile, and can be characterised by the full width at half maximum (FWHM) of the line, $\delta\omega = |\omega_2 - \omega_1|$, for which $I(\omega_1) = I(\omega_2) = I(\omega_c)/2$. The width of a spectral line is influenced by many parameters including the lifetime of the state and the temperature and pressure of the absorbing medium. Often, one of these factors dominates the broadening and can thus be considered as a limiting case. It is therefore worth discussing each mechanism in turn.

The most fundamental form of line broadening is that due to the natural lifetimes of the quantum states involved in the absorption. Consider a state i with energy E_i and a lifetime τ_i; the uncertainty principle dictates that the energy of this state can only be known within $\Delta E_i \simeq \hbar/\tau_i$. The frequency $\omega_{ik} = (E_k - E_i)/\hbar$ of an absorption terminating in the upper level E_k therefore has an uncertainty shown by equation (1.28), with the upper state k also possessing an inherent uncertainty in its energy, ΔE_k.

$$\delta\omega = \frac{\Delta E_i}{\hbar} + \frac{\Delta E_k}{\hbar} = \frac{1}{\tau_i} + \frac{1}{\tau_k} \tag{1.28}$$

The lifetime of the states are determined by radiative and non-radiative processes, although almost invariably the former dominate for atoms. In this case, the lifetimes of the states are determined by the Einstein A-factors ($A_{ik} = 1/\tau_k$) for spontaneous emission. If the states i and k can decay to other levels (i.e. if i is not the ground state), then the natural linewidth is determined by equation (1.29).

$$\delta\omega = \sum_n A_{ni} + \sum_n A_{nk} \tag{1.29}$$

One can consider the excited electronic states as damped harmonic oscillators such that decay occurs exponentially, and therefore a Fourier transform upon the transmitted radiation produces a Lorentzian line profile (equation (1.21)) in frequency space. The

FWHM, $\delta\omega$, is related to the detuning parameter through $\chi = 2(\omega - \omega_c)/\delta\omega$, and the amplitude attenuation at line centre by $\delta_c = 2/\pi\delta\omega$, where ω_c is the line centre of the transition.

In general, the Lorentzian line profile associated with the natural linewidth cannot be observed as it is obscured by other broadening effects. The major contribution to the spectral linewidths of gases at low pressures (exclusively used in this thesis) is the Doppler width, due to the thermal motion of the absorbing (or emitting) species. The frequency of absorption, ω_c, is shifted to higher frequencies for species moving towards the radiation source, and lower frequencies for those moving away. If the absorption gas is in thermal equilibrium, the observed velocities in the gas have a Maxwellian distribution. As the frequency of the absorption will change linearly with velocity, this distribution can be used to provide the basis for an absorption profile, which is found to be Gaussian (equation (1.23)) with a FWHM given by equation (1.30), where $\delta\omega_D$ is known as the Doppler width, T is the temperature and m is the mass of the absorbing species.

$$\delta\omega_D = \frac{\omega_c}{c}\left(\sqrt{\frac{8kT\ln 2}{m}}\right) \tag{1.30}$$

The FWHM is related to the detuning parameter through $\chi = \sqrt{2\ln 4}(\omega - \omega_c)/\delta\omega_D$, and to the attenuation *via* $\delta_c = \sqrt{2\ln 4}/(\delta\omega_D\sqrt{\pi})$. An analysis of the width of a peak can therefore determine the translational temperature of the absorbing species.

A further broadening mechanism arises as a result of the perturbations that occur to the energy levels upon a collision between two absorbing species. The nature of this interaction is complex, and it will suffice to say that for this mechanism, referred to as pressure broadening, $\delta\omega_P = \alpha p$, where α is a species dependent constant and p is the gas pressure. This interaction possesses a Lorentzian lineshape, and is dominant for pressures well above those used in this thesis.

The sources of broadening discussed so far are all a function of the nature of the absorption medium (its lifetime, temperature and pressure). Another possible broadening mechanism arises from the optical pumping of a transition due to the intensity of the probing laser radiation. At sufficiently large laser intensities, the pumping rate from the lower absorbing level increases in proportion to that of the relaxation rate from the upper

level (primarily determined by stimulated emission), resulting in a notable decrease of the lower state population and a broadening of the line profile. In the extreme, the population of the two levels equilibrates and the absorption medium becomes transparent. If one considers a two level system, in which spontaneous emission from the upper level is the only coupling mechanism, a saturation parameter, S, can be obtained. This is given by equation (1.31), where $I(\omega)$ is the laser intensity, σ_{12} is the cross-section for the transition and A_{21} is the Einstein A-factor for spontaneous emission from the upper state.

$$S = \frac{2\sigma_{12} I(\omega)}{\hbar \omega A_{21}} \tag{1.31}$$

The broadening parameter can be used to calculate the effect on the absorption (α) of optical pumping, shown by equation (1.32), where α_0 is the absorption coefficient without the occurrence of optical pumping.

$$\alpha = \frac{\alpha_0}{1+S} \tag{1.32}$$

It is found that under the conditions for the experiments presented within this thesis, the value of S is so low that optical pumping can be neglected.

1.5.3.3 Cross-sections

The integrated cross-section (over all frequencies) of an optical transition is related to the Einstein A-factor (which, as defined here, encompasses the degeneracies of the upper and lower levels) by equation (1.33), where c is the speed of light in m s^{-1}.

$$\sigma_{\text{int}} = \frac{\lambda^2 A}{8\pi}\left(\text{m}^2\text{s}^{-1}\right) = \frac{100\lambda^2 A}{8\pi \text{c}}\left(\text{cm}^2\text{cm}^{-1}\right) \tag{1.33}$$

Alternatively, cross-sections are also reported in terms of the peak cross-section (that is, σ at the line centre)

$$\sigma_{\text{peak}} = \frac{\sigma_{\text{int}}}{1.064\,\delta\omega_D}, \tag{1.34}$$

where $\delta\omega_D$ is the Doppler width of the line profile.

1.5.3.4 Sensitivity and Noise

There is a limit to the precision with which any experimental measurement can be obtained, determined by the level of background noise accompanying the signal. In absorption spectroscopy, this is often considered in terms of the minimum fractional absorbance, I/I_0, that can be detected. In the limit of small absorbances ($\alpha z << 10^{-2}$), equation (1.27) can be written $I/I_0 \approx 1-\alpha z$, and the minimum absorbance is expressed as a value for α_{min} (a product of the cross-section and the concentration). A standardised method for quoting sensitivities is through using a bandwidth reduced value for α_{min}, given by equation (1.35), where σ_{sp} is the single-pass absorption equivalent (calculated from the relative values of the *S*/*N*), *L* is the sample length (in cm), *N* is the number of averages and *B* is the bandwidth of the detector.

$$\alpha_{\text{min}} = \frac{\sigma_{\text{sp}}}{L}\frac{\sqrt{N}}{\sqrt{B}} \tag{1.35}$$

There are many sources of noise which are only outlined here; a more detailed consideration can be found in Ingle & Crouch[49] and Hieftje[50].

Two sources of fundamental noise in an experimental setup are shot noise (arising from the dark current on a photo-detector) and thermal noise (due to thermal motion of the charge carriers within the photo-detector). These noise sources are constant as a function of frequency (and are hence together referred to as white noise), but are rarely the limiting source of noise in a typical homodyne absorption experiment, where, at its best, $\alpha_{\text{min}} \sim 10^{-4}$ cm^{-1}.

The dominant source of noise in homodyne absorption spectroscopy is non-fundamental noise, which decreases inversely as a function of frequency (hence it is also referred to as $1/f$ noise). The exact origins of this type of noise are sometimes not apparent, but may include acoustic noise as well as phase and amplitude noise due to local thermal variations in the laser diode itself. As the spectral density of this noise decreases as $f(\nu)$, it

can thus be seen that shifting the detection to higher frequencies will reduce the contribution of this noise source (see section 2.2).

Further noise sources often occur as discrete noise bands with specific causes. Electrical and optical noise fall into this category, with emission from the plasma being a major contributor. The noise from a mains source at 50 Hz can often be registered on a detector, as can the RF generator used in the creation of a plasma at 13.56 MHz (and its higher harmonics). However, these types of noise can often be filtered out using bandpass filters centered at the appropriate frequency. The oscilloscope used for the collection of data in this thesis is digital and possesses 11-bit resolution, producing an inherent limit for the measurement of fraction absorbance in homodyne absorption spectroscopy of 5×10^{-4}.

1.5.3.5 Polarization Spectroscopy

As discussed earlier in section 1.5.3.2, saturation effects in a line profile can appear if the intensity of the incident laser radiation is so great that optical pumping occurs (i.e. the absorption rate from the lower level increases relative to that of radiative decay from the upper level), resulting in a decreasing population of the absorbing state and thus absorption signal. In this case, there is a non-linear dependence of the absorbed radiation power on the incident power. The narrow bandwidth of CW diode lasers allows this effect to be put to use in the creation of absorption spectroscopy signals free from Doppler broadening.

Polarization spectroscopy is one of the most powerful of the various Doppler-free absorption spectroscopies, and relies on the change of the polarization state of a probe wave induced by a polarized pump wave. It is conveniently described in the context of an experimental setup. The radiation output from a CW diode laser is separated into a weak probe beam and a strong pump beam. The probe beam passes through a polarizer, followed by the sample under study (such as a plasma), and then through a second polarizer which is crossed at 90° to the first, before being incident upon a photo-detector. Without the pump laser the sample is isotropic and the detector receives only a very small signal due to the residual transmission, perhaps as low as 10^{-8}. The pump beam passes through a $\lambda/4$ plate (producing a circular polarization) before being directed through the sample in the opposite direction to the probe beam and in such a way that the two beams intersect across a given portion of the sample.

As the laser frequency is tuned to a transition (J', $M' \leftarrow J''$, M''), molecules in the lower level absorb the pump wave. The quantum number M describes the projection of J onto the direction of light propagation, and for σ^+ circularly polarized light the transition follows the selection rule $\Delta M = +1$. Thus, the degenerate M'' sublevels of the rotational level J'' become partially or completely depleted because of saturation. This degree of depletion depends on the pump intensity, the M and J specific cross-sections and on the possible relaxation processes that may repopulate the lower levels. It can therefore be understood that this pumping will result in an unequal population of the individual M'' sublevels, which is equivalent to an anisotropic distribution for the orientations of the angular momentum vector J''.

The resultant anisotropic sample becomes birefringent to the incident linearly polarized probe beam, whose plane of polarization is slightly rotated after having passed through the anisotropic sample. This can now pass through the second crossed-polarizer before being incident upon the detector and producing a signal. Only the subgroup of absorbing species possessing velocity components within both the laser linewidth (~ 20 MHz for a diode laser) and the natural linewidth about the absorption centre will interact with both waves, resulting in a Doppler-free absorption signal. When the laser frequency is outside the natural linewidth, the probe wave that passes in the opposite direction to the pump wave interacts with a different group of molecules, and will therefore not be influenced by the pump wave. Figure 1.10 shows an example of data obtained using this technique for measurements of the $1s_5$ state of neon (see section 3.1) at 20 W and 10 mTorr plasma power and pressure. The Lorentzian linewidth (FWHM of 55 MHz) can be seen to be Doppler-free, and is solely dictated by the lifetime broadening of this state. The FWHMs of the $1s_2$ and $1s_4$ absorptions are larger due to their higher Einstein A-factors for emission to the ground state. In taking into account the contribution this makes to the linewidths in the Doppler broadened limit (in order to calculate the translational temperature), one finds this additional broadening to be less than the experimental error.

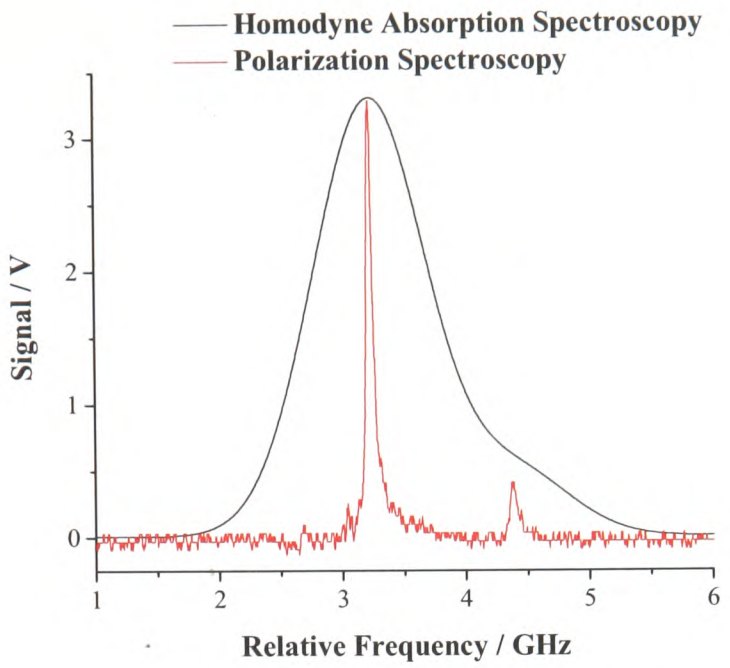


Figure 1.10: The polarization spectroscopy signal recorded in a neon plasma at 20 W and 10 mTorr plasma power and pressure shown with the corresponding homodyne absorption signal; the two peaks result from the two isotopes of Ne (20 & 22 with natural abundances 9:1).

1.6 Aims

Plasmas are not only of industrial importance; they provide a framework in which to explore the fundamental chemistry of the many excited states by probing their populations across various parameters. Combining this data with measurements of the more elemental plasma parameters of electron density and EEDF allows a fuller understanding of the discharge kinetics to be achieved *via* highlighting of the dominant reaction processes and excitation mechanisms.

This thesis describes the use of a range of techniques selected from a general spectroscopic armory in the elucidation of the kinetics of low pressure inductively coupled plasmas. Chapter 2 explains the specifics of these techniques, including their general application and theory, and provides examples of raw experimental data where appropriate. In chapter 3, the four states within the lowest excited electronic manifold of argon and neon are investigated across a range of plasma parameters, with subsequent kinetic modeling based on several postulates used to determine the relative importance of the various chemical processes. Further conclusions are drawn about the nature of such discharges by conducting measurements of the density of higher lying, but optically coupled, excited states. The effect of the addition of various dopant gases (to the neon

discharge) on the concentration of the lowest lying neon manifold is also measured, and it is found that such a method is a convenient way of manipulating the EEDF.

Nitrogen plasmas are the subject of chapter 4, where investigations are conducted to reveal the extent of vibrational excitation within the $N_2(A)$ state (an important energy reservoir). A natural extension of this experimental technique allows for the detection of the $N_2^+(X)$ ion density in a quantitative and absolute manner. Chapter 5 focuses on oxygen plasmas, with the detection of atomic oxygen in its ground electronic state achieved which allows a determination of the oxygen atom density and hence the degree of dissociation of the oxygen molecules. Furthermore, an optical detection scheme is constructed for the probing of the first electronically excited state of molecular oxygen, $O_2(a^1\Delta_g)$, in the near IR region of the EM spectrum.

References

[1] Book, D.L., NRL Plasma Formulary (Revised), Naval Research Laboratory, Washington D.C, (1987)

[2] Liberman, M.A. & Lichtenberg, A.J., Principles of Plasma Discharges and Materials Processing, Wiley, (1994)

[3] Bong-Seok, S. & Won-Jon, L., Thin Film Solids, **295**, 185, (1997)

[4] Pengxun, Y. *et al.*, Material. Chem. Phys., **45**, 167, (1997)

[5] Ueda, Y. *et al*, Surf. Coating. Technol., **98**, 1359, (1998)

[6] Coburn, J.W., Appl. Phys. A: Solid. Surf., **59**, 451, (1994)

[7] Chapman, B, Glow Discharge Processes, Wiley, (1980)

[8] Gudmundsson, J.T., Plasma Sources Sci. Technol., **7**, 330, (1998)

[9] Kiehlbauch, M.W. & Graves, D.B., J. Appl. Phys., **91**, 3539, (2002)

[10] Bai, K.H. *et al*, Physics of Plasmas, **8**, 3498, (2001)

[11] Rao, M.V.V.S. *et al*, J. Electrochem. Soc., **149**, C487, (2002)

[12] Keller, J.H. *et al*, J. Vac. Sci. Technol. A, **11**, 2487, (1993)

[13] Hebner, G.A., J. Appl. Phys., **80**, 2624, (1996)

[14] Mumken, G., J. Phys. D: Appl. Phys., **32**, 804, (1999)

[15] Xu, S, *et al*, Physics of Plasmas, **8**, 2549, (2001)

[16] Wang, W. *et al*, Appl. Phys. Lett., **71**, 1622, (1997)

[17] Bakowski, B., Laser Studies of Species in Plasmas, DPhil Oxford University, (2003)

[18] Freegarde, T. *et al*, Meas. Sci. Technol., **12**, N43, (2001)

[19] Mackinnon, R.A., Philos. Mag., **8**, 605, (1929)

[20] Kortshagen, U. *et al.*, J. Phys. D: Appl. Phys., **29**, 1224, (1996)

[21] Amorim, J. *et al*, J. Vac. Sci. Technol. B., **9**, 362, (1991)

[22] Tsakadze, E.L. *et al*, Physica Scripta, **64**, 360, (2001)

[23] Bakowski, B. *et al*, J. Phys. D: Appl. Phys., **37**, 2064, (2004)

[24] Gudmundsson, J.T., Plasma Sources Sci. Technol., **10**, 76, (2001)

[25] Druyvesteyn, M.J., Zeitschrift fur Physik, , **64**, 781, (1930)

[26] Amemiya, H., J. Phys. Soc. Japan, **67**, 1955, (1998)

[27] Chatterton, P.A. *et al.*, Vacuum, **42**, 489, (1991)

[28] Kroesen, G.M.W. & de Hoog, F.J., Appl. Phys. A, **56**, 479, (1993)

[29] Langmuir, I. & Mott-Smith Jr., H., General Electric Review, **27**, 449, (1924)

[30] Maundrill, D. *et al*, J. Phys. D: Appl. Phys., **20**, 815, (1987)

---

[31] Seo, S.H. *et al*, Appl. Phys. Lett., **74**, 2776, (1999)

[32] Bowden, M.D. *et al*, J. Vac. Sci. Technol. A, **17**, 493, (1999)

[33] Braithwaite, N. St.J. *et al*, Plasma Sources Sci. Technol., **5**, 677, (1996)

[34] Knights J.C. *et al*, J. Chem. Phys., **76**, 3414, (1982)

[35] Mildren, R.P. *et al*, IEEE Transactions on Plasma Science, **30**, 192, (2002)

[36] Crolly, G. & Oechsner, H., Eur. Phys. J. AP, **15**, 49, (2001)

[37] Hancock, G. *et al*, J. Phys. Chem., **94**, 3269, (1990)

[38] McMillin, B.K. & Zachariah, M.R., J. Appl. Phys., **79**, 77, (1996)

[39] Hancock, G., Surface and Coatings Technol., **74**, 10, (1995)

[40] Dobele, H.F. *et al*., Plasma Sources Sci. Technol., **14**, S31, (2005)

[41] Jacob, W. *et al*, Appl. Phys. Lett., **64**, 971, (1994)

[42] Demtroder, W., Laser Spectroscopy, 3rd Edition, Springer, (2002)

[43] Dube, P. *et al*, Chem. Phys. Lett., **234**, 445, (1995)

[44] Bachir, I.H. *et al*, Chem. Phys. Lett., **270**, 533, (1997)

[45] Hori, T. *et al*, J. Appl. Phys., **83**, 1909, (1998)

[46] Costa i Bricha, E. *et al*, J. Appl. Phys., **94**, 110, (2003)

[47] Kramers, H.A., Nature, **117**, 775, (1926)

[48] Kronig, R. de L., J. Opt. Soc. Am., **12**, 547, (1926)

[49] Ingle, J.D. & Crouch, S.R., Spectrochemical Analysis, Prentice-Hall International Inc., (1988)

[50] Hieftje, G.M., *Anal Chem*, **44**, 81A, (1972)

Chapter 2

The techniques of sensitive and selective absorption spectroscopy

The utility of absorption spectroscopy in providing non-invasive, state resolved and quantitative information on potentially any species present in a plasma environment is unrivalled by any other approach. While the basic principles and considerations for this generic method were outlined in chapter 1, the focus here is on the various techniques which can be used to enhance the sensitivity of the measurements for the detection of species with low concentrations and/or absorption cross-sections. The background theory of these techniques and their relation to the interpretation of experimental data are presented, together with examples taken from the measurements discussed in later chapters.

The arrangements for the generation of radiation, both directly using a laser diode and indirectly *via* non-linear optical mixing and frequency doubling techniques, will be discussed. Furthermore, encoding signals at higher frequencies (modulation), and extension of the absorption pathlength (using optical cavities), are highlighted as the two primary channels by which the sensitivity of a measurement can be increased. The parameters under which these techniques can be utilised are discussed, as are their effects on the analysis of the resulting absorption signals.

2.1 Generation of Radiation

While various sources of radiation exist for the spectroscopic investigation of plasmas, from lamps to broadband diodes, the primary source of radiation used in this thesis originates from continuous wave (CW) diode lasers. First invented in 1962[1], these provide tunable, narrow band, CW radiation over a range of different frequencies and powers, and are ideally suited for the spectroscopic investigation of Lorentzian and Gaussian broadened lines. However, they are limited by their occurrence in discrete wavelength regions of the electromagnetic spectrum, although non-linear optical techniques can be used to extend their frequency coverage.

2.1.1 Diode Lasers

The diode laser is based upon a solid state semiconductor that undergoes lasing when an electric current is applied in the forward direction through a p-n junction. On initial application of the injection current, electrons and holes recombine and produce EM radiation in the form of spontaneous emission with a typical bandwidth of the order of several cm^{-1} [2]. The wavelength of this emission is essentially determined by the energy gap between the electrons and holes within the semiconductor, which can be controlled by a careful selection of the semiconductor material dopants and their composition in binary and tertiary compounds. When the current is increased above a semiconductor-dependent threshold, inversion can occur and the radiation field inside the p-n junction becomes so intense that the stimulated emission rate exceeds that of spontaneous emission. On amplification of the radiation after multiple reflections within the junction, laser action ensues provided stimulated emission is faster than any other relaxation processes which may deactivate the population inversion (such as Auger recombination). This process is shown schematically in figure 2.1.

The wavelengths of the laser radiation emitted by a given diode are determined by the spectral gain profile and by the modes of the laser cavity (generally formed using the polished end faces of the semi-conducting medium as the cavity mirrors; a Fabry-Perot (FP) type laser). Only a few modes fit within the spectral gain profile, so while the laser has a large spontaneous emission bandwidth, only a few discrete wavelengths will result in laser action. These modes can typically be scanned by a few tens of GHz by changing the

current and temperature, with their exact character (number, separation, bandwidth and scanning-range) dependent on the specific semiconductor diode under use.

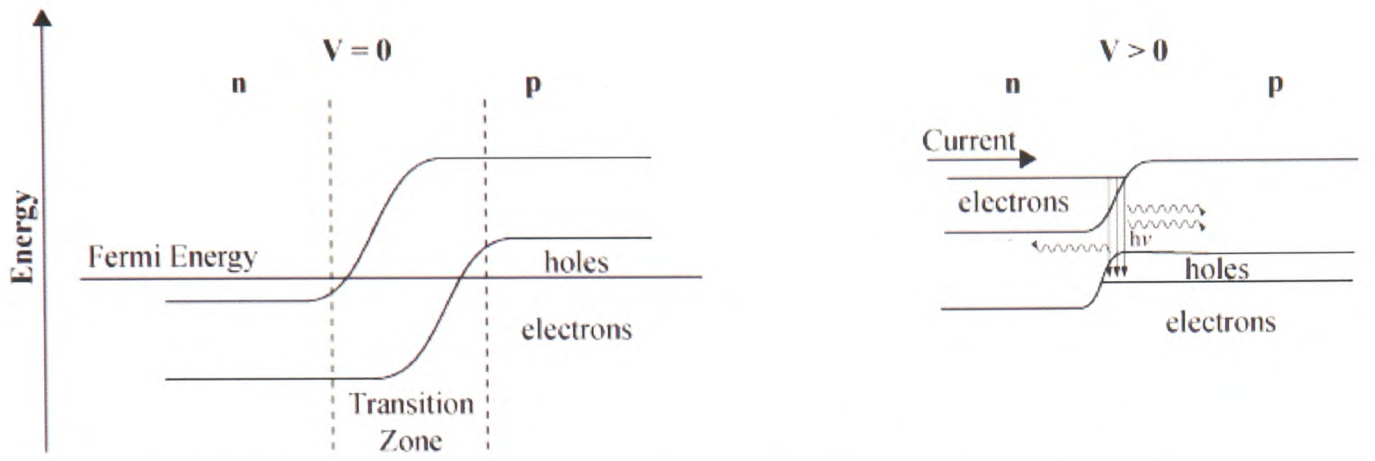


Figure 2.1: A schematic diagram of the p-n junction within a semiconductor laser diode with and without a bias voltage applied.

The wavelength output of a diode laser can be controlled by varying numerous parameters. While these include the application of an external magnetic field or mechanical pressure, commonly only the input current and junction temperature are altered to tune the output wavelength of the diode. Increasing the temperature, which increases the cavity length, has more of an influence on the magnitude of the band-gap and thus shifts the gain profile. On the other hand, current tuning does not change the band-gap but alters the effective occupancy of the upper 'levels' within the bands and causes a change in the refractive index of the junction. However, in an FP type laser no tuning is truly continuous and mode hops occur as the cavity length is not altered simultaneously with the maximum of the gain profile.

To achieve a continuous scan over a larger wavelength range it is necessary to extend the length of the cavity using an external feedback element. Additional wavelength selective elements (such as a grating) must be incorporated into the laser design in order to tune the laser. Furthermore, the output face of the diode must be anti-reflection (AR) coated to minimise reflection losses and promote modes supported by the external cavity rather than by the laser diode itself. In a typical setup, the input current is held constant and the wavelength is scanned by angle tuning of an external grating mounted on a piezo electric transducer. Such a laser is utilised in the detection of $O_2(a^1\Delta_g)$ in chapter 5, while the Fabry-Perot type lasers are applied in chapters 3 and 4 to the detection of Ne, Ar and N_2 metastables. An extensive review of the use of diode lasers in spectroscopy and atomic physics is provided by Wieman and Hollberg[3], while a discussion of the more technical

aspects concerning their use as sensors for combustion flows and gas dynamics is provided by Allen[4]. A recent review by Galbacs[5] charts the major developments in diode laser atomic spectroscopy over the past 12 years.

2.1.2 Background to Non-Linear Optical Techniques

While a number of discrete wavelength regions are now covered by room-temperature semiconductor diodes, these lie mainly in the red and near infrared. Recently, diodes around 410 nm have been produced, but the accessibility of other regions of this part of the EM spectrum, particularly the UV, remains poor. Through the interaction of radiation with non-linear optical media, further frequencies are accessible *via* the phenomena of second harmonic generation (SHG), sum frequency generation (SFG) and difference frequency generation (DFG), the bases of which are discussed below.

Consider a medium with a non-linear susceptibility subject to an electric field $E(t)$. The dielectric polarization $P(t)$ of the medium can be written as an expansion,

$$P(t) = \epsilon_0 \left(\chi^{(1)} E(t) + \chi^{(2)} E^2(t) + \chi^{(3)} E^3(t) + \ldots \right). \tag{2.1}$$

The coefficients $\chi^{(n)}$ ($n \geq 2$) are the k^{th} order susceptibility tensors of rank $k + 1$. While this series continues indefinitely, the laser powers utilized in this thesis only necessitate the inclusion of terms up to $n = 2$. If an EM wave composed of two frequency components is incident on this medium the second order ($P^2(t)$) induced polarization at $z = 0$ is given by

$$\begin{aligned} P^2(t) &= \epsilon_0 \chi^{(2)} E^2(t) = \epsilon_0 \chi^{(2)} \left[E_1 \cos(\omega_1 t) + E_2 \cos(\omega_2 t) \right]^2 \\ &= \epsilon_0 \chi^{(2)} \left\{ \begin{array}{l} \frac{1}{2}\left(E_1^2 + E_2^2\right) + \frac{1}{2} E_1^2 \cos 2\omega_1 t + \frac{1}{2} E_2^2 \cos 2\omega_2 t \\ + E_1 E_2 \left[\cos(\omega_1 + \omega_2) t + \cos(\omega_1 - \omega_2) t \right] \end{array} \right\} . \end{aligned} \tag{2.2}$$

This represents the DC polarization, AC components at the second harmonics $2\omega_1$ and $2\omega_2$, and AC components at the sum and difference frequencies $\omega_1 \pm \omega_2$, respectively.

Considering that the amplitudes E_1 and E_2 are vectors and that $\chi^{(2)}$ has components χ_{ijk}, equation (2.2) can be written in the form

$$P_i^{(2)} = \epsilon_0 \sum_{j,k=1}^{3} \chi_{ijk}^{(2)} E_j E_k \,. \tag{2.3}$$

This gives the i^{th} component of the dielectric polarization $P = \{P_x, P_y, P_z\}$, with indices j = 1, 2, 3 to represent x, y and z, respectively. The components of χ_{ijk} are generally complex and thus the phase of polarization will differ from that of the driving fields indicating that the direction of the polarization vector $P(t)$ may be different from those of E_1 and E_2. Clearly, E_1E_2 will produce the same polarization as E_2E_1, and thus it can be inferred $\chi_{ijk} = \chi_{ikj}$. In isotropic media, the reflection of all vectors at the origin should not change the non-linear susceptibility meaning $\chi_{ijk} = -\chi_{ijk}$, which can only be true if $\chi_{ijk} = 0$. Hence any crystal with an inversion centre cannot be a non-linear medium. It should be noted that in order to reduce the number of indices the components χ_{ijk} are written in the Voigt notation[6], where the first index is written in the convention $x = 1$, $y = 2$ and $z = 3$ and the second and third indices are combined as $xx = 1$, $yy = 2$, $zz = 3$, $yz = zy = 4$, $xz = zx = 5$ and $xy = yx = 6$. The tensor χ_{ijk} can thus be reduced to a scalar using this notation (on the basis of the crystals symmetry), defined by $d_{nm} = ½\,\chi_{ijk}$.

2.1.3 Phase Matching Criterion

The induced non-linear polarization at the atoms or molecules that make up the non-linear medium generates new waves at frequencies $\omega = \omega_1 \pm \omega_2$. These propagate through the medium with a phase velocity given by $v_{ph} = \omega/k = c/n(\omega)$, where c is the speed of light and $n(\omega)$ is the frequency dependent refractive index. This latter quantity is generated by the Sellmeier equation,

$$n_i^2 = A_i + D_i\lambda + \frac{B_i}{\lambda^2 - C_i}. \tag{2.4}$$

The constants A_i, B_i, C_i and D_i are specific for a given material and depend on whether the wave is ordinary or extraordinary. The equation is sometimes expressed with more terms depending on the complexity of the crystal's wavelength dependent birefringence.

The microscopic contributions from the atoms at different positions r_i will only add-up to an overall macroscopic wave if the vectors of these polarization waves and the phase velocities of the incident inducing waves are properly matched. This will occur when

the phases of the contributions to the polarization wave from the different atoms or molecules are all equal at a given point in the interaction volume of the pump beam and the non-linear medium. At this instance, the amplitudes will add in the direction of the pump beam and the intensity will increase across the length of the interaction volume. This can be expressed as

$$k(\omega_1 \pm \omega_2) = k(\omega_1) \pm k(\omega_2). \tag{2.5}$$

Equation (2.5) is known as the phase-matching condition (which can also be expressed as $\Delta k = k_1 + k_2 - k_3 = 0$, where k_3 refers to the generated wave). In the case of collinear beams, this condition can be rewritten as $n_3\omega_3 = n_1\omega_1 \pm n_2\omega_2$ which necessitates $n_3 = n_1 = n_2$, where the indices refer to the incident beams (1 & 2) and the resultant beam (3).

The simplest way to fulfill this condition is by the use of uniaxial birefringent crystals which require two refractive indices (ordinary and extraordinary, denoted n_o and $\overline{n}_e$, respectively) to describe their optical behavior. Uniaxial crystals have a crystallographic axis (also an optical axis) that differs significantly from the other two identical axes. The wave polarized in the xy direction perpendicular to the optical axis is the ordinary wave, while the E vector of the extraordinary wave is in a plane defined by the optical axis and the incident radiation beam. While there is no propagation dependence of the ordinary refractive index n_0, n_e depends on both the directions k and E. This can be understood in terms of the index ellipsoid, shown in figure 2.2, where the crystal axes are coincident with the x, y, z directions and $n_1 = n_2$ (as is always the case for a uniaxial crystal). This is a simplified case of the general expression given by equation (2.6), where $n = \sqrt{\varepsilon}$ and $\left|\hat{R}\right| = 1$.

$$\frac{1}{\epsilon_0}\left(\frac{x^2}{n_1^2} + \frac{y^2}{n_2^2} + \frac{z^2}{n_3^2}\right) = \hat{R} \tag{2.6}$$

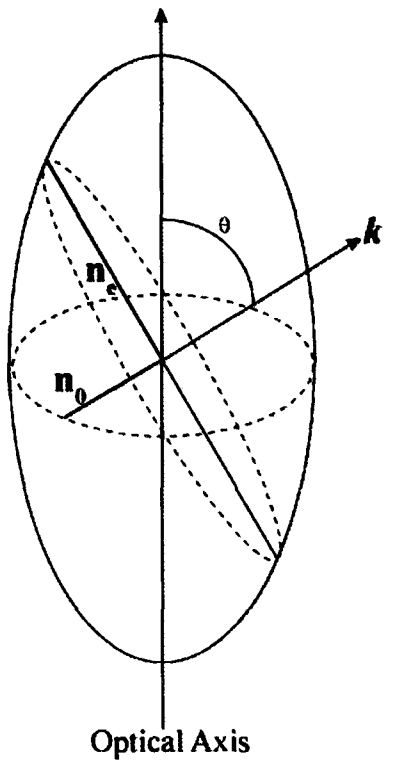


Figure 2.2: Index ellipsoid for a wave in a plane perpendicular to k and the corresponding refractive indices, n_0 and n_e.

Uniaxial crystals can be divided into two categories; positively birefringent crystals have $n_e \geq n_o$, whereas for negatively birefringent crystals $n_e \leq n_o$. A wide variety of crystals exist where the phase-matching condition can be fulfilled if one of the three waves at ω_1, ω_2, or $\omega_1 \pm \omega_2$ propagates as an extraordinary wave and the others as ordinary waves through the crystal in a direction θ (the angle between k and the optical axis). This is determined by equation (2.7), where $\bar{n}_e$ is the principal value of the extraordinary refractive index (i.e. the value at $\theta = \pi/2$).

$$\frac{1}{n_e(\theta)^2} = \frac{\sin^2\theta}{\bar{n}_e^2} + \frac{\cos^2\theta}{n_o^2} \tag{2.7}$$

It should be noted that there are two distinct categories of phase matching, type I and type II, which are distinguished by which of the three waves propagates as the extraordinary (e) or the ordinary (o) wave, shown in table 2.1.

	Positive Uniaxial ($n_e > n_0$)	**Negative Uniaxial ($n_e < n_0$)**
Type I	$n_3^o\omega_3 = n_1^e\omega_1 + n_2^e\omega_2$	$n_3^e\omega_3 = n_1^o\omega_1 + n_2^o\omega_2$
Type II	$n_3^o\omega_3 = n_1^o\omega_1 + n_2^e\omega_2$	$n_3^e\omega_3 = n_1^e\omega_1 + n_2^o\omega_2$

Table 2.1: Definitions of Type I and Type II phase matching

Angle tuning the crystal to achieve phase matching is not always possible as equation (2.7) may determine an angle θ that is not physically meaningful. Furthermore, whenever θ is not either 0 or 90 degrees the extraordinary and ordinary rays with parallel propagation vectors will quickly diverge as they propagate through the crystal. This walk-off limits the spatial overlap of the two waves and causes a reduced efficiency in the non-linear mixing process. This problem can be averted for a certain set of crystals where the birefringence is strongly temperature dependent (e.g. lithium niobate). As a result, it is possible to hold θ at 90 degrees and vary the temperature of the crystal to achieve phase matching.

2.1.4 Quasi Phase Matching

The techniques described so far can be categorized as birefringence phase matching, in which the angle and/or temperature is tuned to fulfil the phase matching condition. However, there are circumstances under which this approach may not be valid. As the refractive index of a material increases with frequency whilst the birefringence tends to remain almost constant, mixing at higher optical frequencies poses a problem. Another instance when this type of phase matching may not be applied is when one requires the use of the d_{33} non-linear coefficient. This coefficient is larger than the other components, but in the instance where it needs to be accessed for all the interacting waves possessing the same polarization, even if birefringence is present, it cannot be used to compensate for dispersion.

Quasi phase matching can be used when the techniques of temperature and angle tuning are not appropriate. It is based around the use of periodically poled materials, in which the orientation of one of the axes (usually the c axis) is inverted periodically as a function of position within a material (shown schematically in figure 2.3a). This periodic inversion results in the alternation of the sign of the non-linear coupling coefficient d_{eff}, and it is this alternation that can compensate for a wavevector mismatch, Δk. If the period of the alternation of the crystalline axis, Λ, is set equal to twice the coherent build-up length L_c, then each time the amplitude of the generated wave is about to decrease as a result of wavevector mismatch, the sign of d_{eff} reverses and the field amplitude is allowed to grow. This is shown in figure 2.3b, which also depicts the increase in field amplitude for a crystal with perfect phase matching and for one with a wavevector mismatch. The coherence length, L_c, defined by equation (2.8) for first order phase matching, is selected in

a given material depending upon the frequencies desired for mixing, and will also be dependent upon temperature (due to thermal expansion) allowing further temperature tuning. The many applications of quasi phase matched materials in non-linear optics are outlined in Byer[7].

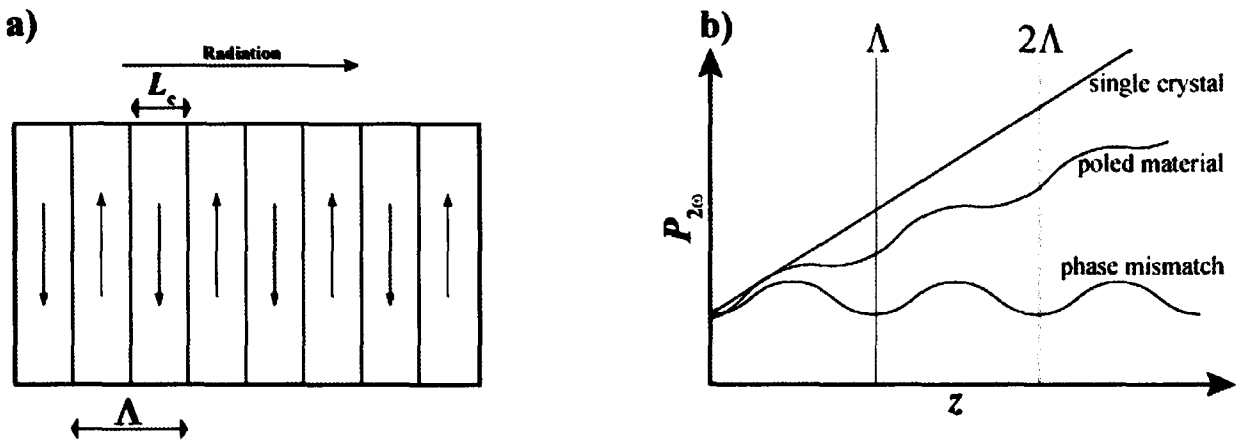


Figure 2.3: Schematic diagram illustrating quasi phase matching: a) the periodically poled crystal and b) the increase in mixed light across the crystal length.

$$\Lambda = 2L_c = \frac{2\pi}{(k_1 + k_2 - k_3)} \tag{2.8}$$

2.1.5 Second Harmonic Generation (SHG)

The most experimentally simple form of non-linear mixing is that of frequency doubling, which occurs for the case $\omega_1 = \omega_2$ (provided by the same radiation source), with the resulting frequency twice that of the optical pump beam. This technique, referred to as second harmonic generation or frequency doubling, was first demonstrated in 1961 using a ruby laser (694 nm) and quartz as the non-linear medium[8]. The intensity of the second harmonic light generated by a non-linear medium is given by

$$I(2\omega) = I^2(\omega)\frac{2\pi\omega^2\chi^2_{\text{eff}}L^2}{n^3c^3\epsilon_0}\frac{\sin^2(\Delta kL)}{(\Delta kL)^2}, \tag{2.9}$$

where n is the refractive index experienced by the incident beam (of frequency $\omega = 2\pi\nu$) and L is the interaction length. The phase difference Δk is as defined in section 2.1.3 and can be calculated from equation (2.5). The equation demonstrates that the power output

depends on the square of the input power, and thus maximizing the incident laser intensity is highly desirable.

The equations presented so far all derive from a theory based on plane EM waves, whereas in reality because light is focused into the crystal to obtain a higher output intensity, theory based around the use of Gaussian beams is more appropriate. This is presented by Boyd and Kleinman[9] who utilize a parameter known as the beam waist size *w*, which must also be optimized to attain maximum doubling efficiency.

Frequency doubling of 860 nm radiation has been reported in this laboratory using non-critical Type I phase matching in a $KNbO_3$ crystal[10], which has been demonstrated on the detection of the 1s states of argon[11,12] (see Chapter 3). Further examples of SHG using diode lasers include Angelis *et al.*[13] who report the generation of tunable UV radiation at 397 nm by doubling the output of a 150 mW AlGaAs diode laser using a lithium triborate crystal placed in an enhancement cavity, and have demonstrated the technique on an atomic Ca^+ absorption line. Hemmerich *et al.*[14] have generated 22 mW of radiation at similar wavelengths from a 100 mW AlGaAs diode laser centered at 860 nm using a monolithic potassium niobate ring resonator which simultaneously served as a reference cavity, used to lock the laser to a cavity resonance frequency. A review by Houe and Townsend[15] provides an introduction to the methods of periodic poling for 2nd harmonic generation.

2.1.6 Demonstration of SHG using Quasi Phase Matching

Recent developments in the field of periodically poled materials have included the extension of their use into the UV region by developing materials with transmission at short wavelengths, and new production methods that allow poling periods of the order of a few microns. One such material is MgO doped periodically poled stoichiometric lithium tantalate (PP-MgO:SLT)[16], which is characterised here for use in SHG.

Two different crystals were used in this characterisation; one of 10 mm length with five tracks of spacing periods 3.1, 3.55, 4, 4.5 and 6.55 μm, and a 30 mm crystal with three tracks of periods 4.2, 4.47 and 4.75 μm. These crystals were placed in an oven which was temperature controlled to within 0.25 K and mounted on a 3D translational stage. After passing through an optical isolator, radiation of varying wavelengths (provided by a range of free-running laser diodes, DFB systems and a Ti:Sapphire laser) was optimally focused into the crystal and the resultant doubled light exited through a filter (to separate the input

radiation) and was subsequently focused onto a calibrated detector. The lack of a Sellmeier equation for PP-MgO:SLT proved problematic in predicting the temperatures at which SHG would occur, and by experiment this was found to vary by up to 30 K from that calculated using the Sellmeier equation for PP-SLT alone[17].

SHG was achieved for a range of wavelengths with the conversion efficiency, γ, (in W^{-1}) of

$$\gamma = \frac{P_{2\omega}}{P_{\omega}^{2}}, \tag{2.10}$$

where $P_{2\omega}$ is the output power, and P_{ω} the input power. Due to the small alternation period of the poling in these crystals, it is possible to generate 2nd and 3rd order doubled frequency radiation where the doubling occurs over coherence lengths of 2Λ and 3Λ, respectively (as opposed to Λ for 1st order generation), allowing access to longer wavelengths. Table 2.2 summarises the wavelengths at which SHG was achieved and the corresponding efficiencies. As can be seen, the efficiency decreases for higher order SHG. While in theory these should be identical, deviations in the poling periods between adjacent sections will result in reduced coherence for the higher orders where the deviations across 2 or 3 periods can be relatively large.

Poling Period Λ	Order	λ_{ω} / nm	$\lambda_{2\omega}$ / nm	Crystal T / °C	Efficiency γ / W^{-1}
10 mm Crystal					
6.55	2	812.01	406.01	38.1	2.8×10^{-5}
4.5	1	892.35	446.18	110	1.4×10^{-4}
4.0	1	858.14	429.07	40.1	3.3×10^{-4}
30 mm Crystal					
4.75	1	904.62	452.31	68	1.1×10^{-3}
4.47	1	888.438	444.22	70	1.5×10^{-3}
4.47	3	659.98	329.99	36.3	4.2×10^{-4}

Table 2.2: Summary of SHG at different wavelengths in PP-MgO:SLT, together with the observed crystal temperature and efficiency.

The tunability of the crystal was measured and is shown in figures 2.4a and 2.4b for 1st and 3rd order SHG at λ_{ω} = 904.108 nm and 658.697 nm, on the 4.47 μm and 4.75 μm poled tracks, respectively. Due to the sensitivity of the SHG to crystal temperature and the

relative instability of the crystal temperature controller, the frequency of the input radiation was scanned at a given temperature to measure an effective SHG bandwidth. Figures 2.4a and 2.4b show this to be lower for 3rd order generation (FWHM ~ 3.5 GHz) than for first (FWHM ~ 11.5 GHz); the same reasoning lies behind this observation as for the differences that exist in the efficiencies (that the precision of the coherence length, L_c, is more critical for 3rd order generation than for 1st).

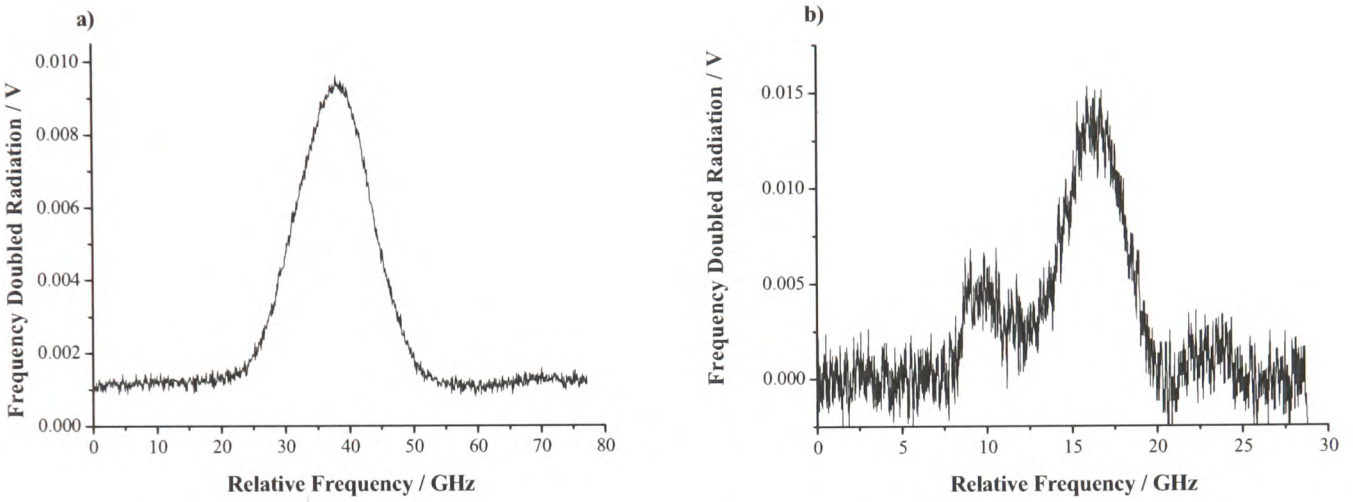


Figure 2.4: Tunability of SHG with input frequency for the PP-MgO:SLT crystal using a) the 4.47 μm track at 1st order and b) the 4.75 μm track at 3rd order.

2.1.7 Sum and Difference Frequency Generation (SFG & DFG)

SHG is often not the most convenient way to generate tunable UV radiation, which can also be achieved through SFG optical mixing of a CW pump laser and a tunable diode laser, a route which allows access to a greater range of frequencies. The radiation output from SFG is, as the name suggests, the sum ($\omega_1 + \omega_2$) of the two input frequencies which are combined in a non-linear optical medium (of the same type as outlined for use in SHG). The frequencies can be selected in such a way that 90° phase matching can be achieved, although for a desired frequency, temperature tuning, or the use of periodically poled materials in quasi phase matching, may be preferable. The lower wavelength limit for SFG (and SHG) in non-linear media is generally determined by the absorption (transmission cut-off) of the crystals. On the other hand, DFG, in which the output radiation is the difference in frequency of the input beams ($\omega_1 - \omega_2$), is a convenient way to probe transitions in the IR and is utilised in Chapter 5.

The intensity of the output wave (ω_3) in SFG is given by the equation

$$I(\omega_3) = \frac{128\pi^3 d_{\text{eff}}^2 \omega_3^2 I(\omega_1) I(\omega_2)}{n_1 n_2 n_3 c^3} L^2 \text{sinc}^2(\Delta kL/2), \qquad (2.11)$$

where the symbols are as defined earlier. DFG has been utilised previously in this research group in the detection of atmospheric methane[18].The output from a 220 mW Nd:YAG (1064 nm) was combined with that from a 50 mW DFB laser at 1560 nm in periodically poled lithium niobate to yield 18 μW of 3.36 μm radiation. A similar method was used with a 785 nm diode laser to produce radiation around 2.968 μm for the detection of atmospheric water[19]. Schnitzler *et al.*[20] demonstrate SFG by the construction of a tunable CW UV radiation source at 313 nm using a Nd:YAG and a Ti:Sapphire or diode laser with a periodically poled lithium niobate crystal for the purpose of Be^+ atom cooling.

2.2 Modulation Techniques

Heterodyne techniques are commonly used and relatively simple experimental methods for increasing the *S/N* of an optical absorption based detection scheme. The interaction between the absorbing medium and modulated radiation generates a signal that varies at the modulation frequency. Providing the necessary frequency and phase sensitive detection electronics are in place, the signal can be detected coherently with only the noise contributions that fall into the bandwidth about the detection frequency. The description of such methods is conveniently presented heuristically[21,22], as outlined below for the cases of wavelength and frequency modulation spectroscopy.

2.2.1 General Theory

The generation of modulated light is achieved by superimposing a time-dependent phase shift upon light of a single optical frequency (ω_0). For sinusoidal modulation, this can be expressed as

$$E(t) = E_0 \exp\left[i(\omega_0 t + M \sin \omega_m t)\right] = E_0 \exp(i\omega_0 t) \sum_{n=-\infty}^{+\infty} J_n(M) \exp(in\omega_m t), \quad (2.12)$$

where M is the modulation index, defined as the ratio of the maximum deviation from the central frequency (the frequency excursion, ΔF) to the modulation frequency, ω_m. The sum characterizes the frequency components of the modulated radiation spectrum described by Bessel functions, J_n. On the assumption that the central line width of the probing laser radiation is narrow and can thus be neglected, one can consider the optical field defined in equation (2.12) passing through an absorption sample of spectral line-width Γ. The effect of the sample on each frequency can be considered in terms of the transmission function (defined in equation 1.19), where the transmitted optical field $E_T(t)$ will now be

$$E_T(t) = E_0 \exp(i\omega_0 t) \sum_{n=-\infty}^{\infty} T(\omega_n) J_n(M) \exp(in\omega_m t). \qquad (2.13)$$

The attenuation and dispersion experienced by each frequency component will unbalance the phase-modulated radiation, resulting in a time-dependent intensity, $I(t)$, where

$$I_T(t) \propto |E_T(t)|^2. \qquad (2.14)$$

This gives rise to the signal (a consequence of the beating of those frequencies that are separated by ω_m), which can be readily calculated by combining equations (2.13) and (2.14). Assuming that the difference in absorption and dispersion experienced by the frequency excursion is small (as is often the case for modulation measurements, given that the technique is generally used to detect weakly absorbing species), and that the overall absorption and dispersion associated with the spectral line of width Γ are weak, one obtains, at a frequency ω_m, the signal

$$|E(t)|^2 = E_0^2 \exp(-2\delta_0) \begin{bmatrix} 1 + 2\cos\omega_m t \sum_{n=0}^{\infty} J_n J_{n+1} \times (\delta_{-n-1} - \delta_{n+1} + \delta_{-n} - \delta_n) \\ +2\sin\omega_m t \times \sum_{n=0}^{\infty} J_n J_{n+1} \times (\phi_{-n-1} - \phi_{n+1} + \phi_{-n} - \phi_n) \end{bmatrix}. \qquad (2.15)$$

Note the sum is now between $n = 0$ and ∞. The terms that oscillate at higher frequencies (e.g. $2\omega_m$) have been neglected and would need to be retained for experiments conducted using harmonics of ω_m. It can be seen that the sample can still have a strong

background absorption that is frequency independent, given by the DC part of equation (2.15). The cosine and sine terms are time dependent with a modulation frequency ω_m, and refer to the absorption and dispersion components, respectively, and can be detected separately using phase-sensitive electronics.

2.2.2 Frequency Modulation Spectroscopy (FMS)

Frequency modulation spectroscopy is generally carried out with a small modulation index ($M \leq 1$) and a large modulation frequency. The output signal is detected at a high frequency where the laser technical noise is lower than that at DC, thus resulting in an increased *S/N*. FMS was first developed in the early 1980's[23,24] where an electro-optic modulator (EOM) was used to impose weak sidebands centered about the carrier frequency provided by a narrowband dye laser. Subsequent investigations involved applying a modulation to the input current of a diode laser to produce the frequency modulated radiation[25,26,27] (due to the dependence of the refractive index of the laser medium on the charge density and therefore current).

Typically in FMS there is only one pair of sidebands to consider if M is small (as shown in figure 2.5a), and thus $J_n(M)$ is negligible for $n > 1$ (as $J_n(M) = M^n/2^n n!$ for small M). This simplifies equation (2.15), as only the terms with $n = 0$ & 1 need consideration, and using $J_0(M) = 1$ and $J_1(M) = M/2$ for $M << 1$, it follows that

$$\left|E^2(t)\right| = E_0^2 \exp(-2\delta_0)\begin{bmatrix} 1 + M(\delta_{-1} - \delta_1)\cos(\omega_m t) \\ + M(\phi_{-1} + \phi_1 - 2\phi_0)\sin\omega_m t \end{bmatrix}. \qquad (2.16)$$

In the case of $\omega_m >> \Gamma$ (the FWHM of the absorption profile) the cosine component in equation (2.16) will directly display the absorption profile when either the upper or lower frequency sideband is resonant with the optical transition. The sine component will display three dispersion curves, one when each frequency component is resonant with the spectral feature (arising from the two sideband frequencies and one for the central frequency). The signal shapes arising from the varying types of line-shape profile have been presented and discussed in the literature[28,29].

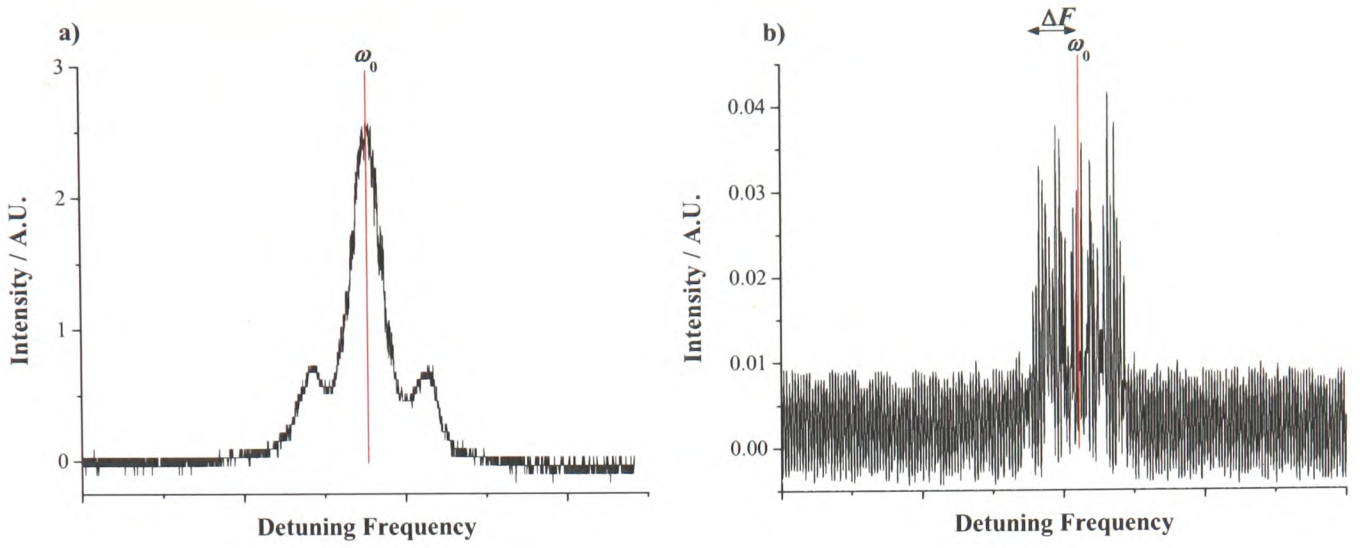


Figure 2.5: The frequency excursion about the carrier frequency, ω_0, in a) FMS for $M = 0.2$ and $\omega_m = 300$ MHz and in b) WMS at $\omega_m = 5$ kHz.

FMS has found extensive use in both the detection of low concentrations of species and in time-resolved measurements of transient radicals. Only a selection of examples from the literature is presented here. Gulluk *et al.*[30] have measured with high precision the concentrations of CO_2, CH_4, N_2O and CO in air samples of a few cm^3 obtained from polar ice cores. Bloch *et al.*[31] have utilized time resolved FMS with a phase modulated CW Ti:Sapphire ring laser in the detection of transient radicals, specifically CN from the 193 nm dissociation of NCCN. More recently, Gustafsson *et al.*[32] performed two-tone FMS using GaN lasers around 400 nm, and demonstrated a sensitivity of 5×10^{-6} for 120 Hz bandwidth on spectral lines in potassium and lead. An extensive review on the use of FMS for the detection of transient species is provided by Hall & North[33].

2.2.3 Wavelength Modulation Spectroscopy (WMS)

In contrast to FMS, wavelength modulation spectroscopy is carried out with a high modulation index ($M >> 1$), the result of which is a large frequency excursion represented by the time averaged spectral output shown in figure 2.5b. It is a well established technique that historically found favour since it uses low modulation frequencies which were readily available experimentally. It was first applied to the optical output of lead salt diode lasers, which were used for pollution monitoring in the early 1970's[34]. The technique lends itself particularly well to external cavity diode lasers (ECDLs), where the laser frequency is controlled by adjusting the external cavity length using a piezoelectric current which allows wavelength modulation in the kHz region[35].

To aid in the description of the theory behind WMS and its connection to FMS, it is useful to define the parameter of instantaneous frequency, $\omega_i(t)$, the derivative of the phase of the modulated radiation with respect to time (equation (2.17), where ΔF (= $M\omega_m$) is the maximum deviation from the carrier frequency, ω_0). The phase of the modulated probe is the complex argument of the exponential in equation (2.12)

$$\omega_i(t) = \frac{d}{dt}(\omega_0 t + M \sin \omega_m t) = \omega_0 + \Delta F \cos \omega_m t \qquad (2.17)$$

In the description here, dispersion effects are not considered and the absorption is assumed to be weak ($\alpha(\omega)L << 1$) so that $I_T(\omega) \approx I_0(\omega)[1 - \alpha(\omega)L]$. Expanding the sample absorption ($\alpha(\omega)$) using a Taylor series yields

$$I_T(\omega) = I_0\left[1 - \alpha(\omega_0) - \left.\frac{d\alpha}{d\omega}\right|_{\omega_0} \times(\omega - \omega_0) - \left.\frac{1}{2!}\frac{d^2\alpha}{d\omega^2}\right|_{\omega_0} \times(\omega - \omega_0)^2 \ldots\right], \qquad (2.18)$$

and combining this with equation (2.17) produces

$$I_T(\omega_i) = I_0\left[1 - \alpha(\omega_0) - \left.\frac{d\alpha}{d\omega}\right|_{\omega_0} \times \Delta F \cos \omega_m t - \left.\frac{1}{2!}\frac{d^2\alpha}{d\omega^2}\right|_{\omega_0} \times(\Delta F)^2 \cos^2 \omega_m t \ldots\right]. \qquad (2.19)$$

Provided a sufficiently small frequency excursion is used (referred to as the derivative limit where $\Delta F << \Gamma$), higher terms in equation (2.19) can be neglected and the WMS signal that is detected at the modulation frequency ω_m is proportional to the first derivative of the sample absorption. The intensity of the signal oscillating at ω_m is given by

$$I = -\left.\frac{d\alpha}{d\omega}\right|_{\omega_0} \Delta F . \qquad (2.20)$$

Similar expressions for the intensities of higher harmonics, n, exist as higher-order derivatives of the absorption, and simulations of the lineshapes for the first four harmonics are shown in figure 2.6a. WMS signals, although proportional to the amount of absorbance in a sample, are not absolute and require calibration against a sample of known absorbance.

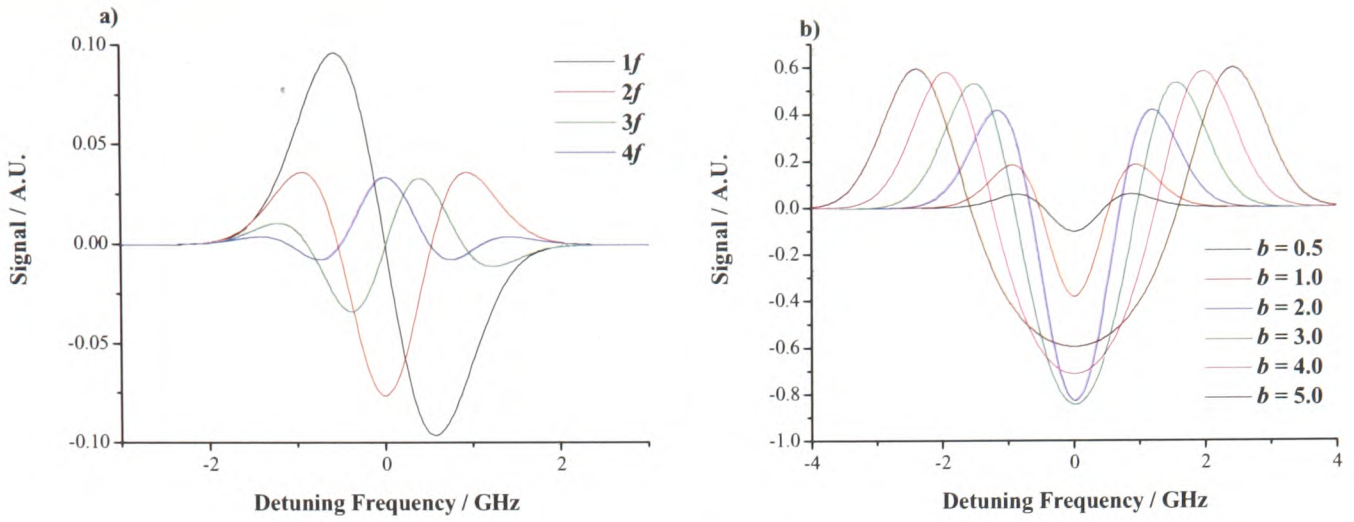


Figure 2.6: a) The first four harmonics of an absorption with a Gaussian profile defined by FWHM = Area = 1 GHz, b) the broadening of a 2*f* absorption profile with the same characteristics as in a).

Using WMS in the derivative limit does not yield the highest sensitivity; this is found to be achieved at $\Delta F \approx \Gamma$ (the exact maximum depending on which harmonic is detected). However, this technique has serious drawbacks in the form of modulation broadening, a type of experimental broadening mechanism arising when the frequency excursion is much greater than the FWHM of the absorption profile. Recovery of the original absorption signal through integration of the observed derivative signal appears to produce a result that is proportional to the original, but with a FWHM $\Gamma_{\text{eff}} > \Gamma$. This broadening is shown for a second harmonic trace in figure 2.6b (where the parameter b characterizes the broadening and is given by $b = 2\Delta F/\Gamma$) calculated from the general expression for WMS line-shapes given by[35]

$$I_{\text{n}}(\omega) = \frac{1}{\pi}\int_{0}^{2\pi} g\left[\omega_0 + \Delta F \sin(\omega_{\text{m}} t) - \omega_c\right]\cos(n\omega_{\text{m}} t)\,\text{d}(\omega_{\text{m}} t). \qquad (2.21)$$

It can be seen that the degree of broadening and signal magnitude are a function of both g (the line-shape function, usually Gaussian or Lorentzian) and b. The fact that the temperature determines the degree of Doppler broadening in g, and thus b, provides a further complication to analysis, especially in a plasma environment. It should be noted that modulation broadening is only important for $\Delta F \approx \Gamma$, and is not of significance when $\Delta F << \Gamma$ (referred to as the derivative limit of WMS). An example of WMS data taken at 2*f* and 4*f* for an absorption of atomic neon is shown in figures 2.7a and 2.7b; note the

asymmetry of the signals arising from the presence of an isotope (~ 10 % abundance) at a slightly higher transition frequency.

Examples exist for the use of WMS across a wide range of wavelengths to detect a variety of species. Detection of methane at 1.65 μm using a DFB laser has been reported[36,37], with a sensitivity using a modulation frequency of 5 MHz found to be 0.3 parts in 10^6 m for a sample time of 1.3 s[38]. The parameters of pressure broadening in O_2 have been measured at 760 nm[39], as have the same parameters in H_2O at 1320 nm[40]. Zybin *et al.*[41] have made measurements on atomic O, Cl and F in a DC discharge to infer the concentrations of their parent molecules. Finally, Pavone and Inguscio[42] have offered a comparison of the experimental methods of FMS and WMS using an AlGaAs diode laser and report sensitivities of 4.5×10^{-7}, 9.7×10^{-8} and 6.4×10^{-8} (for a *S/N* of unity and a 1 Hz bandwidth) for 1 kHz WMS, 100 MHz FMS and two-tone FMS (TTFMS), respectively. A recent review by Song & Jung[43] highlights developments in using modulation spectroscopy with tunable diode lasers for the detection of trace gases, while Werle[44] discusses tunable diode laser absorption spectroscopy in a wider context including the continued development and use of WMS, FMS and two-tone FMS.

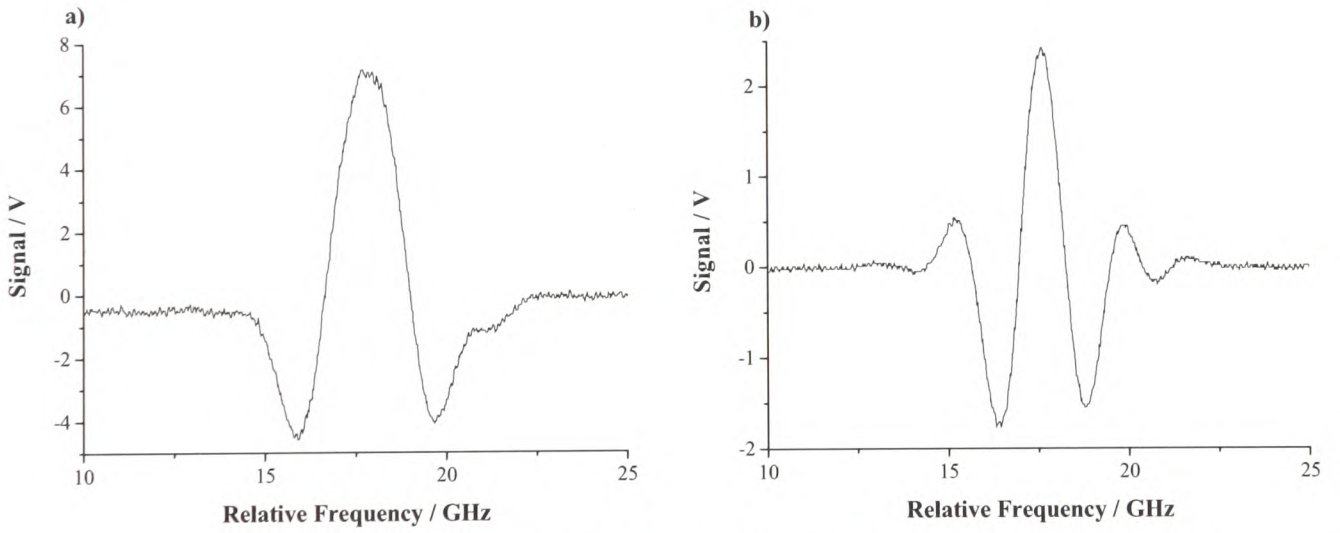


Figure 2.7: WMS signals arising from an absorption in neon at 100 mTorr and 100 W plasma pressure and power, respectively and a modulation frequency of 1.1 kHz, a) 2*f* and b) 4*f*.

2.3 Cavity Methods

As discussed in the last section, one commonly used technique for increasing the *S/N* of absorption spectroscopy lies in phase sensitive detection, where the signal is effectively encoded at higher frequencies (using modulation techniques) to reduce the

effects of the background noise. An alternative approach, however, is to increase the amount of absorption signal, which from a consideration of equation 1.27 can be achieved by increasing the pathlength through the absorption medium, resulting in an decrease in I/I_0. In many situations, this is preferable to the use of modulation spectroscopies as it is essentially absolute and does not therefore require calibration. Very long path absorption measurements (~ 1 km) have been carried out in the area of pollution monitoring using the technique of differential optical absorption spectroscopy (DOAS)[45]. One obvious way to increase the pathlength in a laboratory is by simple multi-passing through the absorption medium, as has been achieved using a White[46] or Herriott[47] cell arrangement. The probing radiation is passed many times though the sample using high reflectivity mirrors, and path lengths of a few hundred meters can be achieved. The optical cavity methods discussed here (primarily cavity ring-down spectroscopy (CRDS) and cavity enhanced absorption spectroscopy (CEAS)) make use of a high finesse optical cavity composed of two high reflectivity (HR) mirrors to effectively increase the path-length to several kilometres within a small footprint (~1 m).

2.3.1 Optical Cavities

Optical cavities are produced by arranging two high-reflectivity mirrors such that they face each other at a set distance apart, allowing light to be reflected back and forth in the region between the mirrors (also known as linear or standing wave cavities). These can be divided into two categories on the basis of loses; geometrically stable and unstable. If a paraxial ray bundle (rays whose deviations from the optical axis are small, i.e. $\sin\alpha \approx \alpha$) is refocused within the cavity after successive reflections between the mirror pair, the optical energy is contained (or trapped) within the cavity forming a geometrically stable configuration. If this ray bundle escapes after some number of reflections, the cavity is said to be unstable geometrically. An analysis of optical cavities using matrix methods[48] allows the establishment of the stability condition for optical cavities in terms of g-parameters, where a cavity is stable if

$$0 \leq g_1 g_2 \leq 1, \tag{2.22}$$

with

$$g_1 = \left(1 - \frac{L}{R_1}\right) \quad \& \quad g_2 = \left(1 - \frac{L}{R_2}\right), \tag{2.23}$$

where L represents the distance between the two mirrors of radii of curvature R_1 and R_2.

Using this definition, it is possible to highlight different types of cavity in the limiting cases of the variables defined previously. These cavities have different properties in terms of spot size (the cross-sectional diameter of the beam trapped inside the cavity) and sensitivity to misalignment. In symmetrical cavities (like those used in CRDS and CEAS), $R_1 = R_2$, and in the specific case where $R_1 = R_2 = \infty$ (flat mirrors), $g_1 = g_2 = 1$ and a Fabry-Perot cavity is formed. Long-radius resonators are a variation of the Fabry-Perot variety, and are produced when $R_1 = R_2 >> L$. At the situation where $R_1 = R_2 = L$, $g_1 = g_2 = 0$, and the cavity is referred to as a symmetrical confocal cavity, since the focal points of both mirrors ($R/2$) coincide halfway between the mirror separation. When $R_1 = R_2 = L/2$, $g_1 = g_2 = -1$ and a symmetrical concentric cavity is formed. These various cavity types are summarized by the diagram shown in figure 2.8. A slight variation on the latter type of arrangement is the near concentric cavity where $R_1 = R_2$ and $|R_1 + R_2| > L$, and is the type of cavity used for the experiments described in this thesis.

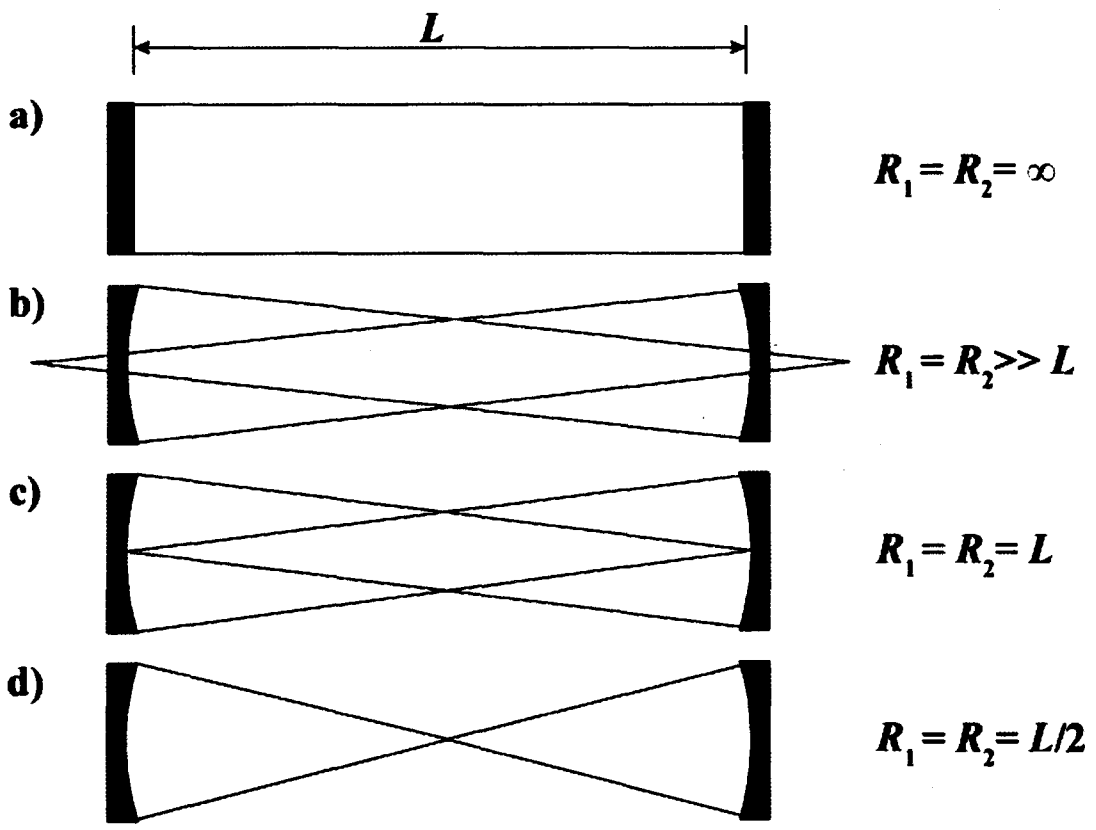


Figure 2.8: Various types of two-mirror cavities, a) Fabry-Perot, b) long radius, c) symmetrical confocal and d) symmetrical concentric.

2.3.2 Fabry-Perot Cavity

One of the simplest types of cavity is the Fabry-Perot (FP) etalon in which $R_1 = R_2 = \infty$. A schematic diagram of a FP cavity is shown in figure 2.9, in which a plane wave strikes the cavity at an angle θ to the normal. The cavity reflects and transmits a series of waves, with the transmitted electric fields summed to determine the transmission of the cavity,

$$I(t) = \frac{I_0 T^2}{(1-R)^2}\left[1 + \frac{4R}{(1-R)^2}\sin^2\left(\frac{\phi}{2}\right)\right]^{-1}. \qquad (2.24)$$

This is known as Airy's formula, where R is the reflectivity of the mirrors. The transmission of the cavity will be a maximum whenever ϕ is an integral multiple of 2π. This will correspond to

$$\nu_{max} = \frac{pc}{2nL\cos\theta}, \qquad (2.25)$$

where p is an integer known as the mode index, c is the speed of light and ν_{max} is the frequency corresponding to a transmission maximum of the cavity. A special case of this type of cavity can be constructed if $\theta = 0$, p is an integer and the reflection coefficient R is nearly 1. Here, the radiation beam will be transmitted through the cavity so long as the separation between the reflecting surfaces of the mirrors is equal to an integral multiple of half the wavelength of the light. In such a scenario, a FP cavity can be used across a spectral range by varying the value of L. If the spacing between the mirrors (L) is fixed, this is known as a Fabry-Perot Etalon.

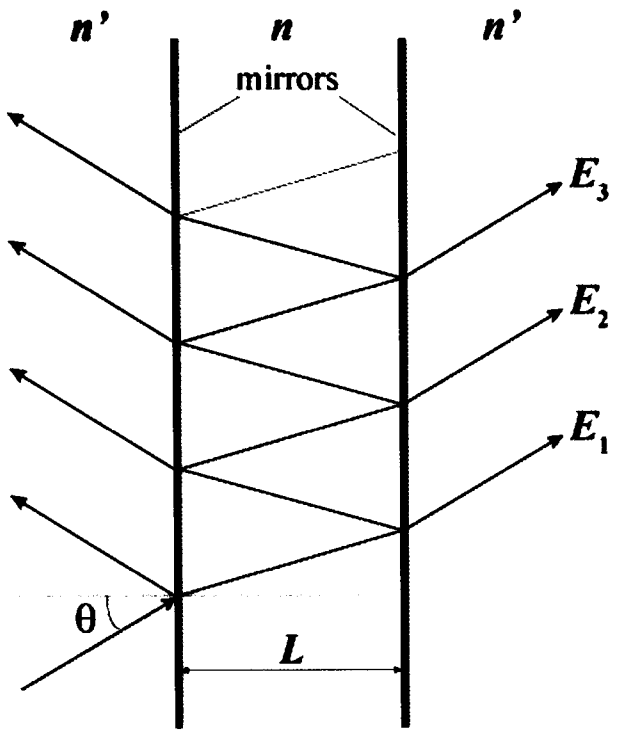


Figure 2.9: Schematic of a Fabry-Perot Cavity.

Several defining characteristics of a cavity can be illustrated at this point by using the FP cavity as an example. The free spectral range (FSR, $\Delta\nu_{FSR}$) is defined in terms of the frequency separation between two successive transmission frequencies (or resonant modes). Using equation (2.25) at normal incidence ($\cos\theta = 1$) this is found to be:

$$\Delta\nu_{FSR} = \frac{c}{2nL} \tag{2.26}$$

Similarly, the FWHM of a transmission band can be obtained with substitutions of 0.5 for I/I_0 and $\phi = \phi/2$:

$$\Delta\nu_{1/2} = \frac{c}{2\pi nL\cos\theta}\left(\frac{1-R}{\sqrt{R}}\right) \tag{2.27}$$

This expression shows that the widths of the transmission bands obtained with the FP cavity become progressively narrower as R approaches 1. The resolution attained with a cavity can be expressed by the ratio of the FSR to the FWHM of a transmission band. This is known as the finesse, F, and with $\theta = 0$ is given by:

$$F = \pi\frac{\sqrt{R}}{1-R} \tag{2.28}$$

2.3.3 Optical Modes

The discussion so far has focused around optical cavities in the context of geometric optics, and the interaction of these cavities with radiation has been neglected. To understand resonant mode formation in optical cavities, one must consider the oscillating nature of the light beam as it passes back and forth within the cavity. For a mode to develop the electric vector of the oscillating light wave must be zero at the boundaries of the cavity; the standing waves that result are known as cavity modes and fall into two basic categories. Longitudinal (or axial) modes determine the resonant oscillation frequencies that satisfy the wavelength requirements of the cavity along a given optical path (i.e. the electric vector is zero at the reflecting surface in order to attain an integer number of $\lambda/2$). Transverse modes travel over slightly different optical paths and determine the intensity pattern and divergence of the propagating beam (i.e. the cross-sectional geometry). Each transverse mode propagates along a unique direction and has multiple allowed longitudinal modes associated with it. In other words, all transverse modes can have any longitudinal index and vice versa. These are characterized as $TEM_{l,m,n}$ modes which describe the spatial distribution of the E-field, where the index l denotes the number of longitudinal nodes, and m and n denote the number of nodes in the y and x plane. The resonant frequencies of such modes are given by equation (2.29)[49], where the variables are as defined previously.

$$\nu_{l,m,n} = \left[l + (m+n+1)\frac{\cos^{-1}\pm\sqrt{g_1 g_2}}{\pi} \right] \times \frac{c}{2L} \qquad (2.29)$$

The spacing between successive transverse modes will generally be much less than that between longitudinal modes, and will depend on the characteristics of the cavity (mirror radii and cavity length). The lowest order mode is the $TEM_{1,0,0}$, which is preferentially used in CRDS (see section 2.3.4) due to its spatial coherence, low angular divergence and the fact that it can be focussed into a small spot size[50].

2.3.4 Techniques 1: Cavity Ring-down Spectroscopy (CRDS)

The power of CRDS for trace gas detection and quantitative absorption measurements was recognised in the late eighties by O'Keefe and Deacon[51]. In such a

setup, a cavity is constructed around the absorption medium of interest (in the case here, a plasma chamber) into which radiation from a pulsed laser is coupled. The light is reflected back and forth within the cavity and with each reflection a small fraction is transmitted and 'leaks out' of the cavity. Rather than measuring the level of light absorbed, the rate of absorption is determined by measuring the decay time of the light leaking out of the cavity; the more the sample absorbs, the shorter the measured decay time. The advantages of CRDS over traditional absorption techniques include the fact that the absorption signal is derived from time-dependent decay measurements, so is independent of pulse-to-pulse intensity fluctuations. Furthermore, the pathlength can be very long (several kilometres) while the sample volume remains relatively small. The technique also provides measurements on an absolute scale (unlike modulation spectroscopies), although the absolute mirror reflectivity must be determined (using CRDS with an empty cavity, i.e. no absorption).

When the cavity is empty, the decay time is a single exponential function which is dependent solely on the mirror reflectivities, R, and the distance between them, L. The presence of an absorber introduces an additional loss mechanism, and if this absorption follows the Beer-Lambert law, the decay rate remains exponential. Generally, the intensity of light exiting the cavity will be given by

$$I_{\mathrm{CRDS}}(t) = \int_0^\infty I(\nu) e^{-t/\tau(\nu)} d\nu, \tag{2.30}$$

where the ring-down time, $\tau(\nu)$, is determined by all the light absorption and scattering processes. Since the contributions of broad-band scattering and absorption to the decay rate are generally small compared to that arising from mirror losses, and that generally $R >$ 0.99, one can write $\left|\ln(R)\right| \simeq (1-R)$, and $\tau(\nu)$ can then be written (averaged over the line of sight),

$$\tau(\nu) = \frac{L}{c\left[(1-R)+\alpha(\nu)L\right]} \tag{2.31}$$

where $\alpha(\nu)$ is the absorption coefficient (a product of the frequency dependent cross-section and number density) and the other symbols have their usual meanings.

In practice, the detector does not often 'see' the individual transmissions for each reflection cycle; the electronics average these to provide a smoothed exponential decay. The importance of using the $TEM_{l,0,0}$ can now be appreciated since higher order modes will have a slightly different ring-down time due to modified path-lengths and increased cavity losses (especially diffraction). A cavity ring-down experiment measures both the ring-down time with (τ') and without (τ) the presence of an absorber, and hence $\alpha(\nu)$ can be determined using the equation

$$\frac{1}{\tau'} - \frac{1}{\tau} = \alpha(\nu)c. \qquad (2.32)$$

This absorption coefficient, $\alpha(\nu)$, is recorded as a function of ν to determine the actual absorption profile in frequency space. The effective pathlength traveled by the radiation over the course of a ring-down is given by $L_{\text{eff}} = \tau c = L/(1-R)$, an enhancement of $1/(1-R)$, which for mirror reflectivities of R = 99.99 % corresponds to an enhancement of 10^4. A sensitivity of 5×10^{-10} cm^{-1} $Hz^{-1/2}$ has been reported for pulsed, single mode CRDS[52].

The excitation of a single longitudinal mode in CW-CRDS (an alternative to using pulsed lasers) can be achieved *via* a ramping of either the optical cavity length or the laser frequency, allowing the two to come into resonance periodically. However, this does not yield true exponential decays but superimposes a ringing cavity field upon the time-dependent decay[53,54,55]. In order to obtain the required first order exponential decays, the output of the cavity is monitored and once the detector has reached a threshold value, consistent with a high cavity field and $TEM_{l,0,0}$ excitation, a fast optical switch is triggered (usually an AOM which diffracts and deflects the laser beam from its original path) and a ring-down trace acquired. Romanini *et al.*[56] were the first to apply the technique of CW-CRDS and demonstrated its gain in spectral resolution, signal intensity and data acquisition rate on the weak overtone transition of acetylene near 570 nm. A sensitivity of 8.8×10^{-12} cm^{-1} $Hz^{-1/2}$ has been reported for locked CW-CRDS[57]. In this thesis, all CRDS measurements were conducted using an AOM.

It is also possible to apply the methodology of CW-CRDS to experiments where an analysis of the temporal evolution of the ring-down time is not required. In phase shift CRDS, developed by Herbelin *et al.*[58], extraction of the absorption coefficient and the

mirror reflectivities are obtained from a measurement of the wavelength dependent phase shift experienced by an intensity modulated CW radiation beam on passing through the high finesse optical cavity. This technique has been demonstrated by Engeln *et al.*[59] on the weak $b^1\Sigma_g^+(\upsilon = 2) \leftarrow X^3\Sigma_g^-(\upsilon = 0)$ band of $^{18}O_2$, and its sensitivity is comparable to that of multi-mode pulsed and CW-CRDS techniques[60].

A historical review of cavity enhanced methods is provided by Paldus and Kachanov[61], while Berden *et al.*[62] provide a review on the various experimental schemes of CRDS and show how they can be used to obtain spectroscopic information on atoms, molecules, ions and clusters in a variety of environments. To date, the technique of CRDS has been applied to a wide range of experimental problems. Jongma *et al.*[63] have demonstrated the technique in the UV for the detection of trace gas molecules (NH_3, OH), and were amongst the first to recognize its potential for ultra-sensitive detection. Wheeler *et al.*[64] have provided a review of the early development and application of the technique. Paldus *et al.*[65] applied the technique of cavity locked ring-down spectroscopy by locking a high finesse cavity to the probe laser, and demonstrated this on the detection of water vapour thus offering the promise of shot-noise limited CRDS measurements.

2.3.5 Techniques 2: Cavity Enhanced Absorption Spectroscopy (CEAS)

CEAS (developed in the late 1990's[66,67]) is related to CRDS in that the same optical cavity is used, but is experimentally simpler as no fast switching (using an AOM) or rapid detection electronics are required. Laser radiation from a CW-source is coupled into the cavity *via* accidental coincidences with the cavity modes, with the basic principle that the frequency of the laser should be in resonance with each cavity mode equally long. One way to achieve this is by rapidly scanning the laser frequency (10 – 100 Hz) across the spectral feature of interest so that the interaction time is determined by the scanning speed, and not the cavity instabilities. Alternatively, the laser can be swept slowly with one of the cavity mirrors rapidly ramped using a piezo electric transducer in order to scan the cavity modes. Thus, instead of generating an absorption spectrum point-by-point by stopping and conducting a CRDS measurement at each wavelength, the time integrated intensity of the radiation transmitted by the cavity is recorded on the detector. This allows faster data acquisition and the build-up of the entire absorption spectrum at once. The cavity is deliberately misaligned to excite as many modes as possible and to avoid the background

effects of the sharp transmission profiles which, while essential to CRDS, can distort and even obscure the absorption in CEAS. A detector with a relatively low speed (a time constant ~ ms) is used to smooth the data, and a rapid 'wobble' is sometimes applied to the laser frequency and/or a cavity mirror to further randomise the mode matching[68].

If the laser is swept rapidly enough it can be considered essentially monochromatic over the time interval in which it is resonant with a cavity mode. When these two are in resonance, the E-field within the cavity builds up in the same way as in CRDS, and the exponential decay of the transmission from the rear cavity mirror is recorded (together with the many other laser/cavity resonance events). In this way, the cavity transmission (and thus the CEAS signal) will simply be proportional to the ring-down time, τ. In the absence of an absorber, these will average to form a smooth baseline, $I_0(\omega)$, but with the addition of an absorber the ring-down time will change to τ', producing a signal $I(\omega)$. The absorption can thus recovered using these two traces *via*

$$\frac{I_0(\omega)-I(\omega)}{I(\omega)}=\frac{\alpha(\omega)L}{1-R}=\text{CEAS}\quad\text{Signal},\tag{2.33}$$

where L is the sample length (not necessarily the cavity length), and R is the mirror reflectivity. The intensities $I_0(\omega)$ and $I(\omega)$ need to have any background effects taken into account. These are dominated by optical emission from the plasma (which can be minimised using narrowband interference filters) and amplified spontaneous emission (ASE) from the laser source. It can be seen CEAS has an inherent drawback in that it needs calibration by determination of the value of R, either through CRDS or taking CEAS measurements with a set amount of a known absorber.

O'Keefe *et al.*[69] demonstrated this technique on the vibrational combination bands of CO_2 and H_2O at 1.3 μm using mirrors of R = 99.94 %. Since then, further uses have included that of methane detection at 1.73 μm using a tunable diode laser which reported a sensitivity of 1.8×10^{-7} cm^{-1} Hz$^{-1/2}$ using mirrors with R = 99.84 %[70], and the detection of the (1,0) vibration in the $b^1\Sigma_g^+ \leftarrow X^3\Sigma_g^-$ transition of molecular oxygen at 687 nm where a sensitivity of 3×10^{-8} cm^{-1} Hz$^{-1/2}$ is reported[71]. A sensitivity for CEAS of 1×10^{-7} cm^{-1} Hz$^{-1/2}$ can easily be achieved using a simple experimental setup, as demonstrated with an external-cavity diode laser operating at 1.5 μm to probe the absorptions of ammonia[72]. Off-axis alignment of CEAS (where the laser radiation is coupled into the cavity modes in such

a way as to create a dense mode structure) has been demonstrated on molecular oxygen, and a sensitivity of 1.8×10^{-10} cm^{-1} $Hz^{-1/2}$ has been found[73].

While the simplicity of the CEAS technique described here lends itself to a wide variety of measurements, including those contained within this thesis, it is possible to alter the experimental setup in order to enhance the sensitivity. In the similarly named cavity transmission spectroscopy (sometimes referred to as CEA spectroscopy), the laser frequency is locked to the frequency of a cavity mode, and with subsequent scanning of the laser across an absorption feature the lock is maintained. In this way, the cavity is continually in resonance and the transmission through the cavity is recorded as a function of frequency. The fundamental difference between this technique and that of CRDS lies in the fact that resonance between the laser radiation and cavity frequencies is never broken. The major drawback to this technique is the complicated and expensive electronics required[74]. In a technique combining CEAS and modulation, Ye *et al.* [75] used an external cavity and apply FMS for shot-noise limited signal recovery. Working with a 1.064 μm Nd:YAG laser, they obtain sub-Doppler overtone resonances of C_2HD, C_2H_2, and CO_2 molecules. A detection sensitivity of 5×10^{-13} for an integrated absorption of 1×10^{-14} cm^{-1} over a 1 s averaging time has been achieved.

2.3.6 Intracavity Laser Absorption Spectroscopy (ICLAS)

ICLAS, a further cavity technique (although not one utilised in the experiments described within this thesis), involves placing a narrow-line absorber into the cavity of a laser[76]. Provided the laser is single mode, the laser gain will also be narrow band and thus lasing action will be strongly affected by the absorbers presence. In order to achieve a gain in sensitivity, the laser pump medium must be kept close to threshold with a constant pump power. At this point, a minor change in the intracavity losses may result in a large change in the laser output. The effective pathlength of such an experimental setup is given by,

$$l_{\text{eff}} = \frac{g_0}{\gamma(g_0 - \gamma)} \tag{2.34}$$

where γ is the total passive cavity losses per round trip and g_0 the unsaturated laser gain. However, this simple approach is limited by the increasing instability of the laser output as

the threshold is neared, and by the spontaneous emission background from the laser above threshold.

If the laser is multimode (with a spectral output broader than the absorption features of interest) the laser gain will only be affected by broadband losses such as *via* the cavity mirrors. In this instance, the gain will be determined by the smallest loss among oscillating modes. To obtain an actual absorption spectrum, an acousto-optic modulator (AOM) is used to direct the laser output onto a spectrograph, which resolves the emission spectra on a detector array. Here, the sensitivity gain arises from the fact that the radiation passes through the absorber many times and the cavity functions as a very effective multi-pass cell. Ultimately, the sensitivity of ICLAS is determined by the laser pulse duration and non-linear mode coupling. It can also be used effectively in spatially resolved measurements, due to the confinement of the beam to the laser cavity. Difficulties associated with the technique include the determination of baseline losses, spectral range and a relatively low dynamic value.

References

[1] Hall, R.N. *et al*, Phys. Rev. Lett., **9**, 366, (1962)

[2] Demtroder, W., Laser Spectroscopy, 3rd Edition, Springer, (2002)

[3] Wieman, C.E. & Hollberg, L., Rev. Sci. Instrum., **62**, 1, (1991)

[4] Allen, M.G., Meas. Sci. Technol., **9**, 545, (1998)

[5] Galbacs, G., Appl. Spec. Rev., **41**, 259, (2006)

[6] Yariv, A., Optical Electronics in Modern Communiations, 5th Edition, OUP, (1997)

[7] Byer, R.L., J. Nonlinear Opt. Phys. Mater., **6**, 549, (1997)

[8] Franken, P.A. *et al*, Phys. Rev. Lett., **7**, 118, (1961)

[9] Boyd, G.D & Kleinman, D.A., J. Appl. Phys., **39**, 3597, (1968)

[10] Hancock, G. *et al*, Opt. Lett., **27**, 763, (2002)

[11] Hancock, G. *et al*, Appl. Phys. B., **74**, 569, (2002)

[12] Bakowski, B. *et al*, J. Phys. D: Appl. Phys., **38**, 2769, (2005)

[13] Angelis, M.de. *et al*, Appl. Phys. B., **62**, 333, (1996)

[14] Hemmerich, A. *et al*, Appl. Opt., **33**, 988, (1994)

[15] Houe, M. & Townsend, P.D., J. Phys. D: Appl. Phys., **28**, 1747, (1995)

[16] Huang, L. *et al*, Appl. Phys. B, **72**, 301, (2001)

[17] Meyn, J.P. & Fejer, M.M., Optics Letters, **22**, 1214, (1997)

[18] Clark, H. Y. *et al*, Chem. Phys. Lett., **399**, 102, (2004)

[19] D'Amico, G. *et al*, Opt. Lett. Eng., **37**, 481, (2002)

[20] Schnitzler, H. *et al*, Appl. Opt., **41**, 7000, (2002)

[21] Reid, J & Labrie, D., Appl. Phys. B, **26**, 203, (1981)

[22] Supplee, J.M. *et al*, Appl. Opt., **33**, 6294, (1994)

[23] Bjorklund, G.C., Opt. Lett., **5**, 15, (1980)

[24] Hall, J.L. *et al*, Appl. Phys. Lett., **39**, 680, (1981)

[25] Lenth, W., IEEE J. Quant. Elec., **QE-20**, 1045, (1984)

[26] Gehrtz, A. *et al*, Opt. Lett., **11**, 132, (1986)

[27] Zhu, X. & Cassidy, D.T., J. Opt. Soc. Am. B, **14**, 1945, (1997)

[28] Chou, N. & Sachse, G.W., Appl. Opt., **26**, 3584, (1987)

[29] North, S.W. *et al*, J. Chem. Phys., **104**, 2129, (1996)

[30] Gulluk, T. *et al*, Rev. Sci. Instrum., **68**, 230, (1997)

[31] Bloch, J.C. *et al*, J. Chem. Phys., **101**, 1717, (1994)

[32] Gustafsson, U. *et al*, Appl. Opt., **39**, 3774, (2000)

[33] Hall, G.E. & North, S.W., Annu. Rev. Phys. Chem., **51**, 243, (2000)

[34] Reid, J. *et al*, Appl. Opt., **17**, 300, (1978)

[35] Henningsen, J. & Simonsen, H., Appl. Phys. B, **70**, 627, (2000)

[36] Schafer, S. *et al*, Appl. Phys. B, **66**, 511, (1998)

[37] Shimose, Y. *et al*, IEEE Photon. Technol. Lett., **3**, 86, (1991)

[38] Uehara, K & Hideo, T., Appl. Opt., **31**, 809, (1992)

[39] Dharamsi, A.N. & Bullock, A.M., Appl. Phys. B, **63**, 283, (1996)

[40] Gibb, J.S. *et al*, Appl. Phys. B, **76**, 97, (2003)

[41] Zybin, A. *et al*, Spectrochimica Acta. **48B**, 1713, (1993)

[42] Pavone, F.S. & Inguscio, M., Appl. Phys. B., **56** 118, (1993)

[43] Song, K.S. & Jung, E.C., Appl. Spec. Rev., **38**, 395, (2003)

[44] Werle, P., Spectrochimica Acta Part A, **54**, 197, (1998)

[45] Platt, U. & Perner, D., J. Geophys. Res., **85**, 7453, (1980)

[46] White, J.U., J. Opt. Soc. Am., **32**, 285, (1942)

[47] Herriott, D.R. *et al*, Appl. Opt., **3**, 523, (1964)

[48] Busch, K.W. & Busch, M.A., Cavity –Ringdown Spectroscopy, Chapter 3, ACS Symposium Series 720, (1999)

[49] Siegman, A.E., Lasers, University Science Books, Mill Valley, California, USA, (1986)

[50] Hecht, E., Optics, Addison Wesley, (2001)

[51] O'Keefe, A & Deacon, D.A.G., Rev. Sci. Instrum., **59**, 2544, (1988)

[52] van Zee, R.D. *et al*, Appl. Opt., **38**, 3951, (1999)

[53] An, K. *et al*, Opt. Lett., **20**, 1068, (1995)

[54] Poirson, J. *et al*, J. opt. Soc. Am. B., **14**, 2811, (1997)

[55] Lawrence, M.J. *et al*, J. Opt. Soc. Am. B., **16**, 523, (1999)

[56] Romanini, D. *et al*, Chem. Phys. Lett., **264**, 316, (1997)

[57] Spence, T.G. *et al*, Rev. Sci. Instrum., **71**, 347, (1999)

[58] Herbelin, J.M. *et al*, Appl. Opt., **19**, 144, (1980)

[59] Engeln, R. *et al*, Chem. Phys. Lett., **262**, 105, (1996)

[60] Peeters, R, Cavity Enhanced Absorption Spectroscopy, PhD Thesis, Universiteit Nijmegen, (2001)

[61] Paldus, B.A. & Kachanov, A.A., Can. J. Phys., **83**, 975, (2005)

[62] Berden, G. *et al*., Int. Rev. Phys. Chem., **19**, 565, (2000)

[63] Jongma, R.T. *et al*, Rev. Sci. Instrum., **66**, 2821, (1995)

---

[64] Wheeler, M.D. *et. al.*, J. Chem. Soc., Faraday Trans., **94**, 337, (1998)

[65] Paldus, B.A., J. Appl. Phys., **83**, 3991, (1998)

[66] Engeln, R *et al*, Rev. Sci. Instrum., **69**, 3763, (1998)

[67] O'Keefe, A., Chem. Phys. Lett., **293**, 331, (1998)

[68] He, Y. & Orr, B.J., Chem. Phys. Lett., **319**, 131, (2000)

[69] O'Keefe, A. *et al*, Chem. Phys. Lett., **307**, 343, (1999)

[70] Barry, H. *et al*, Chem. Phys. Lett., **333**, 285, (2001)

[71] Bakowski, B. *et al*, Appl. Phys. B., **75**, 745, (2002)

[72] Peeters, R *et al*, Appl. Phys. B., **71**, 231, (2000)

[73] Paul, J.B. *et al*, Appl. Opt., **40**, 4904, (2001)

[74] Gianfrani, L. *et al*, J. Opt. Soc. Am. B., **16**, 2247, (1999)

[75] Ye, J. *et al*, J. Opt. Soc. Am. B., **15**, 6, (1998)

[76] Baev, V.M. *et al*, Opt. Comm., **62**, 380, (1987)

Chapter 3

Noble gas discharges: Key elements of the chemistry of Ne and Ar plasmas

Noble gas discharges lend themselves particularly well to the fundamental study of the kinetics of plasmas, due in part to their comparative simplicity and relatively inert nature. In this chapter, the four levels of the first electronically excited manifold of neon and argon are probed using various forms of absorption spectroscopy, a technique that allows the absolute determination of the concentration of the individual levels with varying plasma properties. A kinetic model is constructed to aid in drawing conclusions about the key properties of these discharges, and the importance of several such processes is highlighted. Further comparisons are made between the argon and neon data sets to establish the influence of the changing physical properties on the discharge chemistry. Additional measurements are carried out using more sensitive techniques to probe higher electronic levels in argon with the aim of verifying the proposed kinetic scheme. Finally, the EEDF in the neon plasma is altered by the addition of various dopant gasses, and the resultant effect on the concentrations of two levels in the lowest electronic manifold (one radiative and one metastable) is measured with conclusions drawn about the changing nature of the discharge.

3.1. Introduction

In order to gain a general understanding of the underlying physical processes involved in plasmas, there can be few better choices than a study of the kinetics of noble gas discharges. These simple systems, where the vast bulk of the plasma density is neutral ground state atoms, contain ions, electrons and excited state species, all of which are known to play a key role in the chemistry of plasmas. In this chapter, a study of argon and neon plasmas is undertaken in which the populations of the four levels of the first excited manifold are investigated. These lie at considerable energies above the ground state (11.6 eV in argon and 16.6 eV in neon) and arise from the $ns^2np^5(n+1)s^1$ configuration (i.e. the promotion of a ground state np electron to $(n+1)$s). As a consequence they act as energy reservoirs and fuel the chemistry of the plasma. These are used, together with limited measurements of the electron density and electron energy distribution functions (EEDFs), in a kinetic model to quantify the relative importance of the various processes occurring.

The four levels within this manifold can be described by the semi-empirical Paschen notation[1], and are denoted (from lowest to highest energy) as $1s_5$, $1s_4$, $1s_3$ and $1s_2$ whose dominant character corresponds to $^3P_2$, $^3P_1$, $^3P_0$ and $^1P_1$, respectively, in the Russell-Saunders coupling scheme. The ground state is labelled as $1p_0$ ($^1S_0$). The Racah notation can also be used to label these levels, based upon the *jl*-coupling scheme, where the excited atom is treated separately as an ionic core and an excited electron. The unpaired electron in the core experiences strong spin-orbit coupling to give a total angular momentum j_{core}, while the spin-orbit coupling of the electron in the excited state is considered to be small and can thus be neglected. However, the orbital angular momentum of the excited electron, l_{ex}, couples with the core (j_{core}) to give an energy level denoted by the quantum number K. This can then couple to the spin of the electron, s, to give the total angular momentum quantum number J. The resultant energy level is denoted $nl_{ex}[K]_J$.

The $1s_5$ and $1s_3$ states are metastable (with lifetimes ~ 40 s), in that optical transitions from these levels to the ground state are strongly forbidden. Conversely, the $1s_2$ and $1s_4$ levels are radiatively coupled to the ground state with Einstein A-coefficients of 1.2×10^8 s^{-1} and 5.1×10^8 s^{-1} in argon and 4.7×10^7 s^{-1} and 6.1×10^8 s^{-1} in neon[2], respectively. As we shall see, this difference in the properties of these states determines the dominant loss processes for this manifold and thus has a major influence on the plasma kinetics. All of these states are radiatively coupled to the higher levels formed from the

$np^5(n+1)p^1$ and $np^5(n+2)p^1$ configurations and can thus be observed in absorption spectroscopy, as shown by the energy level diagram in figure 3.1.

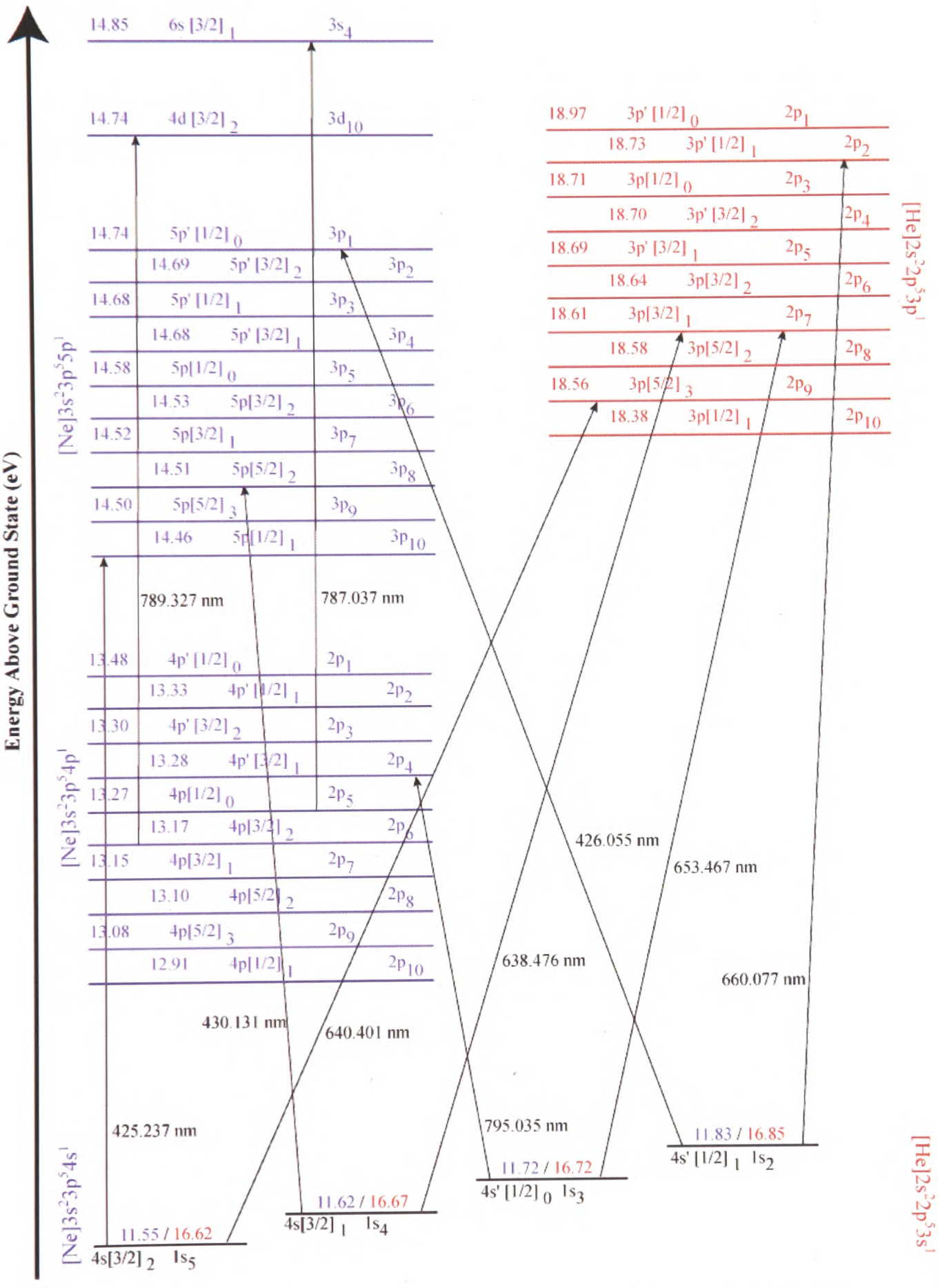


Figure 3.1: The transitions probed in neon (red) and argon (purple) using absorption spectroscopy; the energy of the levels (in eV) is also shown together with their Paschen and Racah labels.

Previous work into noble gas discharges has focussed mainly around argon plasmas. Detailed modelling of such systems has been conducted[3,4,5] and the results compared with data on the electron densities and EEDFs, obtained using electrical probes. However, these techniques shed no light on the presence of excited electronic states for which measurements are best conducted optically *via* either emission or absorption spectroscopy. Investigations into these levels have predominantly focussed on the $1s_5$ state population in the belief that it is the dominant species of the manifold. Several examples of such measurements in an ICP exist[6,7,8,9,10,11,12]

More complete, albeit simple, investigations into this manifold have either grouped together the radiative and metastable concentrations with no distinction between the levels[13,14], or completely neglected the radiative states[15]. The latter approximation is surprising given the importance of radiative trapping (in which a photon is emitted by radiative decay and subsequently reabsorbed by the ground state atoms many times over before it escapes the plasma) and its role in increasing the effective concentration of the radiative states. More conclusive studies, in which the concentrations of the individual levels are probed, include that of Leonhardt *et al.*[16] who measured the $1s_{3,4,5}$ concentrations. Two of the most in-depth studies to date, however, are that of Hebner[17] and Hebner and Miller[12] where spatially resolved densities of all four of the $1s_n$ states were measured in an ICP with varying plasma parameters. This study also comprises a kinetic model which shows reasonable agreement with their experimental data.

The body of research that exists on neon plasmas is somewhat smaller than that for argon. Electrical probe measurements have been used to measure the EEDFs and electron densities in an ICP discharge[18], and also in combination with optical emission spectroscopy in glow-type discharges[19]. Early optical emission studies on the individual states within the $1s_n$ manifold include that by Kalinin & Minaev[20,21] in a DC electric arc plasma and Djulgerova *et al.*[22] in a hollow cathode discharge. Limited diode laser absorption measurements on all four $1s_n$ levels have been carried out by Sheverev *et al.*[23] in a glow discharge.

Fewer simulations of neon plasmas have been conducted and these often ignore the presence of the 1s manifold. A self consistent model of the power balance, ionisation budget and radiation efficiency[24,25] in a DC column discharge has been demonstrated, while Smith *et al.*[26] has utilised an array of optical techniques to provide data for the construction of a kinetic model to glean information on the EEDFs. The optogalvanic effect in neon plasmas is an area of current research interest, and has been studied through

modelling of (amongst other parameters) the $1s_n$ and $2p_n$ levels in a neon positive column[27], and by the pulse-excitation of various $1s_n \rightarrow 2p_n$ transitions[28,29].

3.2 Experimental

Transitions in the region 638-660 nm were used to probe the $1s_n$ levels in neon *via* the $1s_n \rightarrow 2p_n$ absorption lines (shown in table 3.1). Radiation was provided at various wavelengths by a CW diode laser (Sanyo DL-3038-033 and 3147-021 and Sony SLD1132-VS and 5147-041, at 635nm, 655 nm, 640 nm and 658 nm, respectively). These were temperature controlled to within 1 mK *via* a Peltier cooler and heat sink in combination with a home made controller. The laser injection current was controlled by a home-made driver with current ramping to scan across an absorption feature provided by a ramp generator (TTi TG230). The radiation first passed through an optical isolator (Leysop) after which its wavelength was monitored using a wavemeter (Burleigh WA-1000). A beam splitter diverted a fraction of the light into a spectrum analyser (Melles Griot 13 SAD 001) to enable monitoring of its optical spectrum. The radiation then passed once though the plasma chamber and was incident upon a photodiode detector (Thorlabs DET210). A 300 MHz oscilloscope (Lecroy 9314M) received the data which was transferred to a PC *via* a GPIB card for analysis.

The $1s_n \rightarrow 2p_n$ absorption lines in the region 700-850 nm could not be probed as easily in argon due to their large absorption coefficients. For this reason, use was made of the $1s_n \rightarrow 3p_n$ transitions in the 425-430 nm region to probe the $1s_2$, $1s_4$ and $1s_5$ states (see table 3.1) which lie conveniently close in energy and where the absorption cross-sections are lower. However, this necessitates the use of wavelength modulation spectroscopy (WMS, see section 2.2.3) to enhance the sensitivity of the detection. The output of CW diode laser at 860 nm (IDL-50S-870), controlled and monitored as described above but with a sinusoidal wave (generated by a second TTI TG230 function generator) superimposed upon the current ramp using a home-made mixer box, was focussed after the optical isolator into a $KNbO_3$ crystal (Casix $4 \times 4 \times 10$ mm^3, A-cut, AR-coated for 860 nm and 430 nm). This was temperature stabilised by a home-made controller to produce frequency doubled radiation by non-critical 90° Type-I phase matching (see section 2.1.5). Typically, 1-2 μW of blue radiation was produced which corresponds to a production efficiency of 2×10^{-3} W^{-1}. A filter placed after the crystal separated the blue light from the

IR fundamental. The blue radiation was passed five times through the plasma chamber and was incident upon a PMT, with the resultant signal fed into a lock-in amplifier (EG&G Instruments 7265) to be demodulated, before being recorded by the oscilloscope and transferred to a PC for analysis. The $1s_3$ state was observed using fundamental radiation at 795 nm (provided by a SDL-5421-G1 CW diode laser) together with homodyne absorption spectroscopy due to its higher absorption coefficient. The experimental setup is shown in figure 3.2, where the dashed lines represent the additional equipment used for the frequency doubled, WMS measurements.

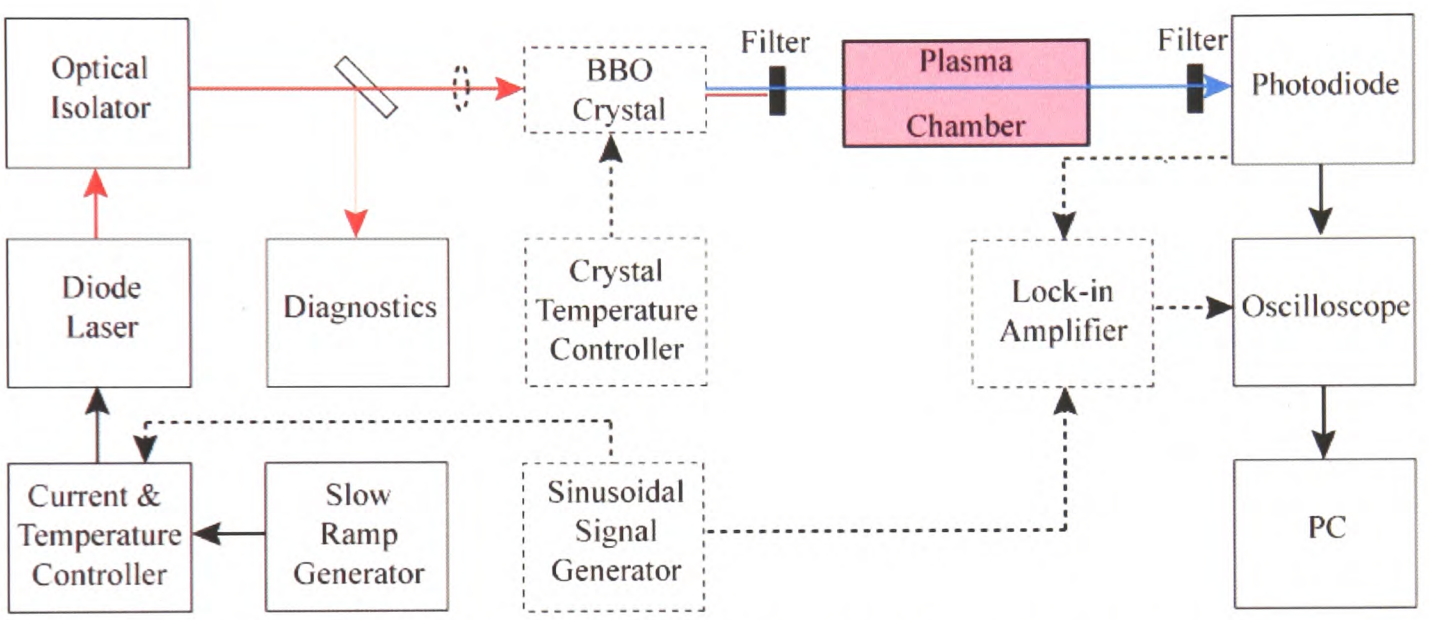


Figure 3.2: Experimental Setup; dashed lines represent additional equipment used in the doubled WMS measurements.

A Langmuir probe (Hiden Analytical ESPion) was used to provide data on the electron densities and EEDFs. This was mounted on a window in the middle of the chamber such that the 15 mm × 0.1 mm tungsten tip was positioned in the centre of the discharge. The RF noise was minimised by passive compensation and the current/voltage characteristics were obtained by sweeping the probe voltage from −30 V to 50 V one hundred times. A total of 100 such averages were obtained, and if no change was observed with time owing to plasma instabilities, these were then averaged to yield the final *I*/*V* traces. Analysis was carried out using the Hiden software suite to yield the electron densities and EEDFs.

Lower State	Energy / eV	Upper State	Wavelength / nm	Cross-section / $cm^2\ cm^{-1}$
Neon				
$1s_2$	16.85	$2p_2$	660.077	1.34×10^{-13}
$1s_3$	16.72	$2p_7$	653.467	1.83×10^{-13}
$1s_4$	16.67	$2p_7$	638.476	1.74×10^{-13}
$1s_5$	16.62	$2p_9$	640.401	3.91×10^{-14}
Argon				
$1s_2$	11.83	$3p_1$	426.055	3.19×10^{-15}
$1s_3$	11.72	$2p_4$	795.036	4.68×10^{-13}
$1s_4$	11.62	$3p_8$	430.131	1.54×10^{-15}
$1s_5$	11.55	$3p_{10}$	425.237	1.60×10^{-16}

Table 3.1: The transitions probed in both Ne and Ar; the wavelength is quoted for a vacuum.

3.3 Results

As discussed in section 1.5.3.1, homodyne absorption spectroscopy is an absolute technique and consequently requires no calibration. An example of the raw data obtained (after 100 averages) is shown in figure 3.3a for the $1s_4$ state of argon at conditions of 20 mTorr plasma pressure and 400 W plasma power. The sloping baseline is a consequence of the changing laser intensity with frequency as the input current is ramped. After taking into account the background, the data are analysed using a Gaussian fit to describe the Doppler broadening (the dominant broadening mechanism at this pressure with natural line broadening being of the order of tens of MHz) and an area of the peak is obtained. This can then be related to a line of sight average concentration using the Beer-Lambert law and the integrated absorption cross-section. The population in the upper p-levels (see section 3.5.1) is low enough not to affect our absorption measurements.

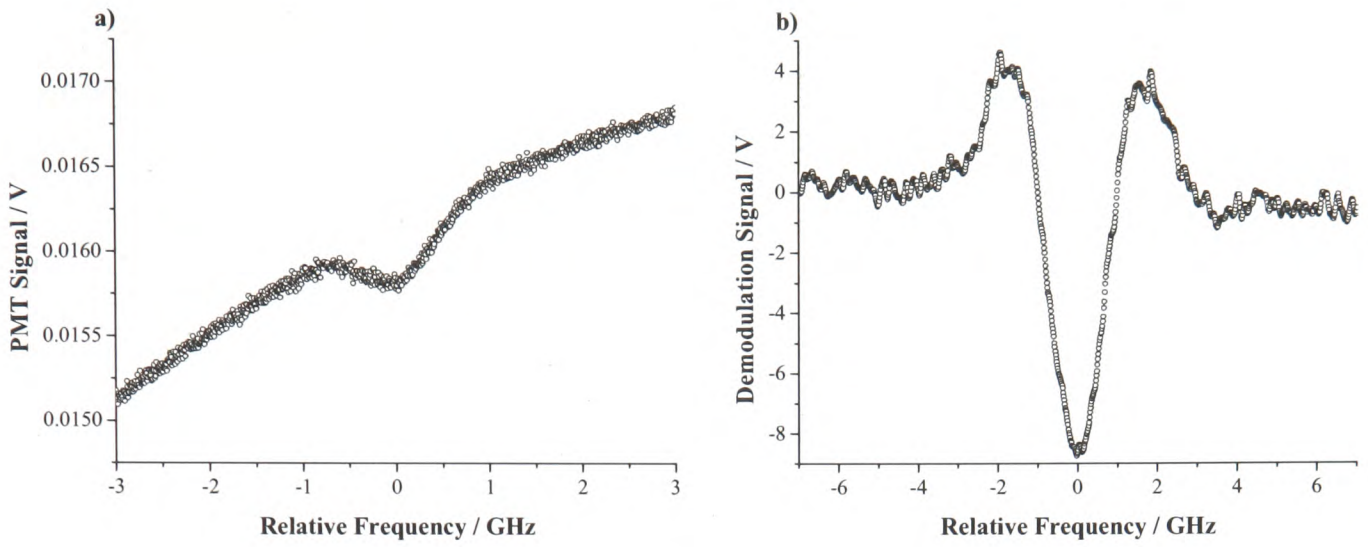


Figure 3.3: Examples of experimental data for absorption from the $1s_4$ state recorded at 20 mTorr and 400 W plasma power and pressure, a) homodyne absorption spectroscopy and, b) a $2f$ WMS trace under the same conditions.

WMS is conducted in the derivative limit (discussed in section 2.2.3,) in order to simplify the analysis of the traces obtained. In the case of the $1s_4$ state in argon the modulation amplitude is 532 MHz and the Doppler width is 1367 MHz (at 300 K); this corresponds to a b value of 0.78. The factors which influence the lineshape remain fairly constant across the plasma parameters (pressure and power) probed here, further simplifying the analysis. This allows one to assume that the relative peak amplitude is proportional to the relative absorption for different conditions, and once the technique is calibrated, to determine the absolute concentrations. Calibration is carried out at conditions where it is possible to observe the peak using both homodyne absorption spectroscopy (typically low plasma pressure and high plasma power) and WMS. Figure 3.3b shows the $2f$ trace obtained for the argon $1s_4$ state under the same conditions as for figure 3.3a, with the additional WMS parameters of 532 ± 73 MHz for the modulation amplitude and a modulation frequency of 10.95 kHz. Detection of the $1s_5$ state was also carried out using $2f$ detection, while the higher absorption coefficient for the $1s_2$ state enabled viable $4f$ detection. The noise on the data that can be seen in figures 3.3a and 3.3b is a consequence of the electrical and optical emission generated by the RF discharge.

Using the data shown in figure 3.3a, and taking into account the absorption is over a pathlength of 175 cm, an average argon $1s_4$ concentration of $(4.85 \pm 0.4) \times 10^9$ cm^{-3} is found. The S/N ratio for the $2f$ WMS trace shown in figure 3.3b is 46.4, and this yields a minimum detectable absorption coefficient of α_{min} of 1.17×10^{-6} cm^{-1} Hz$^{-1/2}$ for the WMS technique.

As mentioned, the Doppler effect is the dominant broadening mechanism in this experimental regime, and thus an analysis of the widths of the absorption profiles will provide a translational temperature (T_{trans}) for the atoms (assuming all the heavy particles are in thermal equilibrium). The data shown in figure 3.3a for the argon $1s_4$ state at 20 mTorr and 400 W exhibit a linewidth corresponding to a T_{trans} of 384 ± 15 K, with the error being one standard deviation of a set of 20 measurements under identical conditions. The value for the $1s_4$ state of neon under the same plasma power but at 100 mTorr is found to be similar at 375 ± 15 K. Within the parameter space explored (10-100 mTorr and 10-400 W), T_{trans} was found to be essentially independent of pressure and to have a weak dependence on power, increasing slightly as the power was increased. In a similar, low-density argon discharge the temperature was found to be 376 ± 20 K[30], and in a neon plasma has been reported as 310 K[23].

3.3.1 Power Variation

Figure 3.4a shows the variation in the $1s_n$ density with plasma power for an argon discharge. The metastable ($1s_{3,5}$) data were recorded at 10 mTorr while that for the radiative states ($1s_{2,4}$) were measured at 20 mTorr, corresponding to conditions at which the signal could be observed but was not saturated for the entire range of powers investigated. Figure 3.4b shows the $1s_n$ density in a neon discharge at a pressure of 100 mTorr for the $1s_{2,3,4}$ states, but at 10 mTorr for the $1s_5$ state (due to the large absorption coefficient the signal saturates at higher plasma powers and pressures). All the data were recorded at a constant height of 15 mm above the lower grounded electrode.

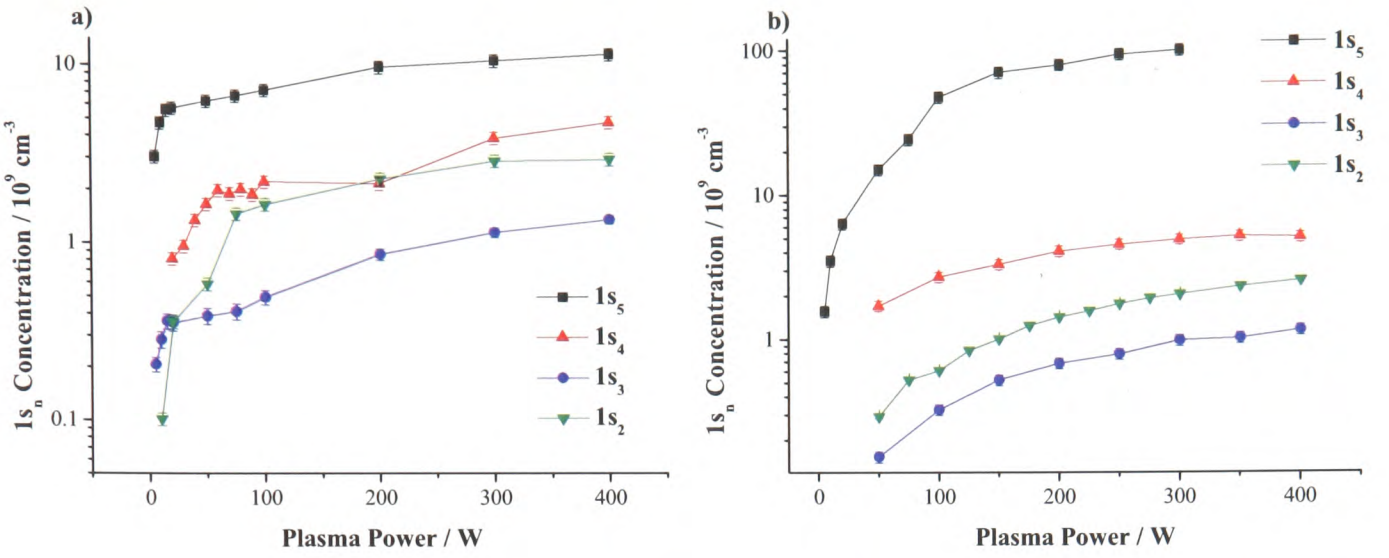


Figure 3.4: The $1s_n$ state concentrations as a function of plasma power, a) argon at 10 mTorr and 20 mTorr plasma pressure for the $1s_{3,5}$ and $1s_{2,4}$ states, respectively and b) neon at 10 mTorr and 100 mTorr for the $1s_{2,3,4}$ and $1s_5$ states, respectively.

The data for both gases show a general increase in $1s_n$ concentration with plasma power before they level off at higher powers. The bimodal operation of the plasma (evident by a shift from capacitive to inductive behaviour) can clearly be seen in the argon metastable concentrations. This switch occurs at around 25-40 W in the argon plasma, and at a much less defined higher power of between 50-100 W in the neon plasma. More precise measurements have been previously made of the switchover power in an argon plasma using optical emission spectroscopy and monitoring of the forward and reverse power coupling. These have shown that the transition occurs at between 35-40 W, at a plasma pressure of 10 mTorr[31], and the methods are in good agreement (once hysteresis effects are taken into account). There is also an increase in the electron temperature and electron density at higher plasma powers (see section 3.3.3). This will increase the production rate of the $1s_n$ manifold as the fraction of electrons with energy above the threshold (11.6 eV and 16.6 eV for argon and neon, respectively) will increase.

3.3.2 Pressure Variation

The variation in the $1s_n$ concentrations with plasma pressure can be seen in figures 3.5a and 3.5b for argon and neon, respectively. The data were recorded at 100 W plasma power with the exception of the $1s_5$ state in neon which was measured at a lower power of 20 W (a consequence of its large absorption coefficient causing optical saturation). It can be seen for both argon and neon that the concentrations of the two metastable and two

radiative states closely track each other across this pressure range, although they follow a somewhat different trend. Furthermore, if one considers the ratio of the concentrations in the case of argon, they closely resemble the ratio of the degeneracies of the respective states. For $[1s_4]/[1s_3]$ and $[1s_5]/[1s_3]$ this is predicted to be 3 and 5, respectively, and the experimental values are found to be ~ 4 and ~ 7. It can also be seen that $[1s_4]$ and $[1s_2]$ are virtually identical. However, this clearly does not hold for the $1s_n$ states of neon.

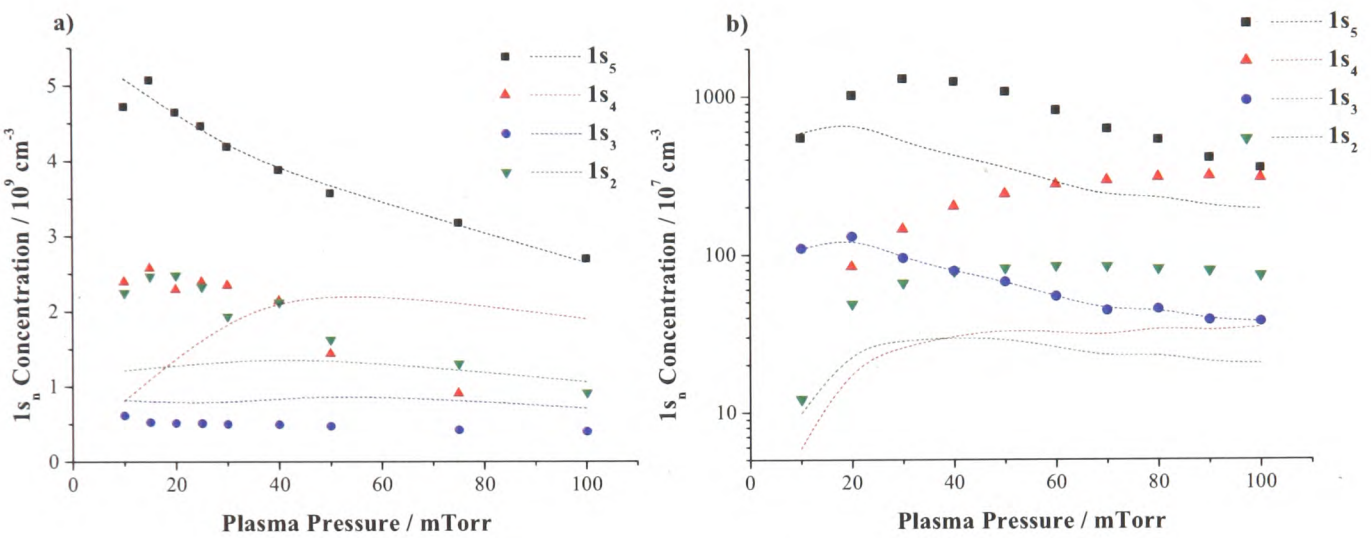


Figure 3.5: The $1s_n$ state concentrations as a function of plasma pressure, a) argon at 100 W plasma power, b) neon at 100 W and 20 W plasma power for $1s_{2,3,4}$ and $1s_5$, respectively.

The metastable states for both argon and neon show an initial slight increase followed by a more dramatic decrease with pressure. In the case of argon, the radiative states show a peak at low pressure followed by a decrease as the pressure increases, while the same states in neon level off at higher pressures after an initial increase at low pressures (over the same pressure range). These general observations may not initially be expected as increasing the pressure increases the electron density and this should lead to an increase in the production rate of the $1s_n$ states. However, increasing the pressure also leads to a decrease in the electron temperature (an effect previously observed[12]) which is not compensated for by the increase in electron density, and the production rate is thus lowered.

3.3.3. Electrical Measurements

The variation in the electron density with plasma pressure for argon and neon, and plasma power for argon, can be seen in figures 3.6a and 3.6b, respectively. The varying

pressure data were recorded at 100 W in argon and in neon, with the varying power data in argon recorded at 100 mTorr. A clear trend of increasing electron density with plasma pressure and power can be seen, although the increase is larger in the former. An order of magnitude difference in the electron densities in the argon and neon plasmas is also observed, which is fairly constant over the pressure range probed.

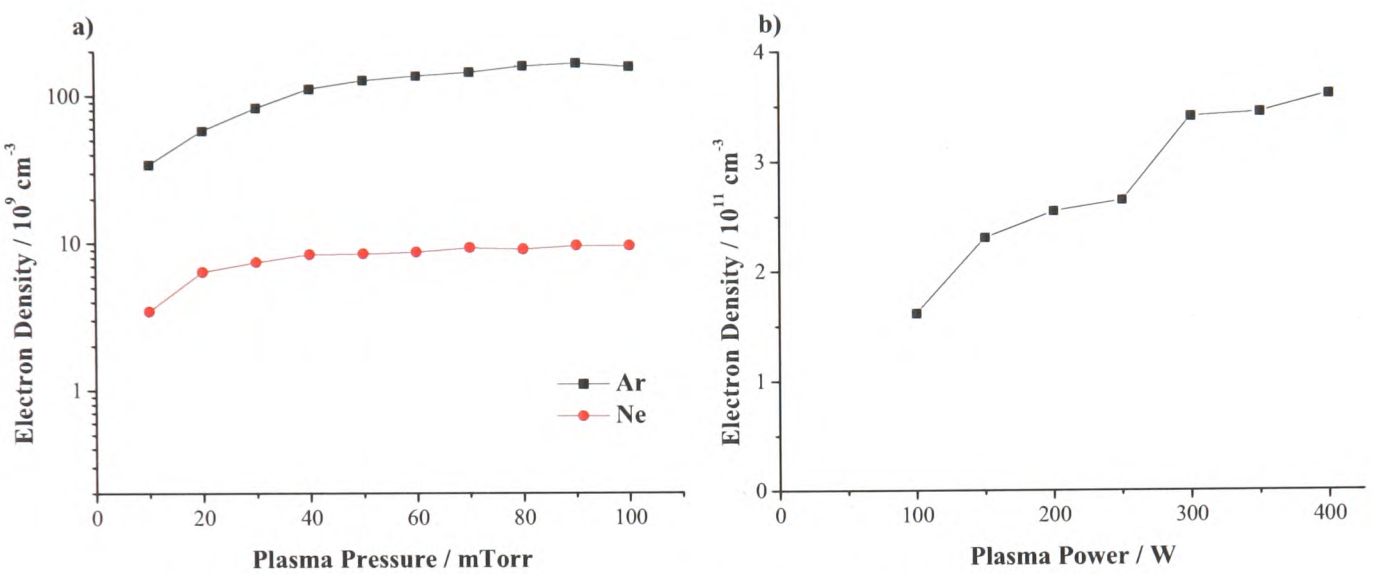


Figure 3.6: Variation in the electron density, a) with plasma pressure at 100 W in an argon and a neon plasma, b) with plasma power at 100 mTorr in an argon plasma.

3.4 Discussion

In order to understand the difference in behaviour of the concentrations of the $1s_n$ states with plasma pressure, the impact of radiative coupling to the ground state needs to be considered. The radiative states ($1s_2$ and $1s_4$) are strongly coupled to the ground state and thus radiative decay is expected to be a dominant loss mechanism (although this effect is somewhat negated by radiative trapping – see section 3.4.1). The metastable states are not coupled at all to the ground state and thus have longer lifetimes (~ 40 s[32]), hence their loss mechanisms are expected to be dominated by collisions.

A global kinetic model for all four $1s_n$ states of argon in an ICP has previously been constructed by Hebner & Miller[12] who managed to obtain good quantitative agreement with their (absorption calibrated) laser induced fluorescence (LIF) data. Electron impact excitation from the ground state was considered to be the only dominant production process (although the cross-sections used included cascade effects from higher levels). Loss mechanisms modelled include de-excitation to the ground state *via* super-elastic collisions, electron impact ionisation, diffusion, intra-manifold conversion and quenching.

Radiative decay to the ground state and subsequent trapping was additionally considered for the radiative states. The gas temperature, electron density and electron temperature were treated as variables with plasma power and pressure, and the EEDF was assumed to be Maxwellian. Radiative decay was highlighted as the ultimate loss process for all four $1s_n$ states, with the population transferred from the metastable levels to the radiative levels *via* electron impact within the 1s manifold.

At present, the author is unaware of any similar studies in neon in which the populations of the four $1s_n$ states have been measured and compared to a kinetic model. However, two simulations of low-pressure neon plasmas of note include those by Smith *et al.*[26] and Stewart *et al.*[27], where modelling has focussed around the behaviour of the optogalvanic effect (OGE). In their models the 1s manifold was deemed to be of crucial importance. In addition to the processes described previously for argon, they also included electron impact excitation to the 2p manifold as a loss process for the $1s_n$ levels (with subsequent radiative decay as a further production route). Although no comments were made on the relative importance of these processes, their model did produce good agreement with their experimental data.

3.4.1 Argon Modelling

A similar model to that of Hebner & Miller[12] fails to reproduce the experimental plasma pressure variation results for a combination of reasons. The radiative decay rate (deemed the most important loss mechanism for the 1s manifold) decreases only slightly for the $1s_2$ and $1s_4$ states with increasing pressure. However, their production rate will increase with plasma pressure as the increasing number density of electrons outweighs their decrease in (Maxwellian) electron temperature. This would result in a large relative increase of the $1s_2$ and $1s_4$ states, possibly even above the $1s_3$ and $1s_5$ concentrations, an effect not seen in the experimental data presented here.

In order to reproduce the experimental trends with plasma pressure seen in our data, an additional kinetic process was considered; that of a fast redistribution of the population of the $1s_n$ levels *via* electron impact excitation and subsequent radiative decay through the 2p manifold. This process can be included in a global model constructed in a similar way to that of Hebner & Miller[12], but with the additional advantage that the EEDFs measured here are accurate in the low energy region where this particular electron impact excitation occurs. The following data are used in the construction of the model:

i. *Electron impact (EI) excitation from the ground state ($1p_0$), k_n^{EI}.*

The experimentally determined energy (E) dependent cross-sections ($\sigma_n^{EI}(E)$) of Chutjian & Cartwright[33], for energies from threshold to 100 eV, were used in the calculation of the rate coefficient for electron impact excitation from the ground state. Theoretical cross-sections are also available in the literature[34], but Chutjian & Cartwright's[33] inclusion of cascades from higher lying levels makes these cross-sections more appropriate under our experimental conditions. The cross-sections were folded with the pressure (p) dependent EEDFs (shown by equation (3.1)) derived from fitting the expressions of Gudmundsson[35] to the Langmuir probe data. Unfortunately, the EEDFs are only accurate up to energies around about 10 eV, and hence the fit at the energies required in the calculation of this rate constant will be crude and it is therefore not possible to obtain quantitative EI rates from the EEDF measurements. However, from the knowledge of the absolute number densities of the $1s_n$ states it is fair to assume that these rate coefficients will be accurate within an order of magnitude. The *relative* strengths of this process leading to the individual $1s_n$ states will also be well represented and therefore the ratios of metastable to radiative state concentrations and their trends as a function of pressure will be relatively unaffected by this uncertainty. To self-compensate the model for this unknown, the rate coefficient for EI to the $1s_5$ state was adjusted so that the model gave good quantitative agreement with the experimental data as a function of plasma pressure. The rate coefficient k_n^{EI} to the other three $1s_n$ levels was consequently adjusted by the same fraction while the calculated ratio between the levels was maintained. This rate coefficient is constructed as a power law of the form $k_n^{EI} = C_n (p/p_0)^{-2}$, a good fit to our experimental data, where p/p_0 is a dimensionless parameter (numerically equal to the pressure in mTorr). The values of C_n used were 1.65×10^{-10} cm^3 s^{-1}, 2.7×10^{-10} cm^3 s^{-1}, 4.2×10^{-11} cm^3 s^{-1} and 7.5×10^{-10} cm^3 s^{-1} for the $1s_5$, $1s_4$, $1s_3$ and $1s_2$ states, respectively. This allows information to be gleaned on how the high energy tail (> 10 eV) of the EEDF changes with pressure.

$$k_n^{EI} = \sqrt{\frac{2}{m_e}} \int_0^\infty E^{1/2} \sigma_n^{EI}(E) f(E,p) dE \qquad (3.1)$$

ii. *EI intra-manifold rates ($1s_n - 1s_n$), $k_{n,m}^{\text{Intra}}$.*

These rate coefficients have been calculated using the energy dependent cross-sections provided by Bartschat & Zeeman[36] ($\sigma_{n,m}^{\text{Intra}}(E)$) and folding them with the EEDFs (accurate at these low electron energies), shown by equation (3.2). Values for the five largest rate coefficients were calculated and found to vary between 1×10^{-8} cm^3s^{-1} and 7×10^{-8} cm^3s^{-1} for the transitions (with the approximate weighting in brackets) $1s_5 \rightarrow 1s_4$ (0.2), $1s_3 \rightarrow 1s_2$ (0.35), $1s_5 \rightarrow 1s_2$ (0.13), $1s_4 \rightarrow 1s_3$ (0.08) and $1s_4 \rightarrow 1s_2$ (0.24). Few experimental literature values exist for these rate coefficients, with Denda[11] reporting values of 4×10^{-7} cm^3 s^{-1} for $1s_5 \rightarrow 1s_4$ and 2×10^{-7} cm^3 s^{-1} for $1s_3 \rightarrow 1s_2$, the only two processes previously thought to be of any importance. These values are larger in magnitude, and reverse in order, to those reported by Bartschat[36] and utilized here. The former is probably a consequence of the low electron temperatures (< 4000 K) for which these values are relevant, and are not useful for typical low pressure RF plasmas which generally have larger electron temperatures (> 19000 K)[37].

$$k_{n,m}^{\text{Intra}} = \sqrt{\frac{2}{m_e}} \int_0^{\infty} E^{1/2} \sigma_{n,m}^{\text{Intra}}(E) f(E,p) dE \qquad (3.2)$$

iii. *Pseudo intra-manifold rates (via the $2p_n$ manifold), $k_{n,m}^{\text{Pseudo}}$.*

The cross-sections for each specific $1s_n \rightarrow 2p_n$ excitation ($\sigma_{n,i}^{\text{Intra}}(E)$) have been provided by Bartschat & Zeeman[36]. Numerous other cross-sections exist in the literature for excitation from the 1s to 2p manifold[38], but the study of Bartschat & Zeeman[36] is the only one known to include state-to-state cross-sections, the key component of our assumption and subsequent model. These are, once again, folded with the pressure dependent EEDFs to obtain rate coefficients which are then weighted by the appropriate radiative decay rates to the $1s_n$ levels ($k_{2p_i \rightarrow 1s_m}^{\text{Rad}}$, determined from the Einstein-A factors), and after summation give a pseudo $1s_n \rightarrow 1s_n$ rate coefficient. This is shown in equation (3.3). A consideration of the magnitude of the A-factors for $2p_n \rightarrow 1s_n$ decay[2] shows the large amount of radiative coupling between these levels and hence the $2p_n$ states quickly depopulate. The resultant couplings between the $1s_n$ levels are extremely strong *via* this mechanism;

for example, the electron impact rate coefficient from the $1s_3 \rightarrow 2p_5$ state is 1.6×10^{-7} cm^3 s^{-1}, and the $2p_5$ state almost exclusively radiates (with an A-factor of 4×10^7 s^{-1}) to the $1s_4$ state. It is found that the $1s_4$ state is strongly coupled to the $1s_5$ state, and that the $1s_2$ state is strongly coupled to all $1s_n$ states by this manner. In total, the rate coefficients for the strongest 40 rate coefficients for this process were calculated for each pressure.

$$k_{n,m}^{\text{Pseudo}} = \sqrt{\frac{2}{m_e}} \int_0^\infty E^{1/2} \sigma_{n,i}^{\text{Intra}}(E) f(E,p) dE \times \frac{k_{2p_i \rightarrow 1s_m}^{\text{Rad}}}{\sum_{\text{all } m} k_{2p_i \rightarrow 1s_m}^{\text{Rad}}} \qquad (3.3)$$

iv. *Electron impact ionisation,* k_n^{Ion}.

The EEDFs are folded with the cross-sections of Hyman[39] ($\sigma_n^{\text{Ion}}(E)$) to give the total electron impact ionisation rate coefficient from the $1s_n$ manifold (equation (3.4)). These are found to vary between 1.5×10^{-8} cm^{3}s^{-1} at 10 mTorr to 3.5×10^{-9} cm^3 s^{-1} at 100 mTorr.

$$k_n^{\text{Ion}} = \sqrt{\frac{2}{m_e}} \int_0^\infty E^{1/2} \sigma_n^{\text{Ion}}(E) f(E,p) dE \qquad (3.4)$$

v. *Diffusion,* k^{D}.

This rate coefficient is approximated by the expression $2646/p$, where p is the pressure in mTorr, taken from Phelps & Molnar[40]. The value of 2646 arises from the value of the diffusion coefficient $D = 1.5 \times 10^{-5}$ m^2 s^{-1}. The effects of temperature have been neglected as there is little change over the pressure range investigated.

vi. *Radiative loss of* $1s_2$ *and* $1s_4$, k_n^{Rad}.

The $1s_2$ and $1s_4$ states are strongly radiatively coupled to the ground state with Einstein-A coefficients of 5.1×10^8 s^{-1} and 1.2×10^8 s^{-1} at wavelengths of 105 nm and 107 nm, respectively. However, this major loss process is tapered somewhat by the effect of radiative trapping in which the emitted photon is absorbed and re-emitted many times over prior to being lost to the chamber walls. This effect is usually modelled by multiplying the A-factor by a trapping factor that reflects the probability of the photon escaping the chamber. The actual line-of-site radiative

trapping factor for the exact geometry of the ICP chamber is unknown and its calculation is beyond the scope of this thesis. However, in the Doppler dominated regime (as is the case here), this factor, γ (the reciprocal of the number of times the photon is emitted and re-absorbed) can be approximated for an infinite cylinder geometry by[41]

$$\gamma = \frac{1.575}{k_0 R\left(\pi \ln\left(k_0 R\right)\right)^{1/2}}, \tag{3.5}$$

where the absorption coefficient is given by $k_0 = \lambda^3 g_2 A_{21}[Ar]/8\pi g_1 c^* \sqrt{\pi}$, g_2 and g_1 are the degeneracies of the upper and lower states, respectively, and c^* is the most probable speed of the atoms. R is the radius of the plasma, and takes a value of 0.11 m for the chamber (calculated from $R = \left(1/r^2 + 1/h^2\right)^{-1/2}$, where r and h are the radial and axial dimensions of the plasma chamber. It can thus be seen that the radiative trapping factor depends not only on pressure, but also on power, through the temperature dependence of the parameter c^*.

The effect of partial frequency redistribution (PFR) outlined in Lawler & Curry[42] is important in this pressure regime and must also be taken into account. Frequency redistribution arises from resonance collisional broadening (in this case collisions between Ar atoms in the ground state and the 1s manifold and a resultant transfer of energy), which influences the lineshapes of the strong UV transitions between these radiative levels and the ground state. The contribution to γ from PFR can be calculated using the reduced parameters outlined in Lawler& Curry[42] and used in analytical solutions to a Monte-Carlo simulation of PFR. This value is combined in quadrature with that from equation (3.5) to give an estimate of values of γ in the regime of PFR. The values of γ for the $1s_2$ and $1s_4$ states at 100 W and 50 mTorr are found to be 1.1×10^{-4} and 1.36×10^{-4}, respectively (corresponding to ~ 9.1×10^3 and 7.4×10^3 re-absorptions). k_n^{Rad} is determined from multiplying together the appropriate A-factor and the trapping factor. It should be noted that while radiative trapping was also considered for the decay process $2p_n \rightarrow 1s_n$, it was found to be negligible under our experimental conditions as $[Ar(1s_n)] << [Ar(1p_0]$.

Figure 3.7 shows a pictorial description of these kinetic processes. Other mechanisms were considered for the production and loss processes of the $1s_n$, but were found not to be important under the conditions of the measurements. These included self-quenching collisions between $1s_n$ atoms, quenching by ground state argon, super-elastic electron de-excitation of the $1s_n$ atoms, three-body processes and stimulated emission from the two radiative states.

Number densities for the four $1s_n$ states were extracted by solving the steady state rate equations simultaneously over all four $1s_n$ states (n = 2-5), shown in equation (3.6), where the square brackets denote a number density of either Ar ground state (Ar_X), Ar in the 1s manifold (state index n), or electrons (e^-).

$$\begin{aligned}\frac{d[\mathrm{Ar}_n]}{dt} &= k_n^{\mathrm{EI}}[\mathrm{e}^-][\mathrm{Ar_X}] - \sum_{\substack{\text{for all}\\ \text{transitions}\\ n\to m}} \{k_{n,m}^{\mathrm{Pseudo}}[\mathrm{e}^-][\mathrm{Ar}_n] + k_{n,m}^{\mathrm{Intra}}[\mathrm{e}^-][\mathrm{Ar}_n]\} \\ &+ \sum_{\substack{\text{for all}\\ \text{transitions}\\ m\to n}} \{k_{m,n}^{\mathrm{Pseudo}}[\mathrm{e}^-][\mathrm{Ar}_m] + k_{m,n}^{\mathrm{Intra}}[\mathrm{e}^-][\mathrm{Ar}_n]\} - k_n^{\mathrm{Ion}}[\mathrm{e}^-][\mathrm{Ar}_n] \\ &- k^{\mathrm{D}}[\mathrm{Ar}_n] - k_n^{\mathrm{Rad}}[\mathrm{Ar}_n] = 0\end{aligned} \tag{3.6}$$

The results of the model for the concentrations of the $1s_n$ states are shown together with the data points in figure 3.5a. It can be seen that there is reasonable agreement with the experimental data, expect for the two radiative states at low pressures. The model shows that radiative loss, modified by the trapping factors, is the ultimate loss mechanism for the entire 1s manifold with electron impact ionization playing a lesser role. The original postulate, that there is a fast redistribution of the $1s_n$ populations through the 2p manifold, is verified by the model as long as it occurs on a timescale faster than that of loss through radiative decay. At lower pressures within the model, radiative decay becomes more significant compared to redistribution through the 2p manifold and the population of the two radiative states thus begins to fall compared to the metastable states. Figure 3.5a shows that this is not observed experimentally, which indicates either the radiative decay rates are lower (i.e. more radiation imprisonment than calculated), or the redistribution is faster.

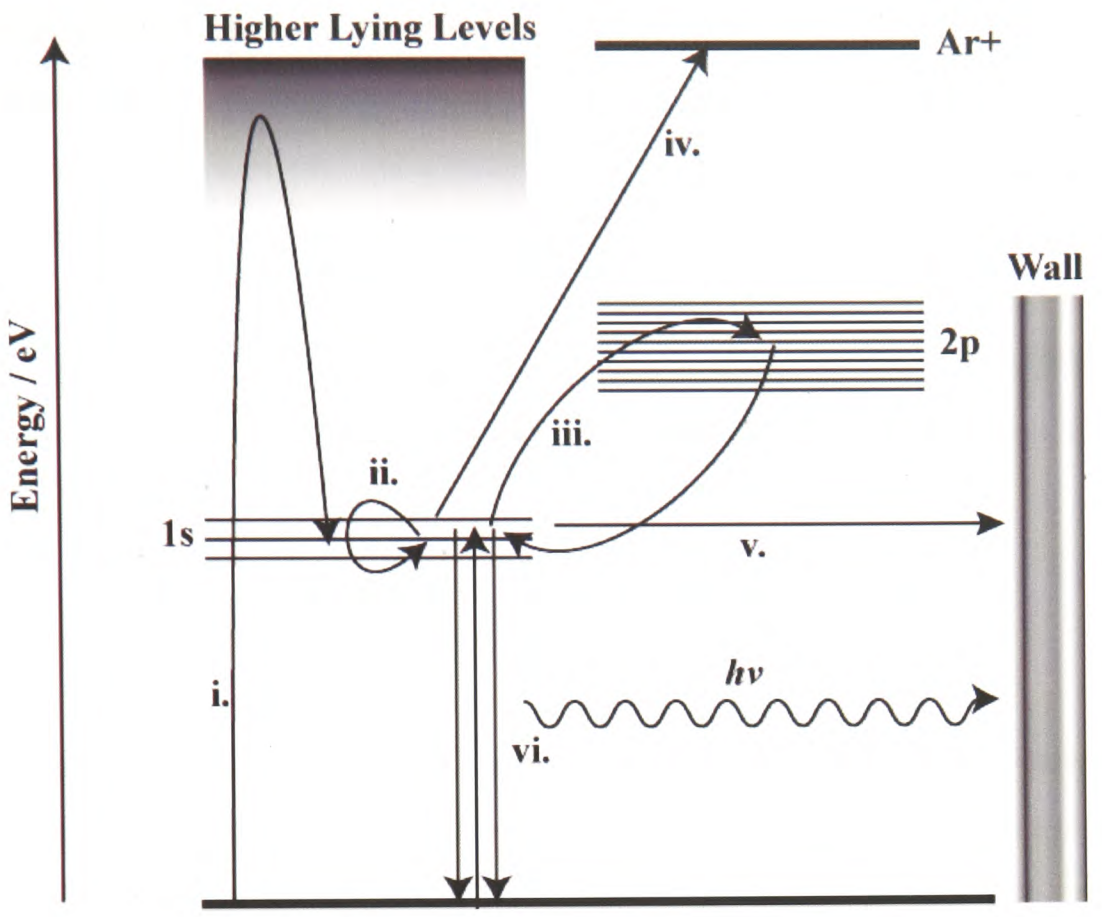


Figure 3.7: Pictorial representation of the kinetic processes modeled.

The importance of the contribution from redistribution *via* the 2p manifold to the relative $1s_n$ populations can also be seen by considering the plasma power dependence of the metastable $1s_n$ states shown in figure 3.4a. Prior to the switchover from the capacitive to inductive mode, the concentrations of these levels can be seen to be low and rapidly increasing, whereas above around 25 W they begin to level-off and increase in a more gentle manner. This implies that an additional loss mechanism is activated after the switchover to limit the $1s_{3,5}$ populations, which can only be attributed to populational redistribution *via* the 2p manifold and subsequent loss by radiative decay from the $1s_{2,4}$ states. This latter loss mechanism is always present in the case of these radiative states, justifying their near linear increase in population with plasma power. The activation of an additional loss mechanism could indicate either a rapid increase in electron density, electron temperature, or a change in the EEDF (specifically a change to encompass a higher fraction of low energy electrons, perhaps from a Maxwellian to a two-temperature distribution). Unfortunately, the noise level on the Langmuir probe was too high to obtain any electrical data at these low powers which would have shed light on the nature of this change.

Improvements to the model could be made by including higher lying manifolds, such as the 3p and 3d. The latter may be of importance considering it lies within 3 eV of

the 1s manifold, an energy at which a large proportion of our electrons lie, and it is strongly radiatively coupled to the 2p manifold. In order to include such levels in the model, accurate cross-sections for electron impact excitation from the 1s to the 3d manifold would be needed in order to calculate the redistribution of $1s_n$ populations through the 3d and (after radiative decay) 2p manifolds. No such cross-sections currently exist in the literature. Quantitative data concerning inelastic collisions involving ground state argon atoms are also necessary to further elucidate the mechanisms involved in population redistribution.

3.4.2 Comparison to Neon

Comparing the data for the $1s_n$ levels of argon and neon shown in figures 3.5a and 3.5b, respectively, reveals that the ordering of the levels in terms of their concentrations remains the same. Furthermore, figure 3.8a shows that the total concentration in the 1s manifold in argon is only around a factor of 2 lower than in neon, and that the trend with increasing plasma pressure is the same, albeit with the peak value shifted to a lower pressure in argon. It can further be seen that the $1s_5$ state dominates in both plasmas, although the actual extent of this dominance in neon is probably underestimated on a like-for-like basis given that the data for this state were taken at 20 W (compared to 100 W for the other states). This is shown in figure 3.8b, where it can be seen that the dominance of the $1s_5$ state in neon decreases with increasing pressure, while in argon it appears constant at lower pressure and increases slightly at higher pressures.

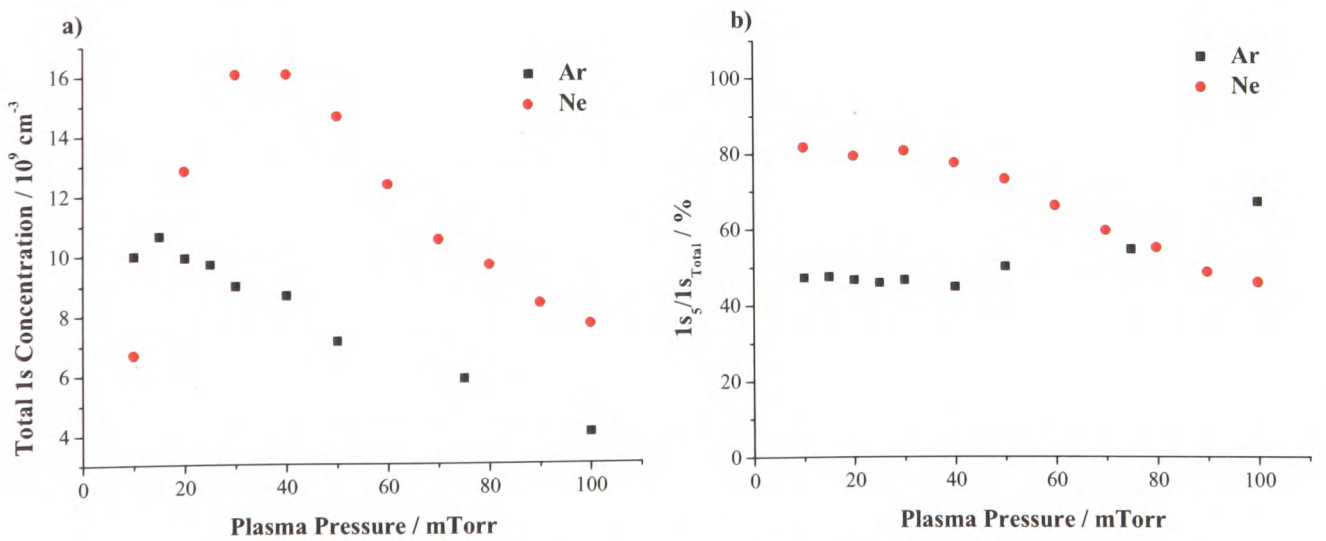


Figure 3.8: a) Total population of the $1s_n$ manifold as a function of plasma pressure, b) population of the $1s_5$ state as a percentage of the total manifold population as a function of plasma pressure.

As shown in figure 3.1, the energy of the 1s manifold in neon lies at ~16.6 eV compared to 11.6 eV in argon. This difference of 5 eV should have a large impact on the energy dependent rate coefficients (arising from a changing fraction of electrons above the various thresholds). However, this effect is virtually mitigated by the expected increase in the electron temperature of around 2 eV in neon compared to argon. Taking this into account and assuming a Maxwellian distribution, the fraction of electrons above the threshold is found to be more or less the same. This can be seen in figure 3.9, where a Maxwellian distribution is shown for energies of 3 eV and 5 eV, and the areas under the curves above the thresholds can be seen to be virtually identical. These values for the electron temperatures are typical for argon and neon plasmas under these conditions and have been measured using Langmuir probes[43], where it was also observed that the electron temperature decreased with increasing pressure. It should be noted that the EEDFs are taken as Maxwellian only to make a comparison, and in reality are unlikely to truly represent this ideal[26].

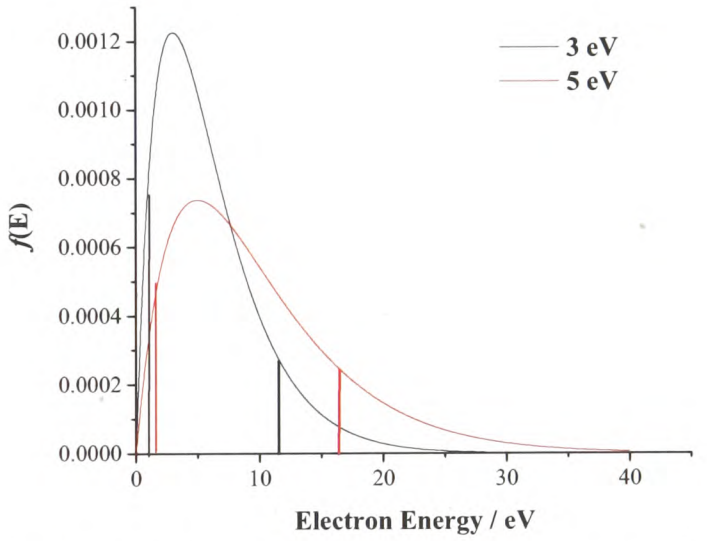


Figure 3.9: Normalised Maxwellian EEDFs at 3 eV and 5 eV.

A varying plasma pressure model along the same lines as that for argon was also constructed for the neon $1s_n$ levels, the results of which are shown alongside the data in figure 3.5b. The key production and loss processes are the same as described previously, and only the values for the rate coefficients for the various processes are now discussed. Whilst experimental cross-sections exist in the literature for electron impact excitation from the neon ground state[44,45] (process i. in section 3.4.1), the state specific and high resolution theoretical cross-sections of Zeman[46] are utilised here. These cross-sections are similar in magnitude, order and shape to those used for argon, although the excitation to the radiative $1s_2$ and $1s_4$ states in neon is marginally higher. However, the same difficulty in folding the EEDFs above the threshold energy with these cross-sections exists for neon

(to an even greater degree than in argon, given the threshold energy is higher at 16.6 eV). It was therefore necessary to again use a pressure dependent power law to describe the rate coefficient of this production process (k_n^{EI}). The best fit values of C_n were found to be 1.2 $\times 10^{-9}$ cm^3 s^{-1}, 8.7 $\times 10^{-10}$ cm^3 s^{-1}, 2.3 $\times 10^{-10}$ cm^3 s^{-1} and 2.5 $\times 10^{-9}$ cm^3 s^{-1} for the $1s_5$, $1s_4$, $1s_3$ and $1s_2$ states, respectively.

While no cross-sections exist in the literature for the intra-manifold $1s_n$-$1s_n$ electron impact excitation (process ii. in section 3.4.1), the rate coefficients for the $1s_5 \rightarrow 1s_4$, $1s_5 \rightarrow 1s_3$ and $1s_4 \rightarrow 1s_2$ transfers have been measured[47] (at an electron temperature of 4000 K) and found to be 1.3 $\times 10^{-7}$ cm^{-3} s^{-1}, 1.7 $\times 10^{-8}$ $cm^{-3}s^{-1}$ and 4.4 $\times 10^{-8}$ cm^{-3} s^{-1}. These values are somewhat higher than those used for argon, but may be explained by their lower electron temperature compared to that found in our ICP (~ 35000 K). Furthermore, the authors determined the rates involving the $1s_2$ state to be so small as to be negligible[47], possibly a reflection of the low $1s_2$ concentration present in their experimental setup. However, the results of private discussions with the authors and investigators of Zeman *et al.*[46] yielded cross-sections for all the $1s_n$-$1s_n$ electron impact excitations. The resultant rate coefficients for the processes varied between 1.4 $\times 10^{-8}$ cm^{-3} s^{-1} and 1.8 $\times 10^{-7}$ cm^{-3} s^{-1}, with relative values of 0.2, 0.03, 0.13, 0.08, 0.19 and 0.37 for the processes $1s_5 \rightarrow 1s_4$, $1s_5 \rightarrow 1s_3$, $1s_5 \rightarrow 1s_2$, $1s_4 \rightarrow 1s_3$, $1s_4 \rightarrow 1s_2$ and $1s_3 \rightarrow 1s_2$, respectively. These values are similar in ordering and magnitude to those found for the argon $1s_n$ levels.

The electron impact ionisation (process iv. in section 3.4.1) cross-sections of neon are gathered from the same source as that for argon[39], and are found to be similar in shape and slightly higher in magnitude. The rate coefficients for this process are calculated to be higher in neon compared to argon (6.1 $\times 10^{-8}$ cm^{-3} s^{-1} at 10 mTorr and 3.3 $\times 10^{-8}$ cm^{-3} s^{-1} at 100 mTorr). This is due in part to the similarity of the ionisation potentials (~ 4.6 eV) from the $1s_n$ levels in argon and neon, and hence folding an EEDF with a higher electron temperature present in the neon plasma results in a higher rate coefficient. The rate of diffusion (process v. in section 3.4.1) for neon metastables is given in Holstein[41] and is found to vary as $7144/p$, a three fold increase compared to argon. It should be remembered that neither of these processes is rate determining in the overall kinetic scheme.

As with the argon $1s_n$ kinetic model, it is logical to postulate that there is a further redistribution mechanism for the $1s_n$ population *via* electron impact excitation to the 2p manifold and radiative decay back to the $1s_n$ levels (process iii. in section 3.4.1). The threshold for this excitation in argon is 1.6 eV, while in neon it is marginally higher at 2.0

eV. It can be seen in figure 3.9 that this difference will have little effect on the rate coefficient as it is virtually mitigated by the increase in electron temperature for neon causing the fraction of electrons above threshold to be similar in both plasmas. State-to-state cross-section data between the $1s_n$ and $2p_n$ levels for neon do not exist in the literature, but were again provided by Zeman *et al.* in a private communication. These compare well with the total $1s_n$-$2p_n$ cross-sections of Hyman[48], and are weighted by the relative radiative rates back to the $1s_n$ levels to give the pseudo $1s_n$-$1s_n$ rate coefficients, $k_{n,m}^{\text{Pseudo}}$. Population transfer into the $1s_5$ level is found to be particularly strong, with rate coefficients of 1.42×10^{-7} cm^{-3} s^{-1}, 8.13×10^{-8} cm^{-3} s^{-1} and 1.33×10^{-7} cm^{-3} s^{-1} from the $1s_2$, $1s_3$ and $1s_4$ levels, respectively. A consideration of the raw data for neon shown in figure 3.5b, but weighted for degeneracy, necessitates a strong electron impact excitation from all the other $1s_n$ states (but particularly the $1s_2$ and $1s_3$) to the states in the 2p manifold that are strongly radiatively coupled to the $1s_5$ level ($2p_5$, $2p_2$ and $2p_1$), in order to justify its large concentration, and this is indeed found.

The major factor yet to be considered in the kinetic scheme of neon is that of radiative decay from the 1s manifold to the ground state. Whilst the A-factors in argon differed by only a factor of ~ 4 (with values of 5.1×10^8 s^{-1} and 1.2×10^8 s^{-1} for the $1s_2$ and $1s_4$ states, respectively), those in neon differ by a factor of ~ 13 (with values of 6.1×10^8 s^{-1} and 4.8×10^7 s^{-1} for the $1s_2$ and $1s_4$ states, respectively). When radiative trapping is taken into account, the rate of decay of these levels can be seen to be different with increasing pressure, as shown in figures 3.10a and 3.10b for neon and argon, respectively. These rate constants, taken together with the electron densities and temperatures determined from the pressure dependent EEDFs measured in neon, are used to solve equation 3.6 (in the same way as for argon) for the four neon $1s_n$ concentrations.

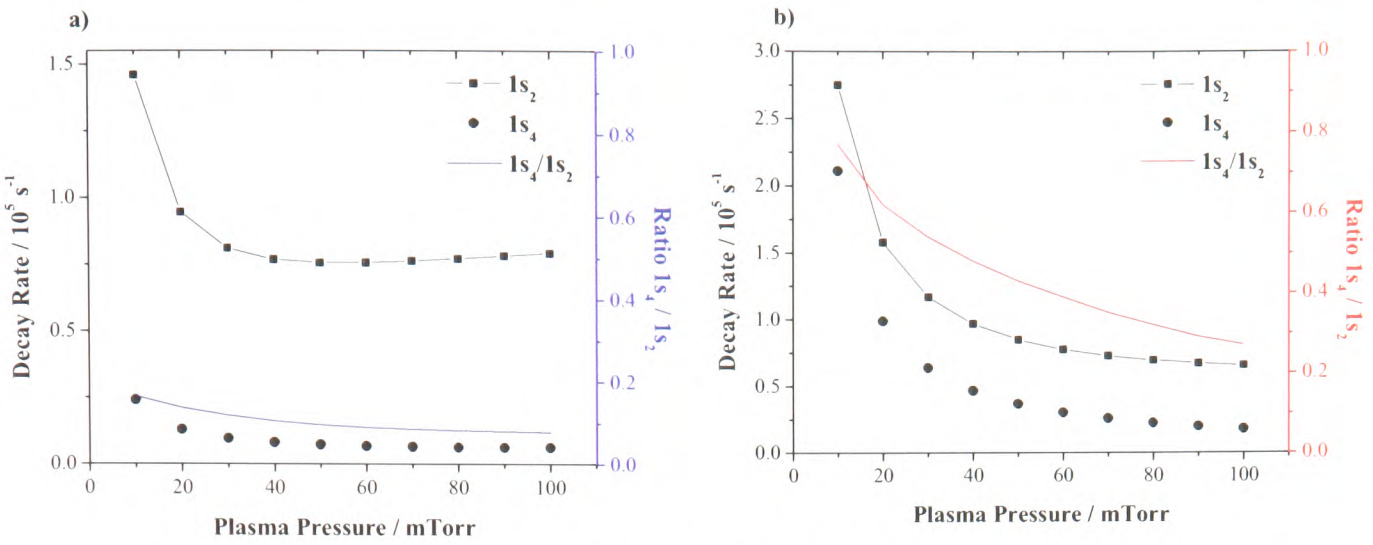


Figure 3.10: Radiative decay rate as a function of plasma pressure for a) argon, and b) neon, radiative states.

Figure 3.5b shows that the model is in good qualitative agreement with the experimental data in that the pressure dependent trends and relative number densities are reproduced, and in reasonable quantitative agreement (especially at lower pressures). It can be surmised, as in the case of argon, that radiative decay is the ultimate loss process for the $1s_n$ levels. The model underestimates the concentrations of both the $1s_{2,4}$ radiative states, indicating that an increased trapping factor and/or faster redistribution through the $2p_n$ levels exists in the plasma. The $1s_5$ population is also underestimated (the true extent disguised by the fact that the data are taken at 20 W instead of 100 W plasma power). Given the strong coupling of this level to the others in the 1s manifold by population redistribution through the $2p_n$ levels, this may be a further consequence of the underestimates made of the radiative state populations. Further populational redistribution *via* other higher-lying levels needs also to be accounted for, as highlighted in the discussion of the argon model.

The success of the kinetic models in reproducing qualitatively the concentrations of the $1s_n$ levels in both argon and neon underlines the importance of the assumption of fast populational redistribution *via* the 2p manifold, and the ultimate loss of population through radiative decay.

3.5 Further Study

Two further sets of measurements complementary to the 1s manifold data were recorded with the aim of gaining more information on argon and neon discharges whilst also aiding in the discussion of the kinetic processes occurring. The concentrations of the

$2p_5$ ($J = 0$) and $2p_6$ ($J = 2$) states of argon were mapped as a function of plasma power and pressure, to help verify the importance of this manifold in the discharge kinetics. In addition, measurements on one metastable state ($1s_3$) and one radiative state ($1s_4$) were conducted in a neon plasma with varying amounts of different dopants in the source gas, with the aim of altering the EEDFs.

3.5.1 Argon $2p_5$ and $2p_6$ Concentrations

The concentrations of the $2p_5$ and $2p_6$ states were measured using the technique of CEAS (discussed in section 2.3.5) due to the low absorption coefficients of the transitions. The output from a 30 mW CW diode laser (Mitsubishi 60116R-01), centred at 789 nm and temperature and current controlled using home build drivers, passed through the optical isolator (Leysop) and was then focussed into an acousto optic modulator (AOM). The light was subsequently focussed into an optical cavity (0.75 m long) bounded by two high reflectivity mirrors (Laseroptik GmbH, AR coated and plano-concave with a radius of curvature of −1.5 m). The output from the cavity was incident on a PMT whose signal was recorded on a digital oscilloscope (LeCroy 9314M), before being transferred to a PC for analysis. A fraction of the light was separated from the beam path after the optical isolator in order to monitor the mode structure of the laser using an optical spectrum analyser (Melles Griot 10 GHz). The wavelength of the light was periodically monitored using a wavemeter (Burleigh WA-1000). The reflectivity of the cavity mirrors was deduced using CRDS (see section 2.3.4) and found to be $R = 0.99909$, which allowed an absolute calibration of the CEAS technique.

The laser radiation was scanned in frequency across the desired transition feature (787.037 nm for $2p_5 \rightarrow 3s_4$, $\sigma_{int} = 8.63 \times 10^{-15}$ cm^2 cm^{-1} and 789.327 nm for $2p_6 \rightarrow 3d_{10}$, $\sigma_{int} = 7.85 \times 10^{-15}$ cm^2 cm^{-1}) for around 30 GHz at a repetition frequency of 25 Hz using a ramp generator (TTi TG230). A total of 1000 sweeps were averaged to obtain an absorption trace, and when taken together with the background, yielded a Doppler broadened peak for each plasma power and pressure. An analysis of the peak widths enabled translational temperatures to be determined, and these were found to be in agreement with those obtained previously for the $1s_n$ states. The variation of the $2p_5$ ($J = 0$) and $2p_6$ ($J = 2$) concentrations is shown with varying plasma power at 20 mTorr in figure 3.11a and with varying plasma pressure at 100 W in figure 3.11b, where the concentration

of the $2p_6$ state has been reduced by a factor of 5 (the degeneracy) to show the deviation of the populations from a thermal distribution.

The variation in concentration can be seen to increase with plasma power (figure 3.11a) with no switchover between capacitive and inductive modes observed, and no saturation at higher powers. This is a reflection of the increasing electron density (figure 3.6b) and electron temperature with plasma power, increasing the production rate (assumed to be electron impact excitation from the ground and $1s_n$ states). The variation with plasma pressure of both the $2p_n$ states displays the now familiar increase and subsequent decrease in concentration across the pressure range, with this change being less pronounced in the case of the $2p_6$ state.

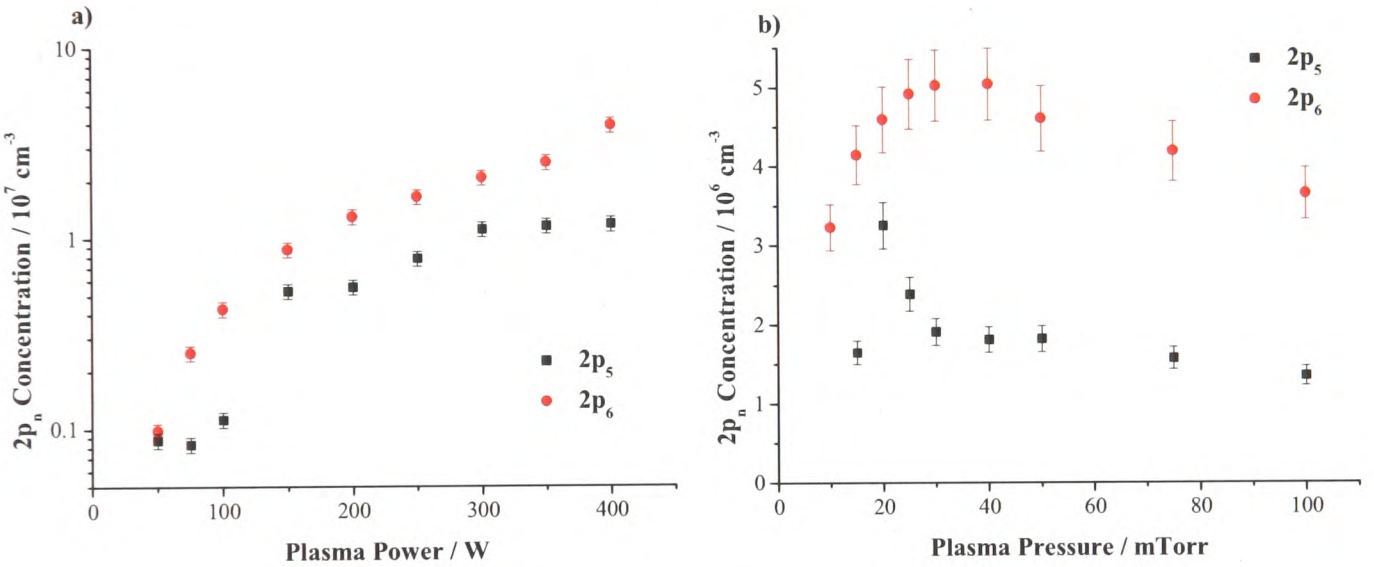


Figure 3.11: Variation in the populations of the $2p_{5,6}$ states in argon (divided by their degeneracy), a) with plasma power at 20 mTorr plasma pressure, b) with plasma pressure at 100 W plasma power.

It is also important to note that the concentrations shown in both the figures are not equal and differ by a factor of up to 4 (with the $2p_6$ being higher), even after factoring in the degeneracy. This suggests that the $2p_n$ levels are not in a thermal equilibrium either through the process of intra-manifold electron impact excitation, or electron impact excitation to the $3d_n$ levels and radiative decay down to the 2p manifold (a similar mechanism to that described in process iii. of section 3.4.1). The only significant loss process for these states will be radiative decay into the 1s manifold. The $2p_5$ state decays solely to the $1s_4$ state, whereas the $2p_6$ state decays to the $1s_{2,4,5}$ states (albeit primarily to the $1s_5$ state), with their total decay rates being almost equal ($A = 4.0 \times 10^7$ s^{-1} and 3.4×10^7 s^{-1} for the $2p_5$ and $2p_6$ states, respectively). Trapping will not be effective here due to

the comparatively low concentration of the $1s_n$ levels, and radiative decay to the ground state is forbidden.

A discrepancy in the production rates of the $2p_5$ and $2p_6$ states could potentially offer a plausible explanation as to the difference in their concentrations. Numerous cross-sections for electron impact excitation to these states from the ground state exist in the literature. These include the theoretical cross-sections of Bubelev *et al.*[49] which do not encompass cascade contributions, and those of Madison[34] which lack data for the $J = 0$ states. The cross-sections of Chilton *et al.*[50] are most appropriate here as they are both complete and include cascade contributions. Analysis of the electron impact excitation cross-sections from the ground state to the $2p_5$ and $2p_6$ states shows that the latter is around three times that of the former, the approximate ratio of the concentrations observed. These cross-sections show a different energy dependence, but are essentially of similar character under the conditions of the measurements. Coupling the cross-sections with the EEDFs to obtain the production rates, and equating these with the radiative loss rate (which is plasma power and pressure independent) produces a concentration trend with plasma power that is consistent with the one observed, but fails to show the observed dependence on plasma pressure. The modelled values are also lower than those observed experimentally. As discussed in the modelling of section 3.4.2, the experimentally determined EEDFs are of limited use in the description of the high energy tail of electrons, and this problem will be exacerbated here as the 2p manifold lies higher in energy than the 1s.

The failure to yield the trend observed for increasing plasma pressure could indicate an additional production process, with electron impact excitation from the 1s manifold the most likely candidate. Utilising the cross-sections of by Bartschat & Zeeman[36] (discussed in process iii. of section 3.4.1) and subsequent folding with the EDDFs, allows the determination of the state-to-state rate coefficients for excitation of the $2p_n$ levels from the 1s manifold. Using this analysis it can be seen that the $2p_6$ state is only significantly excited from the $1s_5$ and $1s_2$ states, with rate constants at 10 mTorr of 6.3×10^{-8} cm^3 s^{-1} and 1.6×10^{-7} cm^3 s^{-1}, respectively. Similarly, the $2p_5$ state is excited only from the $1s_3$ and $1s_2$ states, with rate constants at 10 mTorr of 1.6×10^{-7} cm^3 s^{-1} and 8.5×10^{-8} cm^3 s^{-1}, respectively. Combining these pressure-dependent rate constants with the respective $1s_n$ concentrations and the electron density (also as a function of plasma pressure) allows the overall rate of production from the 1s manifold to be determined. Balancing this against radiative decay as the only loss process allows the creation of a

simple model as a function of plasma pressure, shown for the $2p_5$ and $2p_6$ states in figures 3.12a and 3.12b, respectively (at 100 W plasma power).

The model and experimental data can be seen to approximately track each other, with a discrepancy in the absolute values. The model underestimates the $2p_n$ populations as production routes *via* cascades and populational redistribution have been neglected. Nevertheless, the trends in the $2p_{5,6}$ concentrations as a function of plasma pressure provide further evidence of the importance of the coupling between the 1s and 2p manifolds.

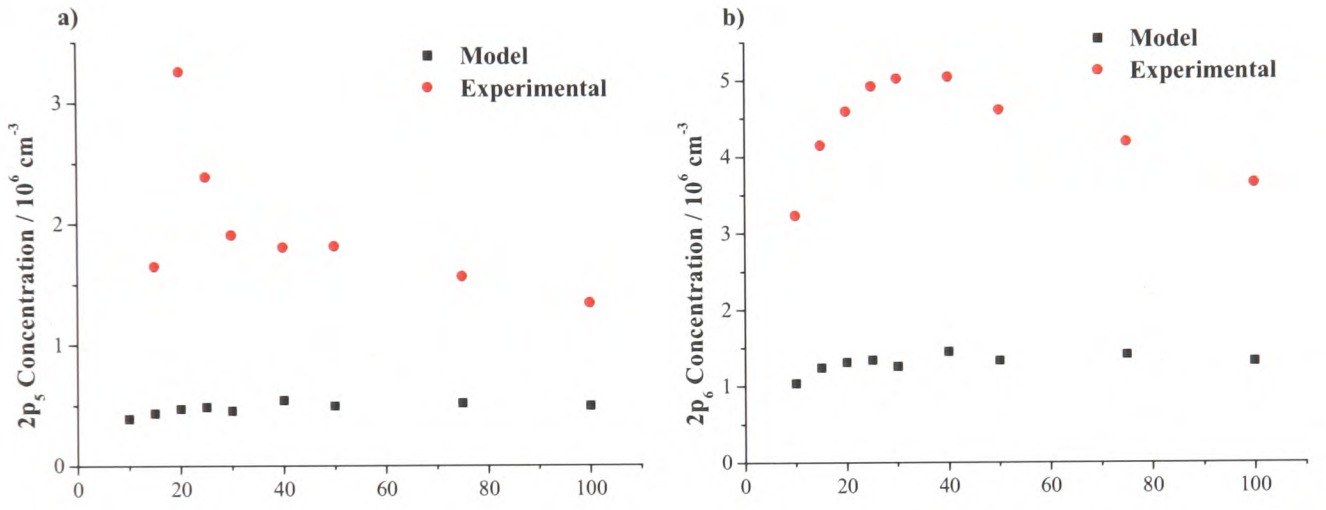


Figure 3.12: Experimental and modeled concentrations as a function of plasma pressure at 100 W plasma power, a) the $2p_5$ state, b) the $2p_6$ state.

3.5.2 Manipulating EEDFs in a Neon Plasma

The concentrations of one radiative ($1s_4$) and one metastable ($1s_3$) state were measured at different plasma powers and pressures using various combinations of feedstock gases. These mixtures were neon doped with varying percentages of nitrogen, argon or helium. The same experimental setup was used as that outlined in section 3.2, with the technique of WMS applied when the concentrations of the relevant states were too low to be observed using homodyne absorption spectroscopy. The composition of the mixtures was maintained using calibrated mass flow controllers.

Figures 3.13a and 3.13b show the variation in the normalised concentrations of the $1s_3$ and $1s_4$ states with plasma pressure at varying powers for a mixture of 1:19 N_2:Ne (5 % N_2, 95 % Ne). Normalised in this context refers to the measured number density divided by the fraction of neon in the feedstock gas mixture. Figures 3.13c and 3.13d show the same scaled concentrations for the $1s_3$ and $1s_4$ states, respectively, at 400 W plasma power for

differing amounts of N_2 doped into the feedstock gas. As expected, the concentrations increase with plasma power for both the $1s_n$ states, but can be seen to decrease with an increasing amount of N_2 doped into the feedstock gas. The pressure dependence at all plasma powers and compositions for the $1s_3$ state demonstrates a sharp decrease with plasma pressure, whilst that for the $1s_4$ state shows a slight initial increase followed by a steady decrease.

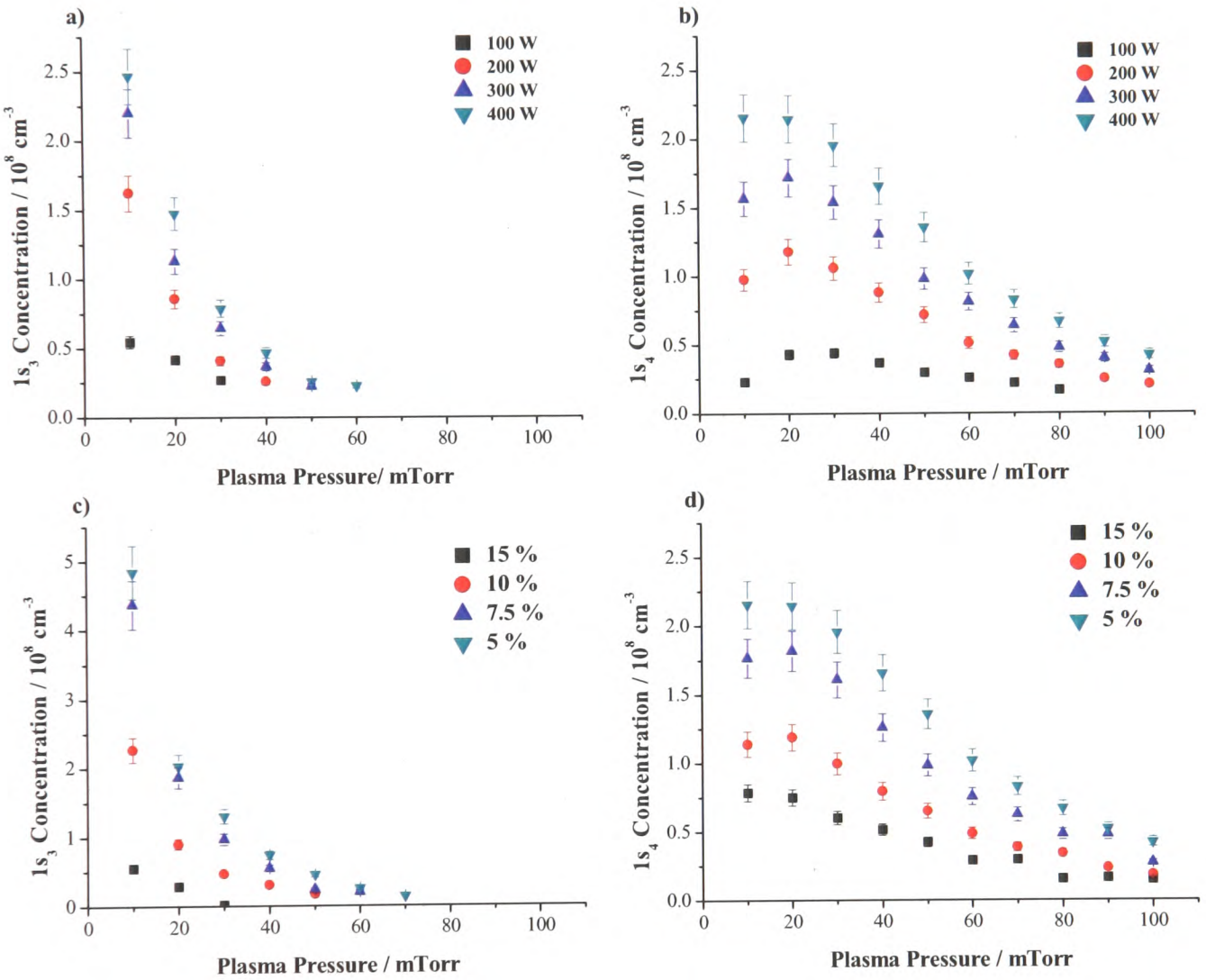


Figure 3.13: Variations in one radiative and one metastable $1s_n$ state concentrations with plasma pressure in a N_2 doped neon plasma, a) $1s_3$ and b) $1s_4$ in 5% doped N_2 at various plasma powers, c) $1s_3$ and d) $1s_4$ with varying dopant amounts of N_2 at 400 W plasma power.

The increasing concentration of the $1s_3$ and $1s_4$ states with increasing plasma power can be understood quite simply in terms of an increasing electron density and electron temperature leading to an increase in the electron impact excitation production rates, without a proportional increase in the loss rates. The data in figures 3.13a and 3.13b show a similar trend with increasing plasma power to that of the pure neon data shown in figure 3.4b.

The reasoning behind the decrease in concentrations for both the $1s_{3,4}$ states with the addition of N_2, and the continuing decrease with the addition of higher amounts of N_2 (even after taking into account the lower neon partial pressure), is based upon changes to the electron density and EEDFs. The lower ionisation potential (E_i = 15.6 eV for N_2 & E_i = 21.6 eV for Ne) in N_2 compared to Ne would be expected to produce a higher electron density. However, the large electron impact excitation cross-sections in N_2 for a wide variety of processes at a range of energies (compared to the few process at low energy in neon) is expected to result in a shift of the electrons from the higher energy tail of the EEDF to a lower energy. This would result in a lower average electron energy (and hence electron temperature) and a decrease in the electron density (by a factor of 2-3) as fewer electrons have enough energy to cause further ionisation. This will have an effect on the production and loss rates directly though the electron density, and more subtly through the energy dependence of the electron impact excitation cross-sections. This type of distribution is far from Maxwellian, and may be more accurately modelled using a bi-Druyvesteyn distribution[51].

The increase in the loss rates (without a corresponding increase in the production rates) that this type of distribution would cause is consistent with the data shown in figures 3.13c and 3.13d. The large decrease in $1s_{3,4}$ concentration in the 5 % N_2 data compared to the pure neon, and a more gradual decrease with increasing amounts of N_2, is a reflection of the changing EEDF. The loss rate will be further enhanced by processes involving collisions with excited N_2 molecules (such as the A-state which is of comparable concentration to the electron density, see Chapter 4). Interestingly, the similar increases in $1s_{3,4}$ concentrations with increasing power and decreasing percentage dopant of N_2 may imply the two effects have a similar influence on the electron density and EEDFs. However, increasing the plasma power just increases the electron density, whereas decreasing the amount of N_2 dopant changes both the shape of the EEDF and the electron number density.

The concentration dependence with increasing plasma pressure of both the $1s_{3,4}$ levels shown in figure 3.13 is of interest in that it differs markedly from that shown in figure 3.5b for a pure neon plasma. The data for the $1s_3$ state show a sharp, exponential decrease with plasma pressure for all the variations of plasma power and percentage N_2 doped (compared to a much more gradual decrease in a pure neon plasma). On the other hand, the concentrations of the $1s_4$ state show a more gentle decrease with plasma pressure

across all conditions of plasma power and percentage N_2 doped, although this in contrast to the levelling-off seen at higher pressures in a pure neon discharge.

This difference in plasma pressure dependence can again be understood in terms of the dominant loss rates for the two states. The $1s_4$ state is radiative and its rate of decay to the ground state (the dominant loss process) will be little affected by the doping of small amounts of N_2 into the feedstock gas (this loss rate will increase slightly with a higher percentage of N_2 as trapping becomes less efficient). This effect arises even though the N_2 is resonant with the trapped UV photon's frequency, as the cross-section for absorption (creating N_2^+) is so low that this loss mechanism can be neglected and the photon will continue to be trapped by the remaining neon atoms. Thus, the decreasing $1s_4$ concentration with plasma pressure will be more a reflection of the decreasing production rate and changing EEDFs.

The dramatic decrease with plasma pressure of the $1s_3$ (a metastable state) concentration must be a consequence of the decreasing production rate and an increasing loss rate. The latter is dominated for this state by intra-manifold quenching and populational redistribution *via* the 2p levels (processes ii. and iii. in section 3.4.1), both of which rely on the number of low energy electrons. The decreasing electron temperature and a change in the actual form of the EEDF with an increasing N_2 composition[43] is commensurate with a large increase in the fraction of low-energy electrons. This in turn increases the low energy threshold loss processes and decreases the high energy threshold production processes causing the pressure-dependent trends observed.

The data in figure 3.14 shows the normalised $1s_3$ concentration as a function of plasma pressure at various powers with 5 % argon doped into the feedstock gas. The trend with increasing plasma pressure can be seen to be similar to that for the 5 % N_2 doped data shown in figure 3.13a, with a concentration higher by around a factor of 3-4 in the case of the argon doped plasma. An argon plasma has a higher electron density (see figure 3.6a) and a lower electron temperature (partly due to the lower ionisation energy of argon of 15.8 eV) than a neon plasma. To a first approximation, it may be thought these two effects would cancel leaving no net impact on the production rate. However, it has been shown using a two-ion-species fluid model that while the increase in electron density is slight, there is a corresponding sharp decrease in the electron temperature upon small scale doping, which decreases more gently with higher proportions of dopant gas[52,53]. The average electron temperature of an argon plasma has been found to be slightly lower than that of a N_2 plasma, with the shape of the EEDF also differing in that there is a higher

fraction of low-energy electrons in an argon discharge[43]. However, coupling this effect with the smaller inelastic electron impact cross-sections for argon (and the lack of the additional loss processes that arise in N_2 mixtures) leads to a reduced loss rate for the $1s_3$ state in the case where argon is the dopant, which consequently leads to a higher concentration.

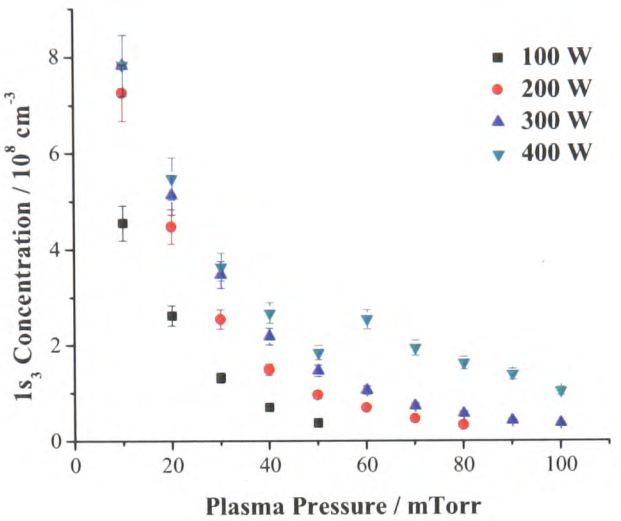


Figure 3.14: The normalized $1s_3$ concentration as a function of plasma pressure at varying plasma powers in a 5 % argon-doped neon plasma.

The data in figures 3.15a and 3.15b show the normalised neon $1s_3$ and $1s_4$ concentrations as a function of plasma pressure at 100 W plasma power in various helium/neon mixtures. In contrast to the N_2 and Ar doped mixtures, the data can be seen to follow the same trend with increasing plasma pressure for both the $1s_n$ states as that in a pure neon plasma (the reader is referred to the earlier sections of this chapter for a discussion regarding the nature of this plasma pressure dependence). Of interest here is that the doping of helium produces a relative increase in the $1s_3$ and $1s_4$ concentrations compared to that found in a pure neon plasma (and in contrast to that found in the N_2 and Ar doped neon plasmas), with the increase more marked for higher proportions of helium. Again, this effect can be understood in terms of the dopant's influence of the production and loss rates *via* the electron density and EEDF.

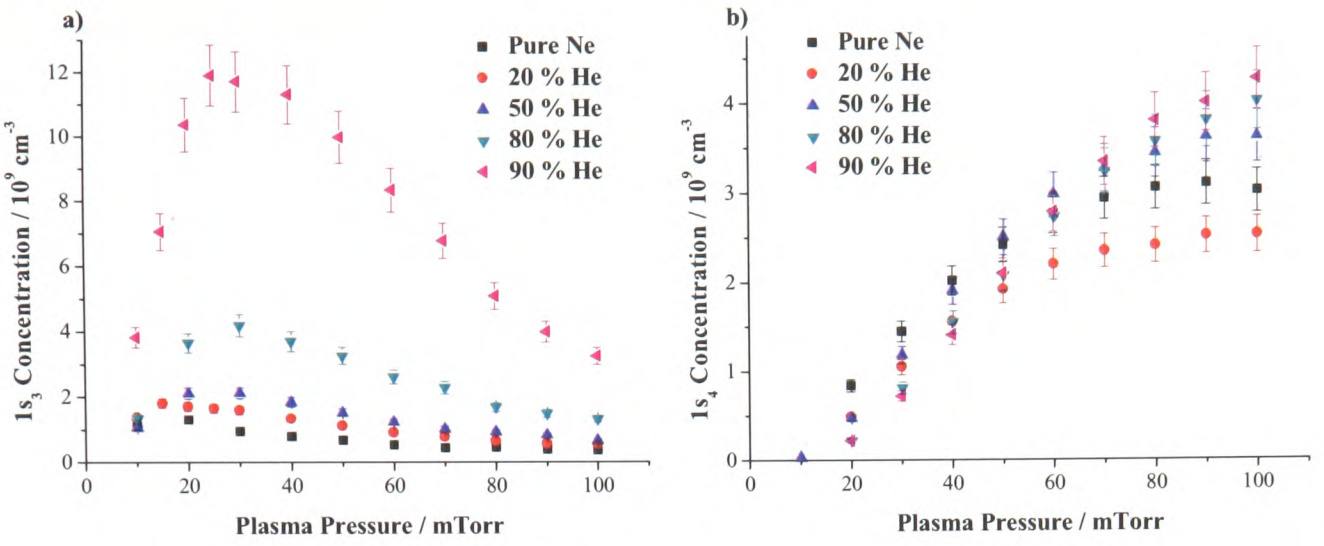


Figure 3.15: The variation in the normalized concentration with plasma pressure, at 100 W plasma power, for different He/Ne mixtures, of a) the $1s_3$ state, and b) the $1s_4$ state.

The electron density is expected to be lower in a helium plasma (E_i = 24.6 eV) than in a neon plasma due to its higher ionisation potential, and consequently a higher electron temperature is expected. This would be in keeping with the trends found for the other noble gasses[43]. A lower electron density will decrease all the rates involving electron impact excitation (both production from the ground state and loss through either intra-manifold population transfer or redistribution *via* the 2p manifold) by a similar proportion. However, a higher electron temperature will increase the rate coefficient for electron impact excitation from the ground state (a threshold of 16.62 eV in neon) proportionally more than the loss rate of intra-manifold quenching (threshold 0.05 eV) or populational redistribution *via* the 2p manifold (threshold of 1.36 eV). It can be seen by considering the threshold energies that the production process depends on the fraction of high energy electrons and the loss processes on the fraction of low energy electrons, the former of which increases compared to the latter upon the addition of higher amounts of helium gas[54,55].

This relative change in the rates of the production and loss processes is clearly manifested in the data for the metastable $1s_3$ state (figure 3.15a), where there is a large increase in concentration upon the addition of helium. These changes can be seen more clearly in figures 3.16a and 3.16b, where the relative increase/decrease (compared to the concentration in a pure neon plasma) in the $1s_3$ and $1s_4$ state populations (at 100 W plasma power and 30 mTorr and 100 mTorr plasma pressure, respectively) is shown for increasing amounts of helium. The combination of an increasing production rate and decreasing loss rate (both based on electron impact) lead to the dramatic increase in the normalised $1s_3$ concentration observed, culminating in an order of magnitude difference between plasmas

of pure neon and in a mixture of 90 % helium. This effect appears to be masked in the case of the $1s_4$ data (a radiative state). Whilst the rate of electron impact excitation from the ground state will increase by the same amount as for the $1s_3$ state, the dominant loss process here is radiative decay. This process increases in efficiency as higher amounts of helium are mixed into the plasma gas due to the increasingly less effective nature of radiative trapping (which decreases with decreasing neon partial pressure in a near linear fashion – see equation (3.5)). Consequently, a slight decrease followed by a marginal increase is seen in the $1s_4$ concentration as the amount of doped helium increases.

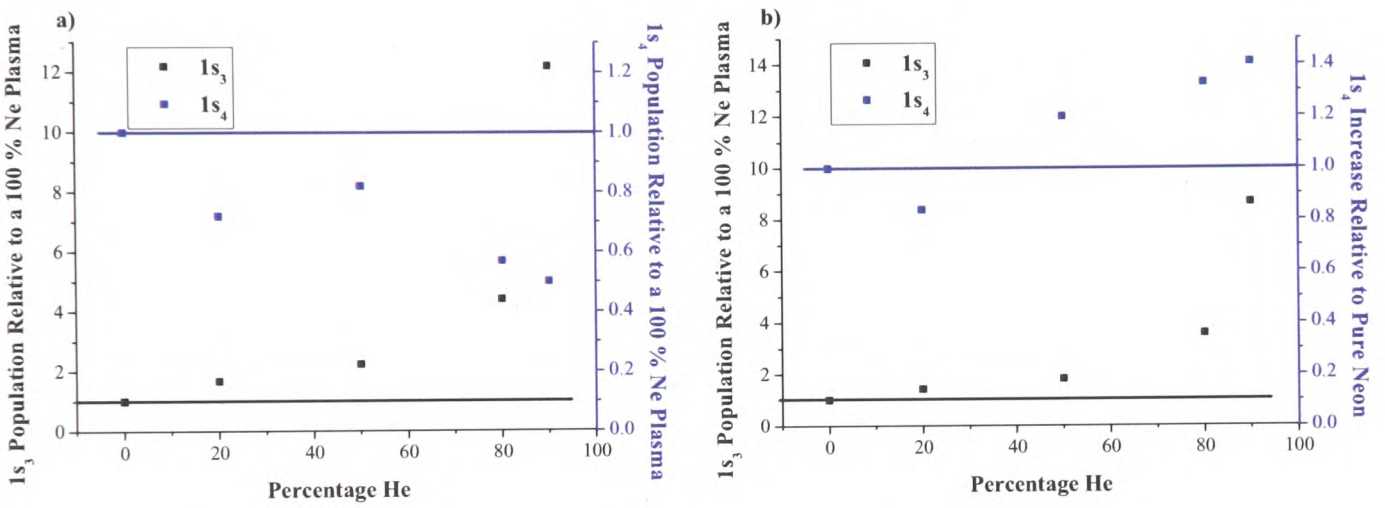


Figure 3.16: Comparative change in the $1s_3$ and $1s_4$ concentrations at 100 W plasma power as a function of the percentage helium plasma composition, a) 30 mTorr and b) 100 mTorr plasma pressure.

The effect that the addition of helium has on the plasma is complicated by the fact it is not limited to altering EEDFs and electron densities. Two of the excited levels of helium ($^3S_1$ and $^1S_0$ arising from the $1s^12s^1$ configuration) lie in resonance with two manifolds of excited neon (the 2s and 3s in Paschen notation, respectively), shown schematically in figure 3.17. Thus, inelastic collisions between these excited states and the neon ground state will result in a resonant transfer of energy, providing an alternative formation route for these excited neon states (as opposed to electron impact excitation from the ground state). A study has shown that this is the dominant production mechanism for many excited neon levels under certain conditions, and can outweigh that for direct electron impact excitation by an order of magnitude[56]. The cross-sections for these resonant transfers of energy are large[57], and the importance of this production route for excited neon states has been shown in a low pressure neon-helium afterglow[58,59]. The exchange of energy *via* this mechanism provides an efficient route for a population inversion resulting in laser action[60], and forms the basis of the He-Ne laser system.

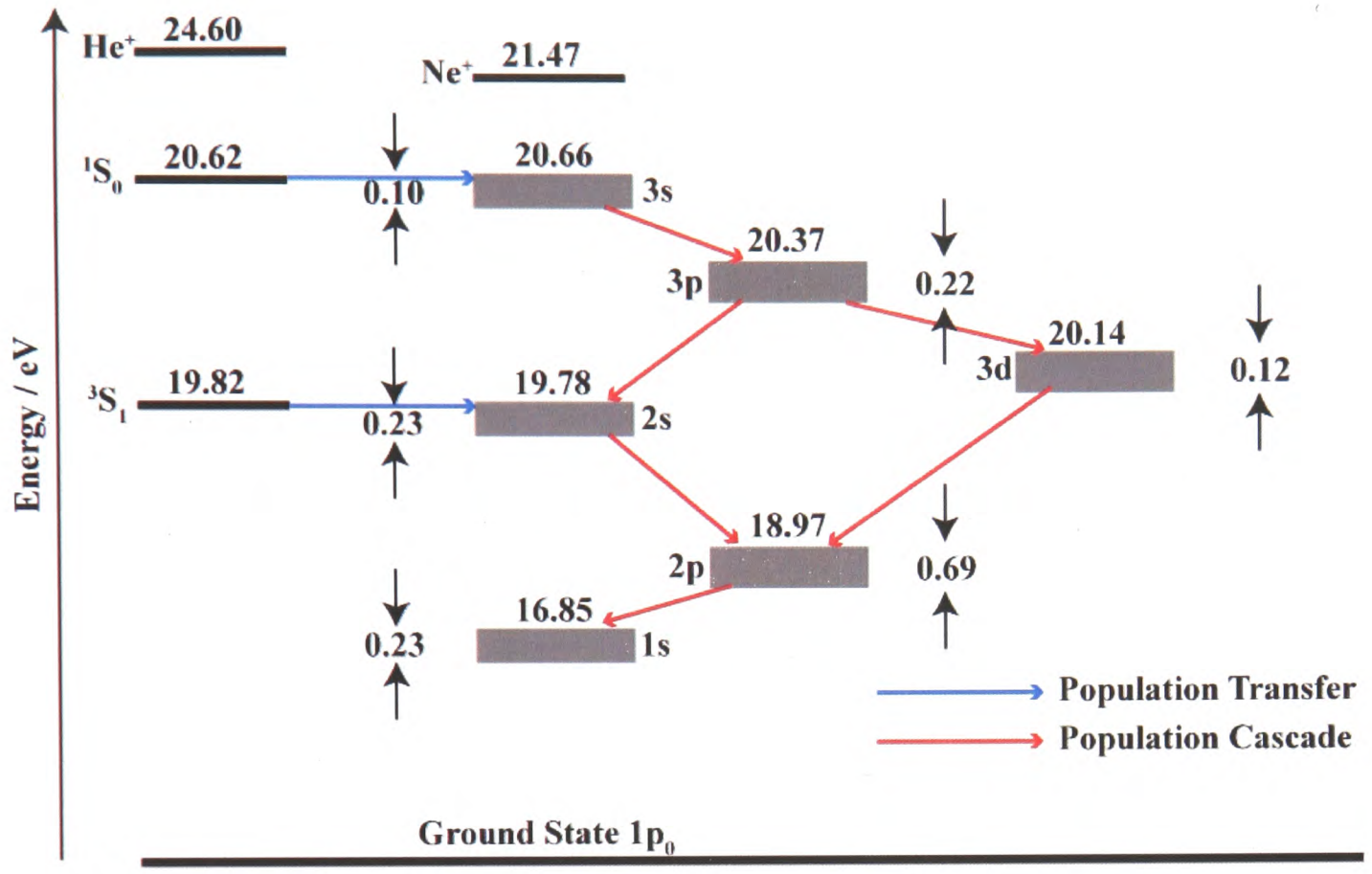


Figure 3.17: Schematic of resonant energy transfer between the various manifolds in a He/Ne plasma.

The excited 2s and 3s manifolds in neon are strongly optically linked to the lower 2p and 3p manifolds, and hence a cascade of their populations will occur. Further cascades will continue this process down to the 1s manifold, resulting in an additional population mechanism. Indeed, it is necessary to invoke this population route in order to explain the exceptionally high populations of the $1s_3$ state shown in figure 3.15a, as this is unlikely to be achieved by an increasing electron temperature alone. While this route will also provide an additional population for the $1s_4$ state, its radiative nature will not result in a significantly increased steady state concentration.

3.6 Summary

Absolute measurements on the concentrations of all four states in the 1s manifold of argon and neon have been carried out with varying plasma parameters of pressure and power. In an attempt to rationalise the results, a kinetic model was constructed for the pressure dependence of the concentrations, using cross-sections obtained in the literature and from private communications, together with additional measurements on the electron

density and EEDF using a Langmuir probe. It was found that while radiative decay to the ground state served as the ultimate loss process for these levels, redistribution of the $1s_n$ levels through electron impact excitation to the 2p manifold and subsequent radiative decay must also play a dominant role in the discharge kinetics. Comparisons between the experimental data and the simulation allowed further conclusions to be drawn about the changing nature of the EEDF with plasma pressure and the relative importance of populational redistribution and radiative decay. The fact that both models qualitatively reproduced the experimental trends in concentration of the $1s_n$ levels allowed verification of the initial assumptions upon which the model was based.

Further measurements of plasma power and pressure dependence were conducted on the lower concentrations of the $2p_{5,6}$ levels of argon (using the technique of CEAS calibrated with CRDS). This data provided a verification of the postulate of populational redistribution of the $1s_n$ levels *via* the 2p manifold, and their concentrations were successfully modelled assuming production from the 1s manifold was the dominant production rate and that radiative decay was the only loss rate. The success of this analysis verified the presence of the strong coupling that is known to exist between the 1s and 2p manifolds.

Attempts were made to alter the EEDFs in a neon plasma by introducing varying amounts of different dopants into the feedstock gas mixture. The affect this had was monitored by measuring the concentrations of one radiative state ($1s_4$) and one metastable state ($1s_3$) across the plasma parameters of power and pressure. The addition of N_2 and Ar, even in small quantities, was found to dramatically lower the concentrations of these 1s states (with the effect more pronounced for the N_2 mixture). This observation was found to be consistent with a cooling of the electron temperature in the plasma (and a changing EEDF) upon addition of N_2 and Ar, with the effect exaggerated for the former due to its possibility of forming excited vibrational and electronic states. On the other hand, the addition of helium to the mixture, even in large amounts, caused a dramatic increase in the normalised $1s_3$ concentration while maintaining the $1s_4$ concentration. This was found to be consistent with an increasing electron temperature and the introduction of additional population mechanisms for the 1s manifold, both of which increase in influence with the percentage of helium in the gas mixture.

References

[1] Paschen, F., Ann. der Phys., **60**, 405, (1919)

[2] Moore, C.E., Atomic Energy Levels as Derived from the Analysis of Optical Spectra, US Department of Commerce, National Bureau of Standards

[3] Matveyev, A.A. & Silakov, V.P., Plasma Sources Sci. Technol., **10**, 134, (2001)

[4] Bogaerts, A., Plasma Sources Sci. Technol., **8**, 210, (1999)

[5] Ferreira, C.M. & Loureiro, J., J. Phys. D., **16**, 2471, (1983)

[6] Hart, L.P. *et al*, Spectrochimica. Acta. B, **41**, 1367, (1986)

[7] de Regt, J.M. *et al*, J. Phys. D: Appl. Phys., **29**, 2404, (1996)

[8] Uchida, H. *et al*, Spectrochimica Acta B, **35**, 881, (1980)

[9] Shindo, H. & Imazu, S., J. Quant. Spectrosc. Radiat. Transfer, **23**, 605, (1979)

[10] Jonkers, J *et al*, J. Phys. D: Appl. Phys., **30**, 1928, (1997)

[11] Denda, T. *et al*, J. Appl. Phys., **95**, 870, (2004)

[12] Hebner, G.A. & Miller, P.A., J. Appl. Phys., **87**, 8304, (2000)

[13] Kiehlbauch M.W. & Graves D.B., J. Appl. Phys., **91**, 3539, (2002)

[14] Kimura, T. & Ohe, K., J. Appl. Phys, **89**, 4240, (2001)

[15] Mumken, G., J. Phys. D: Appl. Phys., **32**, 804, (1999)

[16] Leonhardt, D. *et al*, J. Appl. Phys., **83**, 2971, (1998(

[17] Hebner, G.A., J. Appl. Phys., **80**, 2624, (1996)

[18] Isupov, M.V. & Ulanov, I.M., High Temperature, **43**, 169 (2005)

[19] Bogaerts, A. *et al*, Spectrochimica Acta B, **50**, 1337, (1995)

[20] Kalinin, S.V. & Minaev, P.V., High Temperature, **18**, 924, (1980)

[21] Kalinin, S.V. & Minaev, P.V., High Temperature, **18**, 453, (1980)

[22] Djulgerova, R. *et al*, Spectroscopy Letters, **8**, 1001, (1975)

[23] Sheverev, V.A. *et al*, J Appl. Phys., **92**, 3454, (2002)

[24] Uhrlandt, D., J. Phys D: Appl. Phys., **35**, 2159, (2002)

[25] Uhrlandt, D. & Franke, St., J. Phys D: Appl. Phys., **35**, 680, (2002)

[26] Smith, D.J. *et al*, Plasma Sources Sci. Technol., **11**, 115, (2002)

[27] Stewart, R.S. *et al*, J. Phys D: Appl. Phys., **33**, 864, (2000)

[28] Yao, X. & McGlynn, S.P., Int. J. Quant. Chem., **72**, 369, (1999)

[29] Yao, X. *et al*, J. Appl. Phys., **85**, 3068, (1999)

[30] Beverini, N. *et al*, Plasma Sources Sci. Technol., **6**, 185, (1997)

[31] Bakowski, B *et al*, J. Phys. D: Appl. Phys., **37**, 2064 (2004)

---

[32] Katori, H. Shimizu, F., Phys. Rev. Lett., **70**, 3546, (1993)

[33] Chutjian, A. & Cartwright, D.C., Phys. Rev. A., **5**, 2178, (1981)

[34] Madison, D.H. *et al*, J. Phys. B: At. Mol. Opt. Phys., **31**, 873, (1998)

[35] Gudmundsson, J.T., Plasma Sources Sci. Technol., **10**, 76, (2001)

[36] Bartschat, K. & Zeman, V., Phys. Rev. A., **59**, R2552, (1999)

[37] Pokrzywka, B., Phys., Scr., **66**, 437, (2002)

[38] Hyman, H.A., Phys. Rev. A, **18**, 441, (1978)

[39] Hyman, H.A., Phys. Rev. A., **20**, 855, (1979)

[40] Phelps, M.V. & Molnar, J.P., Phys. Rev., **89**, 1202, (1952)

[41] Holstein, T., Phys. Rev., **83**, 1159, (1951)

[42] Lawler, J.E. & Curry, J.J., J. Phys. D: Appl. Phys., **31**, 3235, (1998)

[43] Schwabedissen, A. *et al*, Phys. Rev. E., **55**, 3450, (1997)

[44] Tachibana, K & Phelps, A.V., Phys. Rev. A., **36**, 999, (1987)

[45] Register, D.F. *et al*, Phys. Rev. A., **29**, 1793, (1984)

[46] Zeman, V. & Bartschat, K., J. Phys. B: At. Mol. Opt. Phys., **30**, 4609, (1997)

[47] Pilosof, N. & Blagoev, A., J. Phys. B: At. Mol. Opt. Phys., **21**, 639, (1998)

[48] Hyman, H.A., Phys. Rev. A., **24**, 1094, (1981)

[49] Bubelev, E.V. & Grum-Grzhhimailo, A.N., J. Phys. B: At. Mol. Opt. Phys., **24**, 2183 (1991)

[50] Chilton, J.E *et al*, Phys. Rev. A., **57**, 267, (1998)

[51] Carman, R.J. & Mildren, R.P., J. Phys. D: Appl. Phys, **33**, L99, (2000)

[52] Bai, K.H. & Chang, H.Y., Appl. Phys. Lett., **79**, 1596, (2001)

[53] Bai, K.H. *et al*, Phys. Plasmas, **9**, 2831, (2002)

[54] Zaitsev, V.V. *et al*, High Temperature, **21**, 7, (1983)

[55] Hughes, M.H., J. Phys. B: At. Mol. Opt. Phys., **3**, 1544, (1970)

[56] Willett, C.S. & Young, R.T., J. Appl. Phys., **43**, 725, (1972)

[57] Arrathoon, R., Phys. Rev. A., **4**, 203, (1971)

[58] Akoshile, A.O. *et al*, J. Phys. B: At. Mol. Opt. Phys., **18**, 2793, (1985)

[59] Akoshile, A.O. *et al*, J. Phys B: At. Mol. Opt. Phys., **19**, 349, (1986)

[60] Javan, A. *et al*, Phys. Rev. Lett., **6**, 106, (1961)

Chapter 4

Molecular discharges I: The vibrational distribution of $N_2(A^3\Sigma_u^+)$ and detection of the $N_2^+(X^2\Sigma_g^+)$ ion in a nitrogen plasma

Nitrogen plasmas are of huge research interest, being very commonly used for technological applications. They also allow laboratory studies of the excited nitrogen species present in the upper atmosphere and auroras. Furthermore, their added complexity compared to atomic discharges leads to a fundamental scientific interest. The kinetics of such plasmas are complicated by the many species present including radiative and metastable states, ions, atoms and the propensity for vibrational and rotational excitation. Definitive techniques to aid in the untangling of the discharge kinetics are therefore highly desirable.

In this chapter, the vibrational distribution of the metastable $N_2(A)$ state is probed over a range of plasma operating parameters using CEAS. A vibrational temperature is calculated and its importance discussed in the context of the overall discharge chemistry. Furthermore, CEAS is combined with the technique of WMS to enable detection of the $N_2^+(X, v = 0)$ ion. The work presented in this chapter builds upon that published previously by this research group[1] for the detection of $N_2(A, v = 0)$ using CEAS, and has itself recently been published[2].

4.1. Introduction

Nitrogen plasmas have been a benchmark system for researchers over the course of many decades, due in equal measure to their industrial applications and fundamental interest. Their use in the modification of the surface properties of metals and polymers has been well documented[3,4,5], and the theoretical modelling of nitrogen discharges is extensive[6,7,8,9]. Nitrogen plasmas also play an important role in the auroral emission and chemistry of the Earth's atmosphere[10]. The molecular nature of nitrogen adds complexity to the kinetics of its plasma compared to those formed from atomic species. N_2 has a rich variety of electronically excited states lying at energies as low as 6.2 eV above the ground state (some of which are shown in figure 4.1), and their population in the discharge together with the presence of other species, including atomic nitrogen and the various ions (and, of course, their electronically excited states), results in a particularly complex system. The possibility for rotational and vibrational excitation of the N_2 molecule within any of its excited electronic states also needs consideration.

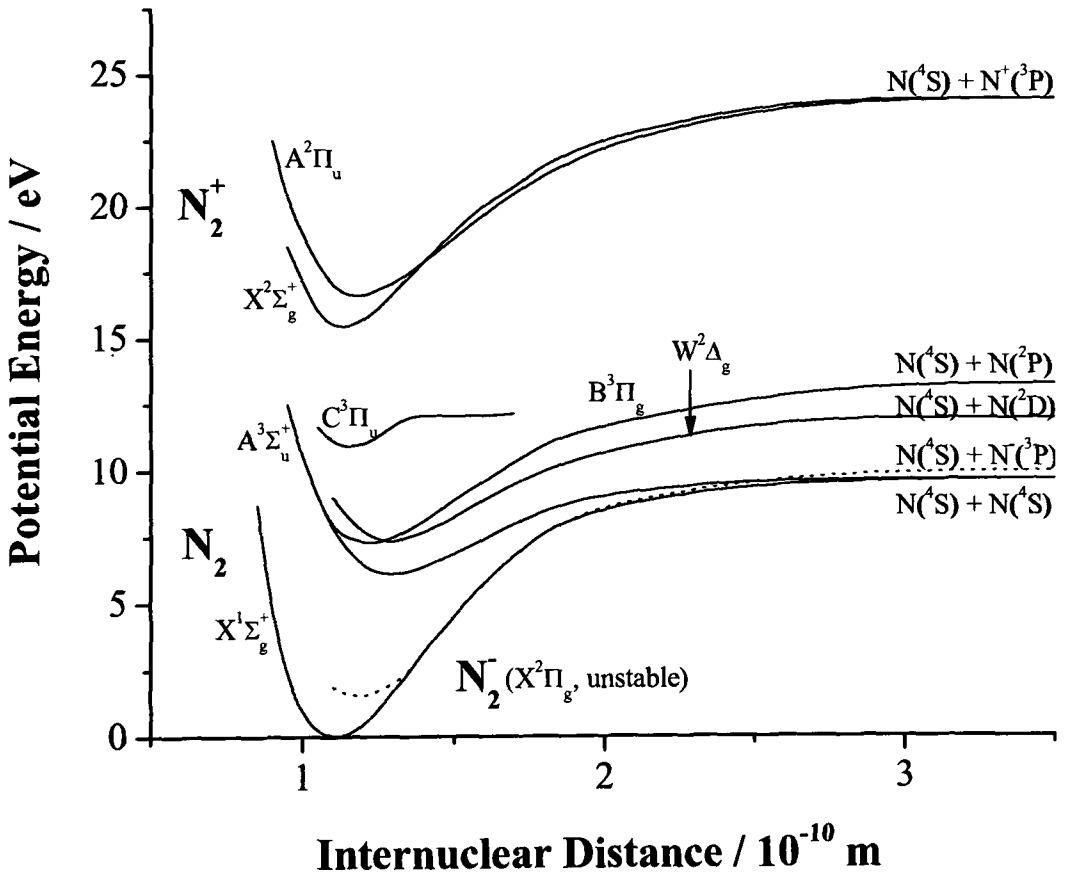


Figure 4.1: Partial potential energy diagram for N_2.

To elucidate the discharge kinetics, measurements must be made of the concentrations of the various species (molecular, atomic and ionic), together with the

electron densities and EEDFs. Several methods have been developed for the observation of N atom densities[11,12], excited electronic states[13,14,15,16,17,18], the N_2^+ ion[19], and EEDFs[20,21]. However, although these techniques can monitor relative trends, their use in making quantitative measurements is often limited by either a need for absolute calibration or applying assumptions when analysing the data (and sometimes both). Examples of such techniques include optical emission spectroscopy, chemical titration and LIF.

The first electronically excited state in nitrogen is the metastable A-state ($^3\Sigma_u^+$), which acts as an important energy reservoir[22,23] due to its relatively long radiative lifetime of ~2 s[24]. It can be formed directly from the ground state by electron impact excitation, or indirectly through N(^{4}S) atom recombination. Furthermore, the extensive degree of radiative coupling to the other electronically excited triplet states enables its formation through cascade mechanisms. The importance of the A state is underlined by its collisional coupling through electron impact excitation and energy pooling reactions with other electronically excited species to form higher lying electronic levels, and its implication in stepwise ionisation processes leading to the formation of the N_2^+(X) ion[25]. The degree of vibrational excitation within a given electronic state will also influence the various reaction rates within the discharge. It can therefore be realised that measurements of N_2(A) and its vibrational distribution, together with the N_2^+(X) ion, will provide an insight into the complex kinetics of the plasma.

In this chapter, an enhanced form of absorption spectroscopy involving an optical cavity (CEAS, see section 2.3.5) is used to measure the vibrational distribution in the first electronically excited state of N_2 ($A^3\Sigma_u^+$) by utilising transitions to the second excited state, $N_2(B^3\Pi_g)$. This technique is then coupled with wavelength modulation spectroscopy (WMS, see section 2.2.3) to further enhance its sensitivity and enable detection of the electronic and vibrational ground state of $N_2^+(X^2\Sigma_g^+)$ on the $N_2^+(A^2\Pi_u \leftarrow X^2\Sigma_g^+, v = 2 \leftarrow 0)$ transition at ~ 784 nm.

Previous measurements on N_2(A) include those of Augustyniak & Borysow[26] who used direct absorption with a pseudo-external cavity diode laser operating on the $B^3\Pi_g(v = 2) \leftarrow A^3\Sigma_u^+$ ($v = 0$) transition at 12858.82 cm^{-1} to measure the time decay of N_2(A) in the near afterglow of a pulsed RF plasma. Although an absolute technique, this method is limited by the narrow scanning range of the laser covering only a few ro-vobrational transitions, and its inherent low sensitivity. Cernogora *et al.*[13] performed absorption

measurements on the $B^3\Pi_g(v = 1) \leftarrow A^3\Sigma_u^+(v = 0)$ transition in a glow discharge, using a second glow discharge as the light source. These measurements are limited by a large line width of the probing radiation and a low sensitivity of the technique. The experiment was extended[27] to measure the population in the v = 0-5 levels of N_2 ($A^3\Sigma_u^+$) which were found to be non-Boltzmann with a population inversion between v = 2 & 3. A kinetic model was constructed to help explain the results, but no satisfactory mechanism was determined to yield the population inversion observed, although vibrationally dependent quenching is raised as a possibility.

De Benedictis *et al.* have produced a large volume of research on $N_2(A)$ using the technique of LIF. The time-dependent decay of $N_2(A, v = 4)$ has been measured both in a pulsed RF He/N_2 discharge[28] and in a pure N_2 pulsed RF discharge[14]. The latter measurement was used in the calibration of previous LIF data taken on the v = 0-9 levels of $N_2(A)$[29] to determine the vibrational distribution, which was again found to be non-Boltzmann, but with no population inversion between v = 2 & 3. Vibrational distributions in $N_2(B)$ have been measured using optical emission spectroscopy in the post-discharge of a pulsed RF N_2 plasma and a non-Boltzmann population distribution was observed[30].

Perhaps the most relevant work to date on the detection of $N_2(A)$ is that by Foissac *et al.*[23] in a flowing N_2 microwave discharge. The technique of intra-cavity laser absorption spectroscopy (ICLAS) is used to measure the absolute densities of $N_2(A)$ in the discharge zone and the short-lived afterglow maximum emission zone. The translational and rotational temperatures are deduced from the Doppler profiles of the spectrally resolved rotational lines and from the rotational distribution of $N_2(A, v = 0)$, respectively. Sadeghi *et al.*[31] have also used the ICLAS technique in the detection of $N_2(A, v = 0)$ in the afterglow of a flowing N_2 microwave discharge, and mapped its spatial dependence within the discharge tube. The spatial distribution of all three triplet states of N_2 ($A^3\Sigma_u^+$, $B^3\Pi_g$ and $C^3\Pi_u$) have been measured by Krames *et al.*[32] in an asymmetric RF discharge using a combination of LIF and optical emission spectroscopy, calibrated with a Rayleigh scattering experiment. A model which includes the production, diffusion and quenching rates of the contributing species (and also fluorescence cascade processes) is used to explain the variations observed.

Guerra *et al.*[6,33] have highlighted the role played by the vibrationally excited $N_2(X)$ and $N_2(A)$ states by modelling the kinetics of stationary discharges, and underline their

fundamental importance to the discharge chemistry. Piper has conducted extensive investigations into the role of $N_2(A)$ in the various kinetic processes present in N_2 flow discharges using emission spectroscopy. These include energy pooling reactions of $N_2(A)$ to form $N_2(C\,^3\Pi_u)$[15] and $N_2(B\,^3\Pi_g,\ v = 1\text{-}12)$[16]; the collisional excitation of $N(^4S)$ by $N_2(A)$ to form $N(^2P)$[17]; and the excitation of $N_2(B\,^3\Pi_g,\ v = 1\text{-}12)$ in the reaction between $N_2(A)$ and $N_2(X,\ v > 5)$[18].

Much of the work carried out to date on the detection of N_2^+ has focussed around electrical methods (to measure the ion flux from which an ion density can be inferred) and quadrupole mass spectrometry[34]. Electrical methods pose two main difficulties in that they are not absolute and require various assumptions in the interpretation of the experimental data, and that any ion present in the plasma will be measured without the possibility of distinction. Thus, detection of $N_2^+(X)$ by absorption spectroscopy is highly desirable for the yielding of absolute concentrations.

Bachir *et al.*[35] have measured the rotational spectrum of $N_2^+(X,\ v = 0)$ on the (2,0) vibrational band of the $N_2^+(A\,^2\Pi_u \leftarrow X^2\Sigma_g^+)$ system using laser optogalvanic spectroscopy (LOGS). This technique measures the resonance laser-induced changes of the impedance of an electric discharge rather than the absorption of radiation or the fluorescence induced by the laser irradiation. It provides sub-Doppler resolution of the spectra and is ideal for measuring temperatures and line positions, although the determination of absolute number densities of the various levels again rests on numerous assumptions. Perhaps most relevant to this work, the technique of pulsed LIF has been applied by Woodcock *et al.*[19] to measure the $N_2^+(X)$ ion velocity components parallel and perpendicular to the electrode in the sheath of a RF capacitively coupled plasma. The absolute number density of N_2^+ ions was also determined by calibration of the technique using the decay in LIF in the plasma bulk after discharge extinction.

4.2 Nitrogen Spectroscopy

The spectroscopy of the nitrogen molecule is complex, evidenced by the large number of triplet electronic states shown in figure 4.1. We shall therefore discuss the relevant states of neutral N_2 and N_2^+ in turn.

4.2.1 Spectroscopy of N_2

The ground electronic state of the N_2 molecule, $X^1\Sigma_g^+$, arises from the $(1\sigma_g)^2(1\sigma_u)^2(2\sigma_g)^2(2\sigma_u)^2(1\pi_u)^4(3\sigma_g)^2$ configuration, while the first and second excited states, $A^3\Sigma_u^+$ and $B^3\Pi_g$, arise from the $(1\pi_u)^3(3\sigma_g)^2(1\pi_g)$ and $(1\pi_u)^4(3\sigma_g)(1\pi_g)$ configurations, respectively. The different angular momenta present in the molecule (electron spin, S, electronic orbital angular momentum, Λ, and the angular momentum of nuclear rotation, N) form a resultant that is always designated J (excluding nuclear spin). If S and Λ are both zero (as in the $N_2(X^1\Sigma_g^+)$ ground state), the angular momentum of nuclear rotation is identical to that of the total angular momentum J. In all other cases, there is necessarily a distinction between different modes of coupling of the angular momentum, originally considered by Hund.

For Hund's case a), relevant to $N_2(B)$, the interaction of nuclear rotation with the electronic (spin and orbital) angular momentum (Ω) is weak, although the electronic angular momentum is very strongly coupled to the internuclear axis. Thus, Ω and N couple to form the resultant J. Since Ω is the component of J along the internuclear axis, it follows J is defined by equation (4.1), with the consequence that levels with $J < \Omega$ do not exist.

$$J = \Omega, \Omega+1, \Omega+2, \ldots \tag{4.1}$$

The energy level, F_v, describing the coupling of Ω with N to form the resultant J is given by,

$$F_v = B_v J(J+1) + (A_v - B_v)\Omega^2 - D_v J^2(J+1)^2 + \ldots \tag{4.2}$$

where A_v is the spin-orbit coupling parameter, B_v is the vibrationally dependent rotational constant and D_v is the centrifugal distortion constant. The interaction between the electronic orbital angular momentum, Λ, and the rotation of the nuclear framework, N, has been neglected. In fact, electron slip produces a doublet splitting (lambda doubling) in states with $\Lambda \neq 0$, including $N_2(B)$. The magnitude of this splitting increases with increasing J.

Hund's case b) arises from the failure to define the quantum number Ω. This could either be when $\Lambda = 0$ and $S \neq 0$, such as for $N_2(A)$, where S is not coupled to the

internuclear axis at all. Alternatively, even when $\Lambda \neq 0$, S may only be weakly coupled to the internuclear axis, still leaving Ω undefined. In either case, Λ couples with the angular momentum N to give the resultant K, the total angular momentum excluding spin:

$$K = \Lambda, \Lambda+1, \Lambda+2, ..., \Lambda+N. \tag{4.3}$$

For $N_2(A)$, $\Lambda = 0$ and hence $K = N$. K and S then couple to give J, the total angular momentum including spin:

$$J = K+S, K+S-1, ..., |K-S|. \tag{4.4}$$

In general (except for $K < S$), each level with a given K consists of $2S+1$ components, so the number of components is equal to the multiplicity. Rotation of the molecule causes a magnetic coupling between K and S, splitting J levels with the same K value. Two further spin-splittings must be taken into account. One is dependent primarily on the proximity in energy of other electronic states and has a magnitude λ, and the second is a spin-spin interaction with magnitude γ. Thus, for $N_2(A)$ where $K = N$ and $S = 1$, the resulting energy levels for this spin-rotation coupled molecule are given by

$$F_1(N) = B_v N(N+1) + (2N+3)B_v - \lambda - \sqrt{(2N+3)^2 B_v + \lambda^2 - 2\lambda B_v} + \gamma(N+1), \tag{4.5}$$

$$F_2(N) = B_v N(N+1), \tag{4.6}$$

$$F_3(N) = B_v N(N+1) - (2N-1)B_v - \lambda + \sqrt{(2N-1)^2 B_v + \lambda^2 - 2\lambda B_v} - \gamma N, \tag{4.7}$$

where F_1, F_2 and F_3 refer to the levels with $J = N+1$, N, and $N-1$, respectively.

The rotational wavefunctions in Hund's cases a) and b) have specific symmetry properties. In $N_2(A\,^3\Sigma_u^+)$, the rotational wavefunction for odd N states changes sign under inversion and are thus labelled negative (−), while for even N states it retains its sign and is labelled positive (+). A further symmetry label is required to take into account the fact that both nuclei are identical, such that odd N levels are symmetric (s) and even N levels are

antisymmetric (a) with respect to exchange. The lambda doubling in $N_2(B\,^3\Pi_g)$ leads to a splitting of the rotational states into two states with positive and negative parity. The appropriate selection rules ($\Delta J = 0, \pm 1$, $\Delta N = 0, \pm 1$, $\Delta\Omega = 0, \pm 1$, $+ \leftrightarrow -$, s $\leftrightarrow$ s and a $\leftrightarrow$ a) give rise to the 27 bands shown in figure 4.2, where the upper $N_2(B)$ state is shown both in terms of Hund's case a) with the $^3\Pi_{0,1,2g}$ labelling scheme, and Hund's case b), denoted in terms of $F_{1,2,3}$. In reality, this state will lie between the two limits. The ordering of the F_n levels arise from the negative values of the spin-splitting constants (λ and γ)[36]. The extent of the lambda-doubling in $N_2(B)$ is exaggerated for clarity.

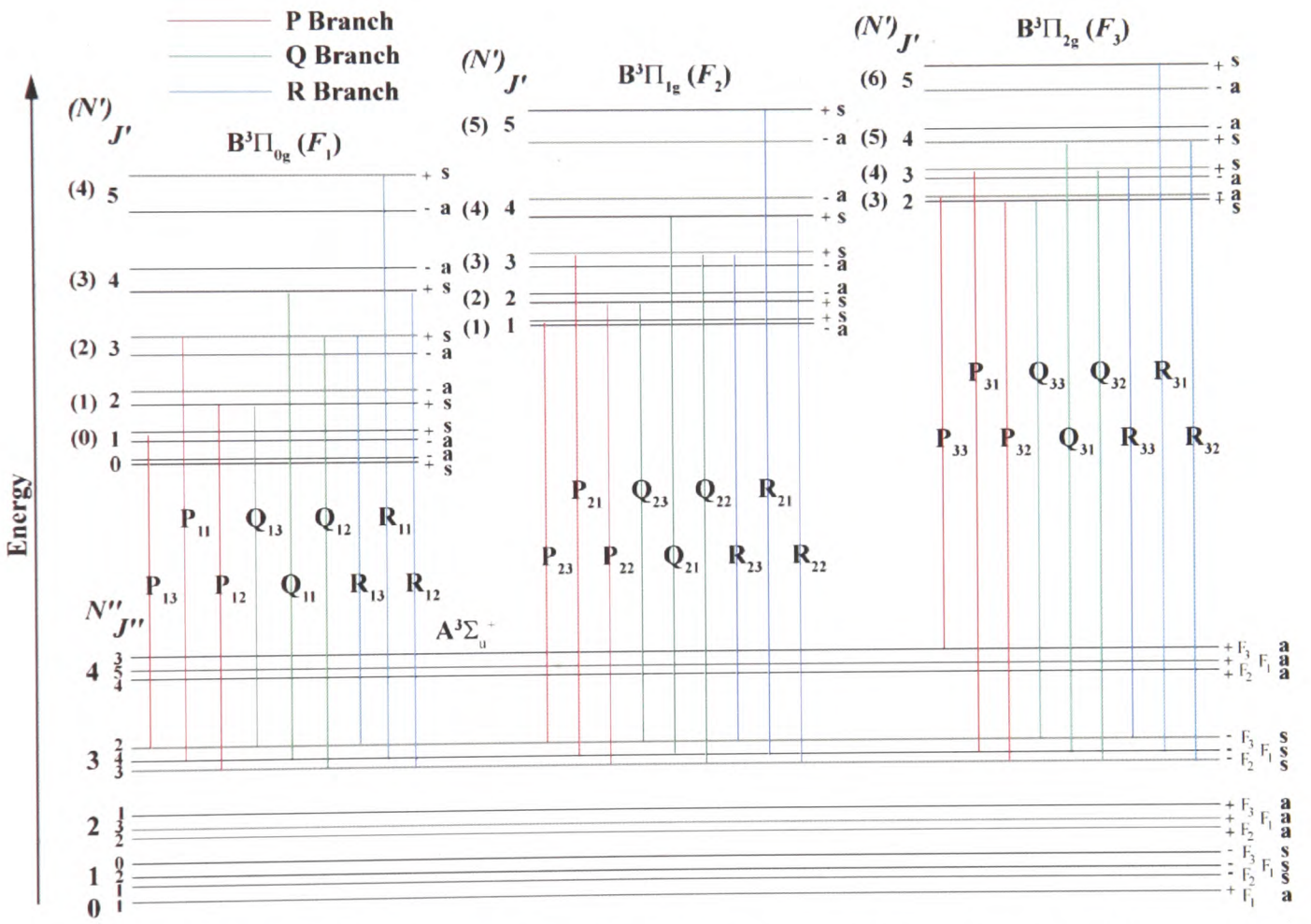


Figure 4.2: Energy level diagram showing the 27 branches of the $N_2(B \leftarrow A)$ transition.

4.2.2 Spectroscopy of N_2^+

The ground electronic state of N_2^+ is $X\,^2\Sigma_g^+$, arising from the $(1\sigma_g)^2(1\sigma_u)^2(2\sigma_g)^2(2\sigma_u)^2(1\pi_u)^4(3\sigma_g)^1$ configuration, while the first excited state, $N_2^+(A\,^2\Pi_u)$, arises from the $(1\pi_u)^3(3\sigma_g)^2$ configuration. $N_2^+(X\,^2\Sigma_g^+)$ can be considered as Hund's case b), and using the discussion for the $N_2(A)$ state above and considering that for $N_2^+(X\,^2\Sigma_g^+)$,

$S = ½$ and $\Lambda = 0$, equations (4.8) and (4.9) for the two levels are deduced, with the symbols retaining their previous meaning, but where F_1 and F_2 now refer to the levels with $J = N + ½$ and $N - ½$, respectively.

$$F_1(N) = B_v N(N+1) + 1/2\,\gamma N \tag{4.8}$$

$$F_2(N) = B_v N(N+1) - 1/2\,\gamma(N+1) \tag{4.9}$$

The $N_2^+(A\,^2\Pi_u)$ state can be considered as Hund's case a) with its energy levels given by equation (4.2), where all the symbols have the same meaning as previously (and now Ω = 1/2 or 3/2). Figure 4.3 shows the energy level diagram for these two electronic energy levels (again with the Π state rotational levels denoted with both Hund's cases a) and b) notation) and the 12 allowed bands that arise from the application of the appropriate selection rules. Note the ordering of the levels in $N_2^+(\,X\,^2\Sigma_g^+)$, where the spin-splitting constant γ is positive[37].

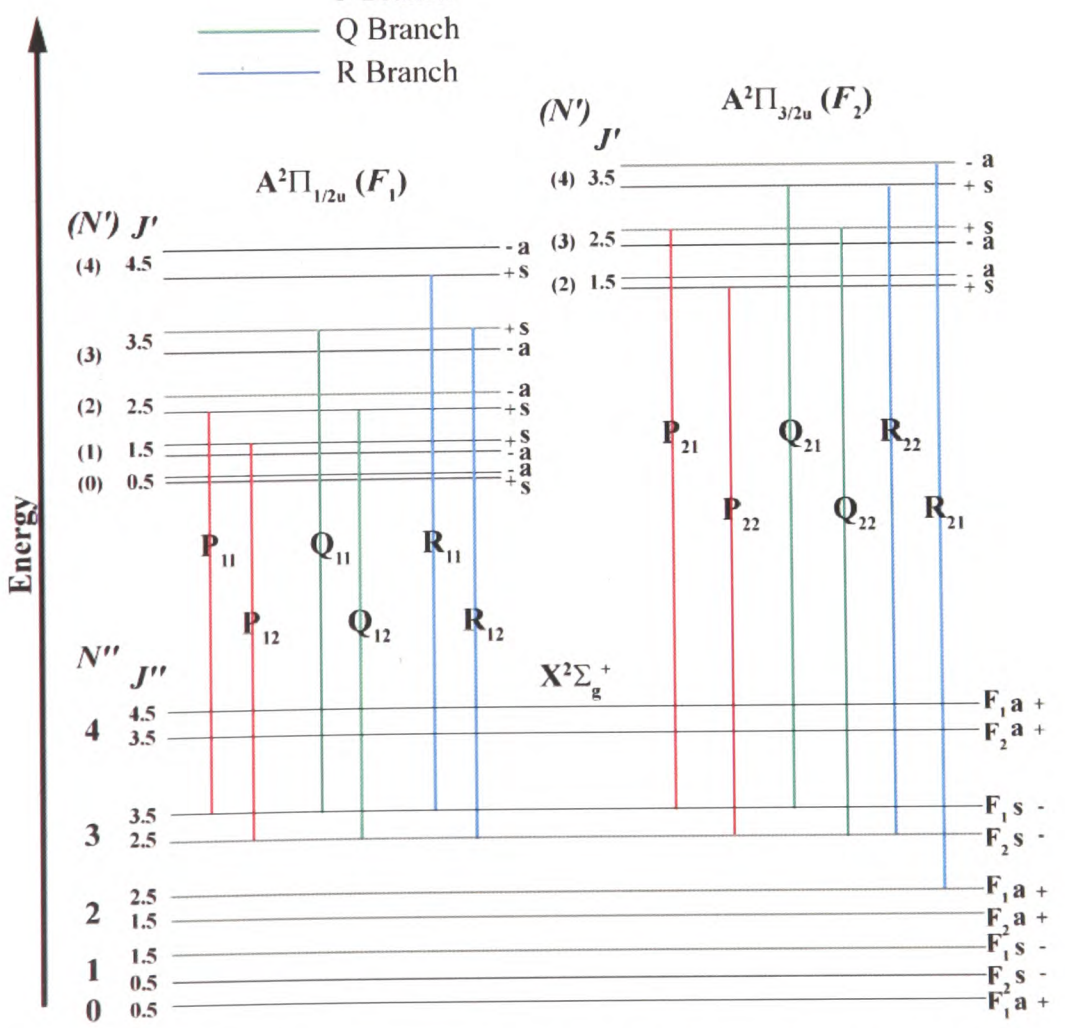


Figure 4.3: Energy level diagram showing the 12 bands for the $N_2^+(A \leftarrow X)$ transition.

4.3 Experimental

Four different vibrational levels of $N_2(A)$ were probed *via* the vibrational transitions v = 3←0, 3←1, 6←3 and 7←6 to the upper $N_2(B)$ state using CEAS. The radiation for this experiment was provided at the wavelengths 684 nm, 760 nm, 662 nm and 784 nm, respectively, by a selection of narrow band (< 20 MHz) CW diode lasers (Sacher TEC500, QLD-760-10S, ML 1016R-01 and ML 601J24-01). These were temperature and current controlled by home-made systems. Initially, the laser light was passed through an optical isolator (> 60 dB rejection) after which a small fraction was diverted into a spectrum analyser (Melles Griot) to provide a frequency calibration scale, or into a wavemeter (Burleigh WA-1000) to allow the absolute determination of the wavelength.

The main radiation beam subsequently passed through an acousto-optic modulator (AOM, AA Opto-Electronique MT200) before being focussed into a cavity that bounded the plasma chamber, formed by one of four pairs of high-reflectivity mirrors (0.75 m apart). The mirror refectivities were determined using CRDS (see section 2.3.4) and found to be R = 0.99860 at 684 nm, R = 0.99934 at 760 nm, R = 0.99961 at 662 nm and R = 0.99947 at 784 nm. The radiation transmitted through the cavity was filtered using an interference filter (FWHM 10 nm) and then focussed onto a PMT (Q130F/RFI Thorn EMI), the response of which was recorded on an oscilloscope (LeCroy 9314M) before being transferred to a PC for analysis.

$N_2^+(X)$ was detected utilising the v = 2←0 transition of the $N_2^+(A\,^2\Pi_u \leftarrow X\,^2\Sigma_g^+)$ band at 784 nm with the radiation again provided by a CW laser diode (ML 601J24-01). The setup is as described for the $N_2(A)$ experiment, with a mirror reflectivity R = 0.99947. Due to the even lower concentration of this state, WMS (see section 2.2.3) was utilised in combination with CEAS to enhance the sensitivity of the detection. The wavelength modulation was achieved by sinusoidal modulation of the injection current of the diode laser at a frequency of 5.18 kHz with an excursion of (481 ± 43) MHz (the maximum deviation from the central (carrier) frequency as a result of the modulation). This was combined with the slow ramping (~ 10 Hz) of the laser input current (to sweep its output radiation frequency) using a home-made mixer box. The PMT signal was demodulated at either the first or second harmonic of the modulation frequency by use of a lock-in amplifier (EG&G Instruments 7625 DSP). The data recorded using CEAS combined with

WMS was calibrated against CEAS data recorded at the conditions of maximum concentration of $N_2^+(X)$. The experimental setup can be seen in figure 4.4, where the dotted lines represent the additional equipment used in the combined CEAS/WMS measurements.

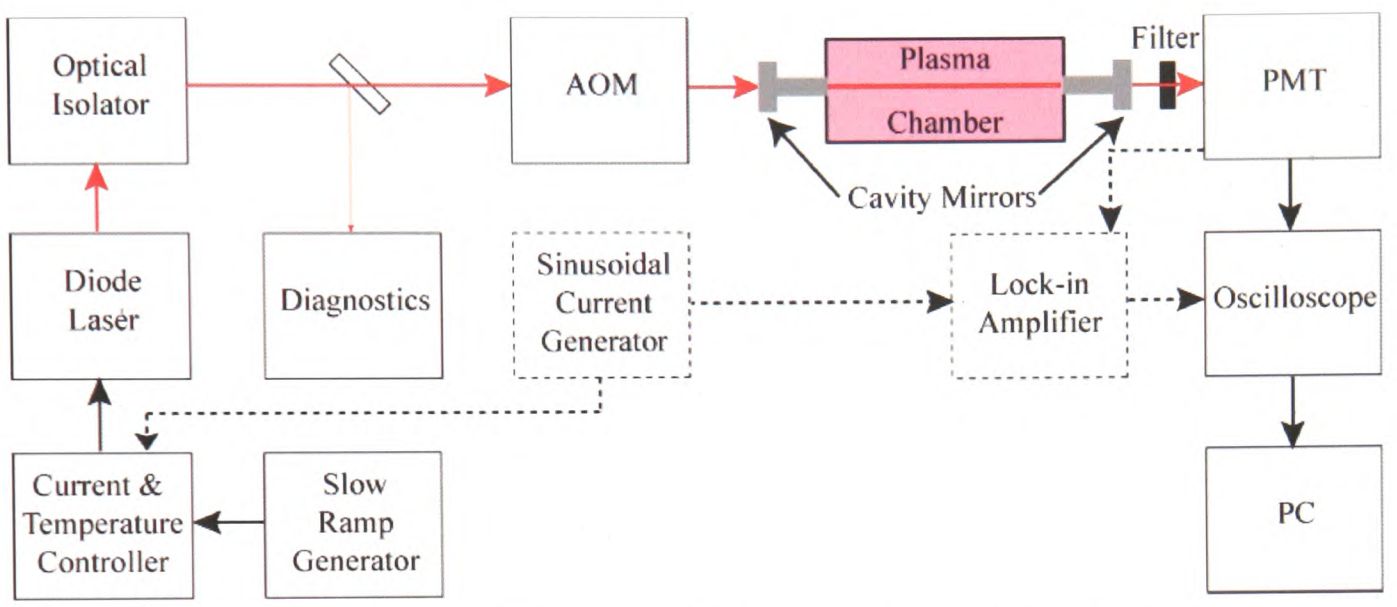


Figure 4.4: Experimental setup; dotted lines represent the additional equipment used in the CEAS/WMS detection of $N_2^+(X)$.

4.4 Results

4.4.1 $N_2(A)$ Detection

The narrow bandwidth of the laser radiation allows observation of the individual rotational lines associated with each vibrational transition. Figures 4.5a, b, c show sections of the (3,1), (6,3) and (7,6) bands, respectively, recorded at a plasma power of 300 W and a plasma pressure of 10 mTorr. The spectroscopic notation used corresponds to $\Delta J_{F'F''}(J'')$, where $F = 1$ for $J = N + 1$, $F = 2$ for $J = N$ and $F = 3$ for $J = N - 1$, for the upper (') and lower (") levels, respectively. Assignment of the spectra is achieved using a spectral simulation program[38] with spectroscopic constants taken from the literature[39,40,41] and shown in table 4.1.

	N_2		N_2^+	
/cm^{-1}	$A^3\Sigma_u^+$	$B^3\Pi_g$	$X^2\Sigma_g^+$	$A^2\Pi_u$
T_e	50203.6	59619.3	0	9166.9
ω_e	1460.64	1733.39	2207.00	1903.7
$\omega_e x_e$	13.87	14.122	16.10	15.02
$\omega_e y_e$	0.0103	−0.0569	−0.04	-
B_e	1.4546	1.6374	1.93176	1.7444
α_e	0.0180	0.0179	0.01881	0.0188
γ_e	-8×10^{-5}	7×10^{-5}	-	-
D_e	6.15×10^{-6}	5.9×10^{-6}	6.1×10^{-6}	5.6×10^{-6}

Table 4.1: Spectroscopic constants used in the assignment of the spectra of N_2 and N_2^+.

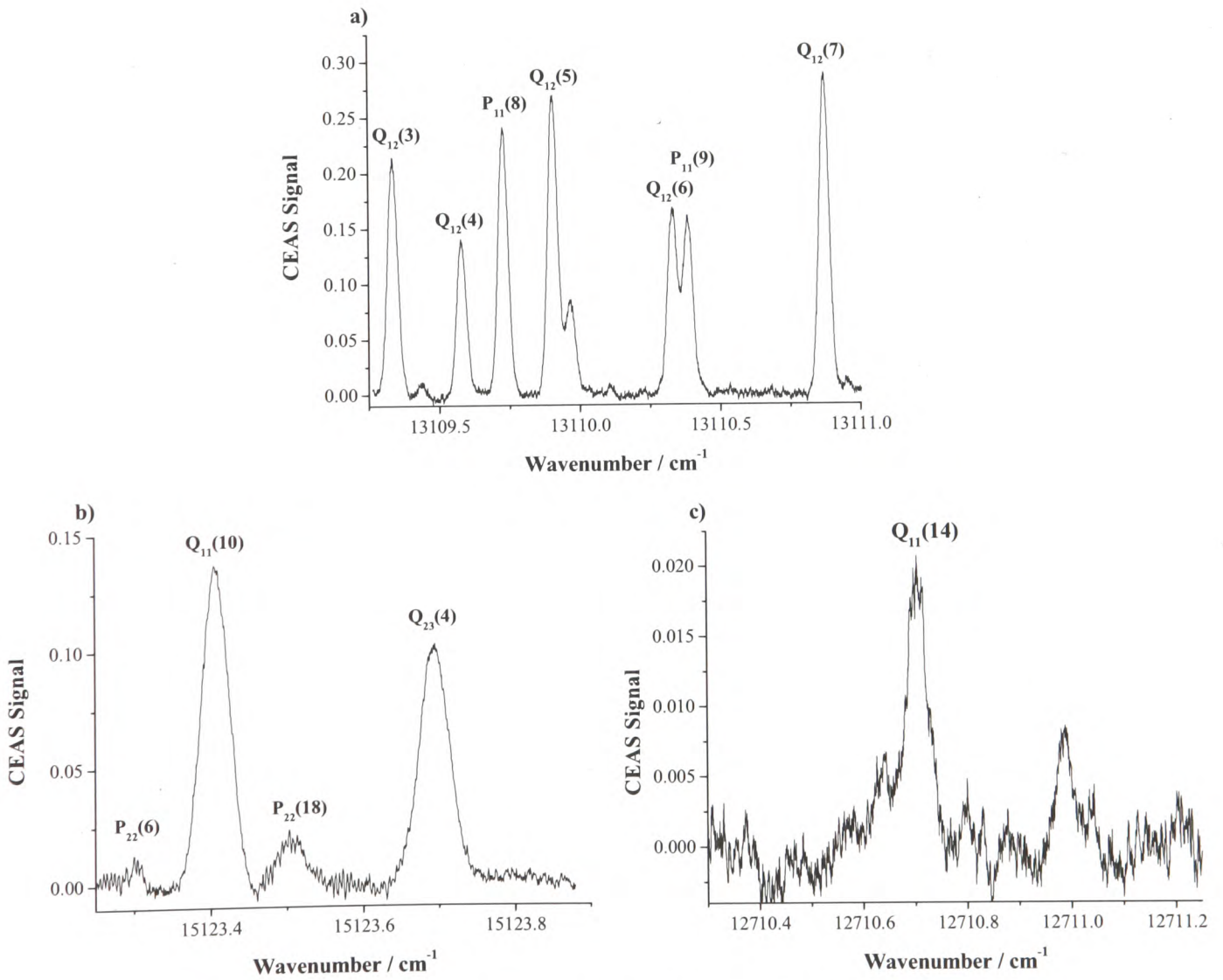


Figure 4.5: Sections of spectra recorded at 300 W and 10 mTorr plasma power and pressure for the bands a) (3,1), b) (6,3) and c) (7,6).

The spectral lineshapes are well described by Gaussian functions, and the widths of the profiles shown in figure 4.5a return a translational temperature of (270 ± 32) K at 50 W plasma power rising to (500 ± 60) K at 500 W plasma power. There is no observed dependence of translational temperature on plasma pressure. The rotational distribution in the v = 1 & 0 levels is well represented by a temperature, initially obtained using a Boltzmann plot across seven rotational lines (a lack of a sufficient number of rotational lines in the v = 3 & 6 spectra preclude an extension of this measurement to these levels). In the case of the v = 1 level, we can approximate a rotational temperature by comparing the population of two rotational levels measured *via* the $Q_{12}(3)$ and $P_{11}(8)$ transitions, which are close enough in wavenumber to both be observed in a single laser sweep. The rotational temperature determined using this method is found to be the same as that from the analysis of the seven rotational lines. Furthermore, the rotational temperature is similar to the translational temperature under all operating conditions (shown for varying plasma power at 10 mTorr plasma pressure in figure 4.6), indicating that these degrees of freedom are in equilibrium.

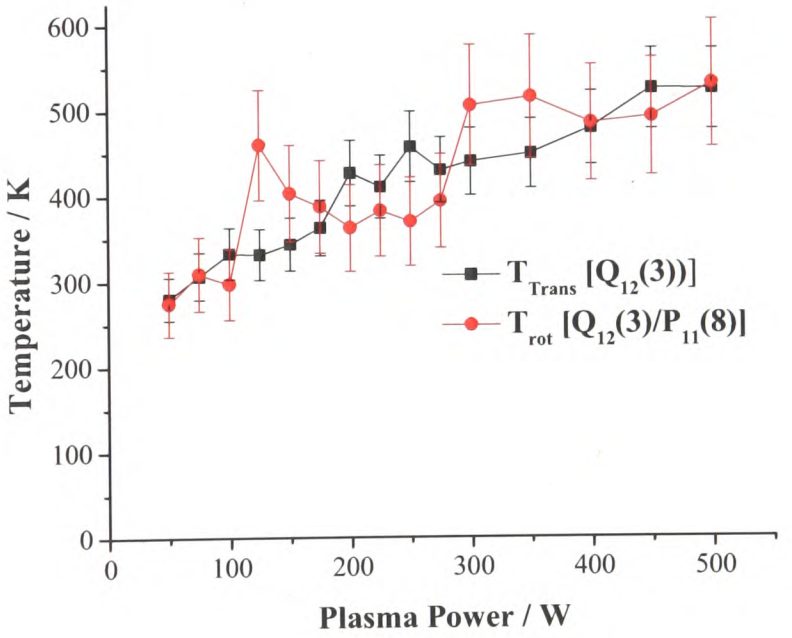


Figure 4.6: The variation of the translational and rotational temperature with plasma power at 10 mTorr plasma pressure for the v = 1 level of $N_2(A)$.

Conversion of the CEAS signal into a value of α (a product of the integrated absorption cross-section and the rotational state concentration) is achieved using equation 2.35. The value of the mirror reflectivity, R, is obtained with the plasma on but the laser off resonance. The integrated cross-section, σ_{int} (in $cm^2\ cm^{-1}$) is calculated using the equation,

$$\sigma_{\text{int}} = \frac{S_{J'J''}}{(2J''+1)} \frac{K 2\pi^2 \nu_0}{3c\varepsilon_0 h} \left| R_e^{v'v''} \right|^2 \tag{4.10}$$

where $S_{J'J''}$ is the rotational line strength calculated from the expressions tabulated by Kovacs[42], J'' is the lower state rotational quantum number, ν_0 is the transition wavenumber at line centre, $R_e^{v'v''}$ is the vibronic transition moment (equal in value to the square root of the Franck-Condon factor multiplied by the electronic transition dipole moment, $R_e^{n'n''}$), and the multiplier K equals 10^4 if ν_0 is in wavenumbers and the units of σ_{int} are $\text{cm}^2\ \text{cm}^{-1}$. Values for the Franck-Condon factors and $R_e^{n'n''}$ are taken from Gilmore *et al.*[43].

As it has been established that the rotational level populations are in thermal equilibrium the equation,

$$\frac{N_{N''J''}}{N_v} = \frac{\Phi(2J+1)}{\rho q_{rot}} \exp\left(-\frac{BN(N+1)}{kT_{rot}} \right), \tag{4.11}$$

can be used to calculate the total population of the vibrational level. Here, B is the rotational constant, the rotational partition function $q_{rot} = kT_{rot}/2B$, ρ is the number of spin rotation manifolds (3 for the $N_2(A^3\Sigma_u^+)$ state) and Φ is the nuclear spin weighting (1/3 for even N and 2/3 for odd N). Using equation (4.11), the values of T_{rot} shown in figure 4.6, and the concentrations of the various rotational levels (calculated from equation (4.10) together with the appropriate areas, A), the total population of $v = 0,1,3$ and 6 levels can be calculated for varying plasma conditions. Figures 4.7a and 4.7b show the total vibrational populations for varying plasma pressure at 100 W and varying plasma power at 25 mTorr, respectively. The vibrational level concentrations all show a general decrease with increasing plasma pressure and are weakly dependent on plasma power, increasing initially at lower powers (< 150 W), before becoming essentially constant at higher operating powers (150-500 W).

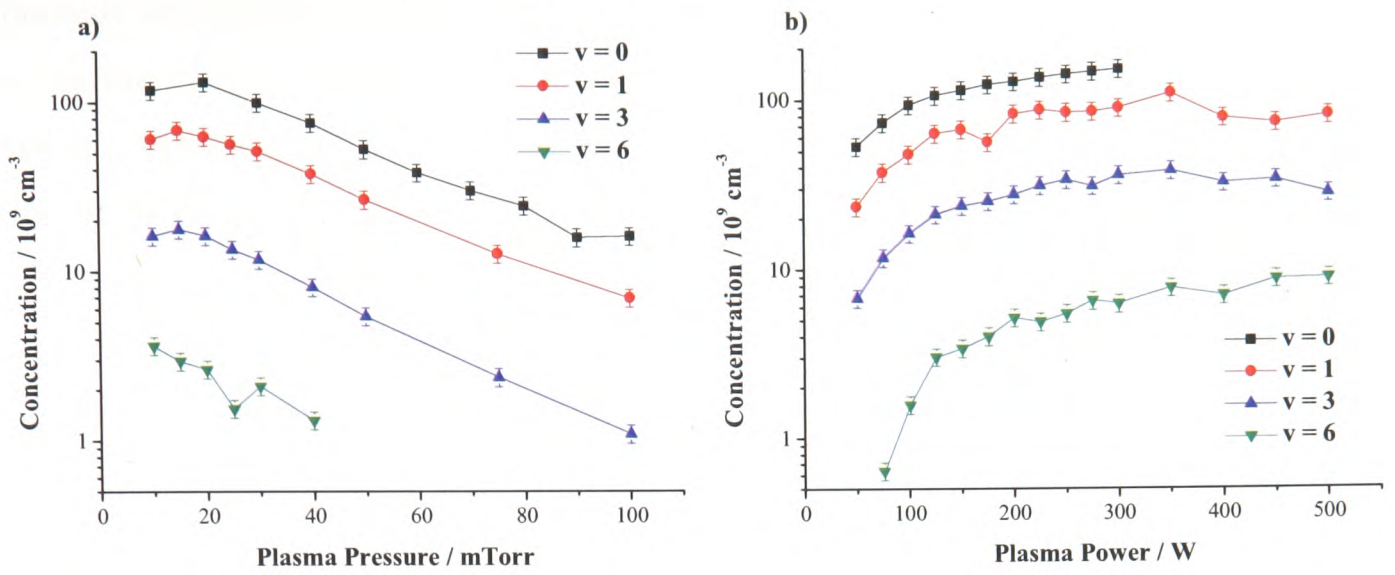


Figure 4.7: Variation in the concentration of $N_2(A, v = 0, 1, 3 \& 6)$ concentrations, a) with plasma pressure at 100 W plasma power and b) with plasma power at 25 mTorr plasma pressure.

A vibrational temperature, shown in figure 4.8 for 25 mTorr plasma pressure and varying plasma power, can be deduced from the relative populations of the $v = 0,1,3$ and 6 levels by using a Boltzmann plot. The vibrational temperature can be seen to increase with plasma power from 2900 K at 100 W to 3700 K at 300 W, with the error in the data reflecting the deviation of the vibrational populations from a Boltzmann distribution. A marginal decrease in the vibrational temperature was observed with increasing plasma pressure.

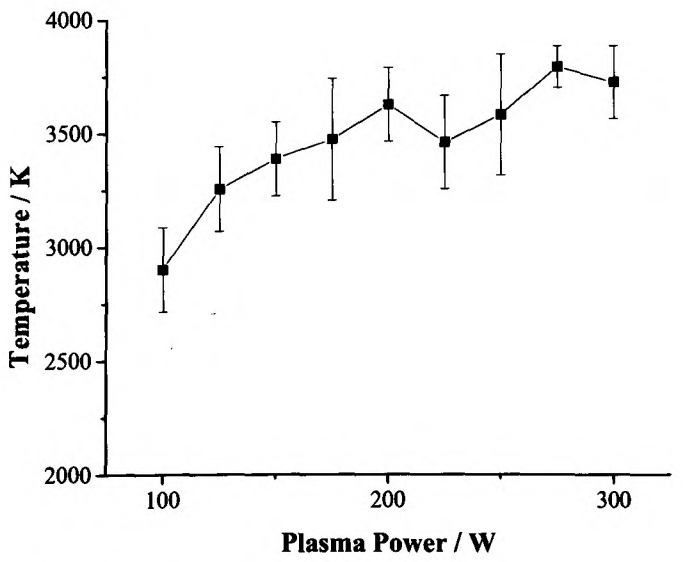


Figure 4.8: Variation in the vibrational temperature of $N_2(A)$ with plasma power at 25 mTorr plasma pressure.

Using this vibrational distribution, the total amount of $N_2(A)$ can be estimated as a function of plasma operating conditions, shown in figures 4.9a and 4.9b for varying plasma

pressure and plasma power, respectively. Also shown is the number of $N_2(A)$ molecules as a fraction, f, of the total number of ground state $N_2(X)$ molecules. The value of f can be seen to decrease by around two orders of magnitude from 9.0×10^{-4} at 10 mTorr to 1.0×10^{-5} at 100 mTorr and 100 W plasma power, while it increases from 2.7×10^{-4} at 100 W to 6.8×10^{-4} at 300 W and 25 mTorr plasma pressure. The total $N_2(A)$ concentration follows the same trend over plasma operating parameters as that for the individual v levels shown in figures 4.7a and 4.7b, with the amount increasing from $(2.03 \pm 0.24) \times 10^{11}$ cm^{-3} at 100 W plasma power to $(3.80 \pm 0.46) \times 10^{11}$ cm^{-3} at 300 W plasma power and 25 mTorr plasma pressure. While the general increase in the $N_2(A)$ state density with increasing plasma power can easily be understood in terms of an increasing electron temperature and density, the reasons behind the variation with plasma pressure are more subtle. The ion flux, and hence the inferred electron density, has been observed to decrease (along with the electron temperature) with increasing plasma pressure[1], which will offset the increase in the production rate of $N_2(A)$ expected simply from the increased feedstock gas density. The increasing magnitude of the loss rates with plasma pressure (primarily through quenching) must therefore be responsible for the decrease in $N_2(A)$ density with increasing plasma pressure.

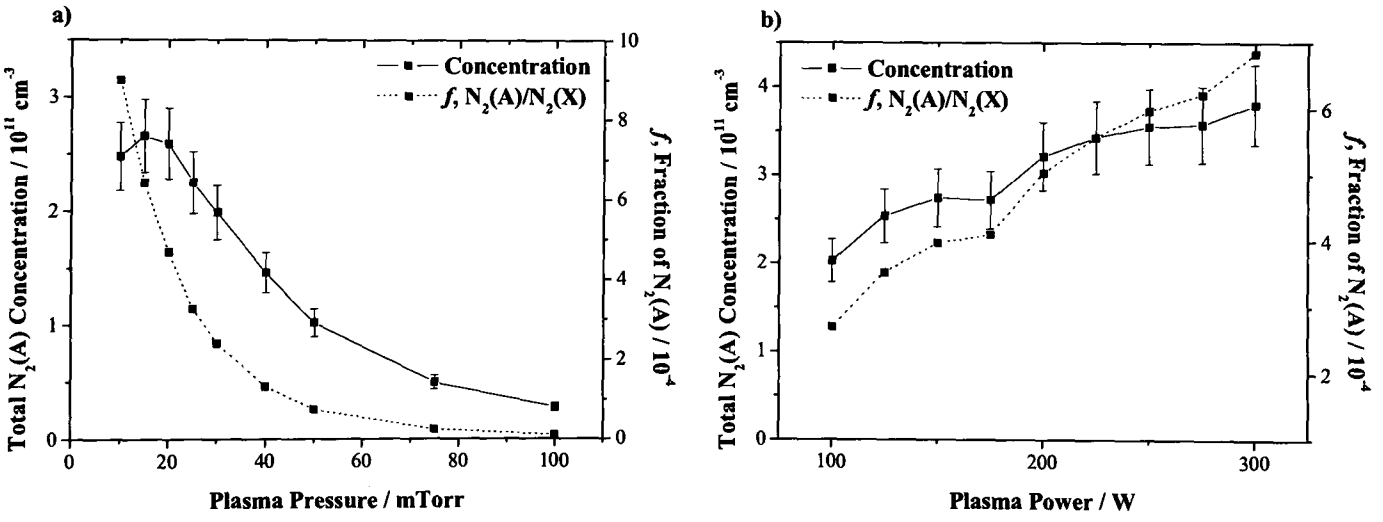


Figure 4.9: The total $N_2(A)$ concentration and as a fraction of ground state $N_2(X)$, a) with varying plasma pressure at 100 W plasma power and b) with varying plasma power at 25 mTorr plasma pressure.

The signal-to-noise ratio (S/N) of the data at plasma conditions of 25 mTorr pressure and 100 W power is found to be 39 for the $v = 3 \leftarrow 1$ band, 28 for the $v = 6 \leftarrow 3$ band and 8 for the $v = 7 \leftarrow 6$ band, and corresponds to minimum detectable concentrations (to yield a signal to noise ratio of unity in a one second timescale) of 1.02×10^{10} cm^{-3}, 3.43

$\times 10^9$ cm^{-3} and 1.23×10^9 cm^{-3} for the $v = 1$, 3 and 6 levels, respectively. For comparison, a minimum detectable concentration in one second for the v = 0 level can be calculated using the highest mirror reflectivity presently observed of 0.99961 (as opposed to the lower 0.9986) and is found to be 1.84×10^9 cm^{-3}.

4.4.2 N_2^+(X) Detection

Figure 4.10 shows the $Q_{11}(11.5)$ rotational line for the (2,0) transition of the Meinel ($A\,^2\Pi_u \leftarrow X\,^2\Sigma_g^+$) band of N_2^+ at 12677.783 cm^{-1}, measured at 400 W plasma power and 10 mTorr plasma pressure, with the data averaged over 10000 sweeps. This line was chosen due to its location in a region free from the overlapping rotational lines of the (7,6) band of the N_2(B←A) transition, and its comparatively large integrated cross-section resulting in an increase in the signal size. The line positions were calculated using a spectral simulation program[38] together with the constants shown in table 4.1, and are verified by Bachir *et al.*[35]. Confirmation of the detection of N_2^+(X, $v = 0$) was achieved in the observation of further rotational lines including $Q_{11}(13.5)$, $Q_{11}(7.5)$ and $Q_{11}(6.5)$, although $Q_{11}(11.5)$ was the most intense.

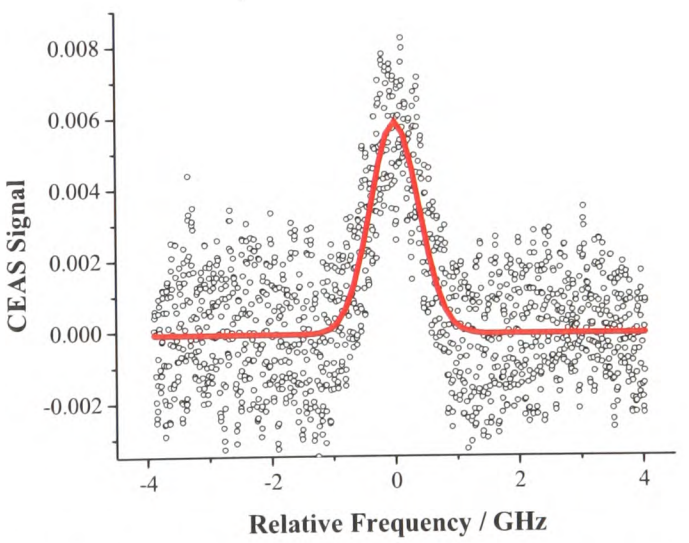


Figure 4.10: The $Q_{11}(11.5)$ transition in the (2,0) band of the N_2^+(A←X) system observed at 400 W plasma power and 10 mTorr plasma pressure.

The primary source of noise within our experimental setup can be attributed to the electrical and optical emission from the plasma chamber. In an attempt to reduce its effect on the experimental noise level, the technique of CEAS was combined with that of WMS (see section 2.2.3) under the conditions outlined in section 4.3. Figures 4.11a and 4.11b

show the WMS traces obtained (for first and second harmonic demodulation, respectively) under the same conditions as for figure 4.10, with the exception that only 1000 sweeps were averaged. As expected, the signals show a first and second derivative type spectrum. The second harmonic trace can be seen to have a far lower *S/N* than the first harmonic trace, primarily as a consequence of the reduced signal intensity.

The concentration in the rotational level $N = 11$, $J = 11.5$ of $v = 0$ can be calculated in the same way as that for the $N_2(A)$ state. After converting the area, A, of the peak shown in figure 4.10 into a value for α, and using an integrated cross-section calculated from equation (4.10) (where the constants all have the same meanings and are obtained from the same sources), the concentration is found to be $(2.74 \pm 0.33) \times 10^7$ cm^{-3}. Analysis of the Doppler profile of this absorption returned a translational temperature of (431 ± 80) K, in good agreement with the $N_2(A)$ data. Assuming the translational and rotational modes are in thermal equilibrium (as was found to be the case for $N_2(A)$) and using equation (4.11) (with values of $\rho = 2$ and $\Phi = 2/3$ for even N and 1/3 for odd N), a total population of the $v = 0$ level in $N_2^+(X)$ is found to be $(1.26 \pm 0.15) \times 10^9$ cm^{-3}. On the assumption that the vibrational levels in this electronic state show the same population distribution as for $N_2(A)$ (where around 50 % lay in $v = 0$), then the total $N_2^+(X)$ concentration can be deduced and is found to be $(2.7 \pm 0.3) \times 10^9$ cm^{-3}. This is in agreement with electrical measurements taken previously in the plasma chamber using Langmuir and planar probes[1] (if we assume that N_2^+ is the dominant ion), where $[e^-] \sim 10^9$ cm^{-3}.

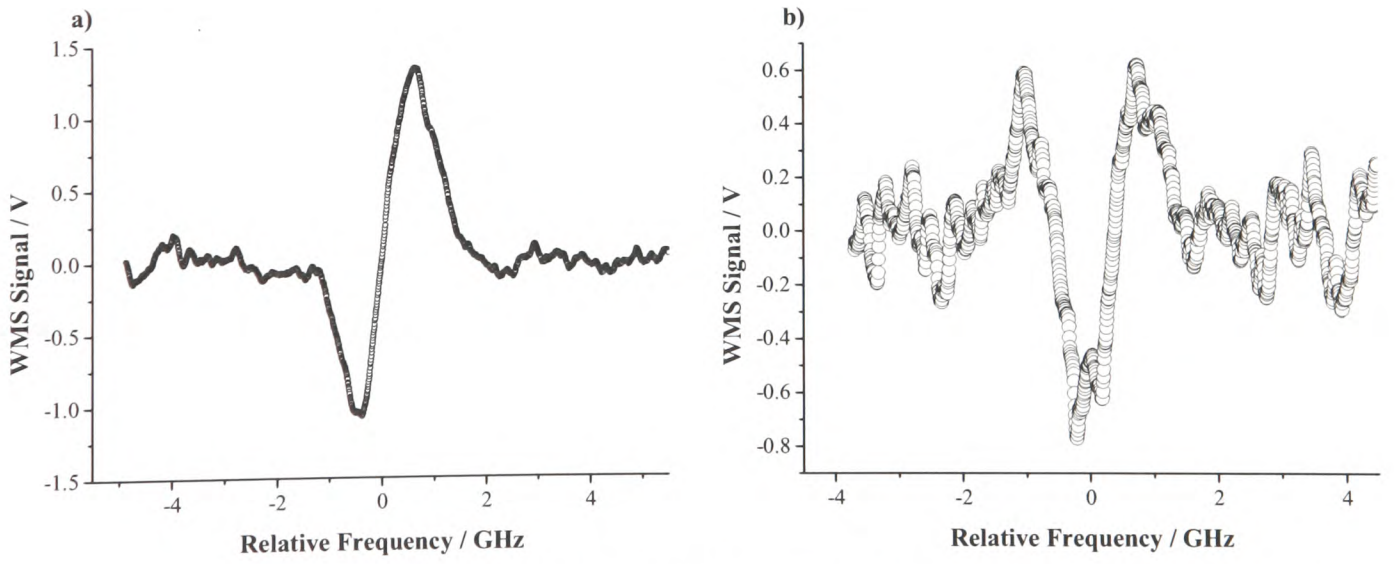


Figure 4.11: WMS signals observed for the same transition, and under the same conditions, as in figure 4.10, a) 1*f* and b) 2*f*.

Using the technique of CEAS/WMS, data at lower plasma powers and higher plasma pressures were obtained, calibrated against the absolute concentration determined

from the pure CEAS measurement at 400 W and 10 mTorr. Shown in figures 4.12a and 4.12b are the total $v = 0$ concentrations in $N_2^+(X)$ with varying plasma pressure at 400 W and varying plasma power at 10 mTorr, respectively. The concentrations can be seen to decrease with decreasing plasma power and increasing plasma pressure, before the signal becomes too weak to be observed above the background noise. These trends are the same as those observed for $N_2(A)$ across the same operating parameters, although less drastic in their absolute change. The $N_2^+(X)$ density increases by a factor of 2 between 100 W and 400 W, due to an increasing electron temperature and electron density increasing the excitation rate of this species. Increasing the plasma pressure between 10 mTorr and 30 mTorr results in a factor of 2 decrease in the $N_2^+(X)$ density, the same decrease observed previously in the N_2^+ ion flux[1]. The width of the CEAS/WMS signal is determined by both Doppler and modulation broadening[44], and taking the latter into account *via* a simulation returns temperatures across the operating conditions that are consistent with those observed for $N_2(A)$ (varying between 300 K and 480 K with increasing plasma power from 100 W to 400 W, and constant at around 480 K with plasma pressure at 400 W).

The sensitivity of the techniques can be compared by calculating a minimum detectable concentration for a 1 second scan across 1 wavenumber, quoted as an α_{min} value (with units $cm^{-1}\ Hz^{-1/2}$). This is calculated using equation 1.35, where the S/N of the CEAS data shown in figure 4.10 is 5:1, and the values for the first and second harmonic CEAS/WMS signals are 83:1 and 18:1, respectively. Using L = 35 cm, B = 500 seconds and N = 10000 for the CEAS signal and B = 159 seconds and N = 1000 for the combined CEAS/WMS signal, values of α_{min} are found to be 8.5×10^{-8} $cm^{-1}\ Hz^{-1/2}$, 3×10^{-9} $cm^{-1}\ Hz^{-1/2}$ and 1.4×10^{-8} $cm^{-1}\ Hz^{-1/2}$ for the pure CEAS, 1st harmonic CEAS/WMS and 2nd harmonic CEAS/WMS, respectively. The combined CEAS/WMS method can be seen to provide over an order of magnitude improvement in sensitivity on the CEAS technique alone.

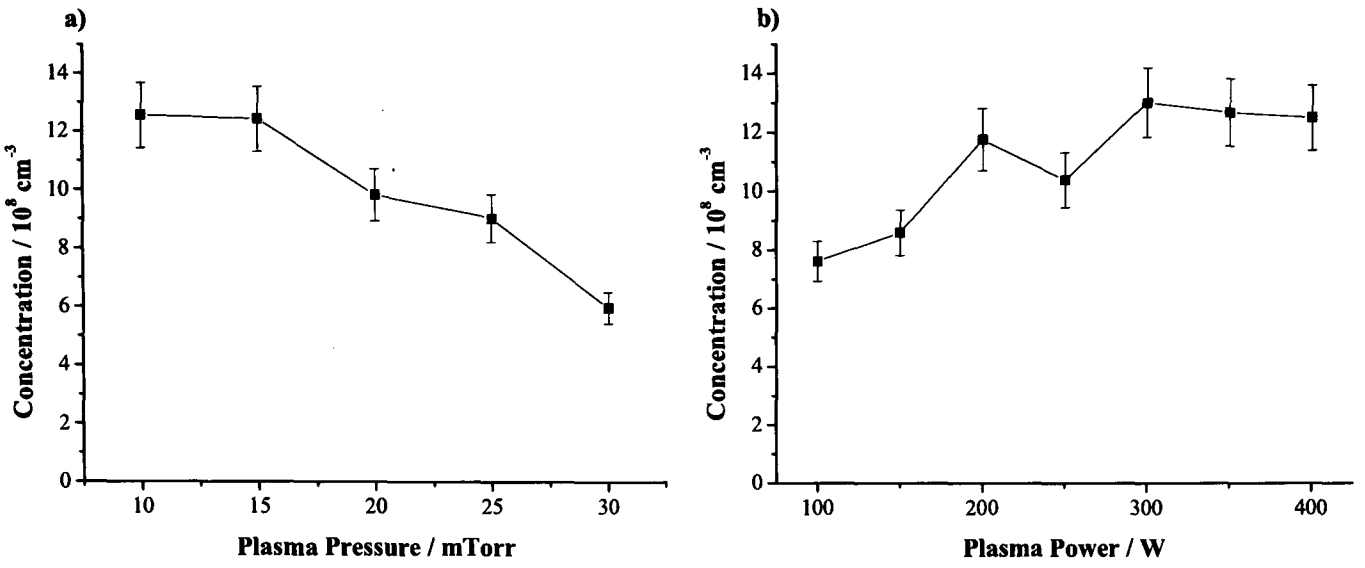


Figure 4.12: Variation in the concentration of $N_2^+(X, v = 0)$ with a) plasma pressure at 400 W and b) plasma power at 10 mTorr.

4.5 Discussion

As can be seen, $N_2(A)$ exists in the discharge in high densities and with a significant vibrational population under all plasma operating conditions. While $N_2(A)$ is already considered to be an important species within the plasma due to its role as an energy reservoir, a high vibrational temperature will augment its position in the various kinetic processes. For example, collisional deactivation of $N_2(A, v \geq 2)$ with $N_2(X)$ results in the production of vibrationally excited ground state nitrogen (shown by equation (4.12)), which is further implicated in the production of $N_2(B)$ through the process shown in equation (4.13). Vibrationally excited $N_2(A)$ has also been invoked in the formation of $N_2(C)$[15] and $N(^2P)$ atoms[17]. The central importance of $N_2(A)$ can be further understood due to its coupling to $N_2(X,B,C)$ both optically *via* cascades, and kinetically through further formation and loss routes.

$$N_2(A,v'\geq 2)+N_2(X,v'')\rightarrow N_2(A,v'-2)+N_2(X,v''+1) \qquad (4.12)$$

$$N_2(A)+N_2(X,v)\rightarrow N_2(B)+N_2(X,v') \qquad (4.13)$$

The role of $N_2(A)$ in sustaining the plasma through ionization should also be singled out for its importance. Using electron impact ionization cross-sections taken from the literature[45,46] (shown in figure 4.13) for the production of $N_2^+(X)$ from $N_2(X)$ and $N_2(A)$, together with a Maxwellian EEDF of $T_e \sim 2$ eV, rate constants of 3.0×10^{-12} cm^3

s^{-1} and 7.5×10^{-11} cm^3 s^{-1}, respectively, are calculated. At 100 W and 10 mTorr plasma power and pressure, the fraction of $N_2(A)$ is around 10^{-3} of $N_2(X)$ which results in the ionization from $N_2(A)$ consisting of 2 % of the total ionization rate (the remaining being from $N_2(X)$). As the threshold for electron impact ionization is 6.2 eV higher in $N_2(X)$ than $N_2(A)$, a lower electron temperature will decrease the electron impact ionization rate from $N_2(X)$ proportionally more than that from $N_2(A)$.

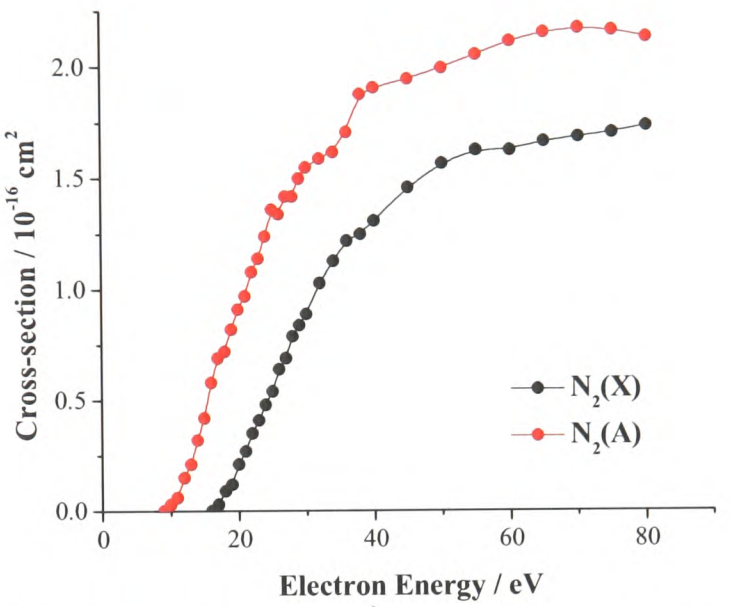


Figure 4.13: Electron impact ionization cross-sections to form $N_2^+(X)$ from $N_2(X)$ and $N_2(A)$[45].

Many previous studies have focussed exclusively on the $v = 0$ level of $N_2(A)$. Augustyniak & Borysow[26] used a high sensitivity absorption technique to measure the time decay of $N_2(A, v = 0)$ in the positive column of a pulsed discharge, and returned a concentration of 3×10^{11} cm^{-3} 100 μs after the discharge is deactivated at conditions of 250 mTorr plasma pressure and 0.4 A discharge current. They also highlight the role of diffusion and N-atom quenching as the dominant loss mechanisms for the $N_2(A)$ state under their operating conditions. Foissac *et al.*[23] used an absorption technique to measure the concentration of $N_2(A, v = 0)$, which yielded a value of 5×10^{11} cm^{-3} in a flowing microwave discharge at operating conditions of 3.3 Torr plasma pressure and 300 W plasma power. They also reported a thermal equilibrium between the translational and rotational modes with a temperature of 1000 K. While their observed concentrations are similar to that found here, the substantially different discharge conditions make direct comparison difficult. At the plasma pressure used in their experimental setup, they again highlight the importance of diffusion and N atom quenching as the dominant loss mechanisms for $N_2(A)$. A value for [N] is reported as 10^{15} cm^{-3} measured *via* NO

titration[47], which at 3.3 Torr of pure nitrogen corresponds to a dissociation ratio of $[N]/2[N_2]$ of around 1.5 %.

Cernogora *et al.*[13,27] have measured the $N_2(A)$ concentration of the levels v = 0-5 in a glow discharge, using a second auxiliary discharge as a light source for absorption measurements together with a high-resolution monochromator (the sensitivity of their experimental setup does not permit measurements beyond v = 5). They report total populations of $N_2(A, v = 0\text{-}5)$ of 3-6 × 10^{12} cm^{-3} for the pressure range 0.1-2 Torr, with a highly non-Boltzmann populational distribution, and observe a population inversion between v = 2 & 3. A kinetic model is constructed which reproduces their experimental data reasonably well. It is found that cascades from $N_2(B)$ are the dominant production route for the low vibrational levels of $N_2(A)$, with direct electron impact excitation becoming increasingly dominant for higher v. Both mechanisms are suggested to be effective for v = 3 & 4. Quenching by N atoms, $N_2(A)$ collisional pooling and diffusion are found to be the dominant loss mechanisms, with the former two increasingly important at higher plasma powers and pressures. This may well explain the saturation of the $N_2(A)$ state at higher plasma powers observed in the experimental data presented here (figure 4.7b). Their model does not, however, explain the population inversion observed between v = 2 & 3, and this is suggested to arise from vibrationally dependent quenching, an effect not taken into account in their kinetic model. They conclude by postulating a coupling between the EEDF and the vibrational temperature, which leads to a better fit of their kinetic model to the experimental data.

De Benedictis *et al.*[14,29] report measurements on $N_2(A, v = 0\text{-}9)$ in the post-discharge region of a pulsed RF CCP (operating at 60 W plasma power) using the technique of LIF calibrated against the simulated intensity of a rotational line originating from the v = 4, J = 9 state to account for the various experimental parameters, with an accuracy estimated to be within 30 % of the true value. The total $N_2(A)$ population is reported as 2 × 10^{11} cm^{-3} at 100 mTorr pressure in a pure N_2 discharge, a value that closely resembles the one reported here. A "first level" vibrational temperature is calculated by comparing the populations in the v = 0 & 1 levels, and is found to vary between 1600-2300 K. The vibrational distribution is described on the whole as Boltzmann like, with temperatures in the range 2000-2500 K, with some structure superimposed upon the distribution. No population inversion is observed between v = 2 & 3. The importance of $N_2(A)$ energy pooling and quenching by vibrational excited $N_2(X)$, together with electron impact excitation into $N_2(C)$, are highlighted in the loss kinetics of the discharge.

Furthermore, under our plasma operating conditions it is suggested that cascades from $N_2(B)$, and quenching of $N_2(B)$ with $N_2(X)$ are equally important in the formation of $N_2(A)$, with direct electron impact excitation from $N_2(X)$ playing only a minor role.

Krames *et al.*[32] have utilised LIF in combination with optical emission spectroscopy (calibrated against a Rayleigh scattering experiment) to measure the spatial profiles in a RF discharge of a number of species, including $N_2(A, v = 0,1,2)$. At 375 mTorr and a discharge voltage of 100 V, the maximum total concentration of $N_2(A)$ in the radial profile is found to be $\sim 10^{12}$ cm^{-3}, with a vibrational temperature estimated at 1400 K. The spatial distribution of the $N_2(A)$ density shown in their experimental results leads the authors to suggest that diffusion is the primary loss process for $N_2(A)$.

A kinetic model has been previously constructed[1] to account for the variation in the population of $N_2(A, v = 0)$ (shown in figure 4.7) with plasma parameters. A vibrational temperature higher than that found here was assumed, together with an electron temperature of 1.32 eV, in order to account for the observed trends in the data. Inputting the vibrational temperature measured here into the model produces reasonable agreement with the data, but only if a varying electron temperature of between 1.8-2.3 eV is assumed. However, this electron temperature (and its variation) is in much better agreement with that measured previously under the same operating conditions using a Langmuir probe[1]. This model also predicts values for the N atom concentration, and at 20 mTorr and 100 W plasma pressure and power the dissociation fraction is ~ 0.005, increasing to a maximum of ~ 0.02 at higher plasma powers. These values fall within the typical range reported in the literature[32,47,48]. The fact that pooling and quenching by N atoms becomes dominant at higher plasma pressures and powers contributes to the saturation of the $N_2(A, v)$ concentration observed here.

The importance of the $N_2(A)$ state and its vibrational distribution is highlighted in the modelling of Guerra *et al.*[6], where its total concentration is mapped as a function of plasma operating conditions in a stationary discharge. This is done by finding self-consistent solutions to the Boltzmann equation coupled to the rate balance equations for the vibrationally and electronically excited molecules, atoms and charged particles. A strong coupling between the concentrations of $N(^4S)$, $N_2(A)$ and $N_2(B)$ is found, with the quenching of $N_2(B)$ by $N_2(X)$ highlighted as the dominant production route for the formation of $N_2(A)$ (over and above that of cascades from $N_2(B)$ and direct electron impact excitation from the ground state). The dominant loss route is suggested as quenching by vibrationally excited $N_2(X)$, which results in the formation of $N_2(B)$. $N_2(A)$ is thus

produced and destroyed *via* $N_2(B)$, and a constant population is merely redistributed through the triplet states. Ultimately, it is suggested that the slower mechanisms (under their operating conditions and also those utilised here) like N atom quenching and diffusion determine the populations of both these states, in agreement with that found in the experimental measurements already discussed[13,14,27,32].

The degree of vibrational excitation in $N_2(X)$ is also a factor in the high vibrational temperatures observed for $N_2(A)$. The electron impact excitation cross-sections for the formation of $N_2(X, v = 1\text{-}6)$, when folded with EEDFs of $T_e \sim 2$ eV (typical of discharges operating under the conditions described here[1]), yield relatively high rate coefficients. Clearly, the vibrational distribution is coupled to the EEDF, and the degree of vibrational excitation can be propagated into $N_2(A)$ *via* both direct electron impact excitation to $N_2(A)$, and also to higher lying levels with subsequent cascades. Electron - $N_2(X)$ scattering in the 2.3 eV $N_2^-(^2\Pi_g)$ resonant region will further enhance the vibrational excitement of the N_2 ground state.

The concentration of $N_2^+(X)$ has been measured previously in a CCP chamber using the technique of pulsed LIF on the (2,0) band of the $N_2^+(B\,^2\Sigma_u^+ \leftarrow X\,^2\Sigma_g^+)$ transition at 330 nm (with the fluorescence observed on the (2,4) band at 458 nm)[19]. Calibration of the technique by analysing the decay in the LIF in the plasma bulk after discharge extinction (and assuming that electron-ion recombination kinetics dominate) yields a value for $N_2^+(X)$ of 1×10^{10} cm^{-3} at 200 W and 20 mTorr plasma power and pressure. A rotational temperature of 355 K under the same operating conditions was also observed, a value in close agreement with that found here. Further measurements on the (0,0) and (1,1) bands of the $N_2^+(B\,^2\Sigma_u^+ \leftarrow X\,^2\Sigma_g^+)$ transition at around 390 nm (with fluorescence observed on the (0,1) and (1,2) bands, respectively) yield a ratio of $v = 1$ to $v = 0$ populations of 0.07:1, equivalent to a vibrational temperature of 1200 K[49].

Gherman *et al.*[50] have applied the broad-band absorption technique of mode-locked cavity enhanced absorption spectroscopy (ML-CEAS) to detect N_2^+ utilising the (0,0) band of the $N_2^+(B\,^2\Sigma_u^+ \leftarrow X\,^2\Sigma_g^+)$ transition at around 391 nm in an N_2 glow discharge. In their experimental setup, the high sensitivity of a cavity is combined with the simultaneous acquisition of data over a broad spectral range. In a 5 mA discharge at 1 Torr plasma pressure, the concentration of N_2^+ was found to be 1.6×10^9 cm^{-3}, with a rotational temperature of 1300 K. No absorptions were found in the regions of the (1,1) and (2,2)

band heads (accessible *via* their experimental setup) indicating a low vibrational temperature.

Visser *et al.*[51] have studied the time-evolution of the N_2^+ concentration and the gas temperatures using optical emission spectroscopy and LIF in a pulsed RF discharge. The detection system was calibrated using a Rayleigh scattering experiment on molecular nitrogen at 1 atm. At 22.5 mTorr and 300 W plasma pressure and power the ion density in the stationary discharge was found to be 1.0×10^{11} cm^{-3}, rising to 2.3×10^{11} cm^{-3} at 225 mTorr and 300 W plasma pressure and power. The results from the two different experimental methods (OES and LIF) are found to be in agreement. No significant population of the $v = 2$ level was observed, and a vibrational temperature was thus determined by comparing the populations of the $v = 0$ & 1 levels, and under their experimental conditions found to be 1200 K. This is larger than the measured rotational temperature of the $v = 0$ level in their experimental setup of 500 K. These observations are consistent with the measurements presented here.

Visser *et al.*[51] also calculate the rotational and vibrational relaxation rates and find them to be three orders of magnitude less than the experimental decay rates and thus conclude that T_{vib} and T_{rot} of $N_2^+(X)$ are in equilibrium with T_{vib} and T_{rot} of the N_2 gas. This provides verification of the assumption used earlier that T_{vib} of $N_2(A)$ is in equilibrium with $N_2^+(X)$, in order to calculate the total concentration of the latter. T_{trans} is also found to be in equilibrium with T_{rot}, in further agreement with the conclusions of this work. Visser *et al.*[51] conclude that the dominant loss mechanisms at low plasma pressure (relevant here) are dissociative recombination of the ions and electrons, and diffusion to the walls. The third body process of formation of N_4^+ becomes increasingly important at higher plasma pressures. Of more interest, however, is their explanation of the difference observed in the translational/rotational and vibrational temperatures. Their observed decay rate of the vibrational and rotational distributions is much faster than the vibrational-rotational energy transfer rate, hence energy exchange between V and R/T can be completely neglected as the two distributions are effectively decoupled. As a consequence, the steady state distributions of the vibrational and rotational levels are completely determined by V and R/T excitation of N_2 by electrons and by energy loss processes (such as diffusion) to the wall. Combining the results of their experiments with a simulation it is determined that the translational and rotational heating of the gas molecules is due to translational energy exchange between electrons and nitrogen molecules and not any other process.

As mentioned, the calculation of the $N_2^+(X)$ concentration rests on the assumption that its vibrational distribution is the same as that found in the $N_2(A)$ state, although the evidence presented here suggests the possibility of a lower vibrational temperature for $N_2^+(X)$. The processes that influence the vibrational population of $N_2^+(X)$ and that are responsible for the two species ($N_2(A)$ and $N_2^+(X)$) having different vibrational temperatures (or populations) include all those that contribute to its formation and destruction, and whether or not they have a vibrational state propensity. Particular aspects that are potentially important in this respect include the electron impact ionization cross-sections to both the $N_2^+(A)$ and $N_2^+(X)$ states (separated by only ~ 1.2 eV) from $N_2(X, v)$, which are similar in magnitude[52]. The Einstein A-factors for the radiative decay of the $N_2^+(A, v = 0\text{-}4)$ are weighted towards the lower vibrational levels of $N_2^+(X)$ (predominantly $v = 0\text{-}3$), adding further complexity to the vibrational distribution which may result in a lower vibrational temperature[43].

4.6 Summary

The concentrations of the $N_2(A, v = 0,1,3 \& 6)$ levels were measured as a function of operating conditions in a pure N_2 RF ICP discharge using CEAS, calibrated by determination of the mirror reflectivities in a CRDS experiment. At 25 mTorr and 200 W plasma pressure and power, the populations of the $v = 0$, 1, 3, and 6 levels are $(1.31 \pm 0.16) \times 10^{11}$ cm^{-3}, $(8.44 \pm 1.01) \times 10^{10}$ cm^{-3}, $(2.83 \pm 0.34) \times 10^{10}$ cm^{-3} and $(5.27 \pm 0.63) \times 10^{9}$ cm^{-3}, respectively, corresponding to a vibrational temperature of 3600 ± 150K. These concentrations were found to increase with plasma power, a result of an increasing electron density and temperature causing an increase in the excitation rate. The decrease in $N_2(A)$ density observed with increasing plasma pressure is attributed to an enhancement of the quenching loss rates, with the effects of the decreasing electron density and temperature (with increasing plasma pressure) on the excitation rate offset by the gain resulting from an increase in the feedstock gas density. Translational and rotational temperatures were also determined and found to be in equilibrium (at a plasma pressure of 25 mTorr rising from (270 ± 32) K at 50 W plasma power to (500 ± 60) K at 500 W, with no observed temperature dependence on plasma pressure). This is somewhat lower than the corresponding vibrational temperatures (at a plasma pressure of 25 mTorr rising from 2900 K at 100 W plasma power to 3700 K at 300 W). Reasons for the difference in the

rotational/translational and vibrational temperatures are discussed. A consideration of the discharge kinetics leads to the conclusion of a strong coupling between the $N_2(A)$ and $N_2(B)$ concentrations, and highlights the importance of electron impact excitation of $N_2(A)$ in the production of $N_2^+(X)$.

CEAS was further used in combination with WMS (to enhance the sensitivity of the detection) in order to probe the (2,0) band of $N_2^+(A\,^2\Pi_u \leftarrow X\,^2\Sigma_g^+)$ with varying plasma parameters. The concentration was calibrated against a measurement made using pure CEAS at the conditions of greatest signal intensity, and was found to decrease with increasing plasma pressure and increase with increasing plasma power. A total $N_2^+(X)$ ion density was calculated on the assumption the vibrational distribution is the same as that found in $N_2(A)$, and a comparison of the processes that determine the two vibrational distributions is made. Further analysis leads to the conclusion that under the conditions of the experiment presented here, diffusion to the walls and dissociative recombination are the dominant loss mechanisms for $N_2^+(X)$. The sensitivity for the CEAS and CEAS/WMS measurements is calculated, and it is shown that there is an order of magnitude gain in sensitivity by using the two techniques in combination (for 1st harmonic detection).

References

[1] Bakowski, B. *et al*, J. Phys. D: Appl. Phys., **37**, 2064, (2004)

[2] Hancock, G. *et al*., J. Phys. D: Appl. Phys., **39**, 1846, (2006)

[3] Cho, J *et al*, Surf. Coat. Technol., **136**, 106, (2001)

[4] Okuji, S *et al*, Surf. Coat. Technol., **136**, 102, (2001)

[5] Jama, C *et al*, Surf. Coat. Technol., **116**, 59, (1999)

[6] Guerra, V. *et al*, J. Phys. D: Appl. Phys., **34**, 1745, (2001)

[7] Loureiro, J. & Ferreira, C.M., J. Phys. D: Appl. Phys., **22**, 67, (1989)

[8] Loureiro, J., Chem. Phys., **157**, 157, (1991)

[9] Loureiro, J. *et al*, J. Phys. D: Appl. Phys., **23**, 1371 (1990)

[10] Cartwright, J.C., J. Appl. Phys., **49**, 3855, (1978)

[11] Niemi, K. *et al*, J. Phys. D: Appl. Phys., **34**, 2330 (2001)

[12] Mazouffre, S. *et al*, Plasma Sources Sci. Technol., **10**, 168, (2001)

[13] Cernogora, G. *et al*, J. Phys. B: At. Mol. Opt. Phys., **14**, 2977, (1981)

[14] De Benedictis, S. *et al*, J. Phys. D: Appl. Phys., **31**, 1197, (1998)

[15] Piper, L. G., J. Chem. Phys., **88**, 231, (1988)

[16] Piper, L. G., J. Chem. Phys., **88**, 6911, (1988)

[17] Piper, L. G., J. Chem. Phys., **90**, 7087, (1989)

[18] Piper, L. G., J. Chem. Phys., **91**, 864 (1989)

[19] Woodcock, B. *et al*, J. Appl. Phys., **81**, 5945, (1997)

[20] Capitelli, M. *et al*, Chem. Phys., **56**, 29, (1981)

[21] Gorse, C. *et al*, Chem. Phys., **119**, 63, (1988)

[22] Simek, M. *et al*, Plasma Chem. Plasma Process., **15**, 427, (1995)

[23] Foissac, C. *et al*, J. Phys D: Appl. Phys., **33**, 2434, (2000)

[24] Lofthus, A. & Krupenie, P., J. Phys. Chem. Ref. Data, **6**, 113, (1977)

[25] Sa, P.A. & Loureiro, J., J. Phys. D: Appl. Phys., **30**, 2320, (1997)

[26] Augustyniak, E & Borysow, J, J. Phys. D: Appl. Phys., **27**, 652, (1994)

[27] Cernogora, G. *et al*, J. Phys. B: At. Mol. Phys., **17**, 4429, (1984)

[28] De Benedictis, S. *et al*, Chem. Phys., **178**, 574, (1993)

[29] De Benedictis, S. & Dilecce, G., J. Chem. Phys., **107**, 6219, (1997)

[30] De Benedictis, S. *et al*, J. Chem. Phys., **110**, 2947, (1999)

[31] Sadeghi, N. *et al*, J. Phys. D: Appl. Phys., **34**, 1779, (2001)

[32] Krames, B., J. Phys D: Appl. Phys., **34**, 1789, (2001)

[33] Guerra, V. & Loureiro, J., Plasma Sources Sci. Technol., **6**, 361, (1997)

[34] Cho, J. *et al*, Surf. Coat. Technol, **136**, 106, (2001)

[35] Bachir, I. *et al*, J. Mol. Spec., **166**, 88, (1994)

[36] Miller, R.E., J. Chem. Phys., **43**, 1695, (1965)

[37] Colburn, E.A. & Douglas, A.E., J. Mol. Spectrosc., **65**, 332, (1977)

[38] Diatomic 1.02, X. Tan

[39] Laux, C.O. & Kruger, C.H., J. Quant. Spectros. Radiat. Trans., **48**, 9, (1992)

[40] Laher, R.R. & Gilmore, F.R., J. Phys. Chem. Ref. Data, **20**, 685, (1991)

[41] Effantin, C. *et al*, J. Mol. Spec., **76**, 221, (1979)

[42] Kovacs, I., Rotational Fine Structure in the Spectra of Diatomic Molecules, Adam Hilger Ltd., 1969

[43] Gilmore, F.R. *et al*, J. Phys. Chem. Ref. Data., **21**, 1005, (1992)

[44] Henningsen, J. & Simonsen, H., Appl. Phys. B., **70**, 627, (2000)

[45] Freund, R.S. *et al*., Phys. Rev. A, **41**, 5861, (1990)

[46] Kosarim, A.V. *et al*, Chem. Phys. Lett., **414**, 215, (2005)

[47] Supiot, P. *et al*, J. Phys. D: Appl. Phys., **32**, 1887, (1999)

[48] Nakano, T. *et al*, J. Appl. Phys., **92**, 2990, (2002)

[49] Freegarde, T.G.M. & Hancock, G., J. Phys. IV. France., **7**(C4), 15, (1997)

[50] Gherman, T. *et al*. J. Phys. D: Appl. Phys., **37**, 2408, (2004)

[51] Visser, R.J. *et al*, J. Appl. Phys., **71**, 5792, (1992)

[52] Kosarim, A.V. *et al*, Chem. Phys. Lett., **414**, 215, (2005)

Chapter 5

Molecular discharges II: Detection of $O(^3P_2)$ and $O_2(^1\Delta_g)$ in an oxygen plasma

The development of diagnostic systems for the detection of two active species known to play a key role in the kinetics of oxygen plasmas is the focus of the research presented in this chapter. Oxygen atoms in their ground state ($^3P_2$) are detected using radiation centred at 630.205 nm corresponding to the highly forbidden $O(^1D_2 \leftarrow ^3P_2)$ transition. A CEAS system is constructed (calibrated using CRDS) to determine the absolute number densities of this state and the concentrations yielded are compared to those determined from other methods found in the literature. An attempt is made to rationalise the data in terms of the dominant kinetic processes occurring.

A difference frequency generation (DFG) system is constructed by combining the radiation output of a doubled Nd:YAG laser at 532 nm and an external diode laser at 737 nm in a newly developed periodically poled material (MgO doped PPLN). The generation of radiation at around 1.9 μm is verified by probing a transition originating from the ground state of ammonia. The technique of WMS is used to enhance the sensitivity of detection in order to probe the (0,0) band of the highly forbidden quadrupolar transition $O_2(b^1\Sigma_g^+ \leftarrow a^1\Delta_g)$ in order to detect $O_2(a^1\Delta_g)$. The singlet oxygen is firstly generated in an ICP and then subsequently in a microwave discharge in an attempt to increase its concentration to enable detection; a range of gas mixtures and pressures are used to further this aim.

5.1 Introduction

The detection of the active species present in oxygen plasmas has long been the subject of research due to their fundamental and industrial interest. Oxygen plasmas are unusual in that they belong to a group of plasmas known as electronegative in which the presence of negative ions (such as O^- and O_2^-) adds complexity to their chemistry, and are perhaps a contributing factor to their utility in a wide variety of industrial processes. In this chapter, methods for the detection of oxygen atoms in their ground state ($^3P_2$) and oxygen molecules in their first excited electronic state ($a^1\Delta_g$, often referred to as singlet oxygen) are developed and observations made regarding their behaviour in oxygen discharges.

The various industrial processes in which oxygen plasmas have found use include chemical vapour deposition, surface treatment and etching in the manufacture of integrated circuits. $O_2(a^1\Delta_g)$ and $O(^3P_2)$ are both known to play a major role in the chemistry of the upper atmosphere[1,2] and oxygen atoms are thought to be responsible for the oxidisation of spacecraft surface protective material[3]. The presence of oxygen atoms in combustion media has also been investigated[4]. Singlet oxygen attracts further attention in its connection with medical applications, in particular the photodynamic[5] or light-oxygen[6] therapy of tumours. The continuing investigation and refinement of the chemical oxygen-iodine laser (COIL)[7] has also renewed interest in the detection of singlet oxygen (one of the components in the active medium).

To date, oxygen atoms have generally been detected in plasmas using various qualitative methods that require either calibration or the modelling of various parameters in order to attain absolute concentrations. Actinometry, a technique which allows the monitoring of a species in its electronic ground state by measuring the plasma induced emission from an excited state, is widely used for the detection of $O(^3P_2)$ with argon as the actinometer gas. This is particularly applicable as the excitation cross-sections of argon and oxygen have a similar energy dependence and threshold, thus monitoring the emission intensities of both species gives a relative oxygen atom density. Actinometry has been carried out by Jasik *et al.*[8] in a pulsed RF oxygen discharge across a range of plasma parameters; construction of a numerical model allowed evaluation of the absolute degree of oxygen dissociation. Booth *et al.*[9] compare actinometry with vacuum ultraviolet absorption spectroscopy (VUVAS) at 130 nm in an oxygen ECR plasma (see section 1.2.3) and find a poor correlation for oxygen atoms, but a well correlated result for ground state O_2.

However, Granier *et al.*[10] compare the same two techniques in a surface wave discharge at 433 MHz and 2.45 GHz and find a reasonable agreement in the oxygen atom density, albeit at higher oxygen pressures; the addition of N_2 to the discharge gas is also investigated.

Optical emission spectroscopy (section 1.5.2.1) is used by Czerwiec *et al.*[11] to monitor O atom density in Ar/O_2 and $Ar/H_2/O_2$ in microwave discharges to yield information on atom and radical chemistry at pressures of around 10 Torr. Similar studies are conducted in the post-discharge using NO titration, and the importance of the surface reactions are highlighted. Mozetic *et al.*[12] present a comparison between the absolute techniques of NO titration and fibre-optic catalytic probes (FOCP) in the determination of oxygen atom density in the post-glow of an Ar/O_2 plasma generated in a surfatron microwave discharge at 2.45 GHz and find a similarity in the results provided by the two techniques.

VUVAS has been employed using a microdischarge hollow cathode lamp by Nagai *et al.*[13] with self absorption, the emission line profile and background absorption of the oxygen molecule taken into account in the quantitative analysis of O atom densities. This was performed in an ICP discharge operating at 13.56 MHz (similar in design to the one used in this thesis) and the results were found to be consistent with those obtained using actinometry. VUVAS is used in combination with pulse modulation of the plasma by Kitajima *et al.*[14] to investigate the effect of driving frequency on the O atom density in a pure O_2 RF CCP. This combination eliminated the effects on the absorption signal of the background emission from the plasma and allowed low power operation of the ICP light source to limit the effects of self-absorption. Third harmonic generation using a strongly focussed 391 nm dye laser has been used as a VUV source for the probing of oxygen atoms by Celii *et al.*[15]. Oxygen atoms were generated both in a microwave discharge and by NO_2 photodissociation, with their detection verified by the change in VUV intensity and peak frequency shift, the relationship between these two was determined by performing NO_2 titration measurements.

Two photon absorption laser induced fluorescence (TALIF) has been applied to the detection of $O(^3P_j)$ with incident photons of wavelength 225 nm causing excitation of an electron to the $3p(^3P_j)$ manifold with subsequent fluorescence observed at 844 nm through to the $3s(^3S_1)$ level. Collart *et al.*[16] have utilised this technique in a low pressure RF CCP for ground state O atom detection with calibration carried out using a microwave discharge containing a known oxygen atom concentration (determined *via* mass spectrometry). Using

their time resolved measurements the reliability of optical emission actinometry in low pressure O_2 RF plasmas for the determination of relative atomic oxygen densities is also examined. Katsch *et al.*[17] provide a comparison of actinometry and TALIF for the determination of atomic oxygen densities in a RF GEC reference discharge cell, and find good agreement between the two methods. The most comprehensive use of TALIF to date is provided by Hancock & Toogood[18], with the measurement of O atom density in a commercial parallel-plate RF (13.56 MHz) plasma chamber (a CCP) operating at pressures between 50-500 mTorr with various CF_4/O_2 gas compositions. However, they urge caution in the interpretation of TALIF results for O atom concentrations under conditions in which stimulated emission is present due to its effect on the fluorescence intensity (which is non-linear with O atom concentration in the presence of stimulated emission). Furthermore, it is found that optical emission measurements deviate markedly from those obtained by TALIF (under conditions in which stimulated emission is not present), which emphasizes the difficulties in using OES for monitoring O atoms in plasmas.

Dillece *et al.*[19,20] use TALIF on the same transitions to monitor oxygen atoms in a plasma jet; calibration is achieved by measuring the collisional quenching of the excited state of the oxygen atom. Similar work by Peze *et al.*[3] in a flowing afterglow allows absolute density measurements of oxygen atoms only when the competitive processes to the fluorescence have been considered, and a correct treatment of the focussing geometry achieved. They find an order of magnitude agreement with results obtained *via* NO_2 titration. An atmospheric plasma jet (essentially a CCP RF discharge at 13.56 MHz) with a high helium flux (containing only 0.5 % O_2) used in the treatment of thermally sensitive surfaces is studied by Niemi *et al.*[21] using TALIF to map the spatial density of O atoms.

A small number of studies have been conducted using absolute techniques that require no calibration; these are generally based around the use of optical cavities (section 2.3). Harris & Weiner[22] demonstrate the first observation of O atoms in absorption using the technique of intra-cavity laser absorption spectroscopy (ICLAS) on the transitions at 630.030 nm and 636.38 nm, with oxygen atoms generated in a discharge flow tube. The sensitivity enhancement over that of conventional absorption spectroscopy ranges from a factor of 3500 to 17000, depending on laser power. More recent measurements by Teslja & Dagdigian[4] use CRDS on the forbidden transition ($^1D_2 \leftarrow {}^3P_2$) at 630.030 nm to detect ground state oxygen atoms in a microwave discharge in either pure O_2 or Ar/N_2O. This enables the concentration of oxygen atoms in the 10^{14} cm^{-3} regime to be detected, and comparison with NO_2 titration yields an accuracy of within 20 %.

Singh *et al.*[23] have conducted measurements on oxygen atom densities to elucidate the recombination rate coefficient of oxygen atoms on the walls of a stainless steel ICP chamber. This is estimated using a steady state plasma model in combination with measurements on the radical density obtained from appearance potential mass spectrometry and on the neutral density using conventional mass spectrometry. The EEDF and electron density (further input parameters) were obtained using a Langmuir probe. Similar measurements using TALIF (calibrated on static neon gas) to determine spatially resolved O atom densities in order to deduce the recombination rate coefficients on steel, aluminium, silicon, silicon dioxide wafers and on polypropylene have been carried out by Gomez *et al.*[24].

Historically, the techniques used in the detection of the $O_2(a^1\Delta_g)$ state have been limited to optical emission, chemical detection and EPR. This is initially surprising given the importance of this state in the operation of the COIL and in plasmas, although upon consideration of the possible options for quantitative absorption measurements this paucity is not altogether unexpected. Attention has recently focused upon observation of this state using cavity techniques due to the increasing availability of diode lasers in the near IR (a point which will be returned to later).

One of the earliest observations of emission of 634 nm radiation from systems with high $O_2(a^1\Delta_g)$ concentration was reported by Arnold *et al.*[25] in 1966. Derwent & Thrush[26] observed the same emission with a high concentration of $O_2(a^1\Delta_g)$ provided by a 2.45 GHz microwave discharge with the effluent passed over mercury oxide to remove atomic oxygen. The formation of a dimole of $[O_2(a^1\Delta_g)]^2$ was subsequently isolated as the cause of this emission in what was one of the earliest observations of $O_2(a^1\Delta_g)$ on a laboratory scale. Rate constants for the formation of this dimole for $O_2(a^1\Delta_g)$ in $v = 0$ and 1 were also calculated, and have since been verified by Fisk & Hays[27]. The utility of such methods is made possible due to the long lifetime of the $O_2(a^1\Delta_g)$ state (originally measured to be around 65 minutes using absorption spectroscopy on the $O_2(a^1\Delta_g \leftarrow X^3\Sigma_g^-)$ (0, 0) and (0, 1) bands[28]). Other photochemical methods to detect $O_2(a^1\Delta_g)$ include its photoionisation using wavelengths less than 111.8 nm, an experiment originally conducted by McNeal & Cook[29].

Falick *et al.*[30] provided the first observation of the paramagnetic resonance spectrum of the $O_2(a^1\Delta_g)$ molecule in a 2.45 GHz, 500 W pure O_2 discharge. Observation of $O_2(a^1\Delta_g)$ was verified by removing the oxygen atoms *via* titration with NO_2. This provided a calibration for the emission measurements of Bernard & Pchelkin[31] at 1270 nm from $O_2(a^1\Delta_g)$ (generated using a microwave source) to the ground state. The intensity of

the radiation was divided by the system pressure to obtain a method for continuously monitoring a fluctuating $O_2(a^1\Delta_g)$ concentration of the order of a few percent. Yagi *et al.*[32] have recently returned to the EPR method to detect $O_2(a^1\Delta_g)$ produced in a chemical mechanism and provide clear and well defined spectra.

Emission spectroscopy (at 1274 nm) has been utilised and compared to EPR in determining the concentrations of the $O_2(a^1\Delta_g)$ state (produced chemically) by Spalek *et al.*[33] in order to determine an accurate Einstein A-factor and radiative lifetime. The two techniques produced results (within experimental error) of $A = (2.24 \pm 0.4) \times 10^{-4}\ s^{-1}$, yielding τ_{rad} = 74 minutes, a value close to the one determined by Badger *et al.*[28]. More recent measurements[34,35,36,37] regarding the lifetime of $O_2(a^1\Delta_g)$, conducted using absorption spectroscopy on the (0,0) band of the $O_2(a^1\Delta_g \leftarrow X^3\Sigma_g^-)$ system suggest values in excellent agreement with the one reported by Spalek *et al.*[33]. A calibrated emission measurement has been attempted by Duo *et al.*[38] using a calibrated piston source of light (simulating a cylindrical volume luminosity source) to determine the concentration of $O_2(a^1\Delta_g)$ in a singlet oxygen generator (SOG). Detection of the emission at 1274 nm from the singlet oxygen at a given solid angle yields an absolute concentration (as opposed to that obtained from normal emission spectroscopy) due to calibration against the radiation emitted from this even intensity light source.

The transition of concern to this thesis, $O_2(b^1\Sigma_g^+ \leftarrow a^1\Delta_g)$, was initially observed in the emission spectrum of a discharge through O_2 and He by Noxon[39] (the system now bears his name) at 1908 nm corresponding to the (0,0) band. It is forbidden by the selection rules for electric dipole (as the transition is of the type g ↔ g), and also as a magnetic dipole since $\Delta\Lambda = 2$. It does not, however, break the selection rules for an electric quadrupole transition. The observation of this transition was the first made of an electronic transition in a diatomic molecule which is primarily quadrupole in nature, a fact that allows observation of $\Delta J = 0, \pm 1$ and ± 2. Its highly forbidden nature required the production of high concentrations of the metastable $b^1\Sigma_g^+$, achieved using a large discharge tube filled with a mixture of 0.5 % O_2 in He. The low resolution of the spectrometer used did not allow observation of the individual rotational lines which were ultimately observed by Fink *et al.*[40] in 1981, still in emission but using a Fourier transform spectrometer. The observation of all five branches (O, P, Q, R & S) verified the transition's expected electric quadrupole nature. Again, the oxygen metastables were produced in a discharge (2.45 GHz, 2 Torr oxygen, 100 W) to yield sufficiently high concentrations for observation.

Several absorption techniques have been used in the detection of $O_2(a^1\Delta_g)$. Coxon & Roychowdhury[41] detect $O_2(a^1\Delta_g)$ using absorptions in the VUV at 144.095 nm and 148.66 nm (generated using a hydrogen discharge lamp), with singlet oxygen created *via* the reaction of chlorine with alkaline hydrogen peroxide. This technique has the advantage that the cross-sections for these transitions are known, although absorption by O_2 must be taken into account. Spontaneous Raman imaging (SRI) has been used to detect both $O_2(a^1\Delta_g)$ and $O_2(X^3\Sigma_g^-)$ in real time, although the spectra obtained are vibrationally and rotationally unresolved[42].

Attention has recently refocused on this transition due to the availability of radiation sources in the near infrared at 1910 nm. ICLAS (section 2.3.6) has been conducted using a Co:MgF_2 laser by Pazyuk *et al.*[43], with singlet oxygen generated using a pure oxygen 2.45 GHz discharge at 5 Torr pressure and 100 W power. The broadband output from the laser cavity was mixed with radiation from a Nd:YAG laser in a non-linear crystal (lithium niobate); the emission at the sum frequency was incident on the entrance slit of a spectrograph. Rotationally resolved spectra were observed, and a sensitivity of 2×10^{14} cm^{-3} for the detection of $v = 0$ in $O_2(a^1\Delta_g)$ was achieved.

Williams *et al.*[44] present the first measurement of the (1,0) band of the $O_2(b^1\Sigma_g^+ \leftarrow a^1\Delta_g)$ transition using a narrow band tuneable DFB laser based around 1505 nm and an optical cavity. Using the technique of off-axis ICOS[45] (similar to CEAS, section 2.3.5), several rotational lines of the Q branch were observed and a sensitivity of 3×10^{12} cm^{-3} per quantum state achieved (compared to 3×10^{13} cm^{-3} per quantum state from Pazyuk[43]). The singlet oxygen was generated in a 13.56 MHz RF ICP by passing a 5% O_2 in He mixture through a 25 mm quartz tube and coupling 250 W of RF power into the gas. The effluent was then passed through the off-axis ICOS measurement system at a total pressure of 32 Torr. The same experimental setup has recently been expanded[46] to detect the Q(2) – Q(18) lines of the (0,0) band of the $O_2(b^1\Sigma_g^+ \leftarrow a^1\Delta_g)$ system at 1910 nm using a DFB laser. However, despite the increase in cross-section of a factor of 20 over the (1,0) band, the higher detector noise and lower laser power resulted in an improvement in sensitivity of only a factor of 2.

The modelling of oxygen discharges is not as extensive as that found for argon or nitrogen, but has attracted attention over the last decade due to their role in industrial processes. Studies of note on low pressure RF discharges include those of Wu[47], Shibata *et al.*[48] and Feoktistov *et al.*[49]. Generally, the density of the electrons, O_2, O_2^-, O, O^-, O_2^+, O^+ and the EEDF are taken into account to predict the spatial properties of various parameters

within the plasma chamber, and to elucidate the relative importance of the kinetic processes occurring.

The experimental investigation of oxygen plasmas *via* the detection of two of their key components, and their variability with plasma parameters, is the focus of the research presented in this chapter. Oxygen atoms are detected in their ground state *via* the forbidden transition $O(^1D_2 \leftarrow ^3P_2)$ at 630.205 nm using the technique of CEAS. Furthermore, radiation is generated at 1910 nm using a DFG system to detect $O_2(a^1\Delta_g)$ using the (0,0) band of the $O_2(b^1\Sigma_g^+ \leftarrow a^1\Delta_g)$ transition. While the narrow-band radiation generated allows probing of the individual ro-vibrational levels, the population of these quantum states is determined to be too low in order for the absorptions to be observed.

5.2 Experimental

5.2.1 O Atom Detection

The experimental setup is similar to that described for the CEAS measurements on N_2 $(A^3\Sigma_u^+)$ discussed in chapter 4. Approximately 2 mW of narrow band (FWHM ~ 40 MHz) radiation from a continuous wave (CW) diode laser (SLD 1132 VS) at 630.205 nm (vac) was used to probe the highly forbidden $O(^1D_2) \leftarrow O(^3P_2)$ transition. The temperature and current (−10.2 C and 38 mA) of the laser diode were controlled by home-made devices. The laser light passed through an optical isolator (Gsanger, > 60 dB rejection) and an acousto-optic modulator (Opto Electronique), and was then focussed into an optical cavity that bounded the plasma chamber. The optical cavity comprised of a pair of high reflectivity mirrors (Laser Optik GmbH R = 0.99905 at 630 nm, with radius of curvature = −1.5 m) separated by 75 cm. The inductively coupled plasma chamber (described in section 1.2.4) was operated with a supply of pure oxygen (BOC) within the range of powers and pressures of 50-500 W and 10-100 mTorr.

Effects of the plasma upon mirror reflectivity using this chamber, which have been reported previously by us in a N_2 plasma[50], have been completely mitigated in this study by using long and narrow (150 mm × 5 mm) baffle arms and a continuous flow of oxygen over the mirror surfaces. No degradation of mirror reflectivity was measured for the duration of the entire study. The optical transmission of the cavity was separated from the optical emission of the plasma using a prism and further filtered using a bandpass filter (λ_T

> 610 nm) before being focussed onto a photomultiplier tube (PMT) (Q130F/RFI Thorn EMI) with the signal recorded on a digital oscilloscope (LeCroy 9314M). The CEAS spectra were then sent to a PC for analysis.

5.2.2 $O_2(a^1\Delta_g)$ Detection

The radiation output from a doubled Nd:YAG laser (Laser Quantum Torus) provided the pump beam at 532.212 nm and 330 mW, which is combined with that from a 40 mW external cavity laser centred at 737 nm (the signal beam, Sacher Lynx) by means of a dichroic mirror. The radiation from the 737 nm radiation passed through an optical isolator (Isowave I-7090-CM) and was constantly monitored for mode structure using a spectrum analyser (TEC Optics) and periodically checked in wavelength using a wavemeter (Burleigh WA-1000). The wavelength of the doubled Nd:YAG was monitored simultaneously using a separate wavemeter (Coherent WaveMaster). A ramp generator (TTi TG230) allowed the frequency of the signal laser (and consequently the frequency of the idler) to be scanned. The overlapping beams are focussed into a periodically poled MgO doped lithium niobate (MgO-PPLN) crystal (HC Photonics, 12 tracks between 8.0 μm – 10.2 μm with 0.2 μm steps, dimensions 40 mm × 14.5 mm × 0.5 mm). The crystal, mounted in an oven (HC Photonics) to control its temperature within 0.1 K (which is itself mounted on a three dimensional translation stage), is anti-reflection coated on its front face for 532 nm & 640-750 nm.

After passing through the crystal, the pump and signal beams are separated from the idler using a silicon window. A 100 mm CaF_2 lens focuses the idler which, after passing through the plasma chamber, is incident upon a calibrated stretched IR detector (Hamamatsu G5852-01). The output from the detector is monitored using an oscilloscope (LeCroy 9314 M) from which the data is transferred to a PC for analysis. The sensitivity of the detection scheme is further enhanced by multi-passing the 1.9 μm radiation through the plasma chamber 5 times, and applying the technique of WMS. This is achieved by modulating the signal beam at a frequency of 12 kHz and a modulation amplitude of 379 MHz (provided by a TTi TG1010A programmable function generator), corresponding to a b value of 2.2 for the Q(12) transition at 5234.325 cm^{-1} and 298 K. A second stretched detector is placed before the plasma chamber to monitor a fraction of the idler beam in order to provide a background signal simultaneous to the absorption signal. The output from both detectors are demodulated using two separate lock-in amplifiers (EG&G

Brookdeal) with the resultant signal monitored using the oscilloscope. A schematic of the experimental setup is shown in figure 5.1.

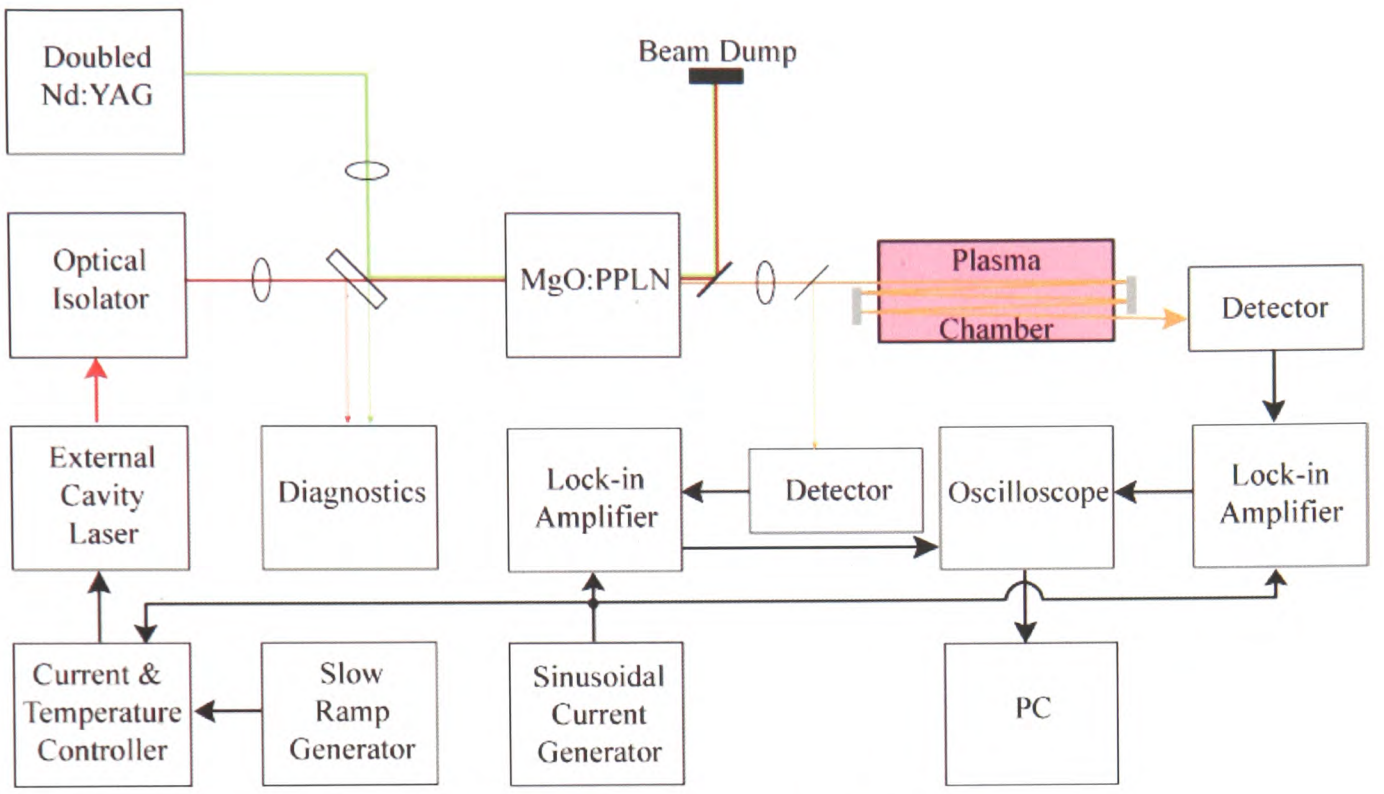


Figure 5.1: Schematic of the experimental set up for $O_2(a^1\Delta_g)$ detection.

The work presented in this chapter for the detection of $O_2(a^1\Delta_g)$ is achieved through the recent development of the MgO doped PPLN crystal. As a consequence, the parameters for the Sellmeier equation of this material are unknown, a fact which proves to be of difficulty in determining the crystal temperature required for the desired DFG. To circumvent this problem, the Sellmeier equation for PPLN provided by Jundt[51] is adjusted using data supplied by HC Photonics[52] to yield

$$n_e^2(\lambda,T)=\left[A_1+B_1f(T)+\frac{A_2+B_2f(T)}{\lambda^2-\left(A_3+B_3f(T)\right)^2}+\frac{A_4+B_4f(T)}{\lambda^2-A_5^2}-A_6\lambda^2\right]\Big/f^2, \quad (5.1)$$

where the temperature dependence (in degrees centigrade) is given by

$$f(T)=(T-24.5)\times(T+570.5). \quad (5.2)$$

The value taken for f in equation (5.1) depends on the type of process; $f = 1$ for undoped PPLN, while for MgO-PPLN, f is given by equations (5.3) and (5.4) for short and long wavelength processes, respectively.

$$f = 1.0270295 - 4.56346827 \times 10^{-5} T \tag{5.3}$$

$$f = 1.01813847 - 8.13965809 \times 10^{-8} T \tag{5.4}$$

The constants take the values $A_1 = 5.35583$, $A_2 = 0.100473$, $A_3 = 0.20692$, $A_4 = 100$, $A_5 = 11.34927$, $A_6 = 1.5334 \times 10^{-2}$, $B_1 = 4.629 \times 10^{-7}$, $B_2 = 3.862 \times 10^{-8}$, $B_3 = -0.89 \times 10^{-8}$, and $B_4 = 2.657 \times 10^{-5}$.

The temperatures predicted by the modified Sellmeier equation for short wavelength processes were found to be about 8 °C lower than those observed experimentally. For example, with the pump at 532.212 nm and the signal at 737.890 nm, 4 μW of radiation was generated at 1.9094 μm (from the 8.2 μm crystal track) using a crystal temperature of 71.1 °C (predicted to be 63 °C). The temperature tuning curve of the crystal was also determined and is shown at this wavelength in figure 5.2 where it can be seen that the permissible temperatures for DFG occur over a narrow range. Furthermore, the pump and idler power were measured to be 300 mW and 30 mW, respectively, which yields a DFG efficiency (using equation 2.10) of 4.4×10^{-4} W^{-1}.

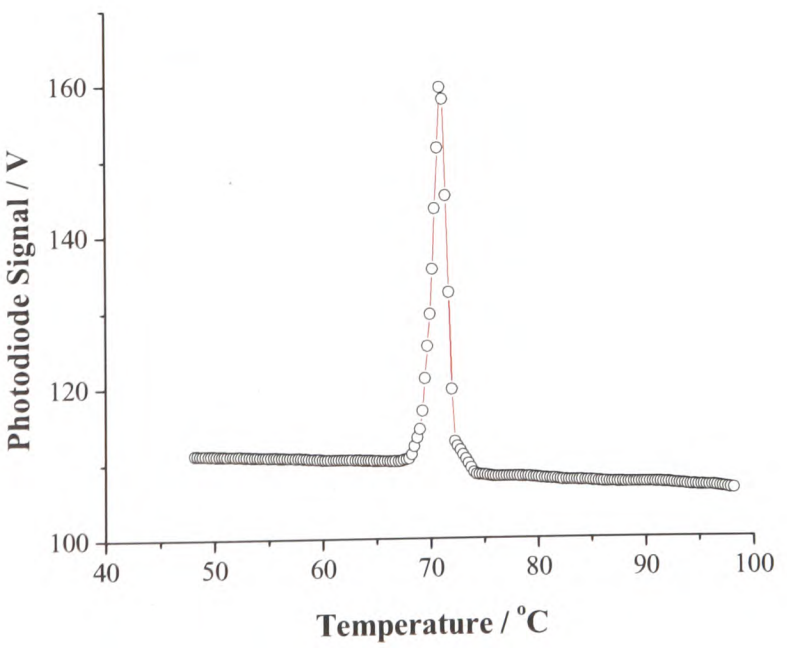


Figure 5.2: Temperature tuning curve for the MgO:PPLN crystal recorded by measuring the DFG output from mixing a pump beam at 532.212 nm and a signal beam at 737.890 nm.

5.3 Results

5.3.1 $O(^3P_2)$ Atom Detection

The CEAS signal (after 1000 averages) obtained at 500 W plasma power and 100 mTorr plasma pressure is shown in figure 5.3. This signal is extracted from the raw data using equation (5.5), where I is the laser signal, I_0 is the laser background, and γ is the optical emission from the plasma.

$$\text{CEAS Signal} = \frac{I - I_0}{I - \gamma} \tag{5.5}$$

The area, A (in s^{-1}), of the peak is related to α, the product of the integrated absorption cross-section (σ_{int}, measured in $cm^2\ s^{-1}$) and density of $O(^3P_2)$, by equation 2.33. Here, L is the physical length of the absorbing plasma (35 cm) and R is the mirror reflectivity (obtained by measuring the cavity ring-down time with the plasma on, but laser off resonance). Using a value of the Einstein A-factor taken from NIST[53], σ_{int} is calculated to be 8.9×10^{-13} $cm^2\ s^{-1}$, which yields an $O(^3P_2)$ concentration of $(4.8 \pm 0.6) \times 10^{14}$ cm^3 at 500 W plasma power and 100 mTorr plasma pressure. Analysis of the width of the peak shown in figure 5.3, which is dominated by Doppler broadening, returns a translational temperature of 490 ± 44K. Using this temperature, a value for the degree of dissociation of O_2 (defined by equation (5.6)) can be calculated at 500 W and 100 mTorr, and is found to be 0.12.

$$\delta = \frac{[O]}{2[O_2]} \tag{5.6}$$

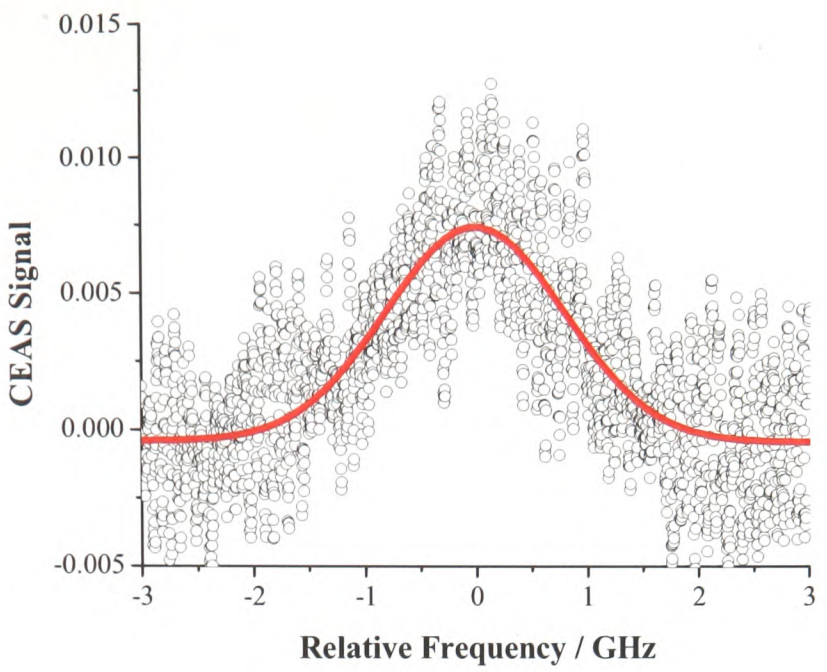


Figure 5.3: The $O(^3P_2 \leftarrow ^1D_2)$ transition observed at 630.205 nm in an O_2 plasma under operating conditions of 400 W power and 100 mTorr pressure.

Attempts were made to obtain further data under different experimental conditions (lower plasma power and pressure), but the low signal to noise ratio of the detection system made this unfeasible. It should be noted, however, that a decrease in the absorption was observed at lower plasma pressures and powers, corresponding to a decrease in the $O(^3P_2)$ concentration.

5.3.2 Measurements of $O_2(a^1\Delta_g)$

The creation of light at around 1.9 μm was verified by probing an absorption in ammonia (originating from the ground state), present in a 10 cm cell at a pressure of 4.6 Torr. This ground state transition is centred at 1.909327 μm (5237.325 cm^{-1})[54] with the probing radiation generated using light at 532.212 nm and 737.889 nm combined in the 8.2 μm crystal track with a temperature of 71.1 °C. Figure 5.4 shows the absorption signal obtained from a single pass and 100 averages recorded over 20 s; the peak observed at the higher frequency is a second ammonia transition with a lower cross-section.

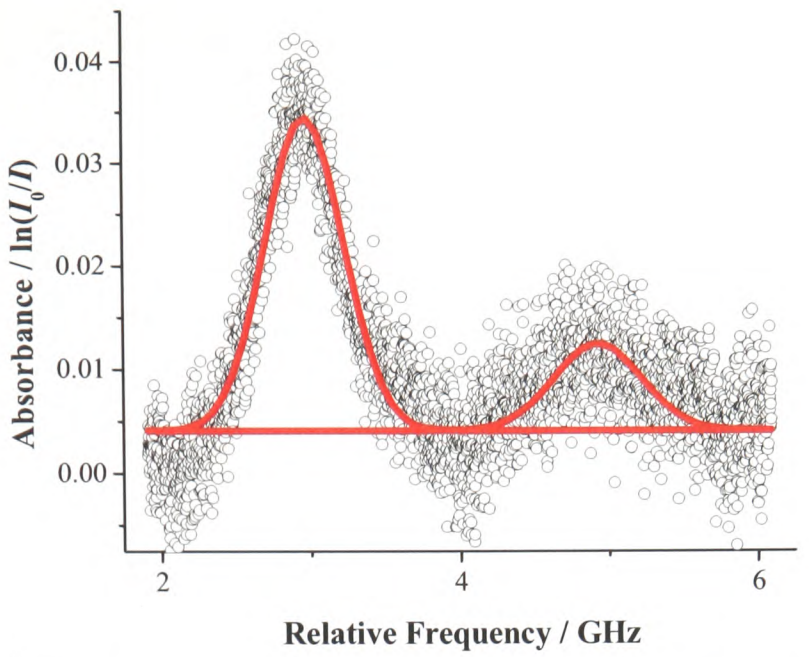


Figure 5.4: The observation of two transitions originating from the ground state of NH_3 at 5237.325 cm^{-1} (larger peak) and 5237.375 cm^{-1} (smaller peak), in a cell of 4.6 Torr ammonia and 10 cm in length.

The larger peak shown in figure 5.4 has a *S/N* of 38.1 and an integrated cross-section of 3.64×10^{-22} cm^2 cm^{-1}. The FWHM of the transition is returned as 0.0157 cm^{-1}, thus the peak cross-section is 2.31×10^{-20} cm^2. The peak absorption is 3.41 %, and taking this together with the *S/N* yields a minimum detectable absorption (I/I_0) of 9.0×10^{-4} over the 10 cm length of the cell. The sensitivity of the detection is enhanced using WMS, and the improvement in the signal for 1st and 2nd harmonics can be seen in figures 5.5a and 5.5b, recorded using the same cell as that in figure 5.4. The etalon effects due to the presence of the crystal, manifest as an oscillating background, can be seen to be considerable even though they are minimised from their maximum influence by slightly misaligning the crystal. The *S/N* of these absorptions is obtained by taking the noise as a standard deviation of a linear fit to a flat part of the background (where the etalon effects are at a minimum), and the signal is taken as the peak-to-peak height. The corresponding values of *S/N* are found to be 2650 and 1170 for the 1*f* and 2*f* traces, respectively, which corresponds to a minimum detectable absorption of 1.3×10^{-5} and 2.9×10^{-5} over the 10 cm cell in 20 seconds and for 100 averages.

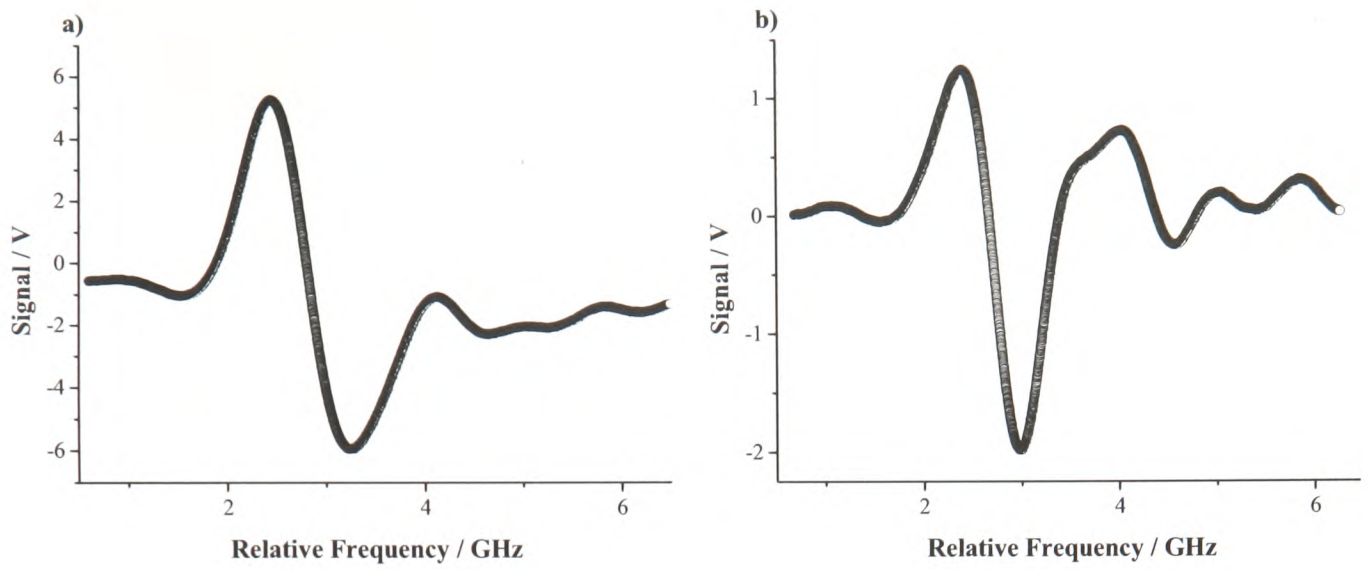


Figure 5.5: The a) 1*f* and b) 2*f* signals observed under the same conditions for the transitions shown in figure 5.4 using WMS at 12 kHz and a modulation amplitude of 379 MHz; note the broadening of the signals causing the peaks to overlap, and the presence of the etalon affecting the background.

The tunability of the 737 nm laser allows access to the Q(8), Q(10) and (Q12) transitions of the (0,0) band of the $O_2(b^1\Sigma_g^+ \leftarrow a^1\Delta_g)$ electronic transition. Light at 737.847 nm, 737.792 nm and 737.725 nm, respectively, was mixed with the output from the doubled Nd:YAG laser at 532.212 nm to produce radiation centred on these transitions at 1.90965 μm, 1.91002 μm and 1.91047 μm. The proximity of these lines negated the need to temperature tune the crystal for each set of wavelengths. After multi-passing the radiation through the ICP chamber a total of five times, no absorption signal due to these transitions was observed at any conditions within the parameter range (50-500 W plasma power and 10-100 mTorr plasma pressure).

In order to increase the concentration of $O_2(a^1\Delta_g)$, a microwave discharge was constructed (shown schematically in figure 5.6). This allows the operation of the plasma at 2.45 GHz with input powers up to 250 W and, crucially, pressures up to 20 Torr. A high flow roots pumping system (Edwards) was used to achieve the high pressure and flow rates required here and used previously when successfully detecting $O_2(a^1\Delta_g)$ in similar setups[44,46]. The large surface area to volume ratio in such a discharge necessitates the use of fast flowing systems to minimise the wall losses of $O_2(a^1\Delta_g)$ in the detection chamber. Again, the radiation was multi-passed through the chamber a total of five times to enhance the detection limit.

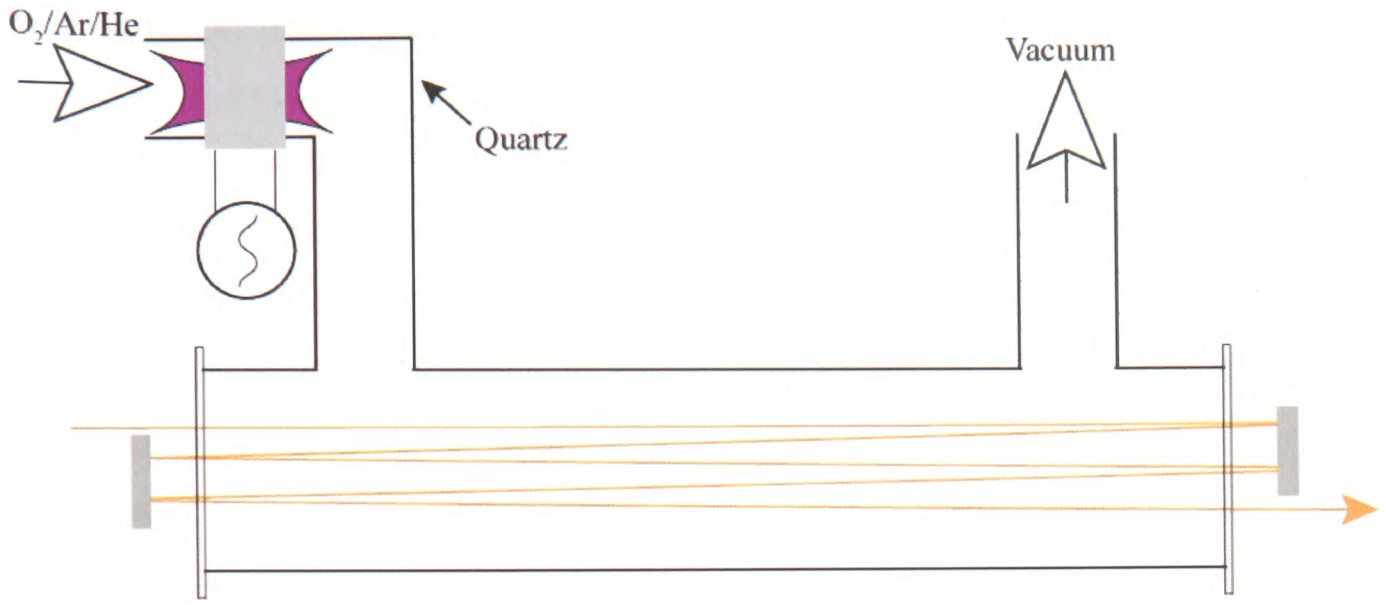


Figure 5.6: A schematic of the microwave discharge operating at 2.45 GHz and various powers and pressures used in an attempt to increase the $O_2(a^1\Delta_g)$ density.

The microwave discharge was operated at various pressures and gas compositions; pure O_2 at 2 Torr and 5 Torr, a 10 % mixture of O_2 in He at 20 Torr, and a 20 % mixture of O_2 in Ar at 10 Torr and 20 Torr. The addition of a bath gas has been found to increase the $O_2(a^1\Delta_g)$ density in previous studies[43,44,46], a result of an increase in the electron temperature within the discharge region increasing the production rate of $O_2(a^1\Delta_g)$. The dominant loss route of $O_2(a^1\Delta_g)$ is believed to be quenching on the chamber walls (with collisional quenching playing only a minor role), although the deactivation of singlet oxygen has been found to be reduced using quartz vessels[43,44,46]. However, no absorption signal corresponding to these transitions was detected under any of the conditions, even after significant averaging.

The quantum-state specific integrated cross-sections for the Q(8), Q(10) and Q(12) transitions can be calculated from equation 4.10 using the line strengths ($S_{J'J''}$) provided by Chiu[55], all of which are shown in table 5.1. The vibronic transition moment, $R_e^{v'v''}$ (in electric dipole moment atomic units), is calculated using equation (5.7)[56], where $\nu^3_{v'v''}$ is the band origin wavenumber (cm^{-1}) and $\delta_{0,\Lambda}$ is the Kronecker delta (equal to 1 if $\Lambda = 0$ and 0 otherwise).

$$A_{v'v''} = \left(2.026\times10^{-6}\right)\nu^3_{v'v''}\frac{\left(2-\delta_{0,\Lambda'+\Lambda''}\right)}{\left(2-\delta_{0,\Lambda'}\right)}\left|R_e^{v'v''}\right|^2 \qquad (5.7)$$

Values found in the literature for the Einstein A-factor, $A_{v'v''}$, range between 1-2.5 × 10^{-3} s^{-1}, with Noxon[39] reporting 2.5× 10^{-3} s^{-1} from his original emission measurement on the

(0,0) transition. More recent values include that of Burch & Gryvnak[57] at 1.7×10^{-3} s^{-1}, based on the *A* value of the b-X (0,0) transition and lying very close to that recently found by Cheah *et al.*[58] (1.6×10^{-3} s^{-1}) using the same method. However, the value of 1.26×10^{-3} s^{-1} determined from *ab initio* calculations by Gupta & Williams[44,46] is considered the most reliable for use here, and yields a value for $R_e^{v'v''}$ of 3.95×10^{-34} C m. It should be noted that nuclear spin statistics allow only the transitions from even rotational levels to appear in the O, S and Q branches, and only those from odd rotational levels in the P & R branches of the $O_2(b^1\Sigma_g^+ \leftarrow a^1\Delta_g)$ system, due to the absence of odd rotational *J* levels in $b^1\Sigma_g^+$.

Transition	Line Strength ($S_{J'J''}$)	Integrated Cross-Section (cm^2 cm^{-1})
Q(8)	8.35	1.50×10^{-23} cm^2 cm^{-1}
Q(10)	10.4	1.51×10^{-23} cm^2 cm^{-1}
Q(12)	12.4	1.51×10^{-23} cm^2 cm^{-1}

Table 5.1: Line strengths and integrated cross-sections for the three transitions probed in the (0,0) band of the $O_2(^1\Sigma_g^+ \leftarrow ^1\Delta_g)$ system.

Previous measurements of $O_2(a^1\Delta_g)$ report concentrations of the order of a few percent of the initial oxygen concentration[26,43,44,46,59]. On the assumption that, as an upper limit, 10 % of the initial oxygen concentration in the microwave discharge at 5 Torr is converted into $O_2(a^1\Delta_g)$, and 5.9 % of that lies in a given *J* level (calculated using equation (5.8) at 298 K, where $q_{rot} = kT_{rot}/2B$ and $q_{el} = 2$ from lambda doubling), a number density of 9.5×10^{14} cm^{-3} for the absorbing species is yielded. At this temperature, the Doppler broadened peak will have a width of 343 MHz (0.0114 cm^{-1}) which gives a peak cross-section for the Q(12) transition of 1.3×10^{-21} cm^2. Taking into account the absorption is over a pathlength of 300 cm (5 passes through a 60 cm cell) the fractional absorbance expected is 3.7×10^{-4}, marginally below the 3.9×10^{-4} limit for $1f$ detection (yielded over 20 seconds and 100 averages) calculated from scaling up the value observed across the 10 cm ammonia cell.

$$\frac{N_{J''}}{N_{v=0}} = \frac{(2J''+1)}{q_{rot} \times q_{el}} \exp\left(\frac{-BJ''(J''+1)}{kT_{rot}}\right) \qquad (5.8)$$

5.4 Discussion

Table 5.2 shows a comparison of the values for oxygen atom concentration, in terms of density and as a fraction of dissociated O_2, with other values reported in the literature using a range of experimental setups and plasma systems. Three of these values deserve highlighting due to the techniques utilised and the similarity of the plasma operating systems and conditions to the ones used in this study. Collart *et al.*[16] use a calibrated TALIF measurement in a CCP operating at a driving frequency of 13.56 MHz and at a plasma power of 100 W and a pressure of 75 mTorr. They report a value for the $O(^3P_2)$ density of 1.6×10^{14} cm^{-3} and an oxygen dissociation of 0.03 on the assumption of a 300 K plasma; using this temperature in place of the one found for the measurements presented here (490 K), the fraction of dissociated oxygen in our ICP would be around 0.07. The agreement between the two values is fair, although the errors in calibrating the measurements of Collart *et al.*[16] from using a known amount of $O(^3P_2)$ in a microwave discharge are not discussed and may be significant. The TALIF measurements of Hancock & Toogood[18] conducted in a 13.56 MHz CCP chamber produce a value of the O atom density of 5×10^{13} cm^{-3} at 200 W and 50 mTorr pure O_2, corresponding to a dissociation degree, δ, of 0.02.

Nagai *et al.*[13] use an ICP chamber of construction similar to the one used here, again at 13.56 MHz driving frequency although at a much higher flow rate of O_2 gas (100 sccm compared to 9 sccm used in this study). The absorption technique of VUVAS (calibrated using a range of assumptions and modelling of the VUV light source) is used to measure the density of $O(^3P_2)$, and at 500 W plasma power and 10 mTorr plasma pressure is found to be 4×10^{13} cm^{-3}, corresponding to a degree of dissociation 0.06 at 300 K, in reasonable agreement with the value found here.

Source	Method	Plasma	Power	Pressure	[O] / cm^{-3}	[O]/2[O_2]
Booth *et al.*[9]	VUVAS	ECR	160 W	6 mTorr	2.8×10^{12}	0.01
Collart *et al.*[16]	TALIF	CCP	100 W	75 mTorr	1.6×10^{14}	0.03
Teslja *et al.*[4]	CRDS	μwave	-	3 500 mTorr	1.6×10^{15}	0.007
Dilecce *et al.*[1920]	TALIF	Jet	550 W	130 mTorr	3.0×10^{15}	0.36
Granier *et al.*[10]	VUVAS	μwave	<1.2 kW	1 000 mTorr	1.1×10^{15}	0.02
Hancock *et al.*[18]	TALIF	CCP	200 W	50 mTorr	5×10^{13}	0.02
Harris *et al.*[22]	ICLAS	μwave	80 W	1 275 mTorr	7.3×10^{15}	0.09
Kitajima *et al.*[14]	VUVAS	CCP	200 W	50 mTorr	3.0×10^{12}	0.001
Nagai *et al.*[13]	VUVAS	ICP	500 W	10 mTorr	4.0×10^{13}	0.06
Shibata *et al.*[48]	Model	CCP	-	500 mTorr	5.0×10^{13}	0.002
Singh *et al*[23]	MS	ICP	700 W	30 mTorr	5.6×10^{15}	0.05

Table 5.2: A range of values for the $O(^3P)$ number density and degree of O_2 dissociation reported in the literature.

It should be noted that the values reported in table 5.2 refer to the total O atom density (i.e. in $O(^3P_2$, $^3P_1$ and $^3P_0)$); the value reported here is that found solely in the oxygen atom's ground state (O^3P_2). Two low lying excited states are present in oxygen atoms, $^3P_1$ and $^3P_0$ at 158 cm^{-1} and 227 cm^{-1} above the ground state, respectively. These values are approximately equivalent to the thermal energy at 298 K, and it can thus be assumed that the levels possess populations determined by a Boltzmann distribution. Taking into account the degeneracy of the levels it is calculated that around 74 % of the total oxygen atom density will lie in the ground $^3P_2$ state. Scaling up the concentration reported here for $O(^3P_2)$ yields a total oxygen atom concentration of 6.4×10^{14} cm^3 at 500 W plasma power and 100 mTorr plasma pressure.

The oxygen atom density observed can be understood in terms of the dominant production and loss processes. The electron impact dissociation of O_2 (equation (5.9)) is by far the dominant production route for ground state oxygen atoms (^3P_j) with a rate constant of $k = 8.9 \times 10^{-10}$ cm^3 s^{-1} (at an electron temperature of 2.5 eV[60,61]). Dissociative excitation (equation (5.10)) producing a ground state oxygen atom and an excited oxygen atom ($O(^1D_2)$) has a rate constant at the same electron temperature of $k = 1.7 \times 10^{-9}$ cm^3 s^{-1} [60,61]. Dissociative attachment of an electron and an oxygen molecule (equation (5.11)) is another possible route to $O(^3P)$ formation, but has a rate constant ($k = 1.5 \times 10^{-11}$ cm^3 s^{-1} at 2.5 eV) nearly two orders of magnitude lower[60,61]. Other processes to consider for $O(^3P_j)$ formation

include charge transfer reactions between charged oxygen atoms and neutral oxygen molecules, and recombination reactions between molecular ions, atomic ions and electrons and cations. However, the rates for these processes are such that under the plasma operating conditions they can be neglected.

$$O_2 + e \rightarrow O(^3P) + O(^3P) + e \quad (5.9)$$

$$O_2 + e \rightarrow O(^3P) + O(^1D) + e \quad (5.10)$$

$$O_2 + e \rightarrow O(^3P) + O^- \quad (5.11)$$

The loss processes essentially consist of three possible mechanisms; wall recombination, gas phase recombination and removal by pump action. The low flow rate of the feedstock gas atoms under the operating conditions of the plasma chamber eliminates the latter process as a dominant loss route. The gas phase recombination reactions are given by equations (5.12)-(5.15). However, the rates for these reactions[61] are so low that they can also by neglected along with any termolecular processes[13].

$$O(^3P) + O^- \rightarrow O_2 + e \quad (5.12)$$

$$O(^3P) + e \rightarrow O(^1D) + e \quad (5.13)$$

$$O(^3P) + e \rightarrow O^+ + 2e \quad (5.14)$$

$$O(^3P) + O_3 \rightarrow 2O_2 \quad (5.15)$$

The only remaining mechanism to consider is diffusion followed by wall recombination, and this has indeed been documented as the primary loss route for oxygen atoms at pressures under a few Torr[62]. The decay rate of the O atoms can thus be estimated by solving Fick's diffusion equation, given by equation (5.16) where D is the diffusion coefficient for O atoms in O_2 and n_0 is their density.

$$\frac{\partial n_0}{\partial t} = D\frac{\partial^2 n_0}{\partial z^2} \quad (5.16)$$

Expressing the result as a diffusion lifetime, τ_D, allows the use of equation (5.17) which conveniently parameterises the rate constant into a few key variables[13].

$$\tau_D = \frac{p\Lambda_0^2}{D} + \frac{2l_0(2-\alpha)}{v\alpha} \tag{5.17}$$

Here, p is the pressure, Λ_0 is the geometric diffusion length (equation (5.18)) determined by the chamber structure (height, L and radius, R), $l_0 = V/S$ (volume to surface area) and v is the velocity of the O atoms (determined from the Doppler width). The quantity α is the surface loss probability on the chamber wall.

$$\Lambda_0^{-2} = \left(\frac{\pi}{L}\right)^2 + \left(\frac{2.405}{R}\right)^2 \tag{5.18}$$

The diffusion lifetime can be calculated for the ICP chamber to check the validity of assuming diffusion and wall recombination as the dominant loss mechanism. Taking values for L and R of 21 cm and 17.5 cm, respectively, yields a value of $\Lambda_0 = 4.9$ cm. The volume, V, of the chamber is 20200 cm^3 and the internal surface area, S, is 4200 cm^2 giving a value of $l_0 = 4.8$ cm. The diffusion coefficient, D, is taken from the literature[63,64] and has a value of 2.9×10^4 cm^2 Pa s^{-1}, while the velocity, v, of the oxygen atoms is calculated to be 8.1×10^4 cm s^{-1} using a translational temperature of 490 K derived from the Doppler width of the absorption profile shown in figure 5.3. The value of α is taken to be the same as that measured for stainless steel, 0.17[23] (the ICP chamber is, however, constructed from aluminium). Using these values in equation (5.17) yields a lifetime, τ_D of 1.2×10^{-2} s. Dividing the total number of oxygen atoms by this lifetime, and balancing the resultant diffusion loss rate against the electron impact dissociation production rate yields a value for the electron density (an unknown in this plasma system). This is found to be around 1×10^{10} cm^{-3} at 100 mTorr plasma pressure and 500 W plasma power, a value at the upper end of those observed in similar plasma environments[10,23], and a factor of three higher than that inferred from planar probe measurements conducted under the same plasma conditions[65].

The value for the O atom density and the inferred electron density are upper limits due to several experimental considerations. As previously stated, the length of the cavity bounding the plasma chamber is 75 cm, while the length of the plasma is assumed to be 35

cm (the diameter of the plasma chamber). However, as the primary loss mechanism for the O atoms is diffusion to the walls followed by recombination, this absorption length may in reality extend beyond the actual chamber and into the baffle arms holding the high reflectivity mirrors. This would increase the line-of-site number density by up to a factor of 75/35 ~ 2.15, and leads to a corresponding decrease in the O atom (and also electron) number density to $(2.2 \pm 0.3) \times 10^{14}$ cm^{-3}, corresponding to a dissociation degree, δ, of 0.06, in closer agreement with the values presented in table 5.2.

As can be seen from equation (5.17), the diffusion lifetime is pressure dependent and will decrease at lower pressures, increasing the rate of loss of oxygen atoms. On the assumption of an increased electron temperature at lower pressures and a decreased electron density, the production rate will not change markedly resulting in a decreased O atom density at lower pressures, as observed. The plasma power will also affect the diffusion lifetime through the temperature and therefore the velocity term in equation (5.17). At lower plasma powers the velocity will decrease resulting in an increase in τ_D and a decrease in the loss rate, hence an increasing O atom density might be expected. However, changes to the EEDF and electron density with plasma power are more extreme than when changing the plasma pressure, and hence the interplay of these competing factors on the production and loss kinetics will result in a far more complex dependence.

The addition of various amounts of dopant gases to the oxygen discharge has been observed to increase the concentration of oxygen atoms. Booth *et al.*[9] added N_2, Kr and SF_6 to the plasma feedstock gas and witnessed an increase in [O] for all three gases, up to a maximum of 30 % dissociation of O_2 with the addition of 10 % SF_6 to the mixture. Granier *et al.*[10] dope varying amounts of N_2 into an oxygen microwave plasma and also find dissociation of up to 30 % when 20 % or more of the feedstock gas is N_2. Hancock & Toogood[18] observe that the addition of just 5 % CF_4 to an O_2 discharge operating at 200 W and 50 mTorr plasma power and pressure (in a RF CCP) is found to increase the O atom concentration by a factor of 2.6, while the wall loss rate decreases by a factor of 2.2. All three researchers attribute this increase in oxygen atom density and dissociation fraction to the blocking of recombination sites on the chamber walls by the dopant gas, thus reducing the loss mechanism for the O atoms.

Despite the lack of detection of $O_2(a^1\Delta_g)$, it is possible to assign an upper limit to the concentration of this species using the absolute sensitivity demonstrated in the 1*f* detection of NH_3 (1.3×10^{-6} cm^{-1}). Taking the $J = 12$ level as an example, its maximum population must be no greater than 1.0×10^{15} cm^{-3} in order to remain undetected (i.e. to

have a *S/N* lower than 1). This translates to a total $v = 0$ population of $O_2(a^1\Delta_g)$ of 1.7×10^{16} cm^{-3}, which corresponds to 11 % of the initial oxygen concentration converted to $O_2(a^1\Delta_g)$ at 5 Torr.

The most obvious method for enhancing the sensitivity (*S/N*) of the detection scheme is by increasing the integration time of the measurements. However, a careful diagnostic of the experimental setup determined the limiting feature to be the frequency stability of the doubled Nd:YAG laser. While in theory this system locks to a given mode, the lack of active temperature stability within the device causes a drift of the order of several hundred MHz in its output frequency. Attempts were made to limit this drift by water cooling of the brass base upon which the Nd:YAG laser is mounted; a small reduction was achieved. Unfortunately, the size of the frequency drift (measured at 542 MHz over 200 seconds) corresponds to more than the FWHM of the absorbing lines, and thus averaging over long periods of time actually results in a decrease in the *S/N*. This effect is quantified by tuning the frequency of the external cavity diode laser to match the DFG radiation to the centre of the ammonia line at 5237.325 cm^{-1}. The 1*f* demodulated output signal was monitored as a function of time over 200 s (figure 5.7a) from which a flat line with zero deviation would be observed for stable system; the real situation can be seen to be far from the ideal case. Plotting this data as an Allan variance[66] (figure 5.7b) allows the effect of integration time upon the *S/N* to be determined, with a time of a few seconds found to produce the optimum sensitivity.

Alternative methods utilising this DFG radiation in the detection of $O_2(a^1\Delta_g)$ include further multi-passing though the chamber, although this is limited by the decreasing amount of resultant radiation after each pass and the collimation of the radiation beam. The construction of a cavity would also provide the enhancement required, however the low power levels of the radiation, the frequency instability of the laser and the need for specialist high reflectivity mirrors would make this option experimentally complicated and expensive.

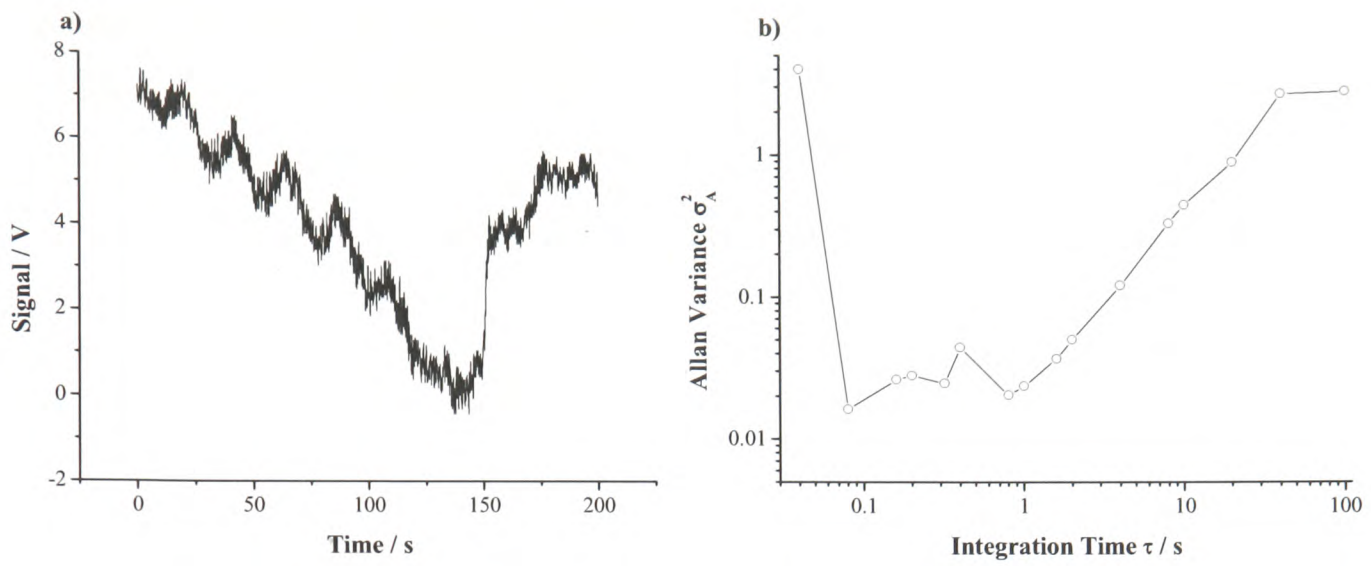


Figure 5.7: The drift in the output frequency of the doubled Nd:YAG laser over time monitored as a) a deviation in the frequency from the centre of the ammonia transition probed using WMS at the first harmonic, and b) the Allan variance of the detection system over time.

5.5 Summary

Oxygen atoms have been detected in their ground state ($^3P_2$) using radiation generated at 630.205 nm to probe the O($^1D_2 \leftarrow ^3P_2$) highly forbidden transition. The small absorption cross-section and low number densities necessitated the use of CEAS in the detection scheme, and a concentration of (4.8 ± 0.6) × 10^{14} cm^{-3} was recorded at conditions of maximum plasma pressure and power. As the discharge consisted of pure oxygen, the dissociation degree of O_2 is found to be a maximum of 0.12. Taking into consideration that the dominant loss route for the O atoms is diffusion to the walls followed by recombination, the length of the Baffle arms holding the cavity mirrors will become relevant. The resultant increase in pathlength yields a lower O($^3P_2$) density of (2.2 ± 0.3) × 10^{14} cm^{-3}, corresponding to a lower limit for the degree of O_2 dissociation of 0.06. The low *S/N* of the experimental setup meant that no further viable measurements of the oxygen atom concentration could be conducted, although the density was seen to decrease with decreasing plasma power and pressure. The concentration and dissociation degree observed were compared to those found in the literature, and an attempt was made to rationalise the data in terms of the kinetic processes.

A DFG system was constructed using a newly developed material, MgO doped PPLN, to generate 1.9 μm light in order to probe the (0,0) band of the $O_2(b^1\Sigma_g^+ \leftarrow a^1\Delta_g)$ quadrupolar transition. The generation of the radiation was demonstrated on a transition from the ground state of ammonia, and a *S/N* of homodyne absorption and WMS was

calculated. Attempts were made to detect $O_2(a^1\Delta_g)$ at a variety of conditions (by altering the plasma power and pressure and feedstock gas compositions) in an ICP and a microwave discharge, but to no avail. However, an upper limit of 1.7×10^{16} cm^{-3} was placed on the $v = 0$, $O_2(a^1\Delta_g)$ population (corresponding to a conversion efficiency of 11 % in a 5 Torr pure O_2 discharge) using the sensitivities determined by optimising the detection system on the ammonia transition.

References

[1] Donahue, T.M. *et al*, J. Geophys. Res., **78**, 6662, (1973)

[2] Slanger, T.G. & Copeland, R.A., Chem. Rev., **103**, 4731, (2003)

[3] Peze, P. *et al*, J. Phys. D: Appl. Phys., **26**, 1622, (1993)

[4] Teslja, A. & Dagdigian, P.J., Chem. Phys. Lett., **400**, 374, (2004)

[5] Kamalov, V.F. *et al*, Quantum Electronics, **15**, 1319, (1985)

[6] Zakharov, S.D. *et al*, Quantum Electronics, **29**, 1031, (1999)

[7] McDermott, W.E. *et al*, Appl. Phys. Lett., **32**, 469, (1978)

[8] Jasik, J. *et al*, Czech. J. Phys., **54**, 661, (2004)

[9] Booth, J.P. *et al*, J. Appl. Phys., **69**, 618, (1991)

[10] Granier, A. *et al*, J. Appl. Phys., **75**, 104, (1994)

[11] Czerwiec, T. *et al*, Surface and Coatings Technology, **98**, 1411, (1998)

[12] Mozetic, M. *et al*, J. Vac. Sci. Technol. A., **21**, 369, (2003)

[13] Nagai, H. *et al*, Rev. Sci. Instrum., **74**, 3453, (2003)

[14] Kitajima, T. *et al*, J. Phys. D: Appl. Phys., **37**, 2670, (2004)

[15] Celii, F.G. *et al*, Appl. Opt., **29**, 3135, (1990)

[16] Collart, E.J.H. *et al*, J. Appl. Phys., **70**, 5278, (1991)

[17] Katsch, H.M. *et al*, J. Appl. Phys., **88**, 6232, (2000)

[18] Hancock, G. & Toogood, M.J., Appl. Phys. Lett., **60**, 35, (1992)

[19] Dilecce, G. *et al*, J. Phys. D: Appl. Phys., **33**, L53, (2000)

[20] Dilecce, G. & De Benedictis, S., Plasma. Sources. Sci. Technol., **8**, 266, (1999)

[21] Niemi, K. *et al*, Plasma Sources Sci. Technol., **14**, 375, (2005)

[22] Harris, S.J. & Weiner, A.M., Opt. Lett., **6**, 142, (1981)

[23] Singh, H *et al*, J. Appl. Phys., **88**, 3748, (2000)

[24] Gomez, S. *et al*, Appl. Phys. Lett., **81**, 19, (2002)

[25] Arnold, S.J. *et al*, J. Chem. Phys., **44**, 2529, (1966)

[26] Derwent, R.G. & Thrush, B.A., Trans. Faraday Soc., **67**, 2036, (1971)

[27] Fisk, G.A & Hays, G.N., Chem. Phys. Lett., **79**, 331, (1981)

[28] Badger, R.M. *et al*, J. Chem. Phys., **43**, 4345, (1965)

[29] McNeal, R.J. & Cook, G.R., J. Chem. Phys., **45**, 3469, (1966)

[30] Falick, A.M. *et al*, J. Chem. Phys., **42**, 1837, (1965)

[31] Bernard, D.J. & Pchelkin, N.R., Rev. Sci. Instrum., **49**, 794, (1978)

[32] Yagi, M. *et al*, Chem. Lett., **33**, 152, (2004)

[33] Spalek, O. *et al*, J. Phys. B, **32**, 1885, (1999)

[34] Newman, S.M *et al*, J. Phys. Chem. A, **104**, 9467, (2000)

[35] Gamache, R.R. & Goldman, A., J. Quant. Spec. Rad. Trans., **69**, 389, (2001)

[36] Miller, H.C. *et al*, J. Quant. Spec. Rad. Trans., **69**, 305, (2001)

[37] Lafferty, W.J. *et al*, Appl. Opt., **37**, 2264, (1998)

[38] Duo, L. *et al*, J. Phys. Chem. A., **105**, 281, (2001)

[39] Noxon, J.F., Can. J. Phys., **39**, 1110, (1961)

[40] Fink, E.H. *et al*, Can. J. Phys., **64**, 242, (1986)

[41] Coxon, J.A. & Roychowdhury, U.K., Appl. Spec., **40**, 203, (1986)

[42] Gylys, V.T. & Rubin, L.F., Appl. Opt., **37**, 1026, (1998)

[43] Pazyuk, V.S. *et al*, Quantum Electronics, **31**, 363, (2001)

[44] Williams, S. *et al*, Opt. Lett., **29**, 1066, (2004)

[45] Baer, D.S. *et al*, Appl. Phys. B, **75**, 261, (2002)

[46] Gupta, M. *et al*, Chem. Phys. Lett., **400**, 42, (2004)

[47] Wu, H.M, Plasma Sources Sc. Technol., **9**, 347, (2000)

[48] Shibata, M. *et al*, J. Appl. Phys., **77**, 6181, (1995)

[49] Feoktistov, V.A. *et al*, J. Phys. D: Appl. Phys., **28**, 1346, (1995)

[50] Bakowski, B. *et al*, J. Phys. D: Appl. Phys., **37**, 2064, (2004)

[51] Jundt, D.H., Opt. Lett., **22**, 1553, (1997)

[52] HC Photonics, Hsinchu 300, Taiwan, www.hcphotonics.com

[53] NIST Atomic Spectra database version 3.0, www.nist.gov

[54] Rothman, L.S. *et al*, J. Quant. Spec. Rad. Trans., **82**, 5, (2003)

[55] Chiu, Y.N., J. Chem. Phys., **42**, 2671, (1965)

[56] Gilmore, F.R. *et al*, J. Phys. Chem. Ref. Data., **21**, 1005, (1992)

[57] Burch, D.E. & Gryvnak, D.A., Appl. Opt., **8**, 1493, (1969)

[58] Cheah, S.L. *et al*., J. Quant. Spec. Rad. Trans., **64**, 467, (2000)

[59] Klopovskii, K.S. *et al*., Plasma Physics Reports, **18**, 1606, (1992)

[60] Gudmundsson, J.T. *et al*, Plasma Sources Sci. Technol., **8**, 22, (1999)

[61] Lee, C. *et al*., J. Electrochem. Soc., **141**, 1546, (1994)

[62] Pinheiro, M.J., Plasma Sources Sci. Technol., **7**, 524, (1998)

[63] Reid, R.C., Prausnitz, J.M. & Sherwood, T.K., *The Properties of Gases and Liquids*, McGraw–Hill, New York, (1977)

[64] R. A. Svehla, NASA Tech. Rep., R-132, (1962)

---

[65] Bakowski, B., Laser Studies of Species in Plasmas, DPhil Thesis, PTCL, Oxford University, (2003)

[66] Werle, P. *et al.*, Appl. Phys. B., **57**, 131, (1993)